



HAL
open science

Thermal and environmental effects on Pt-based hollow nanospheres catalysts: insights from in-situ and operando TEM

Josephine Rezkallah

► **To cite this version:**

Josephine Rezkallah. Thermal and environmental effects on Pt-based hollow nanospheres catalysts: insights from in-situ and operando TEM. Materials Science [cond-mat.mtrl-sci]. Normandie Université, 2023. English. NNT: 2023NORMR105 . tel-04506556

HAL Id: tel-04506556

<https://theses.hal.science/tel-04506556>

Submitted on 15 Mar 2024

HAL is a multi-disciplinary open access archive for the deposit and dissemination of scientific research documents, whether they are published or not. The documents may come from teaching and research institutions in France or abroad, or from public or private research centers.

L'archive ouverte pluridisciplinaire **HAL**, est destinée au dépôt et à la diffusion de documents scientifiques de niveau recherche, publiés ou non, émanant des établissements d'enseignement et de recherche français ou étrangers, des laboratoires publics ou privés.



Normandie Université



THÈSE

Pour obtenir le diplôme de doctorat

Spécialité **PHYSIQUE**

Préparée au sein de l'**Université de Rouen Normandie**

Thermal and environmental effects on Pt-based hollow nanospheres catalysts : insights from in-situ and operando TEM

Présentée et soutenue par
JOSEPHINE REZKALLAH

Thèse soutenue le 14/12/2023
devant le jury composé de :

M. OVIDIU ERSEN	Professeur des Universités - UNIVERSITE STRASBOURG	Rapporteur du jury
M. JAYSEN NELAYAH	Professeur Associé - UNIVERSITE PARIS 7 PARIS DIDEROT	Rapporteur du jury
MME CÉCILE GENEVOIS	Ingénieur de Recherche - Université d'Orléans	Membre du jury
MME SIMONA MOLDOVAN	Ingénieur de Recherche - Université de Rouen Normandie	Membre du jury
M. LUDOVIC PINARD	Professeur des Universités - ENSICAEN	Président du jury
M. XAVIER SAUVAGE	Directeur de recherche - Université de Rouen Normandie	Directeur de thèse

Thèse dirigée par **XAVIER SAUVAGE** (GROUPE DE PHYSIQUE DES MATERIAUX)



ABSTRACT

Heterogeneous catalysis plays a crucial role in enhancing the efficiency, sustainability, and cost-effectiveness of chemical reactions. The use of metal nanoparticles in heterogeneous catalysis boosts catalytic efficiency due to their high surface-to-volume ratio, tunable electronic properties, and high catalytic activity. Noble metal-based catalysts, including Platinum (Pt), are widely recognized for their high effectiveness and selectivity in a broad range of industrial reactions.

The main focus of this thesis is the investigation of synthesized Pt-based hollow nanospheres, which exhibit unique catalytic properties. This is due to their increased surface-to-volume ratio, reduced material density and economic efficiency. The transmission electron microscopy (TEM) is used for these materials' characterization due to its high resolution and adaptability to nanomaterials. Using electron tomography, channels within the shell complex 3D morphology are identified and quantified. This makes a significant contribution to the development of nanoreactors and offers exciting possibilities for enhanced catalytic properties.

Hollow nanospheres used as nanocatalysts are prone to deactivate due to several processes including sintering/collapsing, surface poisoning and coking. This research helps understand these transformations, using the CO₂ hydrogenation reaction as a model. It uses in-situ and operando TEM methodology to monitor the Pt-based hollow nanospheres in real-time within an Environmental Cell (E-cell). It examines the sintering of nanoparticles in the nanospheres shell and the temperature-induced collapse of their hollow microstructure. This work explores how temperature and the gas nature influence the morphological changes in Pt-based nanospheres and the mechanisms behind these changes. It also identifies the CO₂ hydrogenation reaction products and aids determining the reaction pathway. This research identifies the specific temperatures at which the morphological changes occur under different environments (vacuum, H₂ gas and CO₂-H₂ gas mixture). The most reactive environment (H₂) leads to early collapse of such complex system as compared to inert atmospheres. The findings of this research have laid the foundation of a novel catalysts design.

Keywords: heterogeneous catalysis, metal nanoparticles, Platinum, hollow nanospheres, Transmission electron microscopy, Electron Tomography, in-situ and Operando TEM, CO₂ hydrogenation, catalytic properties.

RÉSUMÉ

La catalyse hétérogène joue un rôle crucial dans l'amélioration de l'efficacité, de la durabilité et de la rentabilité des réactions chimiques. L'utilisation de nanoparticules métalliques dans la catalyse hétérogène renforce l'efficacité catalytique en raison de leur rapport surface/volume élevé, de leurs propriétés électroniques modulables et de leur activité catalytique élevée. Les catalyseurs à base de métaux nobles, dont le platine (Pt), sont largement reconnus pour leur grande efficacité et leur sélectivité dans un large éventail de réactions industrielles.

Le but principal de cette thèse est l'étude de nanosphères creuses à base de Pt synthétisées, qui présentent des propriétés catalytiques uniques. Cela est dû à leur rapport surface/volume augmenté, à leur densité de matière réduite et à leur efficacité économique. La microscopie électronique en transmission (MET) est utilisée pour la caractérisation de ces matériaux en raison de sa haute résolution et de son adaptabilité aux nanomatériaux. En utilisant la tomographie électronique, des canaux au sein de la morphologie tridimensionnelle complexe de la coquille sont identifiés et quantifiés. Cela contribue de manière significative au développement de nanoréacteurs et offre des perspectives passionnantes pour améliorer leurs propriétés catalytiques.

Les nanosphères creuses utilisées comme nanocatalyseurs sont sujettes à la désactivation en raison de plusieurs processus, notamment le frittage/effondrement, l'empoisonnement de surface et la cokéfaction. Cette recherche aide à comprendre ces transformations en utilisant la réaction d'hydrogénation du CO₂ comme modèle. Elle utilise une méthodologie MET in situ et Operando pour surveiller en temps réel les nanosphères creuses à base de Pt au sein d'une cellule environnementale (E-cell). Elle examine le frittage des nanoparticules dans la coquille des nanosphères et l'effondrement de leur microstructure creuse induit par la température. Ce travail explore comment la température et la nature du gaz influencent les changements morphologiques des nanosphères à base de Pt et les mécanismes à l'origine de ces changements. Elle identifie également les produits de la réaction d'hydrogénation du CO₂ et contribue à déterminer la voie de la réaction. Cette recherche identifie les températures spécifiques auxquelles les changements morphologiques se produisent dans différents environnements (vide, gaz H₂ et mélange de gaz CO₂-H₂). L'environnement le plus réactif (H₂) entraîne un effondrement précoce de ce système complexe par rapport aux atmosphères inertes. Ces découvertes ont jeté les bases d'une nouvelle conception de catalyseurs.

Mots-clés : *catalyse hétérogène, nanoparticules métalliques, platine, nanosphères creuses, microscopie électronique en transmission, tomographie électronique, MET in-situ et Operando, hydrogénation du CO₂, propriétés catalytiques.*

ACKNOWLEDGMENTS

I extend my deepest gratitude to my esteemed thesis committee for their dedicated time and thorough review of my work. I would also like to thank you for the insightful and constructive discussions we've had. Your collective expertise in the different fields of my thesis provided valuable perspectives that enriched the content of my research.

I extend my heartfelt appreciation to my thesis Director, Xavier Sauvage, for his constant encouragement, and guidance. Your mentorship during this thesis journey has been invaluable, and I consider myself fortunate to have had a director who not only guided me academically but also was a role model in every aspect of scholarly pursuit. I extend my gratitude to my co-supervisor, Simona Moldovan, for the time and effort dedicated to this Ph.D. journey. Your substantial contributions have played a crucial role in shaping the individual I am today, and for that, I am appreciative.

To my family, my mother Christine, my father Michael, my brothers Charbel and Georges and my cousins Elie, Maha, Maroun, Hanna and Fadi, your unwavering love, encouragement, and understanding have sustained me during the challenging phases of this journey. Your belief in my abilities have been the driving force behind my accomplishments.

To my dear friends, Michella, Taline, Matteo, Rania, Antonio, Antoun, Sami, Rita, Youssef, Mohammad, Louis, Sonia, Chantal, and many others—there aren't sufficient pages to individually acknowledge each one of you. You collectively became my second family in France. Your unconditional support and the shared moments we've experienced have enriched this chapter of my life beyond measure. I am deeply grateful for the warmth and friendship you've generously extended to me throughout this journey. Whether in the darkest or happiest moments, your presence has been a constant source of comfort and joy. I hold each of you dear, and I love you all.

Finally, to my fellow colleagues and all individuals at the GPM laboratory, each one of you has contributed to making this experience truly wonderful in his own way. Thank you all.

TABLE OF CONTENTS

GENERAL INTRODUCTION	1
-----------------------------------	----------

CHAPTER I: Catalysts transformations and In-Situ TEM for heterogeneous catalysis: Literature Review	5
--	----------

1. Principles of catalysis in chemical reactions.....	6
1.1. Brief history about catalysis	6
1.2. Catalysis principles	6
1.3. Heterogeneous catalysis.....	7
2. Different types of catalysts and their properties	12
2.1. Bulk materials: unsupported catalysts	12
2.2. Noble metal nanocatalysts	13
3. Pt-based nanocatalysts	16
3.1. Catalytic applications of Pt-based nanoparticles	16
3.2. The CO ₂ hydrogenation reaction	18
3.3. Pt-based hollow nanospheres by the galvanic replacement method.....	21
4. Transformations of nanocatalysts during a chemical reaction.....	27
5. Transmission electron microscopy.....	32
6. In-situ and operando transmission electron microscopy	37
6.1. Differentially vacuum pumped environmental TEM	37
6.2. Window-gas cell environmental TEM.....	39
6.3. The advantages and disadvantages of using the environmental gas cell	40
6.4. Operando transmission electron microscopy	40
6.5. Examples of applications of the Environmental cell in catalysis research	41
7. The problematic and the strategy of the project.....	43

CHAPTER II: Experimental Approach: Pt-Based Material Synthesis and In-Situ and Operando TEM technology	45
---	-----------

1. Synthesis of the Co-templated Pt hollow nanospheres (HNS).....	46
1.1. Synthesis basic principle.....	46
1.2. Synthesis of Co-templated hollow nanospheres: batches 1 and 2	47
2. Techniques used for basic characterization.....	48
2.1. The scanning electron microscopy (SEM)	48
2.2. The X-Ray diffraction (XRD) technique	49

3.	TEM investigations	51
3.1.	Basic principle of the transmission electron microscopy	51
3.2.	Characteristics of the transmission electron microscope utilized	53
3.3.	The transmission electron microcopy working modes employed and the experimental conditions.....	54
4.	Electron tomography (ET)	57
5.	In-situ and operando TEM	59
5.1.	Furnace type heating holder.....	59
5.2.	Environmental cell technology	60
5.3.	Gas manifold.....	68
5.4.	Residual Gas Analyzer	68
5.5.	Methodology of the TEM experiments.....	73
CHAPTER III: Unveiling 3D Structure and Morphology of Pt-Based Hollow Nanospheres.....		75
1.	Physical characteristics of the Pt-1 hollow nanospheres.....	76
1.1.	Morphology and crystalline structure	76
1.2.	Morphology and size distribution by STEM-HAADF	80
1.3.	Chemical composition by STEM-EDS.....	83
1.4.	3D morphology analysis by Electron Tomography.....	85
2.	Particularities of the Pt-2 hollow nanospheres.....	89
2.1.	Morphology and crystalline structure by SEM and XRD	89
2.2.	Morphology and size distribution by STEM-HAADF	91
2.3.	Chemical composition and crystalline structure by STEM-EDS and SAED	93
2.4.	3D morphology analysis by Electron Tomography.....	95
3.	Discussions.....	97
4.	Conclusions.....	100
CHAPTER IV: Exploring Pt-Based Catalyst Behavior with In-Situ and Operando TEM Under Different Environments		103
1.	Morphological evolution of the Pt-based hollow nanospheres during thermal annealing under vacuum	104
1.1.	Morphological evolution of the Pt-1 system under vacuum.....	105
1.1.1.	In situ TEM/STEM using the furnace-type heating holder	105
1.1.2.	In situ STEM using the MEMS-type holder.....	109
1.2.	Comparison of the thermal stability of the Pt-1 and Pt-2 systems	115

2.	Morphological evolution of the Pt-based hollow nanospheres under hydrogen atmosphere	122
2.1.	Thermal stability of Pt-1 hollow nanospheres	122
2.1.1.	Spatial distribution of Pt and Co post H ₂ assisted experiment in Pt-1 system	125
2.2.	Comparing the Pt-1 and Pt-2 system behavior under H ₂ atmosphere.....	126
2.2.1.	Thermal stability of Pt-2 hollow nanospheres	126
2.2.2.	Spatial distribution of Pt and Co post H ₂ assisted experiment in Pt-2 system	129
3.	Investigation of the Pt-based HNS behavior upon CO ₂ hydrogenation reaction	132
3.1.	Morphological evolution of Pt-based hollow nanospheres during thermal annealing	132
3.1.1.	Thermal stability of Pt-1 system.....	132
3.1.2.	Thermal stability of Pt-2 system.....	135
3.2.	Identification of CO ₂ hydrogenation pathway over the Pt-based hollow nanospheres	137
3.2.1.	Blank experiment to test the RGA data reliability.....	137
3.2.2.	Identification of the reaction products and onset temperature over the Pt-1 ..	138
3.2.3.	Identification of the reaction products and onset temperature over Pt-2.....	143
3.3.	Study of the thermal stability of Pt-based catalysts during isothermal CO ₂ hydrogenation reaction at 180°C	144
3.3.1.	Pt-1 hollow nanospheres.....	144
3.3.2.	Pt-2 hollow nanospheres.....	146
4.	Conclusions	148
	CONCLUSIONS AND PERSPECTIVES.....	151
	APPENDIX	155
	REFERENCES	159

GENERAL INTRODUCTION

Catalysis plays a pivotal role in the chemical industry due to its capacity to accelerate chemical reactions making them more energy-efficient, environment friendly and cost-effective. By reducing the required temperature and pressure conditions for reactions, catalysts contribute to energy savings, sustainability, resource efficiency and economic growth in various industrial processes e.g. clean energy production, pharmaceuticals, and food production. Most of these processes occur in heterogeneous catalysis, where reactions happen at the interface of a solid catalyst and a gas or liquid phase.

Nanomaterials have found applications in heterogeneous catalysis for more than six decades. On the one hand, metal nanoparticles (NPs), with high surface-to-volume ratio, abundant active surface atoms, and unique electronic configurations in contrast to their bulk counterparts, hold significant potential in this area. Among these materials, noble metal NPs including Platinum (Pt) are highly valuable in nanocatalysis due to their unique electronic, chemical, and optical properties. On the other hand, metal hollow nanospheres, present distinctive catalytic characteristics that set them apart from their solid counterparts, offering advantages such as an increased active surface area, reduced material density, resource conservation, and cost-effectiveness. Therefore, the Pt-based nanospheres are the nanocatalysts under investigations during this thesis.

“The smaller the particle, the bigger the problem” holds true as metal nanocatalysts can undergo deactivation through various mechanisms: sintering, surface poisoning and coking, etc. Understanding the microstructural catalyst behavior during the reaction is important for advancing catalyst design. Investigating the influence of individual reaction parameters (Temperature, gas nature) of the catalyst behavior is crucial for gaining a deeper understanding of catalyst dynamics and structure-activity relationships. This study is essential in optimizing catalysts for enhanced performance. Given the various catalytic application for Pt-based nanomaterials, including selective hydrogenation reactions and proton-exchange membrane fuel cells (PEMFC) with H₂-rich environment, the CO₂ hydrogenation reaction is chosen as a model to investigate the catalyst behavior in a reducing environment. The thesis focuses on the effect of temperature under different environments on the catalyst’s morphological evolution and the underlying mechanisms governing this evolution.

For this thesis, two sets of Pt-based hollow nanospheres were synthesized. The Transmission electron microscopy (TEM) is the main technique used for the characterization of each set of the nanocatalysts. The TEM plays a significant role in advancing the understanding of nanomaterials by providing high-resolution insights into their morphological, structural and chemical characteristics. Electron tomography is used to provide valuable insights into the Pt-based nanospheres 3D morphology. Their complex shell morphology affecting their catalytic properties is investigated. A comparison between the two sets of Pt-based materials is conducted. However, TEM traditionally operates under high vacuum conditions, preventing the investigations of the catalyst under realistic reaction environments. Investigating a material's behavior under reaction conditions provides a comprehensive understanding of the mechanisms driving its morphological evolution during chemical reactions.

The in-situ TEM is a pivotal development in TEM technology, and it is indispensable in catalysis research. In this thesis, it enables the examination of the Pt-based hollow nanospheres using an Environmental Cell (E-cell from ProtochipsTM), wherein gas composition, pressure, and temperature can be precisely controlled. This technique facilitates real-time monitoring of the Pt-based nanospheres under the CO₂ hydrogenation reaction conditions. The effect of temperature and gas nature across different temperature ranges are studied. The mechanisms driving the morphological evolution phenomena of the hollow nanospheres are investigated: the NPs sintering and the structural and morphological collapse of the hollow nanospheres.

The Operando TEM approach is also used through a residual gas analyzer (RGA). While monitoring the catalysts morphological evolution, this approach allows simultaneous analysis of the reaction products. It helps to identify the reaction pathway and onset temperature. This approach also contributes to the assessment of possible surface poisoning leading to the catalyst deactivation.

The thesis is structured into four chapters, and a brief overview of what each chapter's content is presented below.

In Chapter I, an introduction of catalysis is presented, including its historical development and fundamental principles. The principles and mechanisms of heterogeneous catalysis are elaborated. Various types of solid catalysts are discussed, highlighting their properties and diverse applications, with a focus on noble NPs, particularly Pt-based catalysts. An overview of the Pt-based hollow nanospheres is presented along with example of their proved catalytic

activity advantages compared to their solid counterparts. Additionally, the deactivation mechanisms that catalysts may experience during a chemical reaction are explained. The model CO₂ hydrogenation reaction mechanisms are presented. Furthermore, the history and principles of both TEM and in-situ TEM are explored, emphasizing their applications in the field of catalysis.

Chapter II provides a detailed presentation of the experimental setup of this work. It starts with the synthesis methods of the Pt-based nanomaterials, then with a brief introduction of the large-scale analysis methods, such as X-ray diffraction (XRD) and scanning electron microscopy (SEM). It goes into the specifics of the TEM setup and its operational modes. The principles and methodology of electron tomography are also covered. More importantly, a comprehensive explanation of the adapted in-situ approach (the E-cell approach), is provided. All the adapted experimental conditions are presented in detail.

Chapter III delves into the results of the initial state investigations of two sets of Pt-based nanomaterials. It provides an explanation of their morphology, size, and chemical compositions. The 3D morphology including their porosity is also elucidated. An analysis comparing the two sets of materials is conducted based on these findings along with their expected catalytic properties.

In Chapter IV, the behavior of both sets of Pt-based materials is monitored under different atmospheres. The influence of temperature on the NPs sintering and its mechanisms is studied. The temperatures at which the hollow microstructure collapses and the associated mechanisms are also examined. These investigations are conducted during thermal annealing under three different conditions: vacuum, H₂ gas, and a mixture of H₂ and CO₂ gases. The spatial distribution of compositional elements in both sets is evaluated after exposure to H₂ gas. Isothermal CO₂ hydrogenation reactions are conducted to assess the thermal stability of Pt-based hollow materials over time. Throughout all studies in the CO₂ hydrogenation conditions (during temperature ramping and isothermal reactions), the reaction products are simultaneously analyzed to determine the reaction's onset temperature and assess the probability of catalyst deactivation due to surface poisoning.

CHAPTER I: Catalysts transformations and In-Situ TEM for heterogeneous catalysis: Literature Review

1.	Principles of catalysis in chemical reactions.....	6
1.1.	Brief history about catalysis	6
1.2.	Catalysis principles	6
1.3.	Heterogeneous catalysis.....	7
2.	Different types of catalysts and their properties	12
2.1.	Bulk materials: unsupported catalysts	12
2.2.	Noble metal nanocatalysts	13
3.	Pt-based nanocatalysts	16
3.1.	Catalytic applications of Pt-based nanoparticles	16
3.2.	The CO ₂ hydrogenation reaction	18
3.3.	Pt-based hollow nanospheres by the galvanic replacement method.....	21
4.	Transformations of nanocatalysts during a chemical reaction.....	27
5.	Transmission electron microscopy.....	32
6.	In-situ and operando transmission electron microscopy	37
6.1.	Differentially vacuum pumped environmental TEM	37
6.2.	Window-gas cell environmental TEM.....	39
6.3.	The advantages and disadvantages of using the environmental gas cell	40
6.4.	Operando transmission electron microscopy	40
6.5.	Examples of applications of the Environmental cell in catalysis research	41
7.	The problematic and the strategy of the project.....	43

1. Principles of catalysis in chemical reactions

1.1. Brief history about catalysis

Catalysis plays a crucial role in the production of most chemicals used in our society. The term "catalysis" was proposed by Jöns Jakob Berzelius in 1835, derived from the Greek words meaning "down" and "loosen." Berzelius described catalysis as a property in which substances act on other bodies, causing decomposition and the formation of new compounds without being consumed in the process. In the late 18th and early 19th centuries, experimental data started accumulating, showing that small amounts of foreign substances could modify chemical reactions. It was observed that solid materials, particularly heated metals, could catalyze decomposition reactions, which was initially attributed to the presence of heat. [1] By the early 19th century, the catalytic properties of various metals, notably platinum (Pt), had been extensively studied. A preliminary understanding of homogeneous catalysis involving unstable intermediates was proposed. In the 1830s, the pieces of the puzzle began to fit together, and the term "catalysis" was formally established. [1] The development of the concept of catalysis and its explanation progressed over time, leading to *Wilhelm Ostwald* receiving the first Nobel Prize in 1909 [2] for his work on catalysis and understanding the basic principles of chemical reactions. In 1912, *Victor Grignard* was awarded the Nobel Prize [3] for discovering the so-called Grignard reagent, and he shared the prize with *Paul Sabatier*, who was recognized for his method of using finely divided metals to hydrogenate organic compounds.

1.2. Catalysis principles

Catalysis is a branch of the scientific and technological field dedicated to controlling the rates of chemical reactions. A catalyst is a substance that affects the course of a chemical reaction without undergoing any permanent changes itself. This unique property allows a small quantity of catalyst material to efficiently convert a large quantity of reactants. This conversion often occurs under less demanding conditions than those required by the stoichiometric reaction pathway, where only reactants are combined in precise ratios to yield products. When multiple reaction products are possible, the catalyst can influence the distribution of these products, enabling precise control over the selectivity and the yield of the chemical reaction. [4]. The selectivity of a catalyst is its ability to favor the formation of a specific desired product over other possible products in a reaction. The yield of product is its amount obtained from a reaction, expressed as a percentage of the theoretically possible amount.

In exceptional cases, a chemical reaction yields a single product. In such cases, it is beneficial to achieve both an acceleration in the reaction rate and a decrease in energy consumption. However, in the majority of reactions, multiple products can be formed, and accelerating the reaction tends to favor the production of the most thermodynamically stable product. [4] Catalysts are divided into two types based on the phase of the catalysts and the phase of the reactants. If the catalyst is in the same aggregation state as the reactants or not, there are either homogeneous or heterogeneous catalysts.

In simple terms, homogeneous catalysis involves a system where the reactants and catalyst components are combined in the same phase, typically in a liquid medium. It is worth noting that there are various interesting reactions and catalysts in homogeneous catalysis that go beyond organometallic or coordination complexes. Examples include general acid and base catalysis, organic catalysts, enzymatic processes, nitrogen oxides, chloride atoms, and more. [5]. Although this thesis mainly focuses on heterogeneous catalysis as, it is worth mentioning that, homogeneous catalysis accounts for approximately 17% to 30% of total industrial synthesis, particularly in the pharmaceutical and polymer sectors [6].

1.3.Heterogeneous catalysis

When the catalyst is in a solid state and the reactants are in either a liquid or gaseous phase, the term ‘heterogeneous catalysis’ is used. The reactions in this case occur at the interface between the catalyst surface and the two phases. This offers practical advantages, as it allows for quite-easy separation of the product from the catalyst post-reaction. Materials adapted to heterogeneous catalysis will be further explored in the following sections of this thesis.

Understanding the fundamental principles of surface chemistry at the atomic level is crucial for a deep understanding of heterogeneous catalysis. To understand the underlying principles of catalyst action, as defined by Ostwald [7], a detailed examination of the energetics and kinetics of catalytic reactions is essential. Figure 1.1 illustrates a simplified representation of the energetics in a catalyzed reaction. The catalyst's influence is linked to the reduction in activation energy (E_A) compared to the uncatalyzed reaction. Lowering the activation energy ($E_{A,cat}$) for the reaction leads to an increase in the reaction rate.

The catalyzed reaction proceeds through intermediate states X and Y, which correspond to the adsorbed states of the reactants and products, respectively. The final state B in the catalyzed

reaction aligns with that of the uncatalyzed reaction. This observation reinforces Ostwald's assertion that the catalyst remains unchanged and is not consumed during the reaction [8]. The catalyst's effectiveness relies on the nature of the intermediate states (X and Y), which are adsorbed molecules on the solid surface of the catalyst. This highlights the significance of surface chemistry in heterogeneous catalysis.

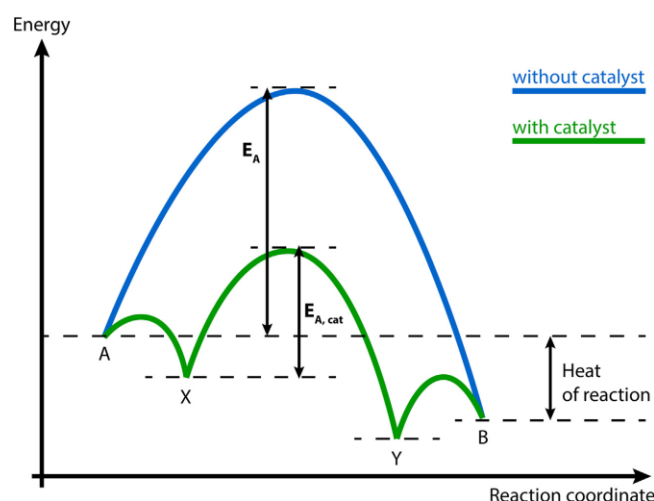


Figure 1.1: Energy diagram of a chemical reaction without and with a catalyst. [8]

Figure 1.1 provides additional information, indicating essential steps in catalyzed reaction: (1) the formation of a complex (X) between the catalyst and at least one reactant, referred to as adsorption in the case of solid catalysts, (2) the reaction of the reactants to produce the adsorbed product (Y), and (3) the detachment of the product from the catalyst, which corresponds to desorption from a solid surface. In heterogeneous catalysis, understanding these elementary processes is closely tied to the role of surface science in clarifying the catalyst's mechanism. Detailed explanation of these processes is provided in the next sections.

– Adsorption

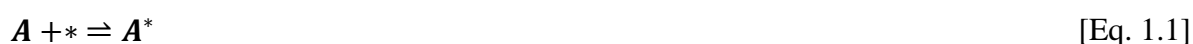
Irving Langmuir's theory on adsorption, developed from 1916 to 1928 [9], remains a foundational concept in modern surface physics and chemistry. Langmuir's theory introduced two significant assumptions. Firstly, it proposed the formation of a single layer of molecules (monolayer) during adsorption, rendering the surface inactive once fully covered. Secondly, it assumed no interactions among the adsorbed particles, although this is generally not the case. Despite these limitations, Langmuir's theory laid the groundwork for understanding adsorption sites and the atomistic perspective of surface chemistry.

The interactions between adsorbed particles greatly influence surface reactivity. It determines the spatial distribution of reactants and the extent of their contact. Attractive interactions facilitate intermixing, while repulsive interactions lead to separation or island formation, resulting in significant differences in reaction kinetics. The presence of impurities in the reaction mixture or one of the reactants can lead to a buildup of unwanted foreign compounds of the catalysts surface. This can either block the active sites of the catalyst or form stable complexes that hinder the desired chemical reaction. This phenomenon is referred to as catalyst surface poisoning during adsorption [10]. A notable example is the adsorption of CO, which reduces the probability of other gases, like oxygen, to adsorb on transition metals [11]. To prevent CO poisoning, substantial efforts are often required, including chemical modification of the catalyst surface through alloying with a second metal [11].

Two fundamental types of adsorption are relevant in heterogeneous catalysis: physisorption and chemisorption. Physisorption refers to a weakly bonded state that has minimal impact on the electronic structure of the adsorbate, while chemisorption induces significant changes in molecular properties and can even cause decomposition of the adsorbed molecule [12]. These phenomena are governed by van der Waals forces in the case of physisorption and chemical (covalent) bonding in the case of chemisorption. Consequently, physisorption energies are much smaller than chemisorption energies. Physisorbed species also exhibit higher mobility on solid surfaces compared to chemisorbed species, which can influence reaction mechanisms. In summary, the adsorption of at least one reactant leads to the formation of the precursor state (X in Figure 1.1) for the targeted reaction. The next section explains about two different reaction mechanisms that can govern a heterogeneous catalytic reaction.

– Heterogeneous catalysis reaction mechanisms

Proposed by Langmuir in 1921 and further developed by Hinshelwood in 1926 [13], [14], the *Langmuir-Hinshelwood mechanism* involves a bimolecular reaction between two adjacent adsorbed molecules on the surface (Figure 1.2). It is assumed that the product subsequently desorbs from the surface. These processes can be represented by a set of reaction equations, with "*" representing adsorption sites on the surface.



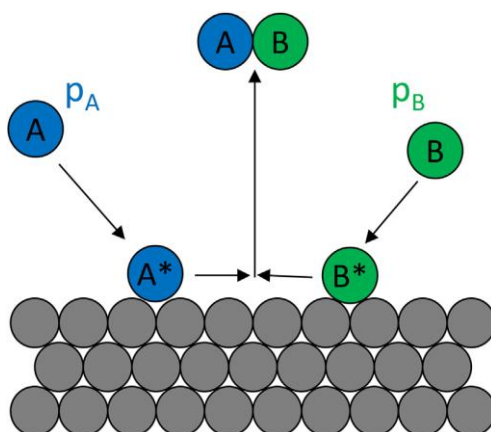


Figure 1.2: Schematic representation of the Langmuir–Hinshelwood mechanism.[8]

The reactants are in thermal equilibrium with the surface due to the strong adsorption of both of them on the surface. A notable example of a reaction following the Langmuir-Hinshelwood mechanism is the catalytic oxidation of CO on palladium (Pd) catalysts [15]. This reaction includes the chemisorption of CO, the dissociative adsorption of O_2 , the reaction between CO and O to produce CO_2 , and the subsequent desorption of CO_2 .

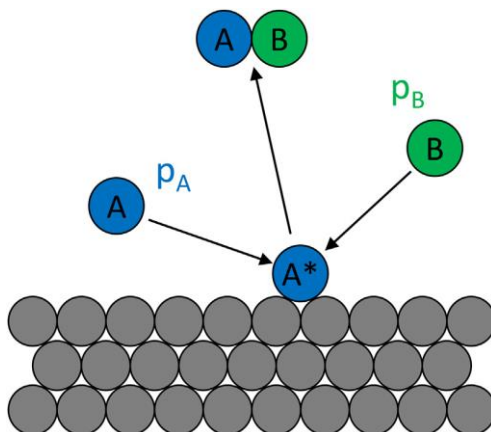


Figure. 1.3: Schematic representation of the Eley–Rideal mechanism.[8]

Shortly after the discoveries of Langmuir and Hinshelwood in 1938, Eley and Rideal proposed a second significant reaction mechanism known as the *Eley-Rideal mechanism* [16], as shown in Figure 1.3.

In this mechanism, only one of the reactants is adsorbed on the surface and directly reacts with an incoming molecule from the gas phase, without the need for an adsorption site. This type of reaction is considered nonthermal, as the temperature of the gas phase and the surface can be different.

The reaction scheme can be represented as follows:



An example of this mechanism is the hydrogenation of CO₂ on ruthenium Ru Catalysts [17]:



To differentiate between the *Langmuir-Hinshelwood* and *Eley-Rideal* reaction mechanisms, an effective approach is to measure the reaction rate 'r' as a function of the coverage of the adsorbed molecule A* (θ_{A^*}).

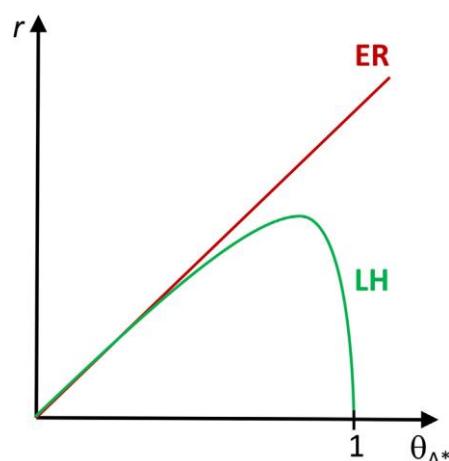


Figure 1.4: Schematic representation of the reaction rate r for the Eley-Rideal (ER) and the Langmuir-Hinshelwood (LH) mechanisms as a function of surface coverage θ_{A^*} of A*.[8]

The reaction rate is expressed by $r = k^*[A]^a[B]^b \dots$ (k is the rate constant, $[A]$ and $[B]$ represents the concentrations of reactants A and B, respectively, a and b are the reaction orders with respect to reactants A and B) and $\theta_A = 1$ represents complete surface coverage by A*.

At low coverage, both mechanisms exhibit a similar rate increase. However, at higher coverage, the rate for the Langmuir-Hinshelwood mechanism reaches a peak and then declines, ultimately dropping to zero at $\theta_A = 1$ due to adsorption site blockage by A. In contrast, the Eley-Rideal mechanism, which does not rely on B adsorption, maintains an increasing rate even when all surface sites are blocked (Figure 1.4).

Different types of solid catalysts are used in heterogeneous catalysis. Each catalyst type possesses distinct properties and selectivity for specific catalytic reactions. In the following section, we will examine some interesting catalyst types, including unsupported bulk catalysts and supported catalysts. We will also delve into the properties of these materials and their main applications in catalysis. Considering the fact that we are using Pt-based nanoparticles (NPs) as catalysts during this thesis, our primary focus will be on noble metal NPs employed in heterogeneous catalysis.

2. Different types of catalysts and their properties

2.1. Bulk materials: unsupported catalysts

– Metal oxides

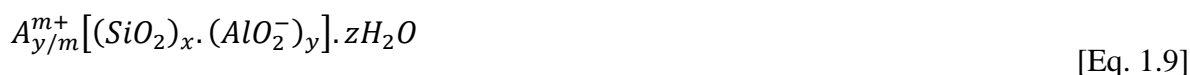
Oxides are Oxygen-containing compounds where oxygen atoms are more electronegative. There are different types of metal oxides with varying properties, including insulators like Al_2O_3 and SiO_2 , semiconductors such as TiO_2 , NiO , and ZnO and metallic conductors like TiO and NbO . They play a crucial role as catalytically active materials. Their surface characteristics and chemical behavior are influenced by factors such as composition, structure, bonding nature, and the arrangement of surface atoms and hydroxyl groups on the exposed crystallographic surfaces. Different categories of metal oxides are presented.

Simple binary oxides, such as Aluminas, Silicas, and transition metal oxides like Titania and Zirconia, can display solid acid, base, or amphoteric properties depending on their dissolution behavior in aqueous solutions. These dissolution properties are important considerations when using such oxides as supports and soaking them in aqueous solutions [18].

Complex multicomponent oxides are high efficiency catalysts, renowned for their unique and remarkable properties. Among this class of materials, zeolites stand out as one of the most interesting branches. These are inorganic microporous crystalline minerals which are frequently employed in ion exchange, gas adsorption, and heterogeneous catalysis [19]. Because of their distinctive shape selectivity, strong intrinsic acidity, and stability, zeolites are among the most valuable solid catalysts in the chemical industry [20], [21].

The classical definition of a zeolite is a “crystalline aluminosilicate built of oxygen-linked tetrahedral silicon and aluminum atoms that form a three-dimensional microporous structure comprising channels and voids occupied by alkali or alkali-earth cations and water molecules”.

The chemical composition of a zeolite can hence be represented by a formula of the type:[22]



Where A is a cation with the charge m, $(x + y)$ is the number of tetrahedra per crystallographic unit cell, and x/y is the so-called framework silicon/aluminum ratio $\frac{n_{Si}}{n_{Al}}$.

– **Metals and metal alloys**

In only a limited number of instances are metals and metal alloys employed as unsupported catalysts in bulk form. In situations where strongly exothermic reactions demand catalyst beds of minimal height, metal grids serve as effective bulk catalysts. Notable examples include platinum-rhodium grids utilized for ammonia oxidation in the nitric acid process [23], as well as silver grids employed in the dehydrogenation of methane to formaldehyde.

– **Carbons**

In addition to serving as catalyst supports, carbons possess the capability to act as catalysts without support [24], [25]. Efforts have been made to use carbons as catalysts in condensed phases. However, when exposed to oxidizing conditions in the gas phase, carbon's susceptibility to irreversible oxidation severely limits its application.

2.2. Noble metal nanocatalysts

Due to the natural tendency of nanocatalysts to reduce their surface areas through particle growth, they often require high surface area supports. The supports play a crucial role in preventing the NPs from undergoing sintering, which is a common phenomenon that can occur during the preparation and use of metal nanocatalysts [26]. While supports are often perceived as inert, they can actively influence the catalytic process. To achieve high surface areas and stabilize the dispersed active phase, supports are typically porous materials with strong heat resistance [18]. Several of the materials mentioned earlier can also serve as supports. Among the commonly used supports are binary oxides like transitional aluminas α -Al₂O₃, SiO₂, ZrO₂ (tetragonal), as well as zeolites thanks to their microporous structure, high surface area and high stability. Carbon in different forms can be utilized as supports, except in cases where oxygen is needed in the feed at elevated temperatures. [18]

– **Metal nanoparticles**

Nanomaterials have been employed in heterogeneous catalysis for over 60 years, before the current focus on nanoscience and nanomaterials [27]. Metal NPs, more specifically, offer

significant potential in heterogeneous catalysis due to their exceptional surface-to-volume ratio, abundant active surface atoms, and distinctive electronic structures in contrast to their larger-scale counterparts [28], [29].

Before discussing the catalytic applications of certain metal nanoparticles, specifically noble metals, it's essential to understand how size variations affect their geometric and electronic properties. This size-dependent influence significantly impacts their catalytic reactivity and justifies the preference for using metal nanoparticles as catalysts over their larger forms.

The size of metals greatly influences their electronic and geometric properties, particularly within the nanometer scale [30]. Geometrically, metal NPs comprise distinct surface metal sites, such as low-coordinated metal atoms at edges and corners (LCSs) and high-coordinated sites on terraces (HCSs) (Figure 1.5). These different local geometries significantly impact chemical bond formation and breaking during catalysis.

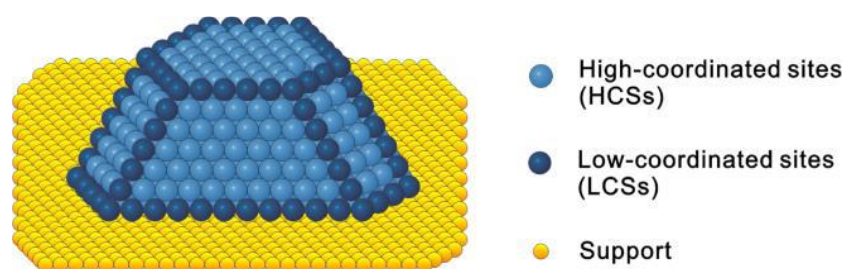


Figure 1.5: Schematic representation showing the geometrical structure of a supported metal nanocatalyst. [30]

The difference in local geometry between HCSs and LCSs have a substantial impact on the energetics of elementary steps involved in catalytic processes. This includes processes like molecule adsorption and desorption, as well as the formation and breaking of chemical bonds during catalysis. Consequently, adjusting the particle size not only affects metal dispersion but also modifies the coordination of surface metal atoms, resulting in size-dependent variations in catalytic behaviors [28]–[30].

In terms of electronic properties, when the particle size decreases into the nanoscale range, the continuous valence band of the bulk metal undergoes a splitting process, resembling the behavior observed in semiconductors (Figure 1.6). This phenomenon, known as the "quantum size effect" (QSE), arises from the substantial alterations in energy levels experienced by the entire particle as its size changes [33], [34].

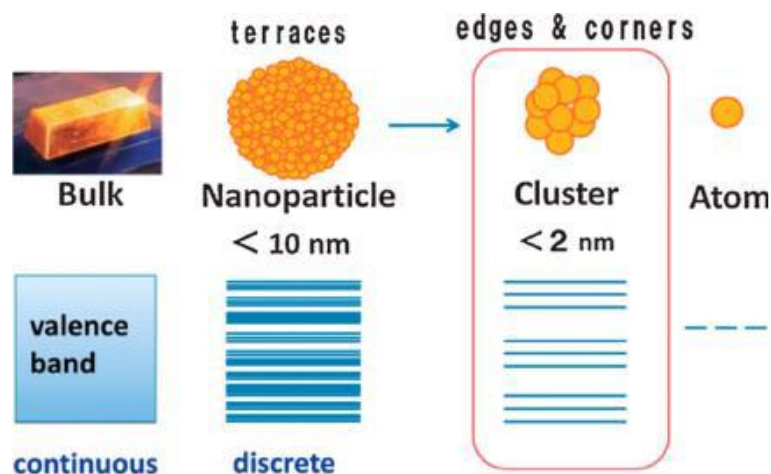


Figure 1.6: Schematic illustration of the electronic structures of bulk, NPs, and clusters of metals. [34]

The QSE has a profound impact on the orbital hybridization and overall charge transfer between the metal and reactants, thereby significantly influencing the intrinsic activities of all surface metal sites. It is also evident that the electronic characteristics of metal particles undergo significant alterations when their size decreases below 1 nm (Figure 1.6). As a result, it can be expected that subnanometric metal particles would interact with reactants in a distinctive manner, exhibiting distinct reactivity compared to larger NPs.

Single-Atom Catalysts (SACs) refer to catalysts where all active metal species exist as individual isolated atoms stabilized either by the support or through alloying with another metal [35]–[37]. While this type of catalyst is not directly connected to the current work, it is worth mentioning because it has shown great potential for eco-friendly production of valuable chemicals. The innovative work by Zhang and his colleagues in 2011 revealed that the Pt_1/FeO_x SAC displayed three times higher activity compared to its nano-Pt counterpart in CO oxidation [37].

SACs are distinct from nanoparticle (NP) catalysts in that they lack metal-metal bonds, and the cationic character of metal is SACs. These unique geometric and electronic properties result in significant modifications in the interactions with reactants, intermediates, and products. It leads to enhanced activity and/or selectivity highly desirable in the production of fine chemicals. As a result, SACs are expected to combine the benefits of high catalytic activity, selectivity, stability, and reusability for environmentally friendly synthesis of fine chemicals. Among metal nanoparticles, noble metal nanoparticles have earned particular attention over the years due to their exceptional properties, which have led to their wide use in catalysis.

– Noble metal nanoparticles

The electronic, chemical, and optical properties of noble metal (ruthenium (Ru), rhodium (Rh), palladium (Pd), silver (Ag), osmium (Os), iridium (Ir), platinum (Pt), and gold (Au)) NPs make them significantly important among other nanocatalysts. The noble metal catalysts have demonstrated numerous advantages, including high activity at low temperatures, good stability, and convenient regeneration and storage properties [38].

Noble metal nanoparticles have proved efficiency in oxidation reactions. Both Au single atoms and Au NPs supported on FeO_x, for example, proved to be active catalysts for low-temperature carbon monoxide (CO) oxidation as reported by Zhang et al [35], [39]. Previous studies have demonstrated that metal NPs, including Pt, Au, Pd, among others, exhibit exceptional activity and selectivity in the process of selectively oxidizing alcohols.[40], [41]

As for hydrogenation reactions, Pd nanocatalysts have found application as catalysts in diverse reactions, such as the hydrogenation of 4-nitrophenol, olefins, and other reactions [42]. Furthermore, there has been research on the utilization of Au-based catalysts in hydrogenation reactions. Bond et al. investigated the use of supported Au catalysts for the selective hydrogenation of 1,3-butadiene [43]. Au-based have also been discovered to exhibit remarkable activity in the selective hydrogenation of unsaturated aldehydes into unsaturated alcohols [44].

In the upcoming section, we will discuss the properties and catalytic capabilities of one of most attractive noble metal NPs, the Pt-based NPs, which is the system investigated in this thesis.

3. Pt-based nanocatalysts

3.1. Catalytic applications of Pt-based nanoparticles

Among the noble metals, Platinum (Pt) possesses a high melting point of 1769 °C. It also exhibits remarkable effectiveness in various chemical applications, making it a highly significant material in catalysis [45]. One crucial characteristic of Pt is its exceptional ability to resist chemical corrosion, with aqua regia being the sole mineral acid capable of effectively dissolving it. Nevertheless, platinum does interact with numerous substrates, leading to its wide range application in catalysis. Beside catalysis, the investigations of Pt NPs have been a captivating field of study as they exhibit a broad spectrum of applications across physical, chemical and biological fields [46]. The exploration of nanoscale Pt catalyst originated from Johann Wolfgang Döbereiner's discovery that finely divided platinum enhances alcohol

oxidation [47]. Ever since, Pt-based materials have found widespread application as catalysts in various reactions, such as energy conversion [48], hydrogenation [26], oxidation [49], and reduction such as oxygen reduction reaction (ORR) for Proton Exchange Membrane Fuel Cells (PEMFC) [50], [51].

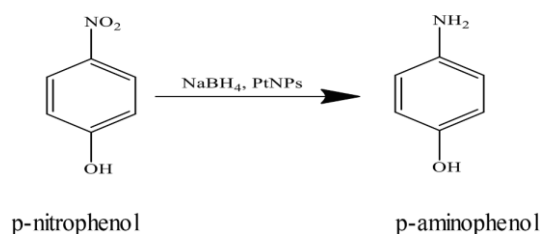


Figure 1.7: Model reaction of the reduction of p-nitrophenol [52]

Pt NPs can be synthesized under diverse morphologies, including cubic shapes, nanotubes, and nanoclusters, each serving different purposes. For instance, cubic Pt NPs function as reactors for CO adsorption and oxidation [46]. Pt NPs also serve as an effective catalyst in various catalytic reactions, including hydrogenation reactions [46], [53]–[56]. For example, the reduction of p-nitrophenol was accomplished by NaBH_4 in the presence of a Pt catalyst supported by wood nanomaterials (Figure 1.7). In the absence of any catalyst, this reaction did not progress even after a considerable duration.

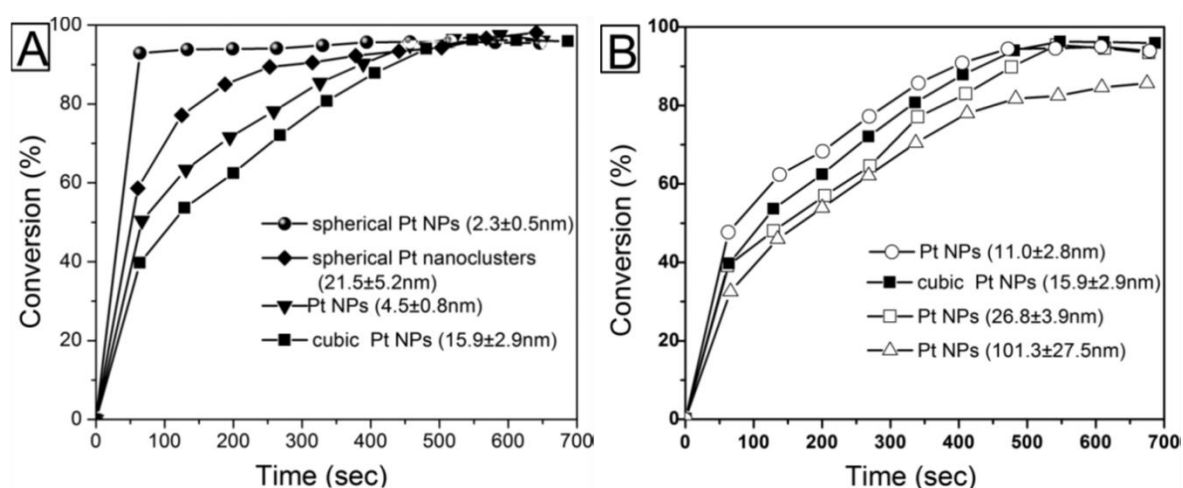


Figure 1.8: (A) Comparison of catalytic activities for Pt NPs with distinct morphologies. (B) Impact of particle size increase on the decline of catalytic activities for Pt NPs. [52]

Various forms of Pt NPs, including spherical Pt NPs, spherical Pt nanoclusters, Pt NPs, and cubic Pt NPs, were synthesized and their catalytic activities were investigated (Figure 1.8). The Pt nanoclusters were larger in size compared to Pt NPs. Among the tested particles, the spherical and cubic Pt NPs, along with the spherical Pt nanoclusters, exhibited superior catalytic activities for the reduction of p-nitrophenol. Analysis of the obtained kinetic data revealed that the nanoclusters displayed greater catalytic activity compared to the cubic structure [52] [46].

Another example of a hydrogenation reaction application for Pt, a synthesized Pt NPs catalyst was used for the hydrogenation of 2-butyne-1,4-diol. As a result, the compound was efficiently transformed into 2-butene-1,4-diol, with an 83% conversion rate achieved using Pt NPs [57].

While Pt is not commonly regarded as the most efficient catalyst for carbon dioxide (CO₂) hydrogenation, it has demonstrated selectivity towards formic acid and methanol in previous studies when utilized with suitable support materials [58]–[65]. Consequently, investigating the behavior of catalysts during this model hydrogenation reaction and examining the influence of a hydrogen (H₂) atmosphere on the microstructural changes of Pt-based materials is valuable. The following section will provide an explanation of the CO₂ hydrogenation reaction into formic acid and methanol, along with a brief overview of the noble catalysts, most importantly Pt-based materials, used in this reaction.

3.2. The CO₂ hydrogenation reaction

With the progress in capture technologies, the utilization of CO₂ through cost-effective renewable H₂ in catalytic hydrogenation emerges as a promising approach to reduce the carbon footprint of industrial processes. This strategy not only offers the potential to produce valuable chemicals and fuels but also offers significant environmental benefits. In the context of CO₂ utilization, hydrogenation presents a promising pathway for the production of various industrially relevant compounds. These compounds include CH₄ [66], a crucial renewable energy source, CO [67], commonly used in large-scale chemical production, oxygenates such as methanol [68], ethanol [69], and formate [70], as well as long-chain hydrocarbons [71], which can be obtained through direct routes [72]. The conversion of CO₂ into alcohols is a highly significant subject that gains the interest of both the chemical industry and the scientific community. Among the various alcohols, methanol, as a prominent C₁ alcohol, holds particular importance as it can serve as a precursor for the production of a wide range of chemical compounds through further processing. Ever since its discovery, the Cu (supported on

ZnO/Al₂O₃) catalyst has demonstrated exceptional performance in methanol synthesis [69]. Despite their advantages, Cu/ZnO/Al₂O₃-based catalysts suffer from deactivation caused by water adsorption leading to the sintering of Cu and ZnO during the reaction [73]. In recent years, several alternative catalysts without Cu have been explored, with particular attention given to those containing noble metals due to their superior stability and resistance compared to Cu-based catalysts [74], [75].

– Reaction mechanisms in CO₂ hydrogenation reaction

The hydrogenation of CO₂ to methanol is an exothermic reaction that occurs more favorably under mild temperatures and high pressures.

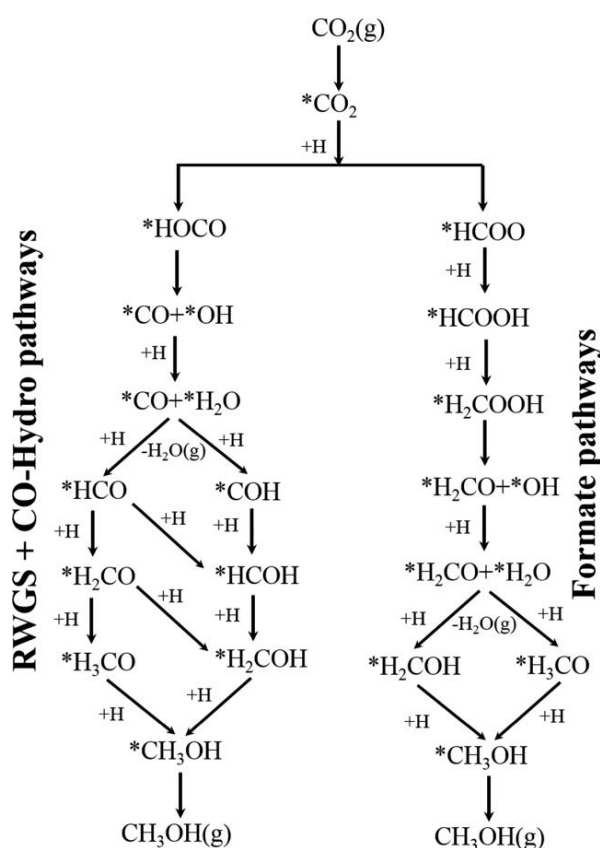


Figure 1.9: Exploration of potential pathways for methanol synthesis through the CO₂ hydrogenation reaction.. [72], [76]

To activate CO₂, which has an inert nature, temperatures above 150 °C are necessary for methanol synthesis [76]. The process of methanol synthesis can proceed through two pathways: 1) the formate pathway and 2) the reverse Water-Gas Shift reaction (rWGS) + CO hydrogenation pathway.

The activation of CO₂ is a critical step in both routes. Figure 1.9 illustrates these pathways which were presented by Kattel et al. [76]. In either pathway, the activated CO₂ molecule reacts with adsorbed atomic H, and this interaction determines the direction the reaction takes [77].

The formate pathway is considered more favorable since the rWGS + CO hydrogenation pathway can result in a higher selectivity for CO due to the rWGS reaction [78]. The proper selection of a catalyst is essential for controlling the reactivity of CO₂ and H₂, as well as determining the specific reaction pathway to achieve desired outcomes.

– **Pt-based nanocatalysts for methanol production in CO₂ hydrogenation**

Recent advancements in Pt-based catalyst research have been dedicated to exploring the optimal conditions for the CO₂ hydrogenation reaction to produce methanol. Toyao et al. [63] conducted a study on a Pt(3)/MoO_x(30)/TiO₂ catalyst, consisting of 3 wt.% of Pt supported on MoO_x/TiO₂. The interaction between Pt and MoO_x was proved to facilitate the reaction at a low temperature of 150 °C and a pressure of 60 bar in a batch reactor, resulting in an impressive methanol yield of 73% and a methanol selectivity of around 91%. This combination of Pt and MoO_x emerged as a key factor in achieving high activity for methanol production at low temperatures, gaining significant interest from both academic researchers and the industrial sector involved in methanol manufacturing.

In another contribution by Men et al. [62], a Pt/film hybrid catalyst featuring highly dispersed Pt NPs over In₂O₃ was investigated for CO₂ hydrogenation using a dielectric barrier discharge (DBD) plasma reactor. Remarkable results were achieved, including a 37% conversion of CO₂ and a methanol selectivity of 62.6% at 1 atm and 30 °C. The exceptional dispersion of Pt NPs played a leading role in promoting enhanced methanol activity, while the high-energy electrons generated by the DBD plasma facilitated the reaction to occur under mild conditions (relatively low temperature ~ 150°C).

Furthermore, Gutterød et al. [61] explored the Pt-based catalysts for CO₂ hydrogenation to methanol under mild conditions. They developed Pt NPs implanted within a Zr-based metal-organic framework (MOF) (UiO-67) and conducted a study on the methanol formation mechanism at 170 °C and ambient pressure. Although the methanol yield was not high, this study stood out as one of the few that demonstrated significant methanol formation from CO₂ hydrogenation over a Pt-based catalyst, particularly when the support alone was inactive. This research opens new possibilities for the utilization of Pt-based catalysts in methanol synthesis.

In studies by Sun et al. [65] and Han et al. [64], Pt NPs supported on In_2O_3 were examined under industrial conditions. The presence of Pt substantially enhanced the catalytic activity of In_2O_3 in both cases. Han et al. reported an impressive methanol selectivity of 71.5% and a CO_2 conversion rate of 8.8% in their study.

As previously discussed, Pt-based catalysts have gained interest as catalysts for various chemical reactions, including the conversion of CO_2 into methanol. This particular reaction serves as a model reaction during this study to evaluate the behavior of the synthesized Pt-based nanocatalysts. However, the high cost and limited availability of Pt pose challenges for its utilization in diverse applications. Consequently, experimental and theoretical studies have been undertaken to explore approaches that can enhance Pt's catalytic performance [79]. Enhancing the catalytic performance of Pt can be effectively achieved by increasing its surface area.

Hollow structures, porous structures, and dendrite structures possess significant specific surface areas and exhibit extensive active sites [80]–[82]. The following section focuses on nanocatalysts based on hollow nanomaterials with a special focus on Pt-based hollow nanospheres.

3.3. Pt-based hollow nanospheres by the galvanic replacement method

In the field of nanocatalysis, there has been a growing interest in the fabrication of metal NPs with hollow interiors, primarily due to the potential to generate supplementary active sites within the NPs [83]–[86]. The ability to control the structure of NPs by introducing hollow interiors offers higher surface-to-volume ratios compared to solid counterparts. This allows for a reduction in the utilization of noble metals and eliminates the presence of "wasted" atoms that do not interact with substrate molecules (atoms located inside a solid nanoparticle) [87]–[89].

A hollow nanomaterial is characterized by the presence of a void or hole in its interior. Several well-defined hollow nanomaterials, including tubes, shells, cages, frames, dendrites, and others, have been developed and utilized in nanocatalysis, as shown in Figure 1.10 [90].

In this section, the galvanic replacement method used for the synthesis of hollow nanospheres will be explained. *The galvanic replacement method* is a chemical templating method used for the synthesis of various types of hollow NPs. It remains the most widely employed and promising technique in this field.

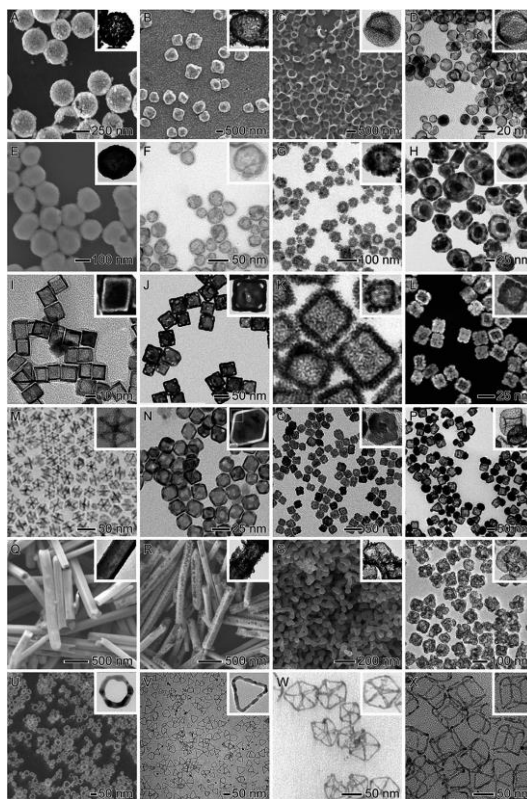


Figure 1.10: (A-X) SEM and TEM images depicting various hollow nanomaterials utilized as nanocatalysts for diverse molecular transformations.[90]

The galvanic replacement reaction offers a versatile and well-established method for synthesizing hollow materials with ultrathin walls and bimetallic compositions in a single step. This process involves a redox reaction between a sacrificial template made of a less noble metal and metal ions in a solution containing a more noble metal than the sacrificial template. The difference in reduction potentials drives the oxidation and dissolution of the sacrificial template while simultaneously reducing the metal ions in the solution, leading to their deposition onto the template's surface. This method is simple, relatively fast (with reactions typically occurring within 15 minutes), and can be performed using water as a solvent under ambient conditions [90]. It is worth mentioning that numerous hollow nanomaterials used for catalysis were synthesized through the galvanic replacement method [90]. These materials have demonstrated improved performance, which can be attributed to their enlarged surface areas.

In a specific example illustrated in Figure 1.11, the catalytic properties of Ag/Au-based nanoboxes, nanocages, and their solid counterparts were explored for the reduction of 4-nitrophenol using NaBH_4 as the reducing agent [91].

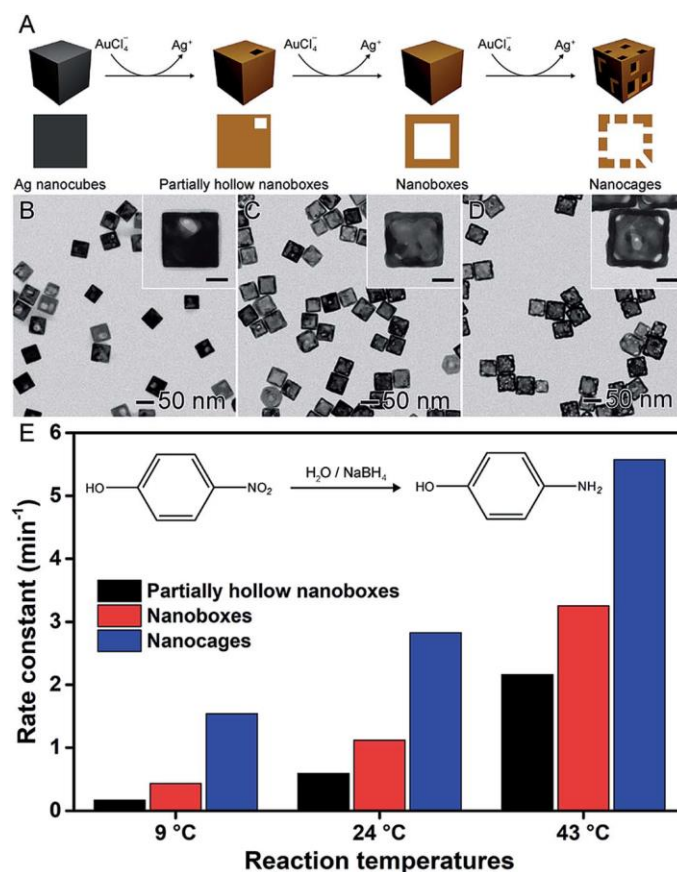


Figure 1.11: Impact of NPs structure (hollow interiors) on catalytic activity. (A) Illustration depicting the synthesis of Au-based hollow nanomaterials through controlled galvanic replacement reaction between preformed Ag nanocubes and $AuCl_4^-$ precursor. (B-D) TEM images showcasing partially hollow nanoboxes (B), nanoboxes (C), and nanocages (D). Insets in the images depict a scale bar of 20 nm. (E) Bar graph presenting the rate constants for the reduction of 4-nitrophenol using $NaBH_4$ at 9, 24, and 43 °C as reaction temperatures with Au-based hollow nanomaterials employed as catalysts. [91]

These materials were synthesized through a galvanic replacement reaction between Ag nanocubes and $AuCl_4^-$ ions. By gradually increasing the amount of $AuCl_4^-$ during the galvanic replacement reaction with Ag nanocubes, three distinct hollow nanostructures based on gold were prepared: partially hollow nanoboxes (Figure 1.11(B)), nanoboxes (Figure 1.11(C)), and nanocages (Figure 1.11(D)). As anticipated, the catalytic activity showed a positive correlation with the degree of hollowing, as indicated in Figure 1.11 (E). This enhanced catalytic performance can be attributed to the significantly larger specific surface area achieved compared to solid nanomaterials. Additionally, the ultrathin and porous walls of the hollow structures contribute to a higher activity due to the exposure of reactive sites.

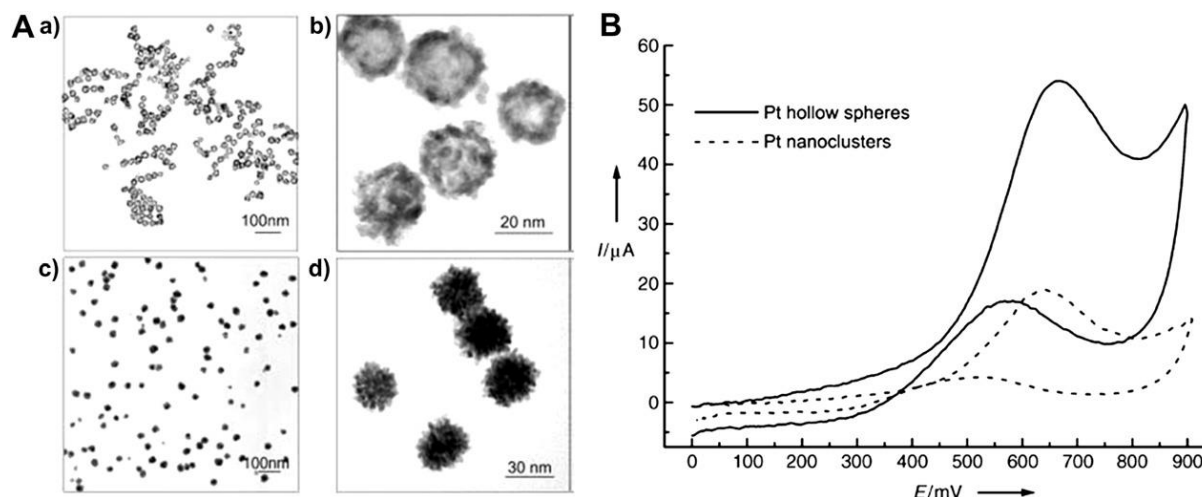


Figure 1.12: A. TEM images of (a, b) Pt hollow nanospheres, and (c, d) solid nanoclusters. B. Cyclic voltammograms comparing the electrochemical behavior of Pt solid nanoclusters (represented by a dashed line) and hollow nanospheres (represented by a solid line) on a glass carbon electrode in a solution containing 0.5 M H_2SO_4 and 0.6 M CH_3OH , with a scan rate of 50 mV s^{-1} . [92]

Liang et al. [92] were the first to describe the production of large-scale Pt hollow nanospheres at room temperature in a uniform solution through an in situ galvanic replacement method. This method involved using cobalt (Co) NPs as sacrificial templates (Figure 1.12). The resulting Pt hollow nanospheres had incomplete and porous shells, leading to a higher surface area and improved electrocatalytic performance. These Pt hollow nanospheres exhibited twice the catalytic activity of solid Pt nano clusters for the electrooxidation of CH_3OH in H_2SO_4 .

Subsequently, Liang et al. expanded the in situ galvanic replacement method to synthesize Pt hollow nanostructures supported on graphene composites, employing Co NPs grown on graphene sheets as sacrificial templates (Figure 1.13) [93].

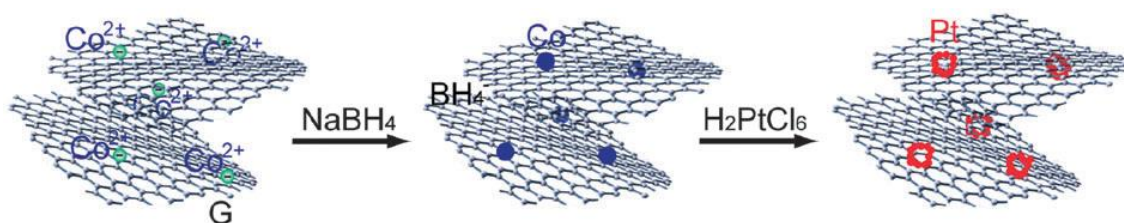


Figure 1.13: Schematic representation of the elaboration process of Pt hollow nanospheres on graphene sheets. [93]

Another study by Zhao et al. [94] reported the synthesis of carbon-supported hollow Pt nanospheres using Co metal NPs as sacrificial templates. These carbon-supported hollow Pt

nanospheres demonstrated enhanced electrocatalytic performance for methanol oxidation compared to carbon-supported solid Pt NPs due to their larger active surface area. The catalytic activity of the Pt hollow nanospheres has been observed to exhibit nearly twice the effectiveness of solid Pt NPs.

Apart from Co NPs, Ag NPs were also commonly used as sacrificial templates to produce Pt-based nanocatalysts with a hollow structure. Yang et al. [68] reported the synthesis of hollow Pt nanospheres by selectively removing the Ag cores of Ag/Pt core-shell NPs using bis(*p*-sulfonatophenyl) phenylphosphine (BSPP). The calculated surface area per Pt hollow nanosphere was approximately 1.52 times that of a corresponding solid particle. According to Wang et al. [95], Ni NPs were also considered suitable templates due to their lower reduction potential and solubility in acid solution compared to Ag and Cu NPs templates. They utilized electrodeposited Ni NPs on carbon powder as templates to fabricate Pt hollow nanocrystals through the galvanic replacement method. The resulting Pt hollow nanocatalysts demonstrated a sustained improvement in Pt mass activity for oxygen reduction in acid fuel cells.

In the upcoming section, various studies of Pt-based hollow nanospheres using Co nanoparticles as templates will be presented.

– **Co-promoted Pt hollow nanospheres**

By employing the galvanic replacement method, it is possible to generate various types of hollow Pt-based alloys rather than pure Pt hollow NPs. Numerous researchers have reported the synthesis of different hollow Pt-M alloys, where M represents elements such as Au, Ag, Co, Ni, Pb, Ru, Pd, Cu, and Se. This section focuses solely on the Co-promoted Pt hollow nanospheres, as this material is synthesized and investigated during this thesis.

Vasquez et al. [96] reported the synthesis of hollow Co-promoted Pt nanospheres using a unique galvanic replacement reaction with an in situ Co NPs sacrificial template. Analysis of Figure 1.14 reveals the formation of large Co-promoted Pt hollow nanospheres with average diameters ranging from 10 to 50 nm. The authors attributed the crucial factors during the synthesis process to the presence of excess reducer NaBH_4 and an appropriate stabilizer, poly(vinylpyrrolidone) (PVP).

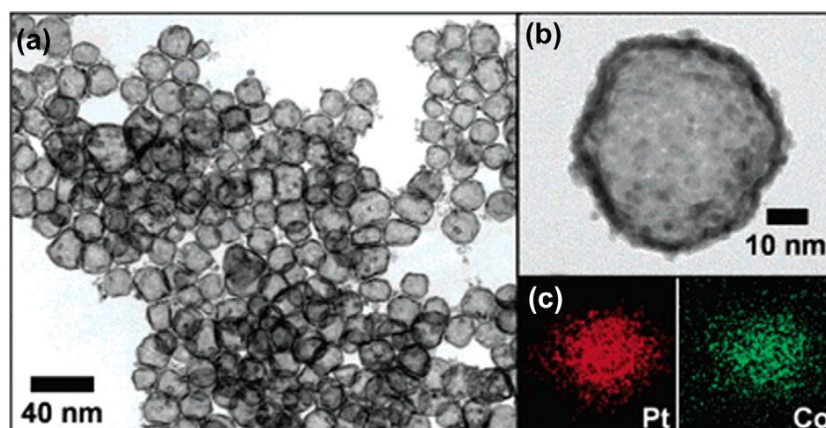


Figure 1.14: TEM micrographs of (a) an ensemble of PtCo hollow spheres, (b) a single isolated hollow sphere. (c) EDS elemental maps of a single hollow nanosphere showing the spatial distribution of both Pt and Co. [96] [97]

Building upon the galvanic replacement method, Pt-Co chainlike nanocatalysts (Figure 1.15(a), (b)) [98] and one-dimensional hollow PtCo nanospheres [99] (Figure 1.15(c), (d)) were successfully synthesized. The catalytic activity of the hollow Co-promoted Pt chainlike nanocatalysts outperformed that of the commercial Pt/C catalyst for the electrooxidation of methanol in H_2SO_4 . The significantly high activity of these nanocatalysts was attributed to their unique hollow structure and the bimetallic functionality.

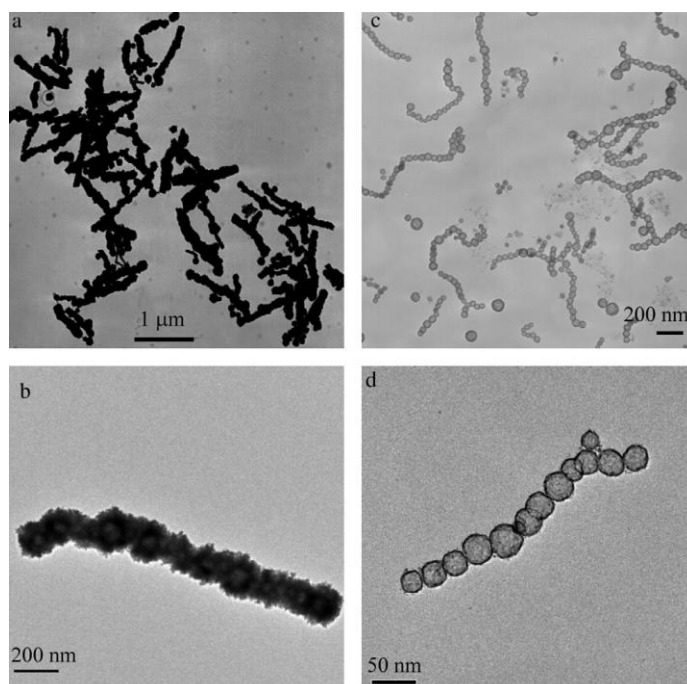


Figure 1.15: TEM micrographs showing (a, b) PtCo nanorods and (c, d) the chainlike PtCo at low and high magnifications, respectively. [97]

Recently, Sun et al. [100] reported the synthesis of well-aligned PtCo hollow nanochains through a magnetic field-induced assembly approach combined with galvanic replacement method, using Co NPs as templates. The synthesized PtCo hollow chains demonstrated excellent alignment under the influence of magnetic fields. The magnetic properties indicated that the shape anisotropy of the aligned nanochains played a dominant role in their controllable behavior.

After introducing the catalyst material used in the CO₂ hydrogenation reaction to produce formic acid and methanol, it's important to note that we have only discussed its initial state. However, catalysts go through various transformations during chemical reactions, which eventually result in their deactivation over time. In the upcoming section, we will discuss the different types of catalyst transformations.

4. Transformations of nanocatalysts during a chemical reaction

The deactivation of heterogeneous catalysts, characterized by the gradual loss of catalytic activity and/or selectivity over time, is a common issue that leads to a decline in the catalytic activity.

Heterogeneous catalysts can experience degradation through various pathways. For instance, the catalyst's solid structure may become poisoned by contaminants present in the feed, leading to a loss of activity. The surface, pores, and voids of the catalyst can also become fouled by carbon or coke, which is produced because of reactions involving hydrocarbon reactants, intermediates, or products. When catalytic reactions are conducted at high temperatures, thermal degradation can occur, leading to changes in the active phase's crystallite growth, pore structure collapse, or solid-state reactions between the active phase, carrier, or promoters. Additionally, the presence of reactive gases in the feed can induce changes in the oxidation state of the active catalytic phase.

Consequently, the mechanisms behind solid catalyst deactivation are diverse, but they can be grouped into six intrinsic categories: (1) poisoning, (2) fouling, (3) thermal degradation, (4) formation of vapor compounds and/or leaching accompanied by transport from the catalyst surface or particle, (5) vapor-solid and/or solid-solid reactions, and (6) attrition/crushing.

While mechanisms 1, 4, and 5 are predominantly chemical in nature, mechanisms 2 and 6 are primarily mechanical. Thus, the causes of deactivation can be attributed to three main factors:

chemical, mechanical, and thermal. In this study, our focus is limited to investigating the potential effects of fouling, poisoning and thermal degradation on the Pt-based hollow nanospheres. Consequently, a brief overview of these deactivation mechanisms is presented in the following section.

– **Fouling/Coking**

Fouling refers to the mechanical deposition of substances onto the catalyst surface, leading to a loss of activity as the sites and pores become blocked. In advanced stages, fouling can cause catalyst particles to disintegrate and result in blockage of reactor voids. Common examples include the deposition of carbon and coke in porous catalysts. These carbon- and coke-forming processes involve the chemisorption of various types of carbons or condensed hydrocarbons, which can act as catalyst poisons. The definitions of carbon and coke are somewhat arbitrary and are typically related to their respective origins. Carbon is often formed through CO disproportionation, while coke is produced by the decomposition or condensation of hydrocarbons on catalyst surfaces, consisting primarily of polymerized heavy hydrocarbons. However, the specific forms of coke can vary widely, ranging from high molecular weight hydrocarbons to predominantly carbonaceous structures like graphite, depending on the conditions under which the coke was formed and aged. [101]

The chemical composition of cokes or carbons formed in catalytic processes varies depending on the type of reaction, catalyst, and reaction conditions. Menon [102] proposed a classification system for catalytic reactions involving carbon or coke formation, dividing them into two categories: coke-sensitive and coke-insensitive, similar to Boudart's broader classification of structure-sensitive and structure-insensitive catalytic reactions.

In coke-sensitive reactions, unreactive coke accumulates on active sites, leading to a decline in catalytic activity. In contrast, coke-insensitive reactions involve the formation of relatively reactive coke precursors on active sites, which can be readily removed by hydrogen or other gasifying agents. Based on this classification, Menon [102] reasoned that the structure and location of the coke are more crucial than its quantity in influencing catalytic activity.

– **Poisoning of the catalyst**

Poisoning refers to the strong chemisorption of reactants, products, or impurities to specific sites that would otherwise be available for catalytic reactions [101], [103]. Therefore, whether

a substance acts as a poison depends on its adsorption ability compared to other substances competing for the same catalytic sites. For instance, oxygen can act as a reactant in the partial oxidation of ethylene to ethylene oxide on a silver catalyst but as a poison in the hydrogenation of ethylene on nickel [104]. Adsorbed poisons can physically obstruct adsorption sites and also bring about modifications in the surface's electronic or geometric structure [105].

Moreover, poisoning can be either reversible or irreversible. An instance of reversible poisoning is the temporary deactivation of acidic sites in fluid catalytic cracking catalysts caused by nitrogen compounds in the feed. Although these effects can be significant, they typically vanish within hours to days after removing the nitrogen source from the feed. Similar outcomes have been observed when nitrogen compounds are introduced into the syngas of cobalt Fischer-Tropsch catalysts, but it takes weeks to months for the lost activity to be fully restored [106]. However, most poisons irreversibly bond to catalytic surface sites, like sulfur on most metals [101].

Regardless of whether poisoning is reversible or irreversible, the deactivation effects while the poison is adsorbed on the surface remain the same. There are various mechanisms through which a poison can impact catalytic activity, as demonstrated by a two-dimensional model illustrating the sulfur poisoning of ethylene hydrogenation on a metal surface (Figure 1.16).

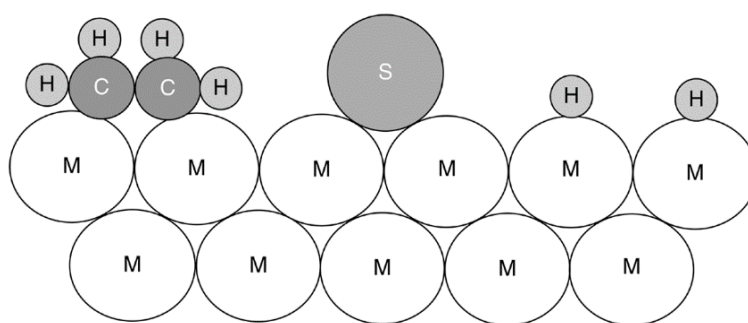


Figure 1.16: Schematic representation of the conceptual process of ethylene hydrogenation on a metal surface and the adverse effects caused by sulfur atom poisoning.[107]

Firstly, a strongly bonded sulfur atom physically blocks at least one three- or fourfold adsorption/reaction site and three or four topside sites on the metal surface. Secondly, due to its strong chemical bond, sulfur electronically alters its neighboring metal atoms, and possibly those slightly further away, thereby modifying their ability to adsorb and/or dissociate reactant molecules (such as H_2 and ethylene), although these effects are limited to a distance of

approximately 5 atomic units [101]. A third effect may involve surface restructuring caused by the strongly bonded poison, leading to significant changes in catalytic properties, particularly for reactions sensitive to surface structure. Furthermore, the adsorbed poison hinders the interaction between adsorbed reactants (fourth effect) and slows down or prevents the surface diffusion of adsorbed reactants (fifth effect).

In Table 1.1, several prevalent catalyst poisons are listed for key representative reactions.

Catalyst	Reaction	Poisons
Silica–alumina, zeolites	Cracking	Organic bases, hydrocarbons, heavy metals
Nickel, platinum, palladium	Hydrogenation/dehydrogenation	Compounds of S, P, As, Zn, Hg, Pb, NH ₃ , C ₂ H ₂
Noble metals on zeolites	Hydrocracking	NH ₃ , S, Se, Te, P
Platinum, palladium	Oxidation of CO and hydrocarbons	Pb, P, Zn, SO ₂ , Fe
Cobalt and molybdenum sulfides	Hydrotreating of residuum	Asphaltenes, N compounds, Ni, V
Iron, ruthenium	Ammonia synthesis	O ₂ , H ₂ O, CO, S, C ₂ H ₂ , H ₂ O
Silver	Ethylene oxidation to ethylene oxide	C ₂ H ₂
Cobalt, iron	Fischer–Tropsch synthesis	H ₂ S, COS, As, NH ₃ , metal carbonyls

Table 1.1: Common catalyst poisons for selected representative reactions. [101]

Figure 1.17 illustrates the selectivity of poisoning showing a plot of activity (reaction rate normalized to the initial rate) against the normalized concentration of poison.

"Selective" poisoning occurs when the poison preferentially adsorbs onto the most active sites at low concentrations. If initially fewer active sites are blocked, the poisoning is referred to as "anti-selective". When the loss of activity is proportional to the concentration of adsorbed poison, it is termed "nonselective".

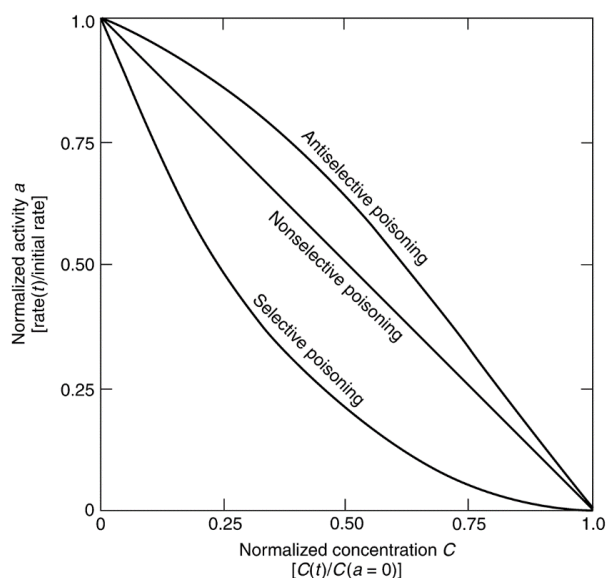


Figure 1.17: Variations of Poisoning Behavior Represented by Normalized Activity vs. Normalized Poison Concentration. [107]

– Thermal degradation and sintering

Thermal deactivation of catalysts occurs due to various factors, including (1) reduction in catalytic surface area caused by the growth of catalytic phase crystallites, (2) reduction in support area due to collapse of the support and loss of catalytic surface area caused by pore collapse on active phase crystallites, and/or (3) chemical changes of catalytic phases leading to noncatalytic phases. The first two processes are commonly known as "sintering," while the third is considered as solid-solid reactions.

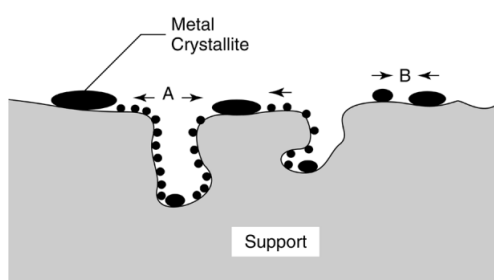


Figure 1.18: Conceptual models illustrating two mechanisms of crystallite growth through sintering: (A) Atomic migration and (B) Crystallite migration. [107]

The majority of prior research on sintering and redispersion has primarily concentrated on metals on support. There are three main mechanisms that explain the growth of metal crystallites: (1) crystallite migration, (2) atomic migration, and (3) vapor transport (which is not

relevant to our study as it involves very high temperatures $\sim 1000^\circ\text{C}$). Figure 1.18 illustrates the processes of crystallite and atomic migration. Crystallite migration involves the movement of entire crystallites across the support surface, followed by collision and fusion. It is known as the particles migration and coalescence (PMC). This migration of entire particles can be attributed to thermally induced atom diffusion on the particle surfaces. The accumulation of diffusing atoms on one side of a particle causes a shift in the particle's center, resulting in Brownian motion [108].

Atomic migration involves the detachment of metal atoms residing on the surface crystal planes of a particle, referred to as an 'adatoms', from the particle and moves toward the another particle where it is adsorbed [109], this is known by the Ostwald ripening (OR) process. Atomic migration is expected to be more favorable at lower temperatures compared to crystallite migration. This preference is due to the higher diffusivity of atoms or small clusters, which facilitates their migration. In contrast, larger crystallites require greater thermal energy for motion, which is typically observed at higher temperatures. Thermal sintering processes are typically characterized by slow kinetics at moderate reaction temperatures, and once they occur, they are challenging to reverse or irreversible. Consequently, preventing sintering is generally the adapted approach to consider for limiting this deactivation process.

Shifting to the microscopy part of the thesis, the transmission electron microscopy (TEM) technique used to characterize the catalyst's initial state is presented in the following section. This technique allows the simultaneous study of the 2D and 3D morphology, chemical composition, and crystalline structure of nanomaterials. The Transmission Electron Microscopy (TEM) offers significantly high resolution for studying nanoscale structures, enabling atomic-level visualization and precise analysis of materials.

Furthermore, we will present the advanced TEM techniques, the in-situ and operando TEM, used to monitor the catalyst's evolution throughout the reaction and assess the impact of individual reaction and catalyst factors on it.

5. Transmission electron microscopy

– Brief history of electron microscopy

In visible-light microscopy, the image resolution is limited by the wavelength of the visible-light: this was the starting point of the TEMs developments [110]. The solution to overcome the technological barrier in visible-light microscopy was L. de Broglie's famous theory

concerning electron wave-particle properties. In 1905, A. Einstein developed the concept of wave-particle duality for light by explaining the photoelectric experiment using the concept of photons [111]. L. de Broglie (1925) proposed that all particles with finite mass have a wavelength that is determined by the particle's momentum [112]. Classic electron-diffraction tests in 1927 proved De Broglie's theory, in which electrons diffracted in the same way that X-rays do [113]. The concept of electron microscopy was proposed as a result of these experiments. M. Knoll and E. Ruska created the first Transmission Electron Microscopy (TEM) in Berlin in 1932 [114]. They made the concept of electron lenses a reality by demonstrating electron pictures captured on the instrument. They reported a resolution of 50 nm only one year after the first prototype was built, which is higher than visible-light microscopes.

– **The potentials offered by the transmission electron microscopy**

Transmission electron microscopy (TEM) is a technique that enables examination of materials at nanometric and even atomic levels by utilizing an electron beam as a probe. The wave-particle duality of electrons, as described by Broglie's equation, dictates that the wavelength of electrons relies on their energy (E). Since the kinetic energy of electrons is dependent on the acceleration voltage, this establishes a relationship between wavelength and acceleration voltage:

$$\lambda = \frac{h}{p} = \frac{h}{\sqrt{2m_0E}} = \frac{h}{\sqrt{2m_0eV}} \quad [\text{Eq. 1.10}]$$

Where h is the Planck's constant, p is the momentum and m_0 is the electron mass, e is the electron charge and V is the accelerating voltage. Thus, for an accelerating voltage range between 100 and 1000 kV, the wavelength associated to electrons goes between 1 and 3 pm [110].

As per the Rayleigh criterion, the spatial resolution power (δ) of an optical instrument depends on the wavelength (λ) of the radiation;

$$\delta \approx 1,22 \frac{\lambda}{\beta} \quad [\text{Eq. 1.11}]$$

Where β is the collection half-angle of the lens used.

Hence, by considering the wavelength of accelerated electrons, it becomes feasible to distinguish two points on the object that are separated by a distance smaller than a nanometer, theoretically around 0.1 nm. However, in practice, the resolution is slightly greater due to imperfections in lenses.

Microscopy techniques rely on the strong interaction between matter and electrons, which is primarily of a Coulomb nature. When electrons encounter the sample, they can undergo various phenomena, including direct transmission without scattering, transmission with electron scattering, absorption, and backscattering. Depending on the energy of the incident electrons, two types of scattering are possible: elastic and inelastic scattering. Elastically scattered electrons are used to form diffraction patterns (DPs), conventional TEM or Scanning Transmission Electron Microscopy (STEM) micrographs. On the other hand, inelastic scattering occurs when there's a loss of energy by the incident electrons as a result of interaction between electrons and the sample. Inelastic scattering generates a multitude of phenomena: ionization, emission of X-rays, secondary electrons, Auger electrons, phonon and plasmon vibration. Thus, the information that can be collected with electron microscopy is multiple. Not only is it possible to get an image of the object, but also to determine its chemical composition, morphology and local structure on a sub-nanometric scale. Chapter II provides a comprehensive explanation of the TEM technology and its operational modes.

Utilizing the TEM in catalysis research enables the examination and analysis of morphology, size, crystal structure, as well as qualitative and quantitative aspects of the catalysts.

– **Transmission electron microscopy for catalysis**

Over the past few decades, it has become clear that the future design of high-performance catalysts relies heavily on a deep understanding of the synthesis and reaction mechanisms at the atomic and molecular scale. Scanning/transmission electron microscopy (S/TEM) has emerged as a primary characterization tool for catalysis research.

Unlike other techniques such as X-ray diffraction (XRD), X-ray photoelectron spectroscopy (XPS), scanning electron microscopy (SEM), Fourier-transform infrared spectroscopy (FTIR), Raman spectroscopy, and other spectroscopic tools that provide information on bulk structures, composition, and electronic states, electron microscopy offers atomic spatial resolution and the unique capability to perform spectroscopy at the atomic level simultaneously. Although the

energy resolution of STEM-EELS and EDX may not match that of Raman and FTIR, the spatial resolution of S/TEM enables the analysis of crucial interfaces and surfaces of individual catalysts, complementing the information obtained from other spectroscopic techniques. [115]

Initially, electron microscopy was employed to investigate the morphological, structural, and chemical properties of materials, establishing connections between these characteristics and their practical functionality under real-world operating conditions. Transmission electron microscopy allows a 3D characterization of nanomaterials using Electron Tomography (ET), enabling to move beyond the analysis of the 2D sample projections.

– **Electron tomography for catalysis**

Three-dimensional electron microscopy, or Electron Tomography (ET), made significant progress in the 1990s when microscopes became computerized for taking pictures. But the initial steps in this field go back further, with early work by *Franck* [116] focusing on studying biological structures using high-resolution microscopy microscopes.

The 1980s brought forth an important development in this field when *Radermacher* [117] introduced the concept of acquiring a series of images by tilting the sample to its maximum extent. This innovative approach helped reducing the ‘missing wedge’ in Fourier space and improve the resolution along the z-axis. While the mathematical theory of tomography has been established during the 20th century by Radon transform [118], practical applications in the field took a while to develop. *Radermacher* played a crucial role in achieving the first 3D reconstruction using mathematics called the Radon transform [119]. He focused on the importance of image alignment prior to the reconstruction process. The earliest image series suitable for analysis were obtained through X-ray imaging, dating back to 1968 [120]. The most well-known application of this methodology is the X-ray scanner, a widely used tool for medical diagnostics. Since the 1990s, electron tomography, has evolved into an indispensable tool for investigating complex biological structures. In recent years, this approach has also found applications in the study of physico-chemical materials. In 2000, the research team at the University of Utrecht, led by Jong, achieved significant success by using electron tomography to locate silver particles in a type of zeolite called NaY [121]. They continued their work by investigating the distribution of gold particles in a support material called SBA-15 [122]. Among many other studies conducted by this team, a research was about the distribution of

Palladium (Pd) particles with the pores of Xerogel-type catalysts [123]. These studies were all achieved using bright-field Electron Tomography.

In 2002, J. Miao and colleagues [124] have introduced an innovative diffraction-based 3D microscopy technique to overcome resolution limitations in high-resolution electron microscopy and tomography. Later on, this same research group have developed novel algorithms for tomographic reconstruction, including the equally-sloped tomography (EST) technique [125]. S. Bals and her team have introduced the concept discrete electron tomography. The discrete tomography algorithm known as the Discrete Algebraic Reconstruction Technique (DART) was used to study Zeotile-4 in order to uncover the 3D arrangement of or pores in the corresponding mesoporous silica matrix [126]. They have showed that the 3D reconstruction allowed for the precise measurement of the thickness of the building units in a quantitative manner.

Another research team in the field of electron tomography for nanomaterials is the Midgley group at the University of Cambridge. They focused on model systems at first, specifically bimetallic Pd-Ru particles inserted into a mesoporous support to determine their spatial distribution[127]. Their distinctive approach involves introducing the concept and implementation of electron tomography in scanning transmission electron microscopy (STEM) mode. Using this mode, they investigated the morphology and distribution of Tin (Sn) particles within a silicon matrix [128]. In particular, they have used high-angle annular dark-field (HAADF) mode, which has the advantage of being insensitive to diffraction contrast. Bals group have also explored electron tomography with the STEM-HAADF mode for analyzing ceramic glasses that had been exposed to high-temperature treatments[129]. Since HAADF-STEM tomography is the preferred mode for examining heavy nanoparticles within a light matrix, it was used to investigate the distribution of Pt and PtCr nanoparticles in carbon black supports, which are commonly used in heterogeneous catalysis[130].

The TEM experiments are typically conducted in a relatively high vacuum ($<10^{-5}$ Pa) to minimize the interaction between the electron beam and air molecules. While this approach is effective in obtaining static information about samples in equilibrium, it does not allow for the observation of their dynamic evolution within their operational environment. To facilitate such investigations, a technological advancement in TEM known as in-situ TEM has been developed. This technique enables the real-time exploration of a wide range of processes and reactions that take place under actual operating conditions. It involves the utilization of

functional sample holders that are capable of applying specific stimuli such as heat, electric bias, light, or operating within gaseous or liquid environments.

6. In-situ and operando transmission electron microscopy

High-resolution transmission electron microscopy (HRTEM) could only be carried out under vacuum and could not produce dynamic observations in real-life conditions. The ex-situ experimental method is thus carried out outside of the electron microscope. Post experiment, electron microscope is used for nanomaterials analysis. Comparative imaging is conducted on the material both before and after the reaction to investigate the catalyst modifications at different stages of the reaction. However, this conventional approach does not provide real-time observation throughout the reaction. In-situ TEM facilitates the real-time monitoring of the atomic structure of nanocatalysts under reaction conditions. It allows the observation of structural evolution during gas-solid interactions. This real-time insight is invaluable in the context of catalytic innovation and development.

Within this section, our specific interest lies in the examination of the gaseous environment through the utilization of environmental transmission electron microscopy (ETEM). This cutting-edge technique allows for the investigation of samples within both gaseous [131]–[135] and liquid [136]–[140] environments. However, for the purposes of this thesis, our attention is solely directed towards the study of the gaseous environment. Over the years, several attempts were made to bring in-situ electron microscopy into practice. The first successful attempt was made by E. Ruska, who played a key role in the development of electron microscopy. Ruska recognized the importance of investigating materials under carefully controlled conditions of temperature and gas. He introduced the initial design of an environmental microscope, known as a differentially vacuum pumped environmental TEM (ETEM) in 1942 [141]. We will provide a brief explanation of the principle behind the open ETEM system, and subsequently move to the detailed explanation of the other environmental TEM technology: the windowed-type gas Environmental cell (E-cell) system.

6.1. Differentially vacuum pumped environmental TEM

In this particular design, the gas system is integrated into the microscope, allowing for the continued use of regular specimen holders. In order to enable differential pumping at different stages, it is necessary to modify the TEM column. By incorporating a series of differential

pumping apertures and additional pumping capacity, it becomes feasible to sustain the pressure differential between the microscope column and the sample region [142].

The ETEM design guarantees the maintenance of a high vacuum at critical levels such as the electron gun, condenser, and intermediate lenses of the microscope. Additionally, it offers the flexibility to accurately set gas pressures within a wide range, spanning from 10^{-5} mbar up to 20 mbar. Previous versions of differentially pumped ETEM systems have facilitated in situ S/TEM capabilities, allowing for the observation of catalysts' structural changes under (near) reaction conditions [142]–[145].

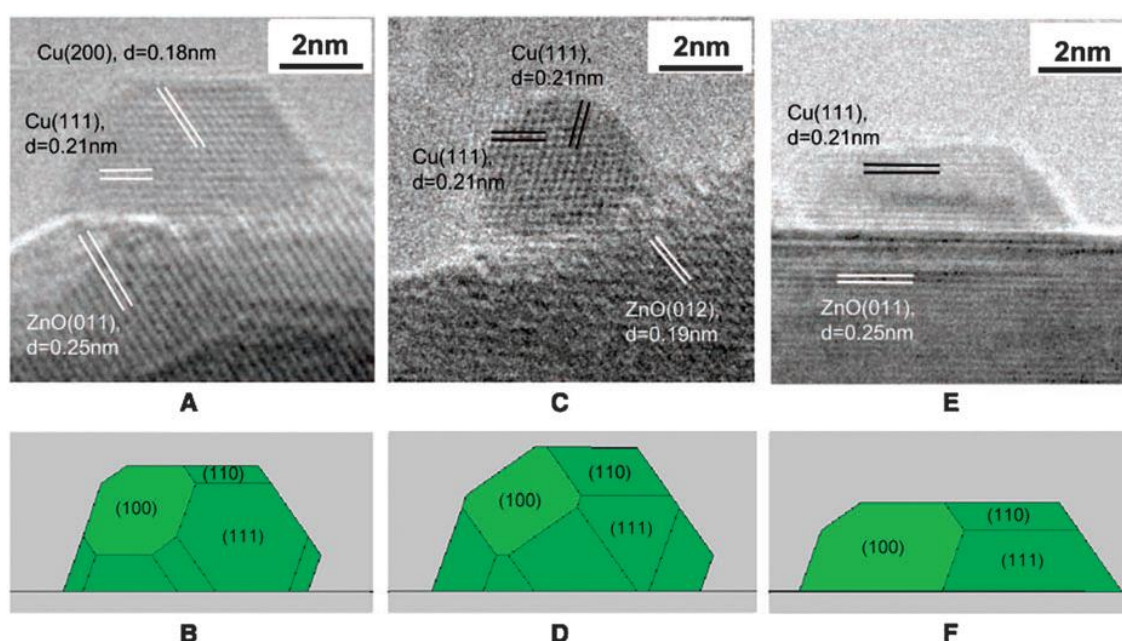


Figure 1.19: In situ TEM micrographs (A, C, and E) showing the reversible shape modifications of a copper (Cu) catalyst on a zinc oxide (ZnO) support under different gas environments, accompanied by the corresponding Wulff constructions of the Cu nanocrystals (B, D, and F). Image (A) captures the catalyst at a pressure of 1.5 mbar of H_2 and a temperature of $220^\circ C$. Image (C) was acquired in a gas mixture of H_2 and H_2O , with a ratio of H_2/H_2O at 3:1 and a total pressure of 1.5 mbar at $220^\circ C$. Image (E) represents the catalyst's behavior in a gas mixture of H_2 (95%) and CO (5%) at a total pressure of 5 mbar and a temperature of $220^\circ C$. [147]

In Figure 1.19, a series of in situ high-resolution TEM images with a remarkable imaging resolution below 0.2 nm depicts the dynamic and reversible shape modifications of the nanocatalyst in response to variations in the gaseous environment [147]. Hansen et al. [148] presented interesting results, showing high-resolution images of copper (Cu) nanocrystals that are catalytically active in methanol synthesis and hydrocarbon conversion processes.

6.2. Window-gas cell environmental TEM

Unlike the dedicated environmental TEM, the closed environmental cell system does not require any modifications to the TEM column. In this setup, the specimen is enclosed within a cell comprising of two electron-transparent windows that are chemically inert and amorphous (Figure 1.20). While maintaining the microscope's high vacuum, gas is introduced into the cell. A specialized specimen-holder is designed to accommodate all the cell components, including gas inlets and outlets. The membranes used in this system have a thickness ranging from approximately 30 to 50 nm and possess high fracture strength, enabling them to withstand pressures up to 1 bar. For instance, for the gas cell manufactured by Protochips®, the E-chip membrane for the window is composed of a 50 nm thick layer of SiN_x . In the case of the thermal E-chip, it features a SiN_x membrane that is 30 nm thick, situated above a ceramic heating material with a thickness of approximately 120 nm. These membranes are deposited onto disposable chips that are compatible with MicroElectroMechanical System (MEMS) devices [149]. Both chips feature a gold electrical contact specifically designed to heat the ceramic membrane, allowing it to reach temperatures of up to 1000 °C. The space between the two membranes measures approximately 5 μm , and the cell has a volume of around 1 μl .

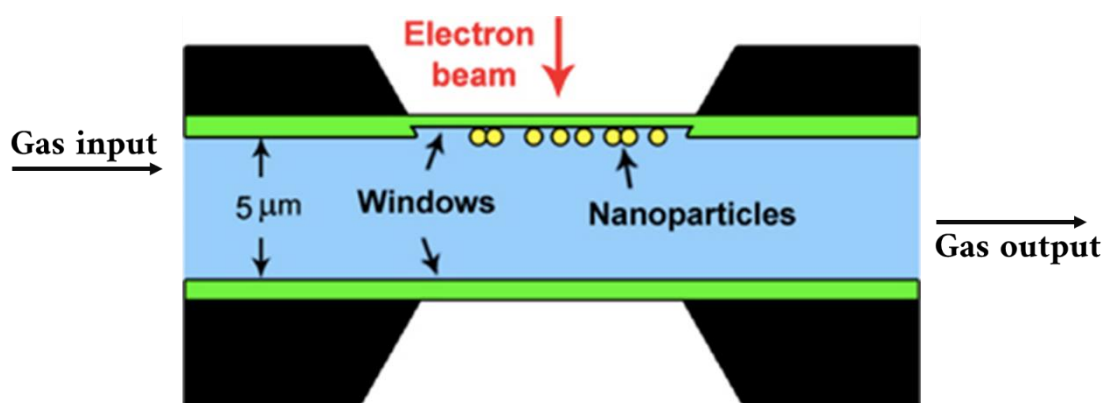


Figure 1.20: Schematic representation of a closed E-cell. [150]

The first closed cell for gas TEM was elaborated by Abrams & McBain in 1944 [151]. The first high temperature closed gas cell TEM was successfully made by H. Hashimoto et Al. in 1968 [152]. An atomic resolution gas cell TEM approach was finally realized by Boyes & Hai in 1997 [153]. Beginning as "home-made" specimen-holders in laboratories [151], E-cells using silicon nitride (SiN_x) membranes have been extensively developed and brought to market by companies such as Protochips, Dens Solutions [154], and Hummingbird Scientific [155].

For the purpose of this thesis, the E-cells provided by Protochips are used and a detailed explanation of this E-cell technology is provided in chapter II.

6.3. The advantages and disadvantages of using the environmental gas cell

The window-type E-cell offers several advantages over a dedicated TEM instrument, making it a more efficient choice. The primary advantage of employing the closed cell approach is its versatility across different microscopes that share the same holder stage, eliminating the need for further modifications to the TEM column. It also has a lower acquisition cost and significantly reduced maintenance expenses. Additionally, closed E-cells can withstand much higher internal pressures, with commercially available ones capable of reaching up to 1 atm gas pressure. Unlike dedicated ETEM, closed E-cells can handle corrosive gases, expanding their applicability beyond non-corrosive gases like H₂, O₂, NH₃, CO, and water vapors. However, the closed E-cell technology also has its disadvantages, primarily associated with the SiN_x windows. The gas-restrictive nature of these windows can result in a reduction in image resolution, which is not a limitation in dedicated ETEM systems. This also poses challenges for reliable EDX spectroscopy. Furthermore, the specimen geometry and field of view are generally smaller compared to conventional TEM, and the setup imposes constraints on sample geometry. [142]

6.4. Operando transmission electron microscopy

Operando TEM involves real-time monitoring of sample evolution under conditions that mimic the studied process, with a focus on analyzing reaction products in heterogeneous catalysis [154]. To achieve this, environmental microscopy techniques are combined with spectrometry techniques. In environmental TEM, which employs a thin carbon membrane (~10nm), electron energy loss spectroscopy (EELS) was initially used to identify the reaction products [155]. Direct analysis of gases is performed at the sample level. An alternative to EELS is the use of a residual gas analyzer (RGA) equipped with a mass spectrometer. Positioned at the outlet of the reaction medium, it enables continuous analysis of reagents and products throughout the reaction. [156] The RGA is commonly employed in both environmental microscopy approaches (environmental TEM and TEM with environmental cell), but it is particularly suitable for closed environmental cell technology. In this case, EELS yield weak signals of the reaction products due to significant electron diffusion caused by SiN_x membranes. The residual gas analyzer (RGA) is a mass spectrometry-based technique for analyzing products in the gas phase. Though

it can detect minuscule volumes of gas down to a few ppm, this is a high-performance device. The RGA mass spectrometer operates at low pressures of approximately 10^{-6} mbar to prevent substantial ion collisions. Consequently, a differential pumping system, comprising a mechanical pump and a turbomolecular pump, is used to reduce the gas pressure when exiting the environmental cell.

The in-situ TEM configuration has found diverse applications in catalysis research. The next section covers briefly a few examples of them.

6.5.Examples of applications of the Environmental cell in catalysis research

A study by Hansen et al. [148] used an advanced electron microscope (ETEM) to demonstrate this effect on a Cu/ZnO catalyst used in methanol synthesis. At 220 °C, the catalyst in Figure 1.21 underwent exposure to different environments commonly found in methanol synthesis reactors: H₂, H₂/H₂O, and H₂/CO.

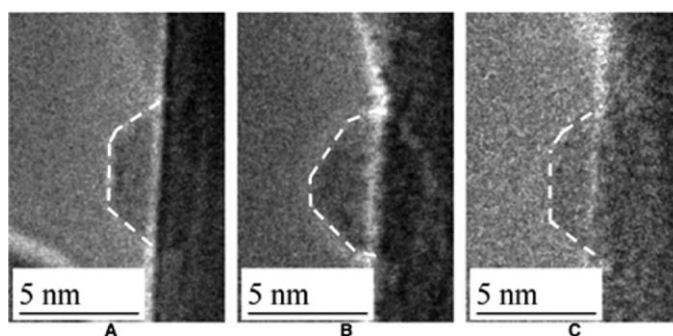


Figure 1.21: TEM images showing the reversible shape transformation of a copper nanoparticle at 220 °C under different conditions: (A) H₂ at 150 Pa, (B) H₂: H₂O (3:1) at a total pressure of 150 Pa, and (C) H₂ at 150 Pa.[148]

When exposed to pure hydrogen, the copper particles exhibited faceted surfaces, specifically exposing the low-index facets (100), (110), and (111). As the environment became more oxidizing with the addition of water (H₂O), the particles took on a more spherical shape due to changes in the specific surface energies of the facets caused by the adsorption of OH species. Despite these changes, the particles remained in a metallic state, as confirmed by HRTEM analysis. Switching to a more reducing environment by introducing CO to the hydrogen, the particles once again exhibited faceted surfaces, but with different facet distributions. Additionally, they wetted the surface of ZnO support.

The sintering of Nickel (Ni) NPs was addressed in another study [157]. As discussed earlier in this chapter, sintering, the growth or agglomeration of NPs, is a common deactivation mechanism in supported metal catalysis. The dominant sintering mechanisms was identified using the Environmental TEM approach.

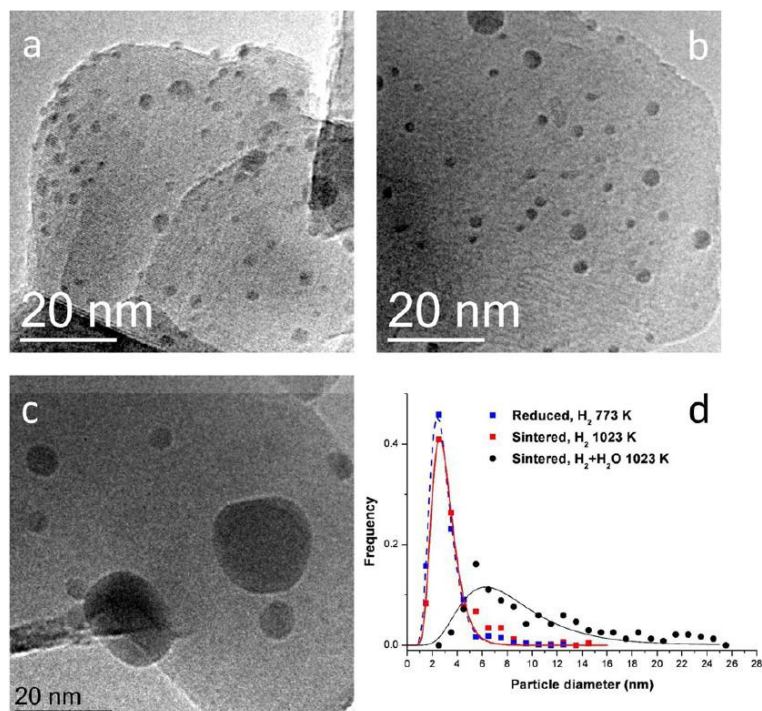


Figure 1.22: TEM images showing the evolution of a Ni/MgAl₂O₄ sample: (a) post-reduction in 3 mbar H₂ at 500 °C, (b) after 5 hours of sintering in 2 mbar H₂ at 750 °C, (c) after 5 hours of sintering in 2 mbar H₂ and 2 mbar H₂O at 750 °C. (d) The corresponding particle size distributions for each case are shown as well. [157]

Figure 1.22 displays TEM images and size distributions of spinel-supported nickel NPs. The sample was first reduced in H₂ and then exposed to sintering environments. The particle size distributions after sintering show a tail on the large diameter side, indicating growth via PMC, with a significant influence of the atmosphere composition. Further observations during exposure to sintering environments supported the PMC mechanism, and three phases of sintering were proposed. Phase 1 exhibits a rapid decrease in activity, dominated by OR, where the catalyst and metal particles reach their equilibrium shape. In phase 2, sintering slows down, but particle growth via migration continues. Phase 3 represents stable operation, with particles have grown large, other parasitic phenomena, such as support restructuring, can become significant, particularly under elevated temperatures.

7. The problematic and the strategy of the project

The primary objective of this study is to address the thermal stability of two different sets of Pt-based hollow nanospheres. The mechanisms governing their morphological evolution are investigated. This research aims to understand how different reaction conditions, encompassing both thermal and environmental variables, influence the microstructural changes of the catalyst during the course of a chemical reaction. An examination of how the different characteristics of the two batches of nanocatalysts affect their behavior is conducted. The CO₂ hydrogenation is chosen as a model hydrogenation reaction to investigate the catalyst's behavior.

The initial state of these catalysts is characterized using the TEM, including electron tomography. Various characteristics of each set of Pt-based hollow nanospheres that affect the active surface area, a critical factor influencing their catalytic performance, are studied. Later in the research, the in-situ TEM approach is employed to track the morphological changes of the synthesized particles during thermal annealing under TEM vacuum conditions. The same study is conducted under a hydrogen (H₂) atmosphere within a TEM Environmental cell (E-cell) to assess the impact of H₂ alone on the behavior of the Pt-based hollow nanospheres. Finally, a thermal annealing of both sets of catalysts is performed under a mixture of CO₂ and H₂ gases to simulate the conditions of the CO₂ hydrogenation reaction inside the E-cell. The morphological changes in each catalyst set are systematically monitored to detect any modifications in their behavior when compared to previous environments. Simultaneously, the reaction products are detected and monitored using the Operando TEM approach. The differences in behavior between the two catalyst systems are assessed and linked to their previously studied features, concluding the most favorable system for catalytic applications.

Chapter II of this thesis elaborates on the experimental approach, including all adapted conditions employed throughout this study.

CHAPTER II: Experimental Approach: Pt-Based Material Synthesis and In-Situ and Operando TEM technology

1.	Synthesis of the Co-templated Pt hollow nanospheres (HNS).....	46
1.1.	Synthesis basic principle.....	46
1.2.	Synthesis of Co-templated hollow nanospheres: batches 1 and 2	47
2.	Techniques used for basic characterization.....	48
2.1.	The scanning electron microscopy (SEM)	48
2.2.	The X-Ray diffraction (XRD) technique	49
3.	TEM investigations	51
3.1.	Basic principle of the transmission electron microscopy	51
3.2.	Characteristics of the transmission electron microscope utilized.....	53
3.3.	The transmission electron microcopy working modes employed and the experimental conditions.....	54
4.	Electron tomography (ET)	57
5.	In-situ and operando TEM	59
5.1.	Furnace type heating holder.....	59
5.2.	Environmental cell technology	60
5.3.	Gas manifold.....	68
5.4.	Residual Gas Analyzer	68
5.5.	Methodology of the TEM experiments.....	73

1. Synthesis of the Co-templated Pt hollow nanospheres (HNS)

1.1. Synthesis basic principle

The main concept behind the synthesis of Pt-based hollowed nanospheres using the chemical route is to take advantage of the replacement reaction between Co nanoparticles and H_2PtCl_6 as proposed by Liang [92]. Due to the significantly higher standard reduction potential of the $PtCl_6^{2-}/Pt$ redox pair (0.735 V vs. the standard hydrogen electrode (SHE)) compared to the Co^{2+}/Co redox pair (-0.277 V vs. SHE), Co nanoparticles undergo immediate oxidation to cobalt ions upon introduction to the H_2PtCl_6 solution. The color of the latter change from pale yellow to black indicates the oxidation of Co nanoparticles and the formation of Pt hollow nanospheres. The replacement reaction proceeds rapidly, leading to the nucleation and growth of Pt atoms into small particles that eventually form a thin shell around the Co nanoparticles. This shell possesses an incomplete porous structure as a result of continuous diffusion of Co^{2+} and $PtCl_6^{2-}$ across it until the complete consumption of Co nanoparticles (Figure 2.1).

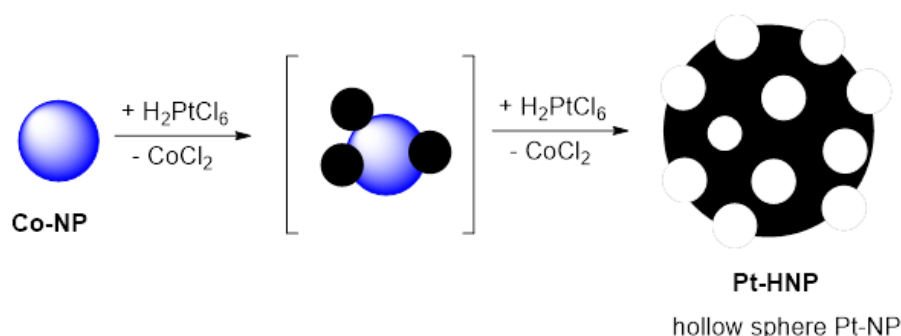


Figure 2.1: Schematic representation of the synthesis process of Co-templated Pt Hollow nanospheres

Based on the stoichiometric relationship described in the following Eq. 2.1, the complete reaction between the solutions of Co nanoparticles and H_2PtCl_6 can be expected.



Two batches of the targeted material are synthesized, the experimental procedure of each one is detailed in the following paragraphs.

1.2. Synthesis of Co-templated hollow nanospheres: batches 1 and 2

A comprehensive description of the materials and process methods is provided, highlighting the differences between the first and second synthesis.

– Synthesis 1

Materials

Sodium borohydride (NaBH_4 , MW: 37,8 g mol⁻¹); citric acid ($\text{C}_6\text{H}_8\text{O}_7$, MW: 192,1 g mol⁻¹); Cobalt (II) chloride (CoCl_2 , MW: 129,8 g mol⁻¹); Platinum salt ($\text{H}_2\text{PtCl}_6 \times 6 \text{H}_2\text{O}$, MW: 517,9 g mol⁻¹)

A 0,4 M stock solution of CoCl_2 (52 mg CoCl_2 dissolved in 1 mL water) was prepared.

Pt/Co = 1.0:1.3 [Pt/2Co = 1:0.7; 2Co/Pt = 1.0:1.5]. A 1.5-fold excess of Pt^{4+} over the stoichiometric amount is to assure that most of the Co^0 particles are consumed prior to air oxidation.

Co NPs were added to a solution of Pt^{VI} salt in water

The reaction was performed in a 100 mL 3-necked flask, sealed with rubber septa and equipped with a magnetic stirring bar. The flask was placed above a magnetic stirring plate and all reactions run at room temperature under Argon (Ar). NaBH_4 (15,1 mg, 0,4 mmol) was dissolved in freshly deoxygenated water (100 mL). Citric acid (7,8 mg, 0,04 mmol) was added and the resulting solution was stirred for 60 min. During this period, the evolution of hydrogen (H_2) gas was visible. Thereafter, CoCl_2 in water (0,1 mL of a 0,4 M stock solution, 0,04 mmol of CoCl_2) was added via syringe while stirring vigorously as shown in Figure 2.2. The solution turned dark during the reduction and Co nanoparticles forming process. The thus prepared solution of Co nanoparticles was added in small portions via syringe to a solution of H_2PtCl_6 in deoxygenated water (30 mL) (15 mg $\text{H}_2\text{PtCl}_6 \times 6 \text{H}_2\text{O}$; 0,03 mmol) during one hour and a half. The resulting solution was exposed to air while stirring vigorously (approximately 1h). The obtained particles were collected by centrifugation (3 times for 45 min. at 250000 rpm). The resulting material will be called Pt-1 in the following sections.

A second batch of was prepared using the same Co/Pt ratio with modifications regarding the addition process of Co nanoparticles to the excess of Pt^{VI} salt.

– Synthesis 2

Co nanoparticles were prepared the same way as in the first synthesis along with the Pt^{VI} salt solution in deoxygenated water.

The Pt^{VI} salt in water was added via syringe pump to a solution of Co NPs

The solution of H₂PtCl₆ was added to the prepared Co nanoparticles solution via a syringe-pump over a period of 2 h. After completion of addition, the reaction mixture was stirred for another hour. Thereafter, it was exposed to air while stirring vigorously to oxidize all remaining Co⁰ particles. The synthesized particles were collected by centrifugation (3 times for 45 min. at 250000 rpm). This material will be called Pt-2 in the following sections.

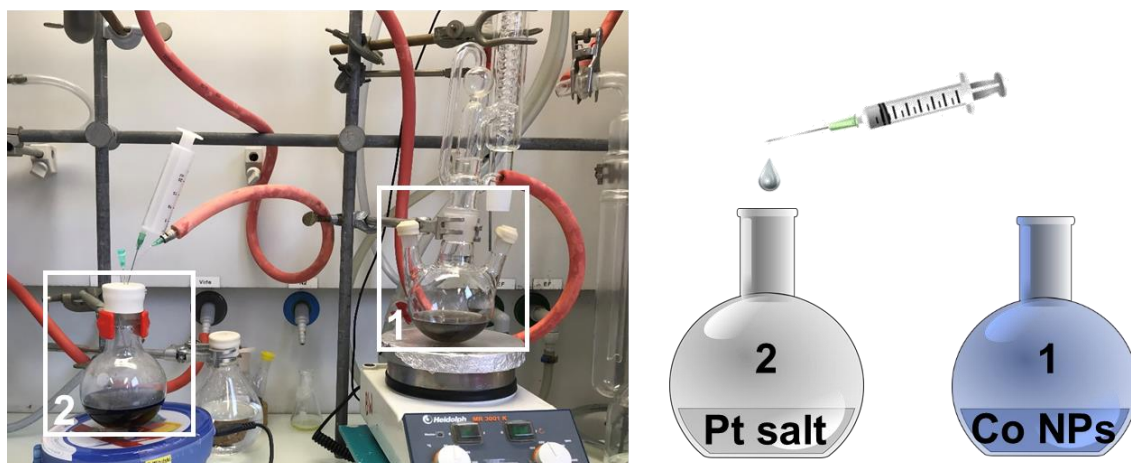


Figure 2.2: The synthesis procedure of the Co-promoted hollow nanospheres: addition of the Co NPs dropwise to an excess of Pt salt

2. Techniques used for basic characterization

2.1. The scanning electron microscopy (SEM)

The scanning electron microscope (SEM), preliminary used for the synthesized particles characterization during this thesis to confirm the formation of spherical nanoparticles, operates on the principle of using a focused electron beam to image the surface of a sample. The instrument consists of an electron gun that emits a beam of high-energy electrons. The beam is then shaped and focused by electromagnetic lenses to form a narrow probe. This probe scans the sample, usually coated with a conductive material if it is not already conductive, in a systematic raster pattern.

As the beam interacts with the sample surface, several signals are generated as shown in Figure 2.3, including secondary electrons, backscattered electrons, and characteristic X-rays. The primary signal used in SEM for imaging is the secondary electrons, which are collected by a detector and translated into a visual representation on a screen. The SEM provides high-resolution, three-dimensional images, which allows to study the surface morphology, topography, and elemental composition of the sample at the micro- and nanoscale. [158] The SEM characterization was carried out using a JEOL JSM-7900F instrument. The as-synthesized particles were dispersed in ethanol then deposited dropwise onto a Carbon scotch tape and left to dry. The SEM analysis was performed with an accelerating voltage of 2 kV, utilizing the Secondary Electron Imaging (SEI) mode for imaging purposes. This mode covered a magnification range from 30,000x to 110,000x. During the scanning process, the Lower Electron Detector (LED) captured the secondary electrons emitted at each point. These electrons were then used to reconstruct the resulting image, which was represented in grayscale pixels.

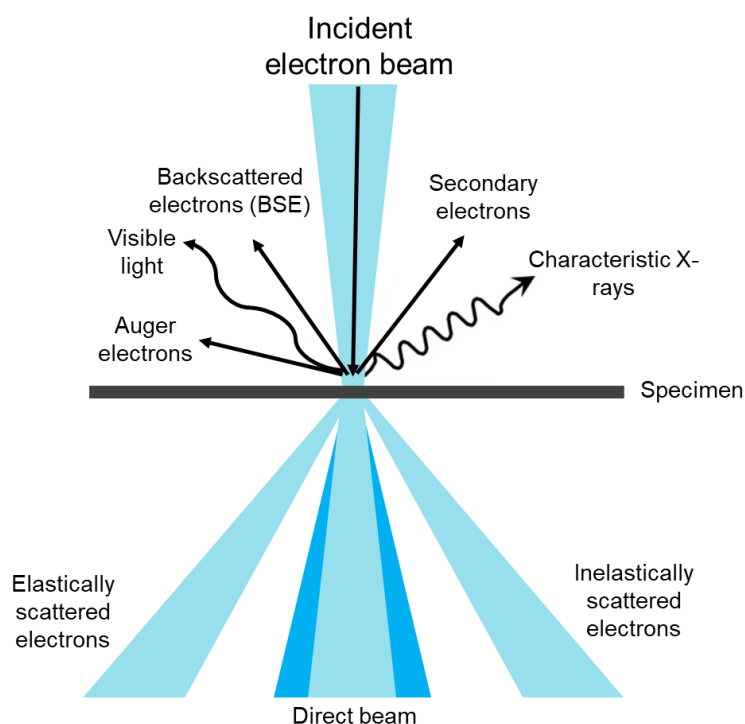


Figure 2.3: Signals generated from a thin specimen through electron beam interaction[110].

2.2. The X-Ray diffraction (XRD) technique

In order to investigate the crystalline structure of the synthesized particles on a non-local range, the XRD was utilized. This relies on the diffraction of X-rays caused by regularly spaced atomic

planes, and the detection of the diffracted signal based on the angle or energy. W.L Bragg provided a geometric explanation for XRD, explaining the constructive interferences. Figure 2.4 provides detailed information about the geometric condition for diffraction and the determination of Bragg's law which is expressed by Eq. 2.2 [159].

$$n\lambda = 2d_{hkl}\sin(\theta_n) \quad [\text{Eq. 2.2}]$$

In Eq. (2.2), n is the order of diffraction, λ is the wavelength of the incident beam in nm, d_{hkl} is the lattice spacing in nm and θ is the angle of the diffracted beam in degree.

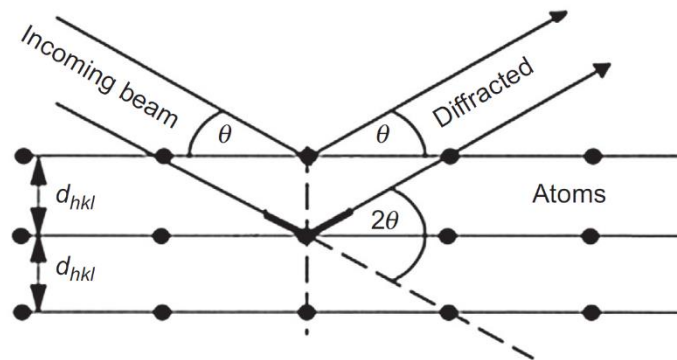


Figure 2.4: Geometrical condition for diffraction from lattice planes explained by W.L Bragg [159]

By directing a beam of X-rays on a sample, the X-rays interact with the atoms in the material and produce a unique diffraction pattern. The diffraction pattern, obtained by analyzing the scattered X-rays, provides valuable information about the crystal structure, including lattice spacing, crystal symmetry, and orientation. XRD instruments typically consist of an X-ray source, a sample stage, and a detector.

The XRD patterns were recorded using an Empyrean X-ray diffractometer with a cobalt $K\alpha$ radiation source ($\lambda = 1.78886 \text{ \AA}$), operated at 40 kV and 40 mA. The sample high concentration ethanol solution was dropped onto a low-background silicon wafer holder and mounted on the goniometer stage. The XRD measurements were carried out in the 2θ scanning mode and the diffraction patterns were recorded in the range of 20° to $120^\circ 2\theta$. To ensure accurate measurements, a background scan of the sample holder alone was conducted and was taken into consideration while analyzing the resulting diffractogram. The primary technique employed for the analysis of the synthesized particles in this thesis is the transmission electron microscopy (TEM). The subsequent sections will delve into comprehensive explanations of this technology.

3. TEM investigations

The TEM played a central role in investigating the morphology, structure, and chemical composition of the synthesized particles. It is a crucial tool in catalysis research, offering in-depth insights into catalysts at the nanoscale and even subatomic levels [160], [161]. Through direct observation and characterization, the TEM enables the assessment of catalyst materials in terms of size, shape, crystalline structure, and surface morphology. Such information is vital for comprehending catalyst performance and reactivity. The following sections provide detailed explanations of the TEM technology, including the operational modes utilized, as well as the experimental conditions adapted throughout this thesis.

3.1. Basic principle of the transmission electron microscopy

The schematic representation of the TEM column in Figure 2.5 shows its three main parts: the illumination system, the object-objective lens level and the magnifying and image projection lens.

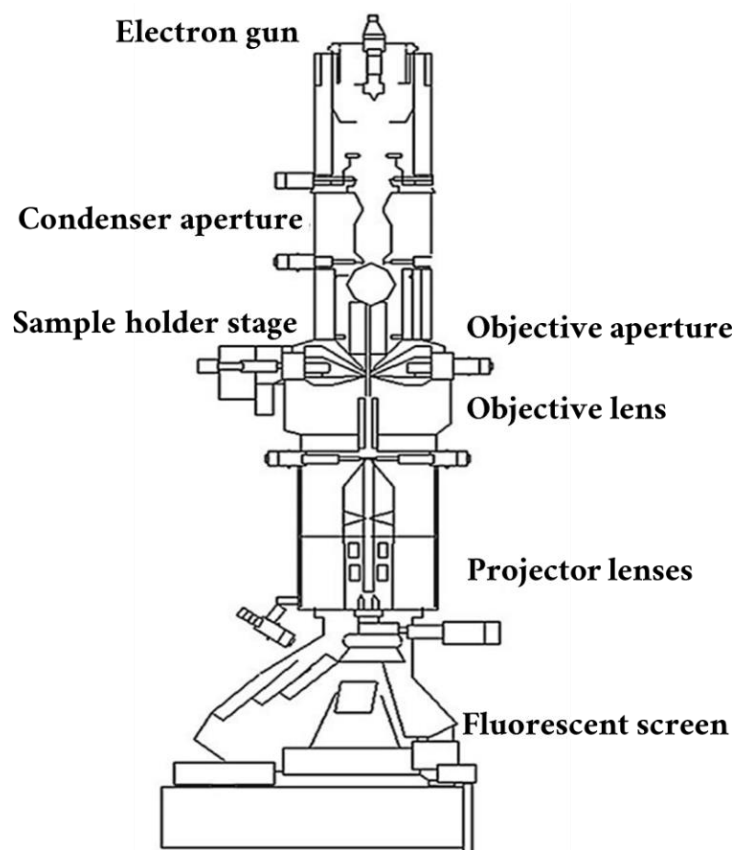


Figure 2.5: Schematic representation of a transmission electron microscope[162]

The illumination system comprises the gun, in which is incorporated the electron source, and condenser lenses. Its role is to extract electrons from the source and accelerate them upon the specimen. This system can be operated in two principal modes: parallel beam and convergent beam. The first mode is used primarily for TEM imaging, selected-area electron diffraction (SAED) and Energy-Filtered TEM (EFTEM), while the second mode is mainly used for scanning (STEM) imaging, analysis via X-rays and electron spectrometry. Electron guns utilize different electron sources, including thermionic, field emission, and Schottky sources. During this thesis, the electron microscope used (JEOL ARM 200CF) comprises the Cold Field Emission (CFE) electron source. It involves applying an intense electric field ($\sim 10^{10} V/m$) to an ultrafine tungsten tip. The surface of the tip must be free of contaminations and oxides. To achieve this pristine surface, Ultra-High Vacuum conditions ($< 10^{-9}$ Pa) are employed in this type of source. Extracted electrons are accelerated by the application of an electrical voltage (80 kV to 200 kV) and guided to the sample by condenser lenses. These latter are magnetic lenses that generate a variable magnetic field making it possible to control the intensity and the spatial distribution of the electron beam on the sample.

The TEM's center comprises the objective lens and specimen holder/stage system. This is where beam-specimen interactions occur and the fundamental TEM operations take place: creating images and diffraction patterns (DP) that are later magnified for viewing and recording. At the sample level, the most crucial lens is the objective lens, which forms the initial image of the object. It possesses the strongest magnetic field among the lenses. The quality of this lens greatly influences high-resolution imaging.

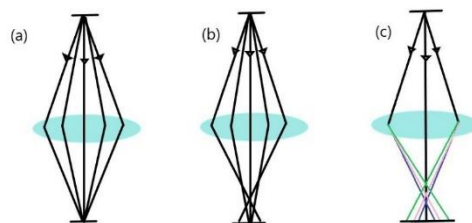


Figure 2.6: Schematic representation of (a) perfect lens and the case of presence of (b) spherical aberration and (c) chromatic aberration.

Electromagnetic lenses in electron microscopy face challenges like their optical counterparts. Aberrations, such as spherical (Fig 2.6(b)) and chromatic aberration (Fig 2.6(c)), limit high-resolution imaging. Spherical aberration occurs when the lens field behaves differently for off-

axis rays, resulting in a point object being imaged as a finite-sized disk. Chromatic aberration stems from electron energy scattering, preventing the precise focusing of electrons from the same point on the sample. While electron energy variations can be minimized, they still exist within acceptable limits for high-voltage supplies. Efforts have been made to address spherical and chromatic aberrations in electron microscopy, with advancements in lens design and the development of correctors and monochromators [163][164]. Astigmatism, caused by non-uniform magnetic fields, is another challenge. Inhomogeneities in soft iron and misalignment of apertures can disrupt the field. Contamination can also affect beam deflection. Astigmatism can be corrected using stigmators, which generate compensatory fields.

Finally, at the lower level of the TEM column, a system of intermediate lenses (projectors) allows the magnification and projection of the sample image onto the detector to be taken by a dedicated Camera or by the Scanning TEM (STEM) mode detectors. [110]

Electron-intensity distributions generated by the specimen are converted into grey-scale level on digital images. This process involves image detection, display, and recording. Different detection methods are used in TEM and STEM modes. In STEM, the image is built up over time through scanning. Detectors are present in the TEM viewing chamber, and cameras enable digitization of analog TEM images for online viewing and analysis. Despite their infrequent usage during this work, it is worth explaining about the two cameras installed on the ARM 200CF with distinguished properties: the US1000XP charge-coupled device (CCD) camera from Gatan, Inc. and the RioTM, Gatan's newest complementary metal-oxide-semiconductor (CMOS) camera. Characteristics of the cameras are found in Appendix 1.

3.2.Characteristics of the transmission electron microscope utilized

Throughout this thesis, we employed a state-of-the-art JEOL® (Japan Electron Optics Laboratory) double corrected Cs probe transmission electron microscope (TEM). Specifically, we utilized the ARM200CF model equipped with a cold field emission gun (CFE) and advanced STEM and TEM correctors from CEOS GmbH (Corrected Electron Optical Systems). By combining the cold field emission gun with the STEM corrector, known as the CESCOR corrector, an exceptionally small electron probe size is achieved, measuring less than 0.1 nm in diameter. This ultrafine electron probe enabled to conduct STEM imaging as well as perform EDS analyses at the sub-angstrom level. The ARM200F model not only provided a diminutive probe diameter but also delivered a significantly increased probe current, thereby facilitating

enhanced analysis with a higher signal-to-noise ratio. Additionally, the incorporated TEM corrector, known as CETCOR, allows for high-resolution TEM imaging.[165]

For sample preparation, particles to be investigated were dispersed in ethanol using an ultrasonic bath and deposited on a gold or copper TEM grid covered by a holey carbon membrane.

3.3. The transmission electron microscopy working modes employed and the experimental conditions

In addition to imaging techniques such as phase contrast, diffraction and Z-contrast, electron microscopy was commonly employed for Energy Dispersive X-ray Spectroscopy (EDS) and Electron Energy Loss Spectroscopy (EELS). These techniques are combined in Analytical Electron Microscopy (AEM). Within the context of this thesis, beside the use of the conventional TEM mode for a preliminary view of the specimen, a comprehensive 2D analysis of the sample was conducted utilizing the STEM mode, as well as employing the Energy Dispersive X-Ray Spectroscopy (EDS) and Selected Area Electron Diffraction (SAED) modes.

The later sections describe the basic principle of each mode and the specific experimental conditions used for each.

– Conventional transmission electron microscopy mode

This TEM imaging mode was used to examine the structure and morphology of samples. Although such data are not explored in the present manuscript, it is worth explaining its principle briefly since it's one of the most commonly used TEM modes. It involves a parallel electron beam and offers two imaging modes: bright field and dark field. In bright field mode, only directly transmitted electrons form the image, while in dark field mode, scattered electrons are used. Depending on the crystal orientation, more or fewer electrons are scattered, resulting in varying image contrast.[110]

– Selected Area Electron Diffraction mode

This mode is mainly used to study the crystallinity of the object. The crystalline sample is illuminated by a parallel electron beam. Part of the electrons is scattered at specific angles due to diffraction (diffracted beams), while others pass through the sample without deviation (transmitted beam). After passing through the microscope's magnetic lens, the initially parallel beams converge in the back focal plane, forming the selected area diffraction pattern. The

transmitted beams converge upon the optical axis, while the diffracted beams intersect at a specific distance from the optical axis (from the transmitted beams). This distance corresponds to the interplanar distance of the sample crystalline planes responsible for the diffraction, following Bragg's law [166]. This interplanar distance, denoted as d_{hkl} , related to a specific set of lattice planes with Miller indices (hkl).

In our case, the particles crystalline structure was determined using this mode with an aperture of 20 μm and a camera length of 20 cm. Afterwards, the GMS3 Gatan software was employed to identify the crystalline structure of the particles and determine the corresponding crystalline planes.

– Scanning transmission electron microscopy mode

The STEM mode is an imaging technique that may offer high-resolution imaging combined with compositional information (Z-contrast) of the materials at the nanoscale level.

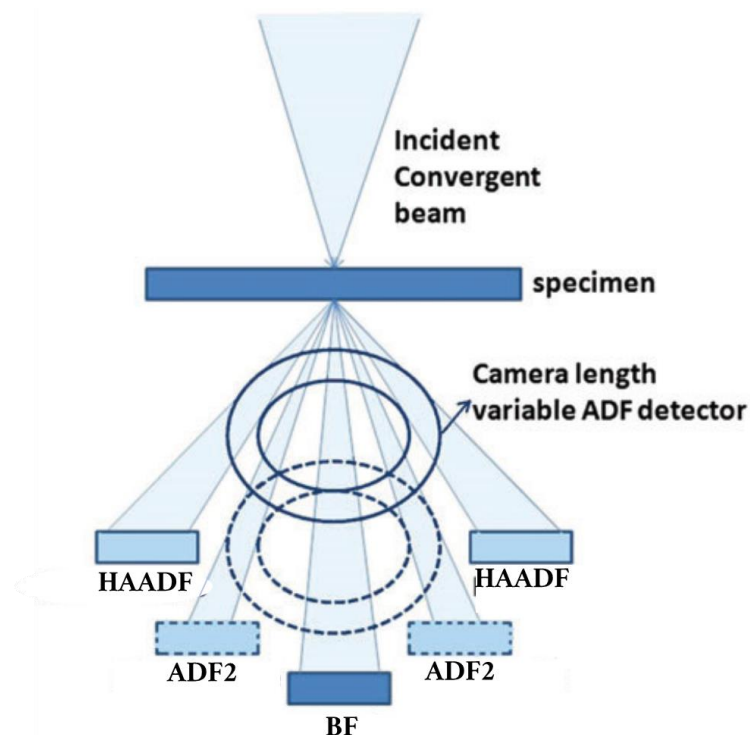


Figure 2.7: Schematic representation of STEM mode detectors.[167]

In this mode, a focused electron beam is scanned across the sample, and the transmitted and scattered electrons are collected by annular circular detectors (fig 2.7). Electrons are either

transmitted or scattered elastically and inelastically. Inelastically scattered electrons at wide angles are collected using a high-angle annular dark-field (HAADF) detector.

The STEM analyses were conducted using HAADF-STEM mode with a convergence angle of 18~22 mrad. Considering the camera length of 8cm we have used for this study, the detector's acceptance angles are 68 mrad and 280 mrad for inner and outer diameter, respectively. In fact, the heavier an atom, the greater the probability of electrons scattering at high angles. Therefore, it provides a Z-contrast which is a contrast linked to the chemical nature of the investigated sample. 1024x1024 px images were recorded with an exposure time of 20 μ s/px. Electrons scattered at lower angles are collected using another annular dark field detector (ADF2). A bright-field (BF) detector may also be used to collect electrons that pass through the sample without being scattered. [163]

This choice of using of the STEM mode was motivated by the complex morphology exhibited by the synthesized particles, as STEM enables efficient visualization and comprehensive clarification of morphological information. Additionally, the STEM mode has an edge over the conventional TEM mode in terms of contrast sensitivity. This enhanced contrast capability makes it possible to distinguish and characterize various aspects inside the particles with more accuracy, leading to a more in-depth understanding of their morphology. It is also an incoherent mode in which the interference effects between the different beams that contribute to the formation of images are eliminated (which is not the case in traditional TEM mode). This facilitates a more straightforward interpretation of the images.

– **Energy Dispersive X-ray Spectroscopy mode**

For quantitative local composition measurements, the employment of Energy Dispersive Spectroscopy (EDS) spectroscopy becomes imperative. This technique enables the analysis of X-ray photon energies emitted by the sample following its interaction with the incident electron beam. By examining the positions of peaks within the resulting spectrum, specific elements present in the sample can be accurately identified. [168]

During this work, the chemical analysis of the particles was carried out using the energy dispersive X-ray spectroscopy (STEM-EDS) using a JEOL® CENTURIO detector that collects X-rays from STEM samples at a collection angle of 1 sr from a detection area of 100 mm² [169]. The energy resolution attained using this detector is 129 eV. 256x256 pixels maps and spectrums were acquired with a dwell time of 0.02 ms. Specimen tracking was activated every

60 seconds during the acquisition. A chemical analysis of the sample was inside the Environmental cell mounted on a special holder (details will be provided later on in this chapter) was conducted. The special holder is optimized for maximum alpha-tilt to ensure a direct line-of-sight between the electron transparent window and the side-angle EDS detector. In order to enhance the EDS signal, the sample has been tilted to a positive angle of 8 degrees.

4. Electron tomography (ET)

Following the 2D examination of the hollow nanospheres, a comprehensive investigation in 3D of the sample was required to validate the complex three-dimensional (3D) structure. Although it takes longer acquisition time, the choice of HAADF-STEM tomography was privileged due to its ability to address the limitations of conventional TEM, where phase contrast reversals can deteriorate the projection quality needed for tomography [170].

– The principle of ET

Electron tomography was used to visualize the complete 3D structure of the hollow nanospheres through a series of two-dimensional projections taken from various viewing angles [171]. Since its development in the 1990s, electron tomography has significantly improved the study of 3D nanomaterials. Moreover, recent progress in computational reconstruction algorithms and 3D visualization tools allows scientists to interactively analyze volumetric representations and extract meaningful statistics from specimens. [170]

To construct a volume (tomogram) through Electron Tomography (ET), four primary steps are involved: the acquisition of a series of projections at various tilt angles (tilt series) followed by the images alignment, reconstruction, and visualization of the results. The tilt series acquisition can be accomplished through various geometries, such as single-axis, dual-axis, multiple-axis, or conical configurations. During the acquisition process, a major challenge arises from specimen shifts caused by instrumental limitations like thermal or mechanical instability. Alignment of the tilt series becomes necessary to correct these shifts before reconstruction. Two types of algorithms are employed for shift correction: automatic and semiautomatic. [172] Automatic alignment relies on cross-correlation [173], while semiautomatic alignment utilizes fiducial markers, such as gold nanoparticles [174]. 3D reconstruction algorithms used in tomography can be categorized into three main groups: Fourier reconstruction methods, modified back-projection methods, and iterative direct space methods. Fourier methods involve restoring the Fourier transform of the object from the Fourier transforms of the projections and

then performing inverse Fourier transformation to obtain the real-space distribution. Direct methods, such as convolution back-projection algorithms and iterative algorithms (Figure 2.8), perform calculations directly in real space.

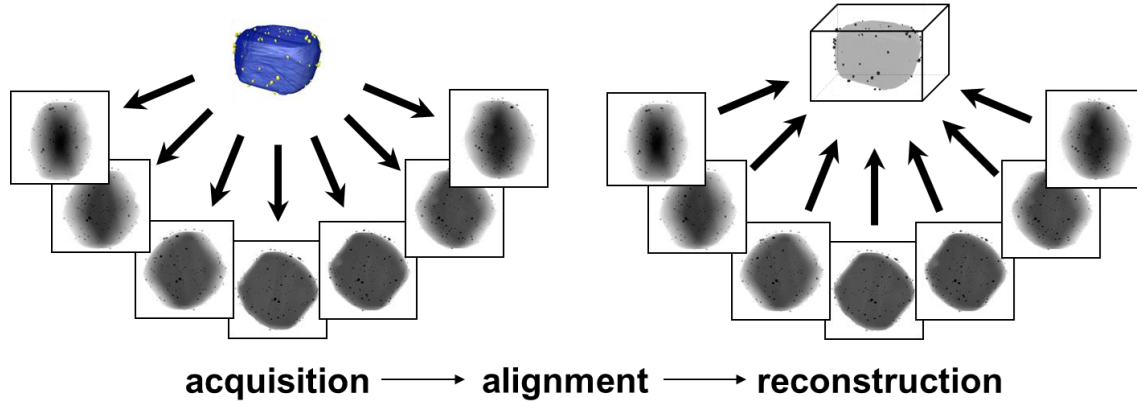


Figure 2.8: A schematic representation of the tomographic reconstruction process: 1) acquisition of projection images from various tilt angles, 2) alignment of the 2D projection images, and 3) real space projection for the volume reconstruction [175]

Weighted back-projection (WBP) methods share similarities with convolution back-projection algorithms but also operate on real-space data. [176] The complexity of the computed tomogram data makes visualization challenging and often requires volume segmentation. According to Crowther [177], there is an inherent tradeoff in electron tomography involving resolution, specimen size, and the number of projections. This relationship is expressed in Eq. 2.3 [178] as follows: the resolution in three dimensions (d_{3D}) is equal to π times the object size (D) divided by the number of projections (N) acquired with equal angular spacing around a single axis of rotation. The resolution attained during this study was approximately 1 nm^3 .

$$d_{3D} = \pi * \frac{D}{N} \quad [\text{Eq. 2.3}]$$

– The experimental conditions used in ET

The 3D morphology of the particles was investigated using electron tomography (ET) via a module in Gatan Digital Micrograph Software (GMS3). Prior to sample deposition, one drop of colloidal solution containing 5 nm Au nanoparticles solution was deposited on the TEM grid membrane followed by a plasma cleaning under an Ar-H₂ gas mixture. Focus was calibrated using the objective lens and stage calibrations. Stacks of 1024 x 2024 px images have been recorded with an exposure time of 10 $\mu\text{s}/\text{px}$ in STEM-HAADF mode along an angular range of -67° to $+68^\circ$ with a step of 3° . The acquisition of the tilt series was performed using the single-

axis geometry. Prior to tomographic volume reconstructions, the alignment of the stacked images has been conducted using the Au nanoparticles as fiducial markers. In this work, TomoJ, a plugin integrated into the image analysis and processing software, ImageJ, was utilized. TomoJ offers an interface that facilitates alignment, reconstruction, and integration of multiple tomographic volumes. It incorporates state-of-the-art algorithms: the algebraic reconstruction technique (ART) and its variant OS-SART (ordered subset simultaneous ART), the simultaneous iterative reconstruction technique (SIRT) and the weighted back-projection approach [172].

The OS-SART algorithm [179] was used for the volume reconstructions with 150 iterations. In OS-SART, the tomographic reconstruction problem is iteratively solved using a set of ordered subsets of projection data. Each subset of data is used to update the image estimate in a simultaneous manner. This helps to reduce the noise and artifacts in the final reconstruction. The algorithm converges to a solution that minimizes the difference between the measured and calculated projections [179]. To enhance image quality and reduce noise, a 3D median filter was uniformly applied across the entire reconstructed 3D volume at the voxel level. The Slicer3D has been employed for the volume visualization after data segmentation and modelling.

5. In-situ and operando TEM

5.1. Furnace type heating holder

For the first thermal annealing experiments, we employed a Gatan furnace-type heating holder.

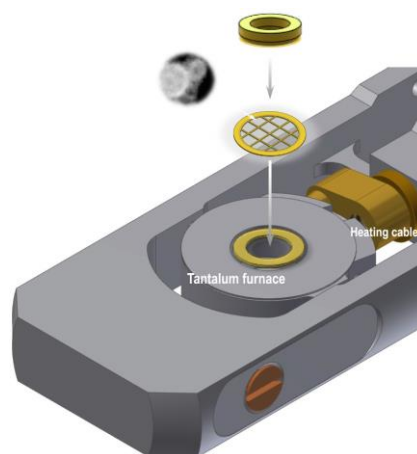


Figure 2.9: Gatan 652 heating holder equipped with a tantalum furnace. [180]

This specific holder features a tantalum furnace design (as shown in Figure 2.9) and enables the observation of changes in the structure of materials when exposed to elevated temperatures up to 1000°C.

To secure the sample, which was deposited onto a gold TEM grid, we utilized a threaded clamping mechanism, ensuring excellent thermal contact between the sample and the furnace. We manually controlled the heating rate, which varied between 0.3 to 0.5°C per second. Subsequent to reaching the desired temperature, the sample underwent annealing for a duration of 15 minutes to achieve thermal stability at each specified temperature point. Afterwards, an in-situ characterization of the sample is conducted at each desired temperature.

5.2.Environmental cell technology

To monitor catalysts in real-time during reactions and study the impact of temperature, gas, and pressure using in-situ microscopy, we employed a closed Environmental Cell system "Atmosphere", commercially available from Protochips ®. The Atmosphere system comprises two main components: a sample holder and a gas manifold (gas controller).

- 1- The sample holder houses the Environmental cell (E-cell) in which the catalysts under investigation can be heated and exposed to a well-controlled gas composition. This allows for real-time monitoring of the catalyst's morphology and chemical composition and crystallography under varying reaction conditions. The cell is designed to be perfectly sealed to prevent any external contaminants from interfering with the reaction. Additionally, the cell can be heated to high temperatures to simulate realistic reaction conditions.
- 2- The gas manifold, on the other hand, is responsible for controlling the gas environment within the cell. It allows for precise regulation of the gas nature, flow and pressure, which is important for accurately simulating reaction conditions. The gas manifold is connected to the environmental cell via a series of tubes and valves, which enable the gas to be introduced or removed from the cell as desired. The manifold is operated by a dedicated software, which allows for automated gas control and manipulation of the gas parameters.

Furthermore, a residual gas analyzer (RGA) is integrated into the setup through a pipe connected the cell gas outlet to perform a qualitative analysis of the reaction products. By incorporating a mass spectrometer, this device aids in confirming the occurrence of the reaction

within the environmental cell, determining the onset reaction temperature, and establishing a connection between the catalyst's behavior during the reaction and the reaction response in terms of products detection.

– The E-cell

To conduct in-situ investigations, a pair of Atmosphere E-chips are mounted on the in-situ TEM holder from Protochips™ (see Figure 2.10(a)). These E-chips play a vital role in creating a sealed gas cell. Comprising a durable and thin silicon carbide (SiC) derived ceramic film heating membrane, along with an amorphous silicon nitride (SiN_x) window (Figures 2.10(b), 2.10(c)), the E-chips act as an effective barrier, confining gases while minimizing electron beam deflection.

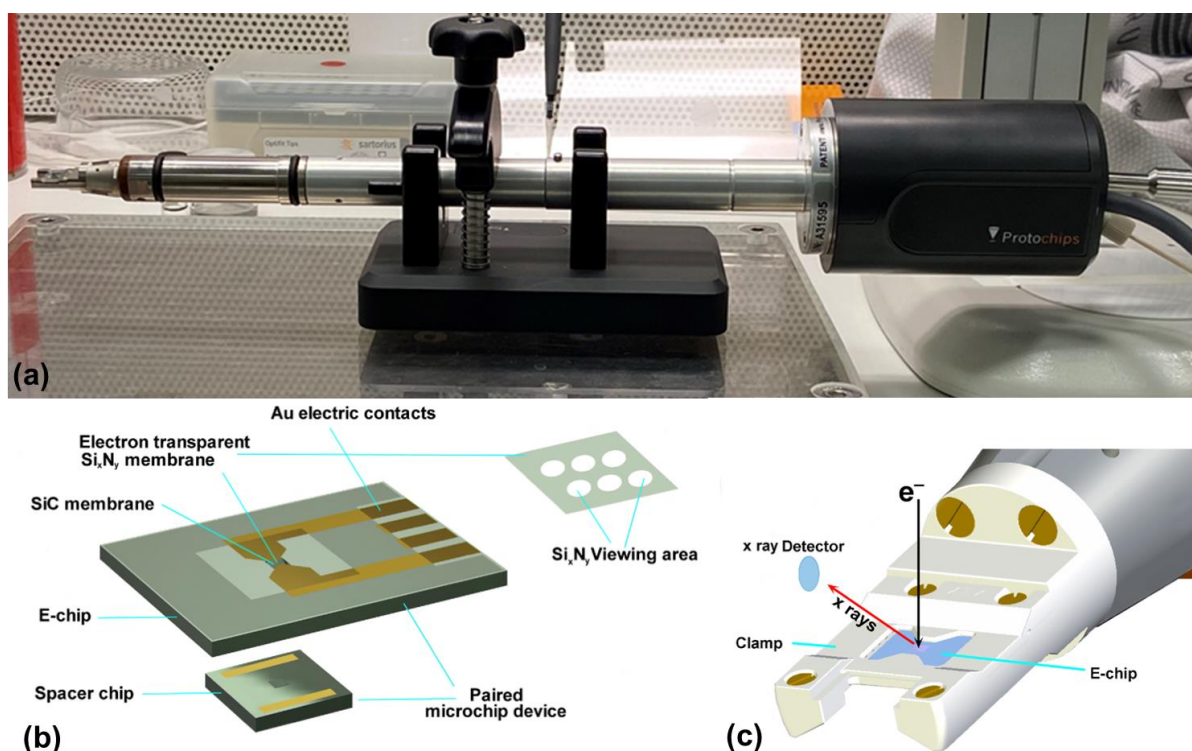


Figure 2.10: (a) The dedicated In-Situ TEM sample holder from Protochips®, (b) the two SiN_x chips forming the E-cell and (c) the environmental cell mounted on the In-Situ TEM holder. [181]

A comprehensive illustration of the assembly steps for the environmental cell employed in the experiment is presented in Figure 2.11(a). Initially, a gasket is carefully positioned at the apex of the titanium holder, enabling to stabilize the two chips and ensure complete enclosure of the cell. This gasket plays a crucial role in creating a vacuum seal around the holder and E-chips within the microscope. Afterward, the small E-chip is placed into the gasket pocket, followed

by the deposition of the large E-chip with the membrane side, where the sample is deposited, facing downwards. The electrical gold pads on the E-chips will naturally align with the contacts on the flexible circuit of the holder. This Finally, a cover is placed, effectively isolating the cell from the microscope and enabling visualization of a designated area measuring $300\ \mu\text{m} \times 300\ \mu\text{m}$.

On a side note, Protochips provides two types of E-chip pairs optimized for either STEM/EDS or TEM investigations to guarantee optimal imaging conditions during TEM investigations. The TEM configuration involves placing the sample on the small thermal E-chip at the bottom of the in-situ gas cell after tip assembly.

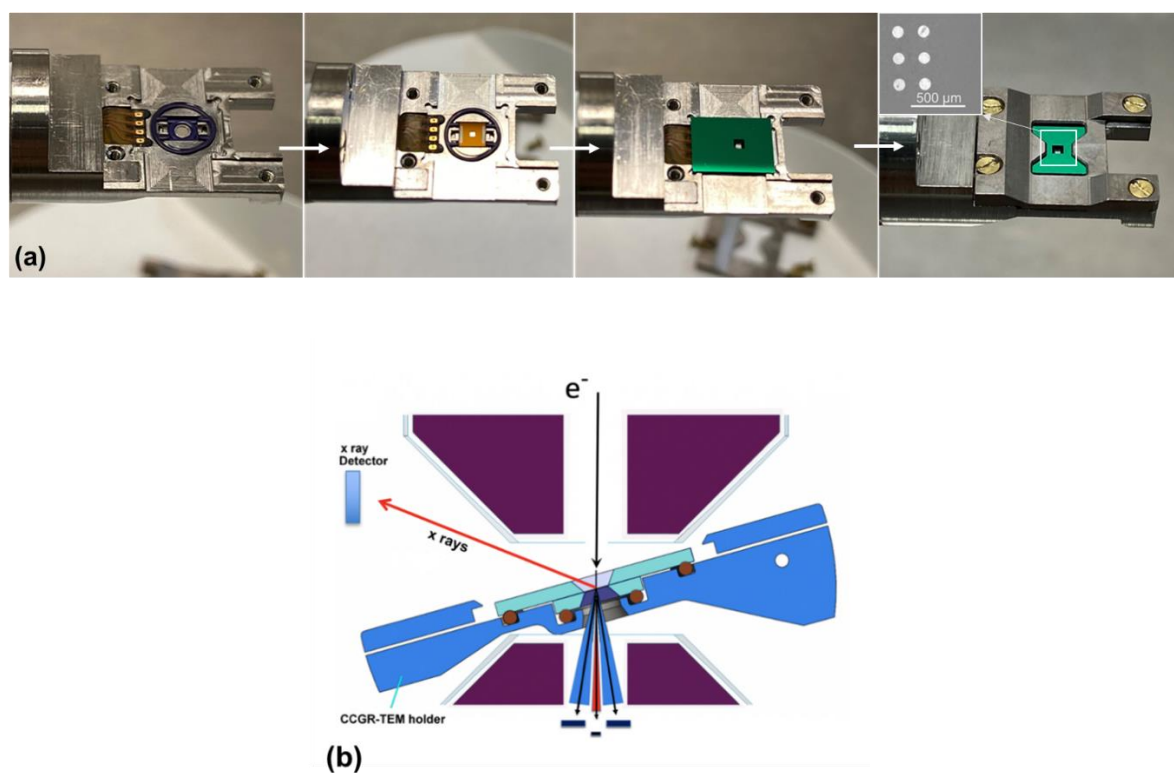


Figure 2.11: (a) the different steps of the E-cell mounting process, (b) the butterfly wing shape in-situ TEM holder optimized for EDS performance. [181]

This configuration optimizes the resolution and signal-to-noise ratios in TEM mode by positioning the sample closest to the point of beam exit. On the other hand, The STEM/EDS configuration employed in this thesis, involves the placement of the sample on the large thermal E-chip that defines the top of the in-situ gas cell after tip assembly. This configuration enables the sample to be closest to the point of beam entry, resulting in the best resolution, particularly when using a probe size corrected microscope. Additionally, mounting the sample on the upper

E-chip enhances the line of sight to the EDS detector, leading to an increase in the signal-to-noise ratio. The E-cell is enclosed by a lid that is flushed with the tip of the object holder, which has a butterfly wing shape, designed to achieve maximum alpha-tilt and STEM compatibility for all JEOL pole pieces (Figure 2.11(b)). This particular holder has been optimized to enhance EDS performance.

– **Experimental protocol of the sample preparation**

To elucidate the experimental protocol, several steps are crucial before the start of each in-situ experiment:

- 1- *The E-chips cleaning:* Atmosphere E-chips were subjected to plasma cleaning using Gatan Advanced Plasma system, Solarus 950, with a mixture of Argon and Hydrogen atmosphere to enhance the hydrophilicity of the E-chip surface. This process involved exposing the E-chips to a plasma of Argon and Hydrogen gases, which alters the surface chemistry and promotes the uniformity of sample distribution during drop casting from a suspension. Plasma cleaning also helps to reduce surface contaminations during imaging for electron microscopy analysis, particularly after prolonged storage of the E-chips.
- 2- *Sample deposition the membrane:* At the beginning, it is essential to consider the delicate nature of the membrane during any manipulations. Moreover, for TEM analysis, it is important to have a sufficient concentration of particles within the SiN_x windows. Due to the nature of the Co-templated hollow nanospheres synthesis process, the quantity of catalysts deposited in the environmental cell could not be precisely controlled as particles were dispersed in ethanol immediately after synthesis. Despite this limitation, efforts were made to standardize the process by working with the same solution and particle concentration. After activating the SiN_x membranes through plasma cleaning, several drops of 0.5 μL of the catalyst's suspension were applied onto the environmental cell membrane.
- 3- *The E-cell mounting:* This particular step, which has been previously described in detail, is the most critical and fragile stage in specimen preparation, as at this stage, the SiN_x membranes tend to break. The electrical contact is verified afterwards automatically by the Atmosphere software after connecting the holder to it.
- 4- *Performing the leak check:* the risk of gas leakage within the microscope column is present in several cases such as broken membranes, inadequately cleaned gaskets, or misaligned

E-chips. Consequently, a leak test is conducted before inserting the holder into the microscope, using the external holder dry pumping station.

Next, and after a bake out of the gas manifold for 12 hours, the gas cell and the entire "Atmosphere" system (including gas tubes at the entrance and exit of the cell, and experimental tanks) are purged at 100 Torr of inert Argon gas. This purging process effectively eliminates potential pollution, such as the presence of air and other impurities during assembly.

Prior to each experiment, an analog scan was made using the RGA to check the system's cleanliness. Subsequently, before starting each experiment, the samples were observed and identified under an Argon flow at 120°C to eliminate water and all other contaminations from synthesis of sample preparation covering the particles. Multiple regions were monitored to ensure representative results.

– **Challenges of sample preparation and cell monitoring**

The preparation and assembly of the environmental gas cell on the SiN_x membrane in in-situ TEM experiments require great care to avoid damaging the membrane.

The challenges arise from the small surface area of the SiN_x membrane, measuring only 90 μm x 90 μm, where the sample deposition occurs, and the relatively small observation holes with a visible heating area of 382 μm² (6 holes, 9 μm in diameter) [182]. These factors make it highly difficult to manually control the deposition process in these confined areas.

Various situations can result in membrane rupture. On the one hand, if the sample thickness exceeds the capacity of the SiN_x membrane, it may fail directly under the weight of the sample or during the assembly of the gas cell. On the other hand, if the amount of sample deposited in the cell is too small, there won't be enough regions for a representative study of the material's behavior. Also, the resulting reaction products may be too small in quantity to be detected by the residual gas analyzer (RGA). Improper placement of the cell chips on the gasket during assembly can create an imbalance, leading to the breakage of the SiN_x membrane. Furthermore, when conducting a test to assess if the cell is well sealed, an air leak caused by faulty chip assembly can also result in the rupture of the SiN_x membranes.

Another challenge lies in ensuring the appropriate electrical resistance of the electrical contacts after deposition and cell assembly. The resistance should fall within the specified range, as

determined during the manufacture of the chips, to enable precise control of the sample's heating temperature.

– **Functioning principle of the E-cell**

Figure 2.12(a) illustrates the operational mechanism of the cell, along with the integration of the residual gas analyzer (RGA). To facilitate the management of purge and reaction gases, a manifold is employed, which incorporates three gas reservoirs.

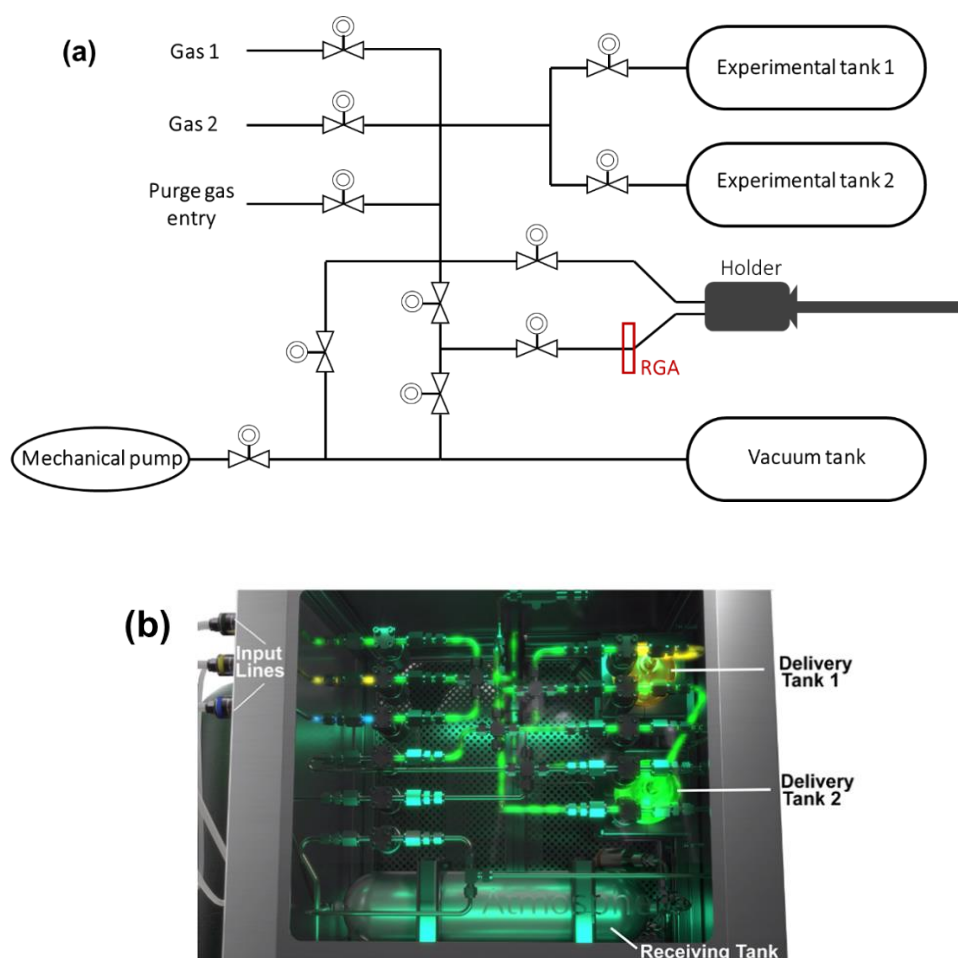


Figure 2.12: (a) A diagram illustrating the operation of the environmental cell with the RGA supplementary device incorporated into the system, (b) illustration of the gas manifold

Gas purging is accomplished through a mechanical pump that operates on both the reservoirs and the sample cell holder. Within the manifold, two experimental tanks are integrated to store and deliver gases of interest to the sample inside the cell. The third gas reservoir, connected to the cell outlet and pump, enables precise regulation of pressure in the experimental reservoirs through a pressure differential mechanism (Figure 2.12(b)).

The "Atmosphere" software application, specifically designed for this system, enables users to input pressure and temperature setpoints. It facilitates the delivery and evacuation of gases from the experimental tanks to the sample cell. The gas supply to the cell is achieved using a capillary tube made of 316 stainless steel, while a 50-micrometer diameter polymer tube composed of PolyEtherEtherKetone (PEEK) ensures laminar gas flow at the cell exit.

The environmental cell utilized in this study allows for experimentation in various inert (e.g., Ar, N₂, He) or reactive (e.g., H₂, CO₂, CO, O₂, etc.) atmospheres, both in static and dynamic modes. It offers a wide range of flexibility in adjusting the working pressure, ranging from 1 Torr to 760 Torr, which allows to conduct experiments under various conditions.

The system incorporates calibrated chips that provide precise control of heating, ensuring high temperature accuracy by MEMS (Micro-electromechanical systems) technology. The MEMS device is designed with a heating membrane that serves two essential functions: it supports the sample and serves as the heating surface. This design eliminates any temperature uncertainty by guaranteeing direct contact between the sample and the heat source. To reach the desired temperature, an external current supply is used to pass electricity through the membrane, generating Joule heating. The temperature measurements obtained from the system are highly reliable, with potential deviations from the actual temperature not exceeding 5% of the measured value. The system allows for rapid heating and cooling, covering a broad temperature range from approximately 25°C (room temperature) up to 1000°C. It is capable of achieving temperature change rates as fast as 10°C per second, making it suitable for rapid thermal cycling experiments. Additionally, the system can operate at much slower temperature change rates, with the slowest rate being as low as 0.1°C per hour. [182] This feature caters to applications that require very slow and precise temperature changes over an extended duration.

– Artifacts of the E-cell technology

The interaction between electrons and matter, which produces analytical signals like electron energy loss, characteristic X-ray emission, and secondary/Auger electrons, can also potentially damage the analyzed material due to radiation, heating, and charging [110]. During in situ analysis inside the E-cell, the interaction of the electron beam with the SiN_x windows forming the cell can impact image formation and, in certain instances, alter reaction kinetics. Moreover, the high-energy electron beam interacts with both the gas and the sample inside the environmental cell, influencing elastic and inelastic scattering processes.

First, similar to interactions with other materials, the most common type of interaction between the incident electrons and the SiN_x membrane is elastic scattering [110]. The image's contrast is altered by the numerous elastic scattering of electrons in the SiN_x membrane, which increases the background. Maintaining a good signal to noise ratio of the recorded images necessitates a strong electron dose. While the inelastic scattering may not significantly affect the resolving power of the electron microscope, it can have an influence on reaction kinetics through two distinct mechanisms: phonon scattered electrons (resulting in local heating) and secondary electron (SE) emission (leading to SE-induced reduction). It is reasonable to anticipate that the electron beam will indeed affect the temperature of the irradiated region. But, considering the temperature control we possess thanks to the used system, this problem will be neglected.

Another type of interactions is between the Electron beam and the gas molecules inside the cell. The separation between the top and the bottom SiN_x membranes determines the electrons path length inside the E-cell. Similar to the interactions with SiN_x membranes, elastic scattering is the most probable outcome on the one hand. A longer path for electrons through the gas and increased gas pressure diminishes the microscope's resolving power. On the other hand, inelastic scattering events lead to gas ionization. This ionization process transforms the molecular gas into a plasma-like environment, generating highly reactive ions capable of significantly perturbing the usual course of chemical reactions [183].

The positioning of the sample inside the environmental cell is a crucial aspect to consider. The preferred configuration is the STEM setup, where the sample is placed on the upper window of the cell. This configuration is advantageous for two reasons: it is well-suited for STEM mode imaging and facilitates EDS analysis.

In the STEM mode, maintaining minimal broadening of the scanning probe is essential. To achieve this, the sample is positioned above the gas layer, ensuring that interactions between the electron beam and the gas phase do not significantly impact the resolution of the STEM image. This way, the image formation, which occurs point by point, remains unaffected by these interactions.

In terms of EDS analysis, having the sample situated above the gas layer offers a significant advantage. This positioning enhances the collection of characteristic X-rays by the EDS detectors, enabling more accurate and comprehensive analysis of the sample's elemental composition.

5.3. Gas manifold

The gas management system controls the flow and pressure of gases within the holder, as well as preparing gas mixtures before experiments. Pneumatic valves are used to regulate the entry, exhaust, and filling of gases in the experiment tanks. A vacuum tank helps create a pressure difference to control and set the pressure in the tanks and holder. To prevent over-pressurization, the system includes a pressure relief valve set at 1.5 bar to avoid potential gas-related errors. During operation, a pump called the roughing (scroll) pump is used to remove gases from the manifold and holder. All the different parts of the system are controlled using the Atmosphere Clarity software. This software is connected to a device called the electronics control unit (ECU), which has several important tasks. The ECU controls the valves, reads pressure sensors, monitors the emergency stop (E-stop) function, regulates the temperature of the heating E-chip, and communicates with the Clarity software. This software gives real-time updates on the status of the system, such as the pressure, temperature, flow rate, and positions and statuses of the valves in the system. Argon gas was employed as an inert gas, whereas CO₂ and H₂ served as reactive gases for the CO₂ hydrogenation reaction. These gases are used in a dynamic flow at atmospheric pressure, with a flow rate of 0.05 sccm (standard cubic centimeters per minute: cm³/min). A temperature range between the room temperature and 800°C was applied.

5.4. Residual Gas Analyzer

The experimental setup includes a device called a Residual Gas Analyzer (RGA). This RGA is placed at the exit of the environmental cell to detect the products of the reactions. The environmental cell system coupled with the RGA are shown in the Figure 2.13.

This setup allows us to investigate the sample's behavior under various controlled atmospheres and directly correlate it with the detected reaction products, which aligns with the principles of operando TEM. The residual gas analyzer (RGA) is a high-performance device based on mass spectrometry. It enables the analysis of gas-phase products, even in extremely small volumes down to a few ppm. It consists of two main components: (a) a mass spectrometer and (b) a differential pumping system. To ensure minimal ion collisions, the RGA mass spectrometer operates at low pressures around 10⁻⁶ mbar. Consequently, a differential pumping system, comprising a mechanical pump and a turbomolecular pump, is employed to decrease the gas pressure as it exits the environmental cell. The mass spectrometry is a destructive analysis

technique utilized to determine the masses of molecules or molecular fragments formed during ionization in a sample. It involves the separation of molecular ions based on their mass-to-charge ratio (m/z).

A mass spectrometer typically consists of three main parts: (i) an ionization source where molecules are ionized, (ii) an analyzer that separates the molecular ions according to their m/z ratio and (iii) a detector that collects ionic currents and converts them into an electrical signal transmitted to a recording system.



Figure 2.13: The Environmental Cell system coupled with the Residual Gas Analyzer from Protochips ®.

Upon leaving the ionization source, the formed ions are accelerated and directed towards the spectrometer's analyzer. The analyzer is responsible for separating the ions based on their m/z ratio. Various types of analyzers exist, including time-of-flight, magnetic, and quadrupole analyzers. The choice of analyzer depends on the range of masses to be scanned and other important parameters such as sensitivity, resolution, and measurement accuracy. Sensitivity represents the ratio between the detected ion current and the partial pressure of the ionization

source. Resolution determines the spectrometer's ability to distinguish neighboring masses and is typically calculated as the ratio $m/\Delta m$, where Δm is the difference between the mass m and the nearest mass. The mass spectrometer we utilized in our study, RGA 200, is composed of a quadrupole probe commercialized by Protochips® and an Electronics Control Unit. The complete probe setup comprises three components: the ionizer (electron impact), the quadrupole mass filter, and the ion detector (Figure 2.14). These components are all located in the vacuum space where the gas analysis measurements are conducted.

The RGA sensitivity is 2×10^{-4} A/Torr. A resolution around 0.5 amu and a minimum detectable partial pressure (PP) of 5×10^{-11} Torr are attained during the experiments using this device [184].

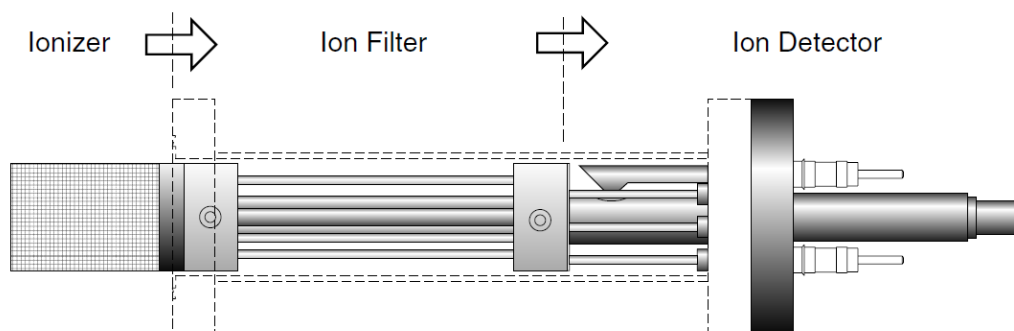


Figure 2.14: Schematic representation of the quadrupole probe used in the RGA200 [184]

In this study, we utilized a mass spectrometer with a mass range of 1 amu to 200 amu to examine the hydrogenation reaction of CO_2 under atmospheric pressure in an environmental cell. Our analysis focused on monitoring the formation of formic acid (HCO_2H) and methanol (CH_3OH), which have molecular weights up to 46 amu.

The resolution of the mass spectrometer was deemed sufficient to differentiate adjacent molecular masses. Detected ionized fragments were directed towards a Faraday detector, as the use of a Secondary Electron Multiplier was precluded due to technical limitations when operating at atmospheric pressure. If operating at lower pressure values, a “Secondary Electron Multiplier” could have been used to amplify the signal from the detector.

– Mass spectrum display modes

Two display modes were employed in our studies to track and identify the masses present in the sample, as shown in the Figure 2.15.

Analog mode is a spectrum with the X-axis representing the mass range selected in the Mass (Da) and the Y-axis representing the cumulated current in the mass interval (Figure 2.15(a)).

The Pressure versus Time (P vs T) mode was used to plot the partial pressure (PP) of the detected elements as a function of time (Figure 2.15(b)).

Like all mass spectrometers, the ionization of each gas differs as it enters the ionizer of the instrument, and in most cases, complete ionization does not occur. Because of these variations in ionization, the RGA cannot be regarded as a tool for quantitative measurements. While the RGA is highly effective at measuring relative changes in gas signals during an experiment, it cannot be reliably used to determine the absolute concentration of a gas species, which is considered as a limitation. The fluctuations observed in Figure 2.15(b) are attributed to another limitation of the RGA, which serves as a safety measure. When the system reaches a certain pressure level, it is pumped down to safeguard the device from damage.

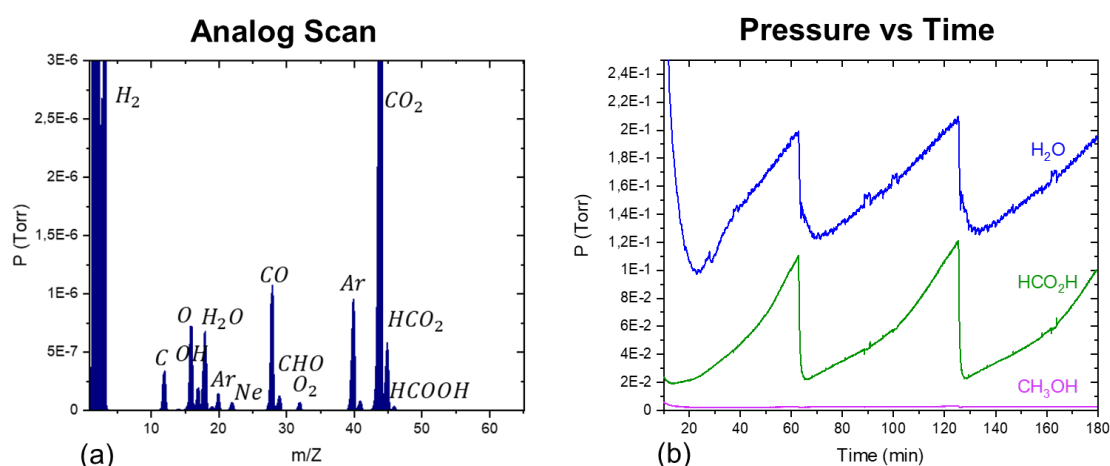


Figure 2.15: Spectrum acquisition in (a) analog scan mode and (b) « Pressure vs Time » mode.

– RGA spectra analysis

The analysis of an RGA spectrum involves several steps to make sense of the data. Firstly, the raw spectrum data is obtained from the RGA instrument, which is typically presented as a plot of ion partial pressure versus masse to charge (m/z) values. The next step is to identify the peaks in the spectrum, which represent different gas species. This is achieved by comparing the m/z values of the peaks with known masses of common gases.

Elements	Formula	Fragmentations
Carbon dioxide	CO ₂	CO ⁺ , C ⁺ , O ⁺
Dihydrogen	H ₂	H ⁺
Formic acid	HCO ₂ H	CHO ⁺ , HCHO ⁺ , HCO ₂ ⁺
Water	H ₂ O	OH ⁺ , O ⁺
Methanol	CH ₃ OH	CH ⁺ , CH ₂ ⁺ , CH ₃ ⁺ , CHO ⁺ , CH ₂ O ⁺

Table 2.1: Molecules of reaction reactants and expected products along with their fragmentations

Considering that electron ionization mechanisms induce both singular and multiple fragmentation events, this identification process consists of two main steps. The first step involves identifying the main molecular ion, which represents the intact molecule. For example, during the hydrogenation of CO₂, water (H₂O) is formed and detected with a predominant ion at $m/z=18$. However, this ion can further fragment into OH ($m/z=17$) and O ($m/z=16$). Additionally, isotopes of the atoms present, such as ¹⁸O, can be detected despite their low abundance. The second step involves examining the main and secondary fragments produced by the fragmentation of the molecules. For instance, CO₂ is predominantly detected with a mass of $m/z=44$. However, it can fragment into CO ($m/z=28$), O ($m/z=16$), C ($m/z=12$), and CO₂⁺⁺ ($m/z=22$). Similarly, formic acid (HCOOH) produces a main ion at $m/z=29$ for CHO, with fragments detected at m/z values of 30, 45, and 46 for HCHO (formaldehyde), HCO₂ (formate, the conjugate base of formic acid), and HCO₂H, respectively.

The generation of several ion fragmentations by electron ionization can lead to the identification of multiple m/z values corresponding to the same compound. For example, the identification of methanol (CH₃OH) and its fragments can be challenging due to overlapping m/z fragments values with other substances like methane (CH₄). However, the formation of methanol is confirmed by a predominant ion at $m/z=31$. In summary, analyzing RGA spectra involves identifying peaks corresponding to different gas species by comparing their m/z values with known masses. It also requires considering the fragmentation processes that can generate additional ions (Table 2.1).[182]

Throughout the gas treatments in this thesis, the residual gas analyzer was used first to identify the reagents and reaction products then to monitor their increase over time and temperature. To begin, we calibrated the mass spectrometer using argon as a reference gas. Next, after selecting

the “P vs t” mode, in order to monitor them, we specifically selected the ionic masses of the gases employed (such as Ar, H₂, CO₂) as well as the expected reaction products.

5.5. Methodology of the TEM experiments

A methodology has been developed to study the behavior of Co-templated Pt hollow nanospheres under different atmospheres. The impact of different environments on the materials morphological evolution is investigated using in-situ and Operando TEM.

The first step of this work is to conduct a deep investigation of the initial state of the catalyst by 2D and 3D TEM analysis. The second step is to apply a consistent thermal treatment under the TEM vacuum to each batch of the Co-promoted hollow nanospheres. This thermal treatment involves a heating rate of 0.4°C/s with a step of 20-50°C. STEM-HAADF micrographs are acquired at each stage using the same parameters as the initial analysis, except for a shorter exposure time of 12 µs/px instead of 20 µs/px to expedite the imaging process at each temperature. Furthermore, using the environmental cell system, the particles behavior is monitored under 1 bar of hydrogen (H₂) atmosphere first then under 1 bar H₂-CO₂ gas mixture during the same thermal treatment conditions performed under the microscope vacuum. Before these investigations, a thorough cleaning process of the atmosphere system is undertaken including the E-cell where the sample is deposited.

Initially, the system is evacuated and then purged with argon gas. The Argon (Ar) is flown inside the E-cell at a flow rate of 0.1 cm³/min. The sample is then heated to 120°C for approximately 30 minutes. This procedure is successfully used to eliminate all contaminants (carbon contaminations, water, contaminations from sample preparation), ensuring the acquisition of the initial state images of the Pt-based HNS under inert atmosphere. After this cleaning step, 1 bar of H₂ gas or H₂-CO₂ is flown into the E-cell with a flow rate of 0.05 cm³/min. This flow rate is consistently used for all the following experiments. Using a relatively low flow rate optimizes the catalytic processes by promoting a better contact between reactants and the catalyst surface. The sample is heated with a precise heating rate of 0.4°C per second, utilizing temperature steps of 20-50°C. A representative temperature-time profile of the in-situ gas experiments is presented in Figure 2.16.

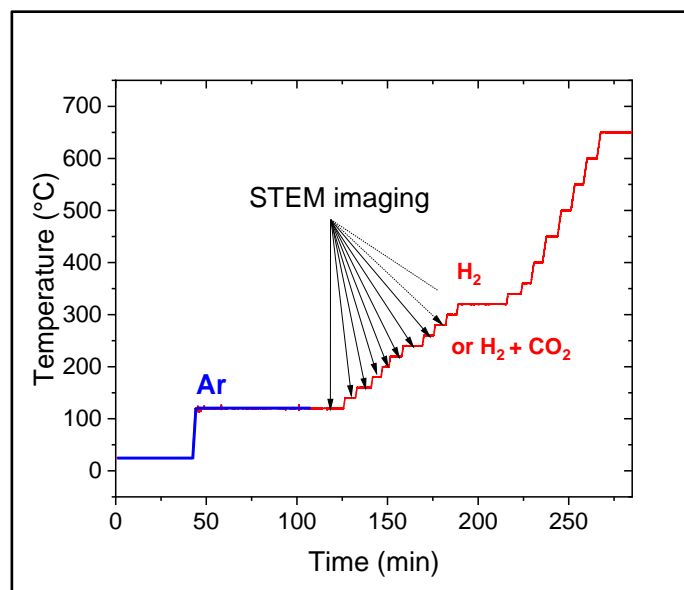


Figure 2.16: Representative Temperature-time profile of the in-situ heating experiment of Pt-based HNS under H₂ gas or H₂-CO₂ gas mixture using the MEMS-type holder.

CHAPTER III: Unveiling 3D Structure and Morphology of Pt-Based Hollow Nanospheres

1.	Physical characteristics of the Pt-1 hollow nanospheres.....	76
1.1.	Morphology and crystalline structure	76
1.2.	Morphology and size distribution by STEM-HAADF	80
1.3.	Chemical composition by STEM-EDS.....	83
1.4.	3D morphology analysis by Electron Tomography	85
2.	Particularities of the Pt-2 hollow nanospheres.....	89
2.1.	Morphology and crystalline structure by SEM and XRD	89
2.2.	Morphology and size distribution by STEM-HAADF	91
2.3.	Chemical composition and crystalline structure by STEM-EDS and SAED	93
2.4.	3D morphology analysis by Electron Tomography	95
3.	Discussions.....	97
4.	Conclusions	100

Two batches of Pt-based hollow nanospheres (HNS) are prepared using the galvanic replacement method and the same concentrations of materials. Details are provided in the synthesis section in chapter 2. The primary difference between the first (Pt-1) and second (Pt-2) batches lies in their synthesis methodology. The first synthesis involves adding cobalt (Co) nanoparticles, used as templates, drop by drop to the Pt salt solution. In the second synthesis, the Pt salt is the one introduced gradually over an extended timeframe into the solution of Co NPs. During this chapter, a thorough characterization of the resulting particles from both syntheses is presented, emphasizing any similarities or distinctions between them.

1. Physical characteristics of the Pt-1 hollow nanospheres

1.1. Morphology and crystalline structure

– Large scale analysis of morphology and crystalline structure

The as-synthesized particles are initially examined using the SEM for an initial morphological investigation. Representative SEM images are displayed in Figure 3.1 at both low and higher magnifications.

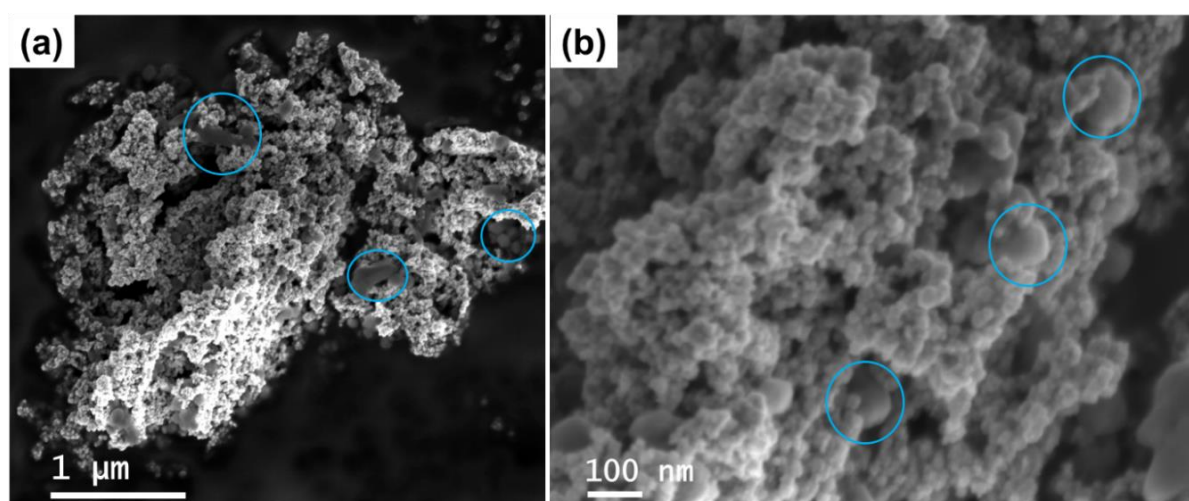


Figure 3.1: SEM images of the Pt-1 particles agglomerations at (a) low and (b) higher magnifications. Few larger nanoparticles are indicated by blue circles.

Figure 3.1(a) shows a field of densely packed agglomerations of nanoparticles. Few larger particles are also observed (indicated by blue circles). Figure 3.1(b) displays in a clearer way both particles type. The agglomerated nanoparticles exhibit an approximate diameter lower than 50 nm while the larger ones, indicated by the blue circles present a diameter around 100 nm. Precise statistics are exposed later on in this chapter.

EDS (Energy dispersive X-ray spectroscopy) analyses are conducted using the SEM to determine the chemical composition of the sample. The EDS spectrum, depicted in Figure 3.2, reveals the simultaneous presence of platinum (Pt) signal and a relatively low cobalt (Co) signal. Additionally, the presence of carbon (C) is from the carbon tape on which the sample is dispersed for SEM analysis. The presence of oxygen signal is attributed to the sample exposure to air prior EDS analysis and thus to partial oxidation of Co within the particles.

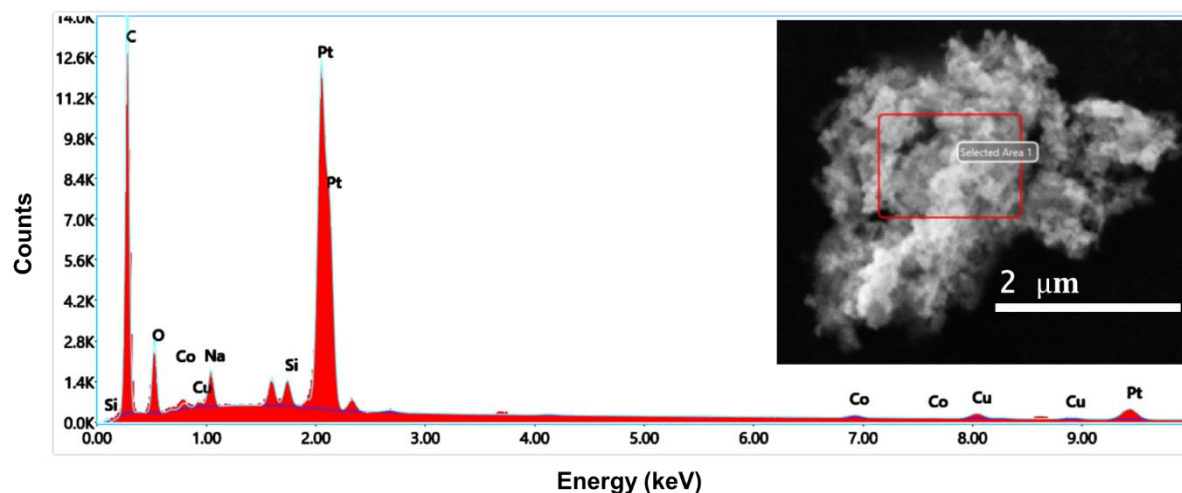


Figure 3.2: EDS spectrum showing the chemical composition of the selected region of Pt-1 particles within the SEM image.

The identification of sodium (Na) in the EDS spectrum originates from the use of sodium borohydride (NaBH_4) as a reducing agent during the synthesis of Pt-1 particles. The large particles indicated by the blue circles in Figure 3.1 are most probably NaBH_4 nanocrystals from the incomplete dissolution of NaBH_4 during the synthesis process. A weak signal of copper is also detected. It can be attributed to contaminations during the sample preparation process.

The X-Ray Diffraction (XRD) technique provides an inclusive study about the crystallography of the entire sample. The volume of the probed sample being rather small, the signal rising from the support is unavoidable. A scan of the Silicon (Si) support alone shows that it only gives rise to a small peak as observed in Figure 3.3(a). Beside the peak originating from the Si support used for the analysis, XRD measurements of the Pt-1 particles (Figure 3.3(b)) generate distinctive broad peaks corresponding to the crystalline planes of (111), (200), (220) and (311) within the PtCo disordered FCC structure [185]. Additional peaks in the angular range between 20 and 45 degrees correspond to the undissolved NaBH_4 residue in the sample from the synthesis process.

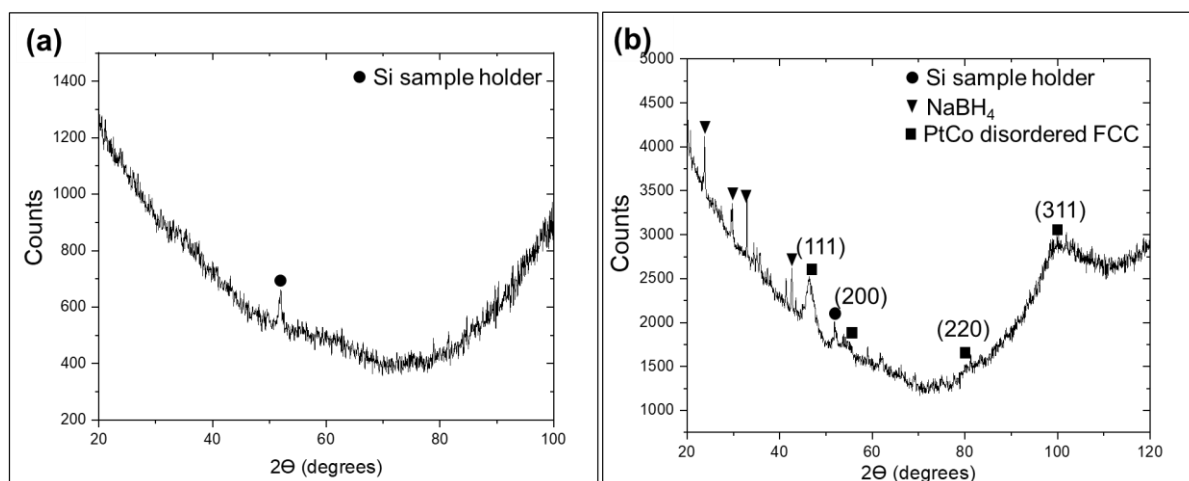


Figure 3.3: XRD patterns (a) of the Si support alone and (b) of the as-prepared Pt-1 particles.

– Nanoscale analysis of morphology and crystalline structure

The conventional TEM mode is first used for the examination of the morphology of the as-synthesized particles. Figure 3.4(a) exhibits a wide-view TEM image showing agglomerations of spherical particles. The TEM mode reveals the formation of thick concentric rings, with each surrounding a much thinner central region. This suggests that hollow nanospheres are obtained, as it is the intended goal of the adapted synthesis process. Variations related to the nanospheres outer diameter and shell morphology are observed. In Figure 3.4, two categories of nanospheres are identified. The first category, indicated by red arrows, exhibits a discontinuous shell and forms 90% of the synthesized particles. The second category (indicated by yellow arrows) displays nanospheres with a continuous shell constituting the remaining 10%. These findings are the result of a statistical analysis of more than 200 particles.

Throughout the entirety of this study, these nanoparticles are exclusively referred as NPs. It is worth mentioning that apart from the nanospheres, independent nanoparticles of approximately 2 nm in size are observed and indicated by red circles in Figure 3.4(b). They appear as agglomerations in adjacent to few nanospheres only occasionally in the TEM sample.

Figure 3.4(b) shows a TEM image showcasing clearly the distinct particles types. These latter, indicated by the red squares, will be referred as nanospheres throughout this work. Within this image, nanoparticles (indicated by white squares) forming the discontinuous shell of the first category of nanospheres are observed.

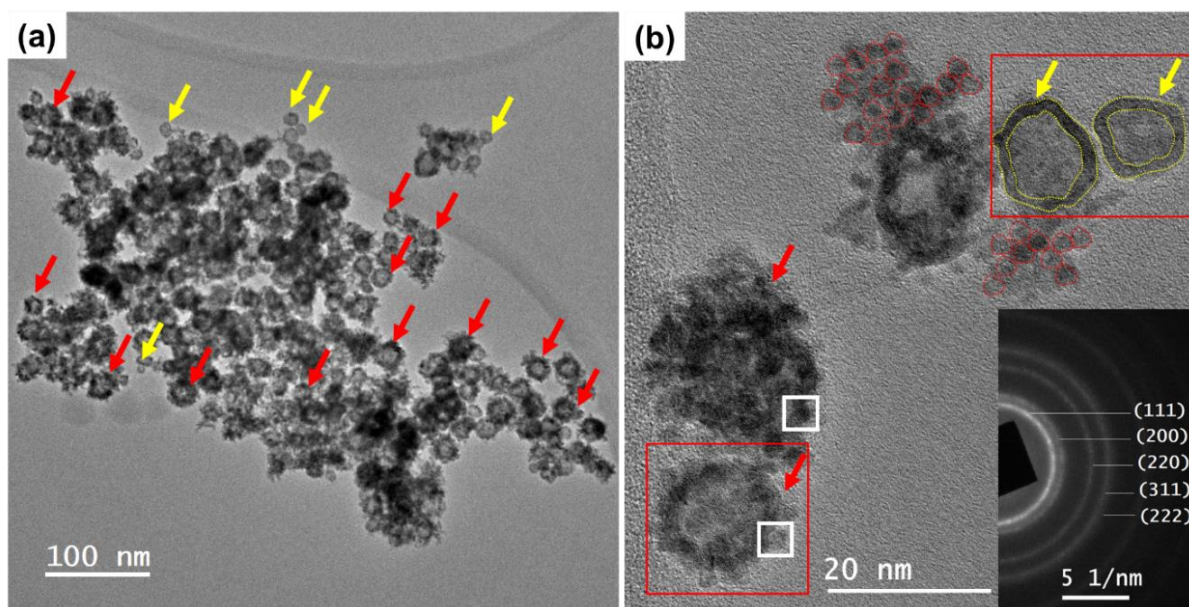


Figure 3.4: TEM images displaying (a) Pt-1 nanospheres, where some exhibit a continuous shell (indicated by yellow arrows), while others present a discontinuous shell (indicated by red arrows); (b) two categories of nanospheres with both discontinuous and a continuous shell (marked by yellow lines), separate nanoparticles adjacent to nanospheres (highlighted by red circles). Inset displays a DP of the Pt-1 nanospheres showing the corresponding lattice planes of the FCC PtCo phase.

Using the Selected Area Electron Diffraction (SAED), the analyses are conducted across distinct regions of the sample to verify the crystalline structure of the Pt-1 nanospheres. The resultant diffraction pattern (DP) (the inset in Figure 3.4(b)) presents five concentric rings corresponding to the (111), (200), (220), (311) and (222) crystallographic planes of the disordered FCC phase in the PtCo alloy [186]. Additionally, no superstructure ring corresponding to the (001) plane of the ordered L_{12} CoPt_3 phase is observed. This suggests the absence of this phase within the examined sample [187]. These results are consistent with the XRD analysis results presented in the previous section.

Compared to the absorption contrast of the TEM mode, the Z-contrast offered by the STEM-HAADF mode provides a better visibility of the complex morphology of the nanospheres shells. Although the TEM mode shows the presence of a shell formed by NPs, the NPs themselves are not clearly visualized, and their arrangement in the shell is not apparent. This lack of clarity limits the ability to conduct an accurate study of the size distribution of these NPs and of the nanospheres. The findings from the STEM-HAADF analysis of the sample is presented in the next section.

1.2. Morphology and size distribution by STEM-HAADF

Representative STEM-HAADF micrographs displayed in Figure 3.5 show agglomerates of the as-synthesized Pt-1 nanospheres. The two different categories of nanospheres identified by TEM are clearly observed: nanospheres with a discontinuous shell (indicated by red arrows) and others with a smooth and thin shell (indicated by yellow arrows). These nanospheres not only exhibit varying shell morphologies but also, variations in their average outer diameter.

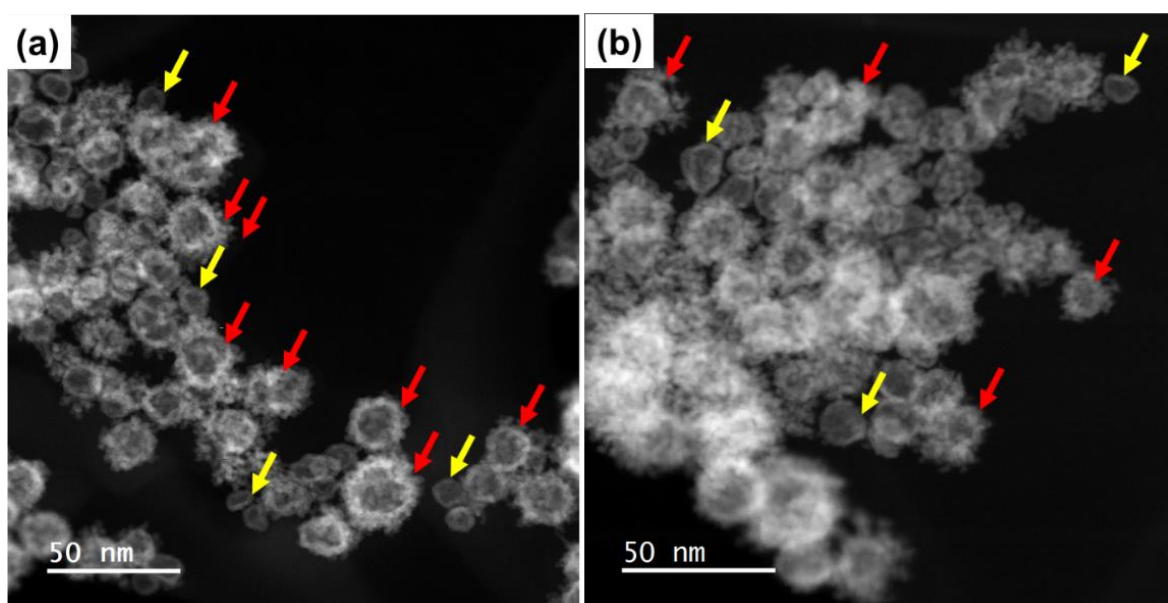


Figure 3.5: (a)(b) Representative STEM-HAADF micrographs of dispersed Pt-1 hollow nanospheres showing two different types of shell (continuous shell (yellow arrows) and discontinuous shell (red arrows)). (c) Diameter distribution of nanospheres with a discontinuous shell.

The high-resolution STEM-HAADF images presented in Figure 3.6 provide complementary details of the observations previously made regarding both types of Pt-1 nanospheres. The chemical contrast image in Figure 3.6(a) highlights a single spherical particle with the corresponding FFT image as inset. Lattice fringes are clearly observed in the high-resolution STEM-HAADF image. This reveals the crystallographic nature of the synthesized nanospheres. The FFT pattern presents bright spots corresponding to the lattice planes of the disordered FCC phase of PtCo alloy, another confirmation of their crystalline structure. The nanosphere shell consists of well-defined NPs. The central region of the sphere appears to be empty or significantly less dense than the shell.

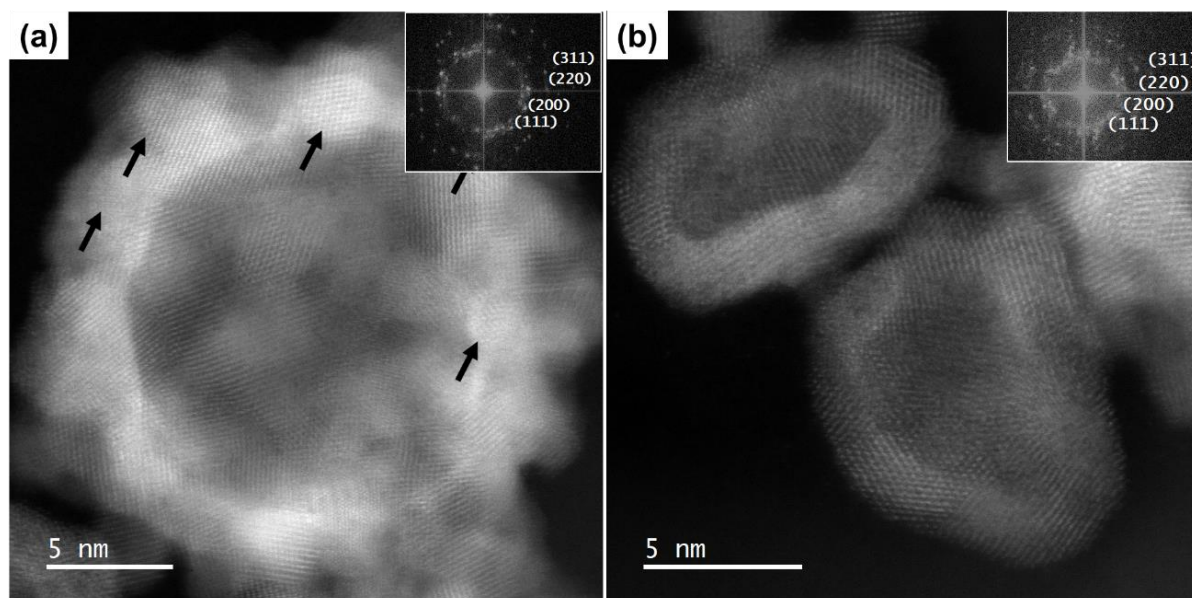


Figure 3.6: High-resolution STEM-HAADF micrographs depicting nanospheres with its shell composed (a) of interconnected NPs indicated by black arrows (b) and a continuous shell. The inset of each image is their corresponding FFT.

This confirms that the first category of particles are hollow nanospheres with a shell formed by randomly distributed and connected NPs. In order to investigate the three-dimensional morphology of these nanospheres including their shells and the potential presence of an empty core, electron tomography is used later on in this work.

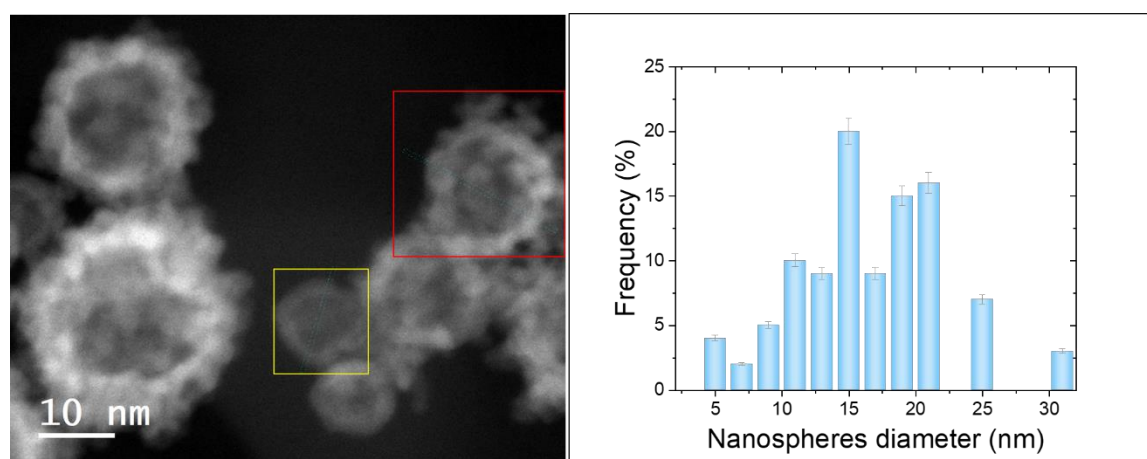


Figure 3.7: Diameter distribution of the Pt-1 nanospheres accompanied by a corresponding STEM-HAADF image highlighting the two categories of the Pt-1 nanospheres.

Figure 3.6(b) shows a high-resolution STEM-HAADF image of the second category of particles e.g. the nanospheres with a continuous shell and the corresponding FFT pattern. The latter

confirms the disordered FCC crystalline structure of the Pt-1 nanospheres. What sets this category of nanospheres from the first one is a smaller outer diameter as it is detailed later in this section. The shell has a relatively uniform contrast with a consistent thickness, and these nanospheres are not perfectly spherical; they have a more elongated morphology.

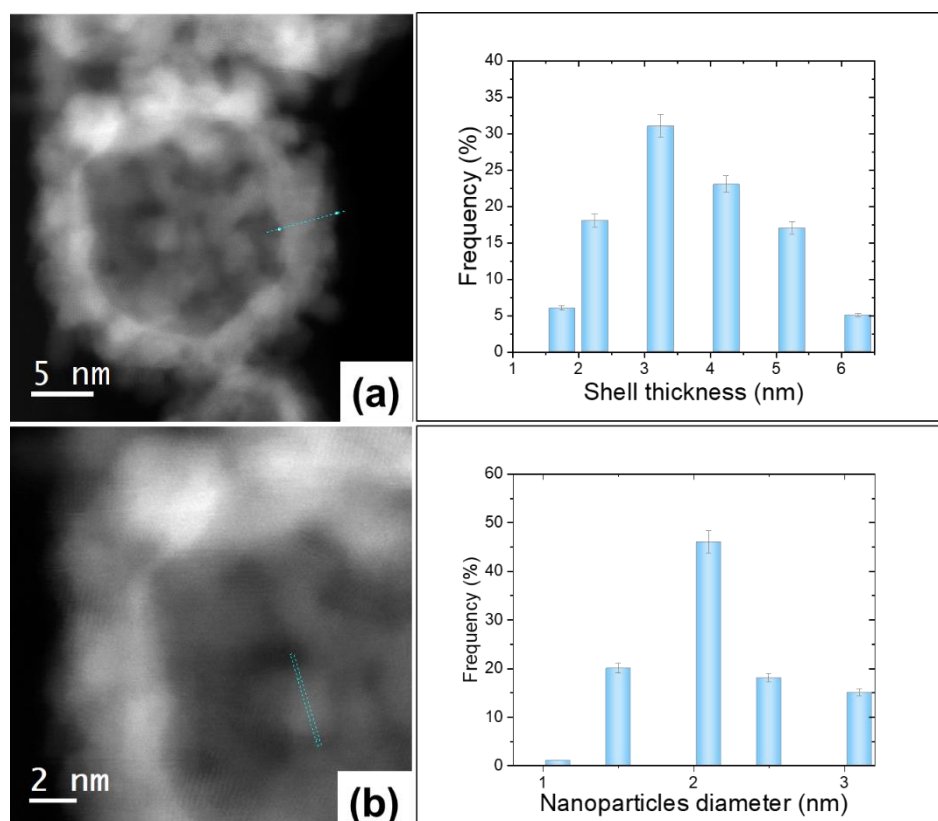


Figure 3.8: Histograms showing the distributions of (a) nanospheres shell thickness (b) and NPs diameters within the shell. Representative STEM-HAADF images highlighting the measured shell and NPs complement the histograms.

From a statistical point of view, it is determined that particles with a thin and smooth shell have an average diameter of approximately 10 nm, smaller than the more abundant nanospheres with the discontinuous shell that have an average diameter of $16 \text{ nm} \pm 4 \text{ nm}$.

The nanospheres diameter distribution covering both categories is presented in Figure 3.7. A statistical study of the NPs that compose the shell determines their average diameter of approximately 3 nm. These NPs collectively form an average 4 nm-thick shell. Both shell thickness and NPs diameter distributions are presented in Figures 3.8(a) and 3.8(b), respectively. Details about the measurements approach are provided in Appendix 2.

The STEM mode coupled with energy dispersive X-ray spectroscopy (EDS) is used next to assess the chemical composition of the synthesized particles. The results of this analysis are presented in the following section.

1.3. Chemical composition by STEM-EDS

The primary focus of this analysis is to ascertain the presence and quantify the Cobalt (Co) content from the template material. Additionally, the aim is to spatially localize the constituting elements within the particles. A statistical study is conducted to determine the Co content within each nanosphere. EDS spectra are acquired over 20 distinct nanospheres (Figure 3.9(a)).

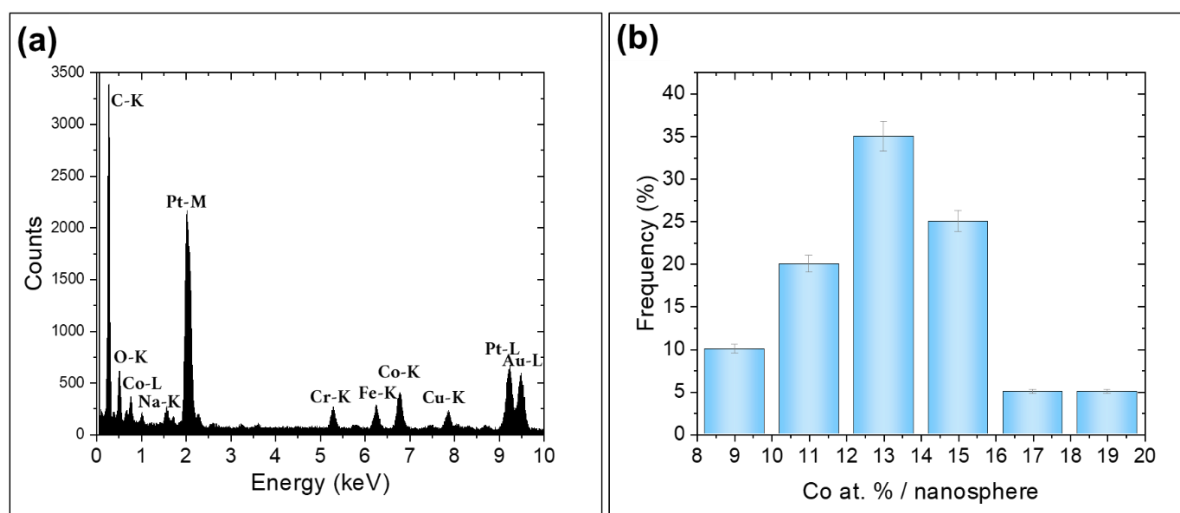


Figure 3.9: (a) EDS spectrum showing the chemical composition of the Pt-1 particles, (b) Co at. % distribution in Pt-1 nanospheres.

The primary signals detected are Pt ($M\alpha$) and Co ($K\alpha$) which confirms the presence of both elements. The carbon (C) signal originates from the carbon membrane used in the TEM grid. The presence of oxygen can be attributed to the sample's exposure to ambient air prior to its analysis and therefore probably to the partial oxidation of Co within the sample. The gold (Au) and Copper (Cu) signals originates from the TEM grid material, while the sodium (Na) signal is attributed to the NaBH_4 used in the synthesis. The signals of chromium (Cr), and iron (Fe) originates from the TEM column and from the sample holder.

Co and Pt at. % are determined over each of the analyzed Pt-1 nanospheres. An average Co content of 13 ± 5 at. % is then calculated from the collected data. The Co at. % distribution proving the presence of Co in all analyzed particles is presented in Figure 3.9(b). Details about the EDS quantification method are provided in Appendix 3.

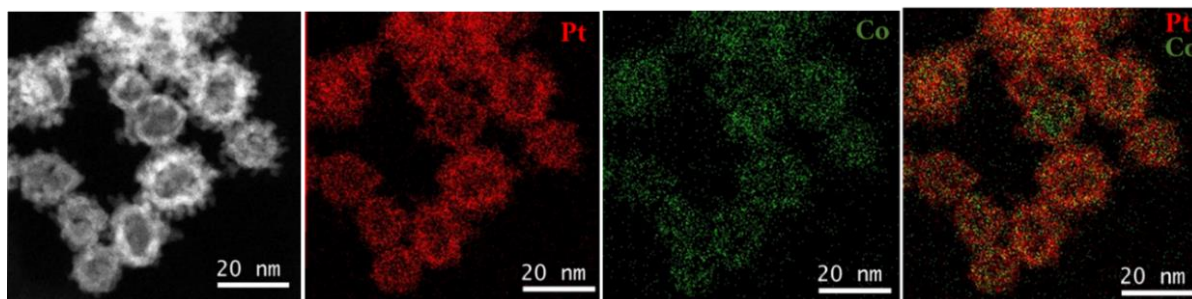


Figure 3.10: EDS elemental maps of an agglomeration of Pt-1 HNS showing the spatial distribution of both Pt and Co along with their superposition

The Co $K\alpha$ line and Pt $M\alpha$ line are used for the construction of Co and Pt maps, along with their superposition displayed in Figure 3.10. These maps visualize the spatial distribution of both Pt and Co atoms within the nanospheres.

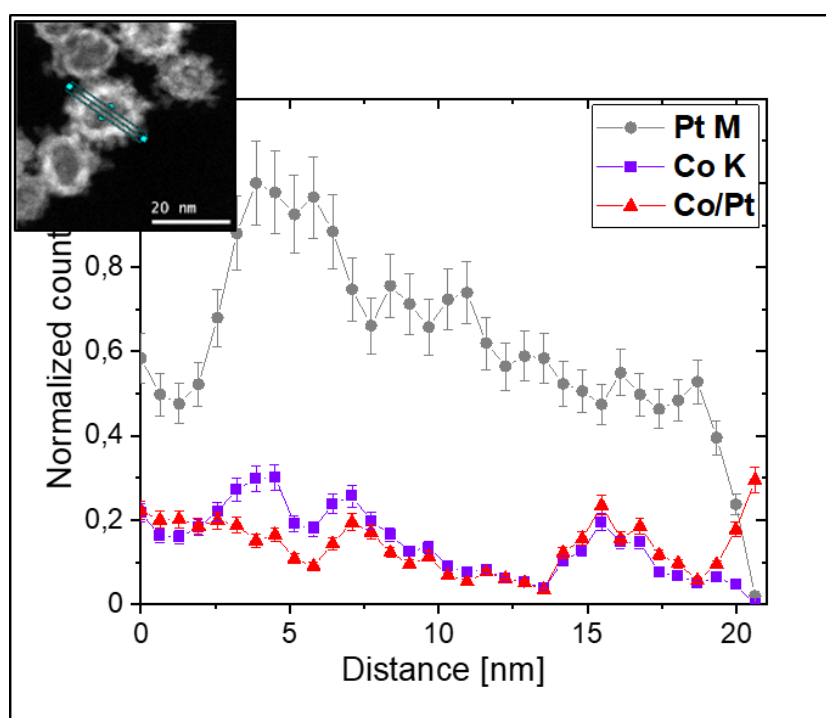


Figure 3.11: A representative EDS line profile showing the intensities of both Pt and Co across an individual nanosphere showing the Co/Pt ratio showing Co-rich regions

The shells of these nanospheres are areas with intense Pt signals, indicating a high concentration of Pt, as shown in the Pt elemental map. As anticipated by the analysis of the 2D micrographs, this elevated Pt concentration is not observed in the central regions of these nanospheres. In contrast, a similar situation is observed in the Co elemental map in a less obvious manner due to the comparatively weaker signal from Co. When overlaying both elemental maps, we observe

that Pt and Co are not homogeneously distributed: Co segregations are observed across the sample.

In Figure 3.11, an EDS profile displays regions with a high Co/Pt ratio, indicating the presence of Co-rich areas, while other regions with a low Co/Pt ratio signify Pt-rich areas, distributed randomly throughout the nanospheres. It is well-established that synthesized Pt-Co systems in their initial state may exhibit compositional heterogeneities, featuring a partial segregation at the atomic level of Co and Pt [188]–[190]. Research has revealed that within such system, Co undergoes oxidation to form cobalt oxide (CoO) and therefore segregations of CoO and Co may be present [191].

After analyzing the sample's morphology through 2D projections, the following section presents the results obtained from the electron tomography 3D analysis of the same sample.

1.4. 3D morphology analysis by Electron Tomography

The 3D analyses are conducted over a group of nanospheres. Figure 3.12 (a) shows the 2D STEM projection of the selected nanospheres assembly of Pt-1.

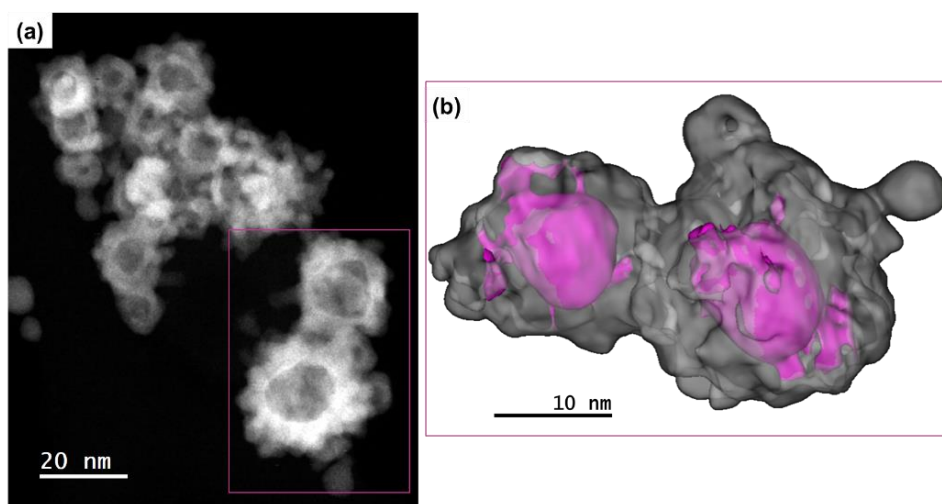


Figure 3.12: (a) STEM-HAADF image of an assembly of Pt-1 nanospheres, (b) 3D model of two Pt-1 nanospheres selected from the nanospheres assembly.

The volume of the whole nanospheres assembly have been reconstructed, but only two selected nanospheres are visualized through segmentation. The resulting 3D model of two of the Pt-1 nanospheres selected from the constructed volume is presented in Figure 3.12 (b). This 3D model of two of the Pt-1 is obtained as a final step of the 3D analysis using the Slicer3D

software after data segmentation and modeling. It shows the synthesized 3D nanospheres of Pt-1 with the rough shell formed by NPs. This approach provides evidence of any potential presence of an inner void within these nanospheres. Additionally, considering the complex morphology of their shell observed in 2D STEM-HAADF projections, ET provides more insights into this shell features.

In order to obtain a 3D dataset, a series of 2D STEM-HAADF projections of the selected area are acquired at various angles as shown in figure 3.13. These images from the tilt series are then aligned, and the volume of the nanospheres is reconstructed using the OS-SART algorithm. The data segmentation is finally conducted for the 3D model visualization. Further elaboration on this process is available in Chapter 2.

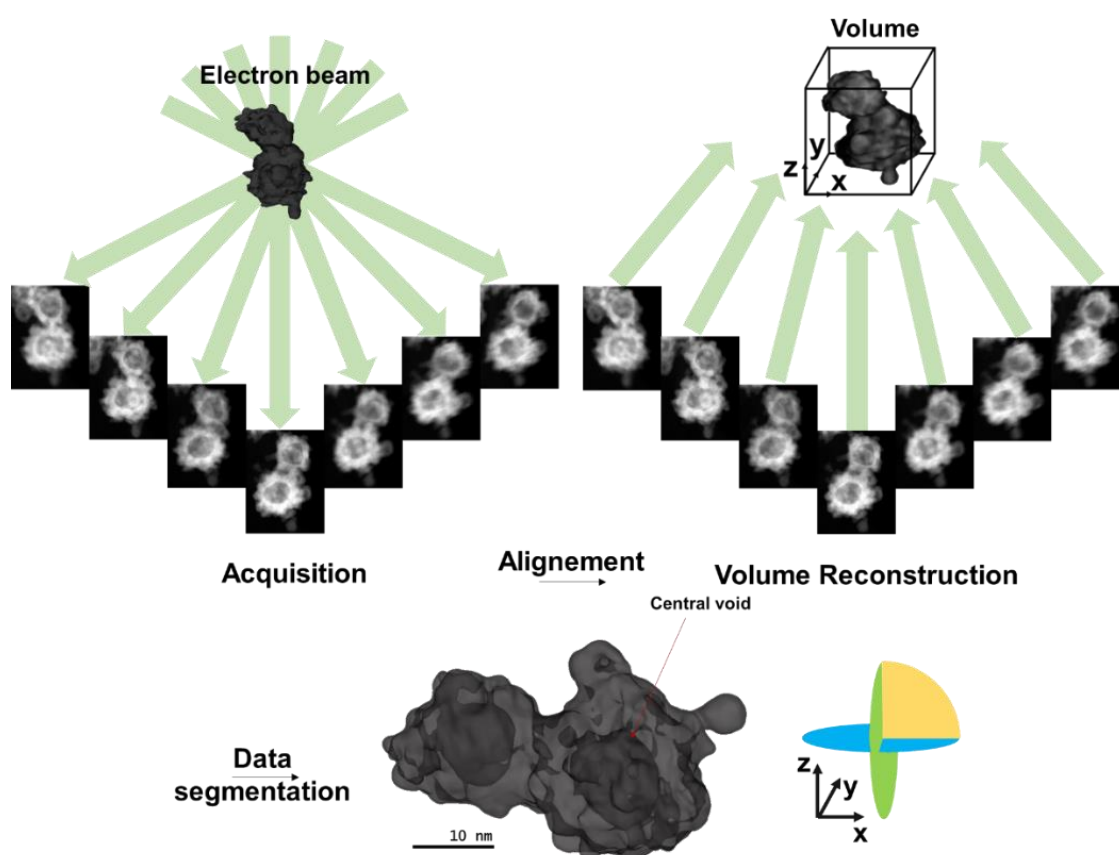


Figure 3.13: Schematic representation of the electron tomography methodology. In a first step a series of projections is acquired while tilting the specimen inside the microscope (top left), in a second step the volume is constructed using OS-SART algorithm. The final step is the 3D image of the object, constructed from the 3D matrix.

A brief explanation of the tomography data is also presented in Figure 3.13 to improve its comprehensibility. The obtained 3D model of the Pt-1 nanospheres is presented along with an

illustrative schematic representation of the XYZ orientations of slices which is extracted from the reconstructed volume for analysis in this section.

Figure 3.14 presents (xy), (xz) and (yz) slices withdrawn from the reconstructed volume of the selected nanospheres group. By analyzing such slices within the reconstructed volume, a clear pattern emerged. It reveals a central void surrounded by a discontinuous shell of NPs (indicated by yellow circles in Figure 3.14). This finding stands as a definite confirmation of the hollow microstructure of the Pt-1 particles.

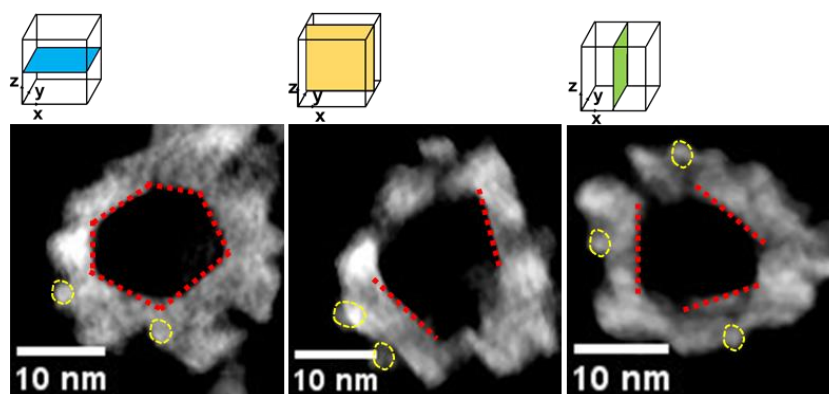


Figure 3.14: (xy), (xz) and (yz) slices through the reconstructed volume of HNS with a shell formed by NPs (yellow lines) and a faceted internal shell surface (red lines).

A statistical analysis throughout the reconstructed volume allowed an additional determination of the nanospheres average diameter, yielding a measurement of 20 ± 2 nm and an average NPs diameter range of 2-3 nm. These results are consistent with STEM-HAADF 2D statistical analysis (Figures 3.7 and 3.8 in section 1.2 of this chapter).

The observed void with the nanospheres does not have a perfect spherical configuration, rather, it actually displays facets (indicated by red lines in Figure 3.14). These facets could be a result of the Co NPs used as templates during the synthesis of the Pt-1 nanospheres. The facets exposed by nanoparticles are affected by their morphology, which is highly linked to their crystal structure [192]. Co is recognized to exhibit three polymorphic forms: the hexagonal close-packed (hcp) phase, the face-centered cubic (FCC) phase, and a pseudo-cubic ϵ -Co phase [193], [194]. All of these structure presents facets which can explain the faceting of the Pt-based HNS inner shell.

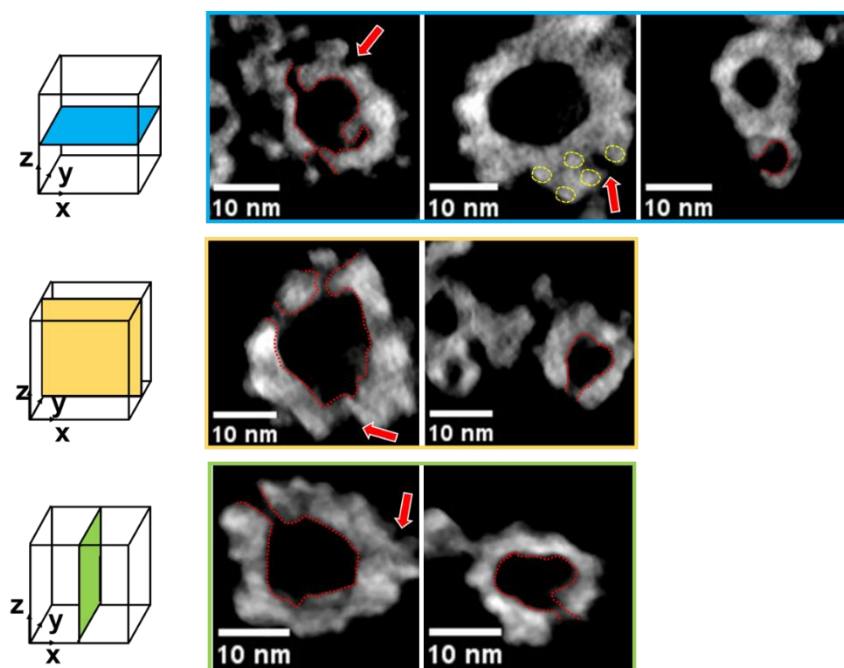


Figure 3.15: (xy), (xz) and (yz) slices through the reconstructed volume of HNS featuring the NPs forming the shell (yellow lines) the open channels (red lines) and surface roughness (red arrows).

According to the cross-sections along different directions, various channels are identified within the shell of the nanospheres (Figure 3.15). These channels directly traverse the nanospheres shell to reach the central void (indicated by red lines in Figure 3.15). NPs forming the shell are also identified within these slices (indicated by yellow circles in Figure 3.15). The surface roughness of the Pt-1 HNS's outer shell is evident and highlighted by the red arrows in Figure 3.15.

The average channel diameter “d” (Figure 3.16(a)) and the average number of these channels per nanosphere are statistically determined. “d” is measured by defining the outlines of the channel using ImageJ software. The channels number for each nanosphere is counted following different directions as illustrated in Figures 3.16(a) and 3.16(b).

Statistics showed the presence of 5 channels with a variability of ± 2 per nanospheres with a channel average diameter of $3 \text{ nm} \pm 2$ (channels number per nanosphere and diameter distribution are shown in Figures 3.16(c) and 3.16(d), respectively).

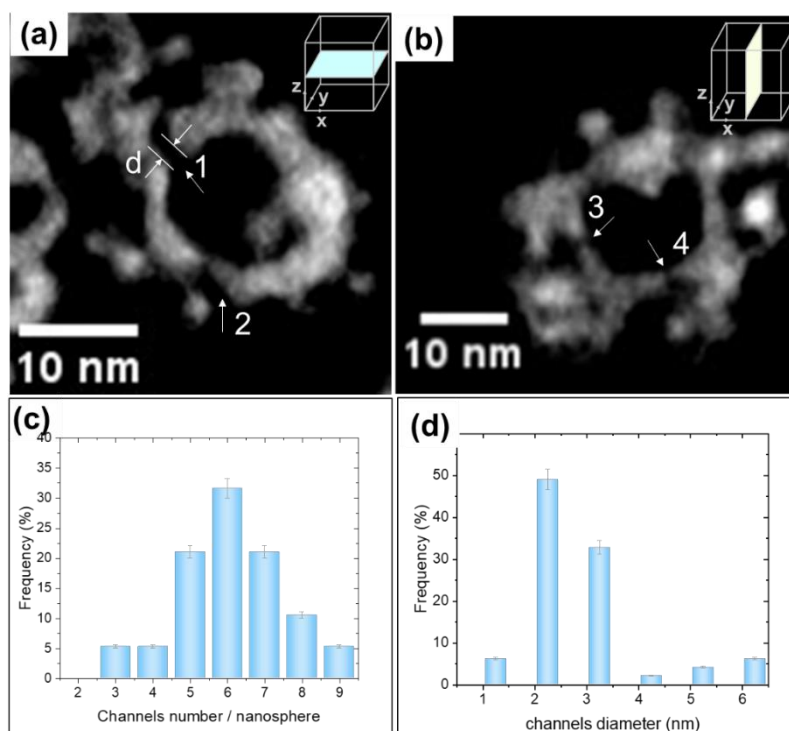


Figure 3.16: (a)(b) (xy) and (yz) slices of the reconstructed volume showing a channel diameter “d” and numbers denoting the channels number for the same nanosphere. Histograms showing (a) the channels number distribution per nanosphere and (b) these channels diameter distribution.

In order to optimize the Pt-based HNS properties, including Co content, shell thickness, and porosity, a second set of nanospheres is synthesized. In the next section, the initial state of the second set of HNS: Pt-2 HNS is introduced.

2. Particularities of the Pt-2 hollow nanospheres

2.1. Morphology and crystalline structure by SEM and XRD

The SEM images in Figure 3.17 illustrate the morphology of large-scale 1D chains. At both low and high magnification, these images show the assembly of extended chains composed by nanospheres. The nanospheres, each possessing a diameter less than 50 nm, are connected to create chains of an estimated length of approximately 600 nm (Figure 3.16(b)). A few large independent particles are also observed within the sample (indicated by blue circles in Figure 3.17(a)). These particles, similarly to the ones found in the Pt-1 sample, presented diameters around 100 nm. The crystalline structure of the Pt-2 particles is investigated by XRD measurements.

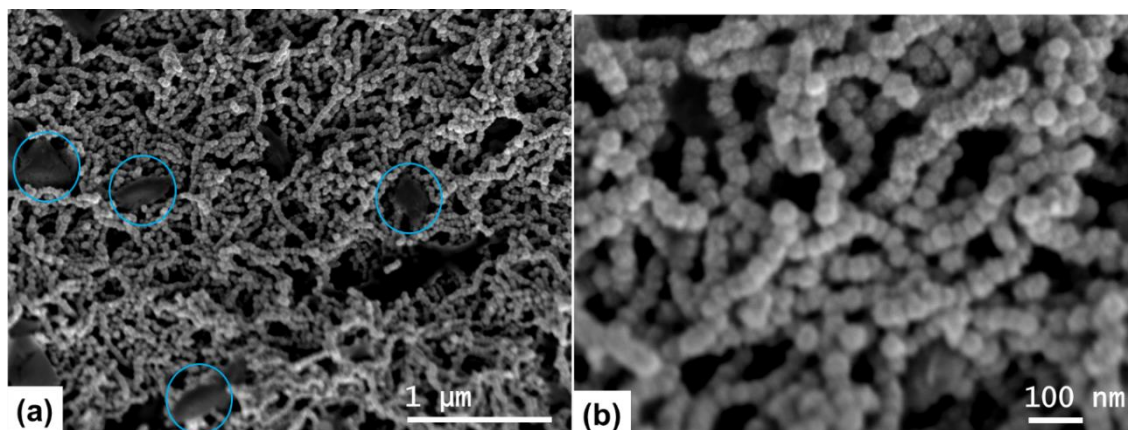


Figure 3.17: SEM images of the Pt-2 particles at (a) low and (b) high magnifications.

The diffractogram of the Pt-2 particles (Figure 3.18(a)) exhibits distinctive peaks corresponding to the disordered FCC phase of the PtCo alloy. Additionally, there are supplementary peaks observed within the angular range of 20 to 50 degrees, suggesting the presence of impurities, more specifically those corresponding to the undissolved NaBH_4 crystal from the synthesis.

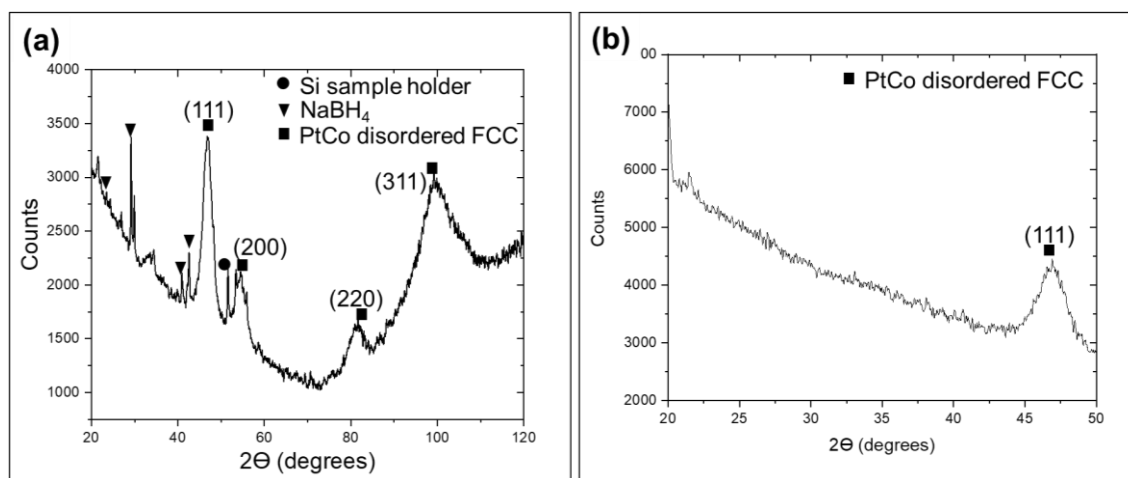


Figure 3.18: XRD pattern of Pt-2 hollow nanospheres, (a) covering an angular range between 20 and 120 degrees, and (b) longer scan over a smaller angular range between 20 and 50 degrees.

In order to validate this, another XRD measurement of a different Pt-2 sample is conducted across the same angular range a relatively long period. The resulting diffractogram presented in Figure 3.18(b) does not show the previously observed impurity-related peaks, thereby ruling out widespread impurities across the sample.

2.2. Morphology and size distribution by STEM-HAADF

The STEM-HAADF images in Figure 3.19(a) illustrates chains of nanospheres.

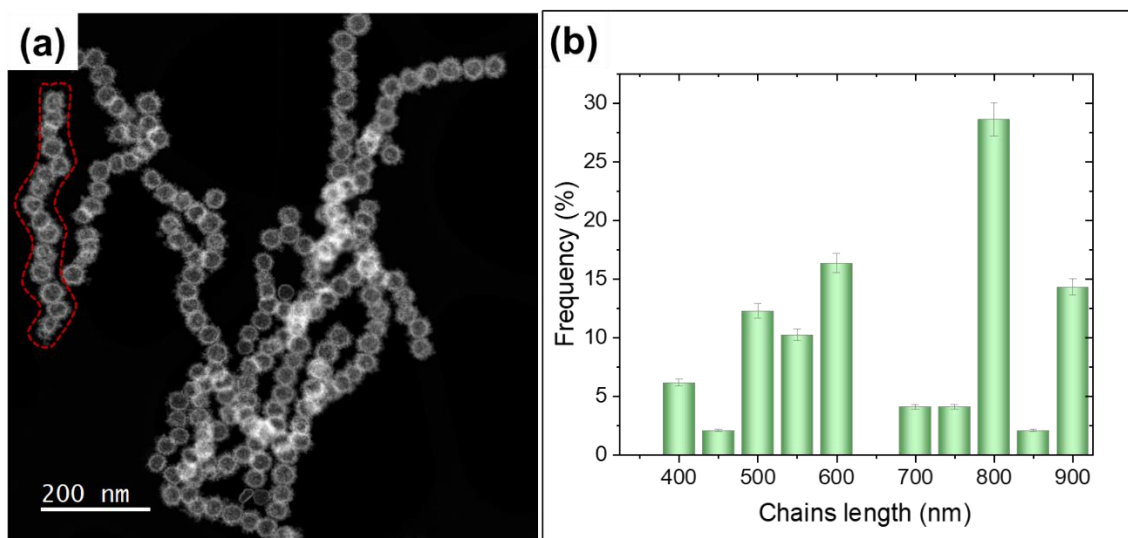


Figure 3.19: (a) STEM-HAADF micrographs showing chains of Pt-2 hollow nanospheres, (b) Histogram showing the chains length distribution.

The average chains length (marked by red lines) is statistically measured to be 700 ± 200 nm corresponding to different number of nanospheres (chains length distribution in Figure 3.19(b)). The STEM images confirm the formation of chain-like configuration of nanospheres, as previously observed in the SEM images.

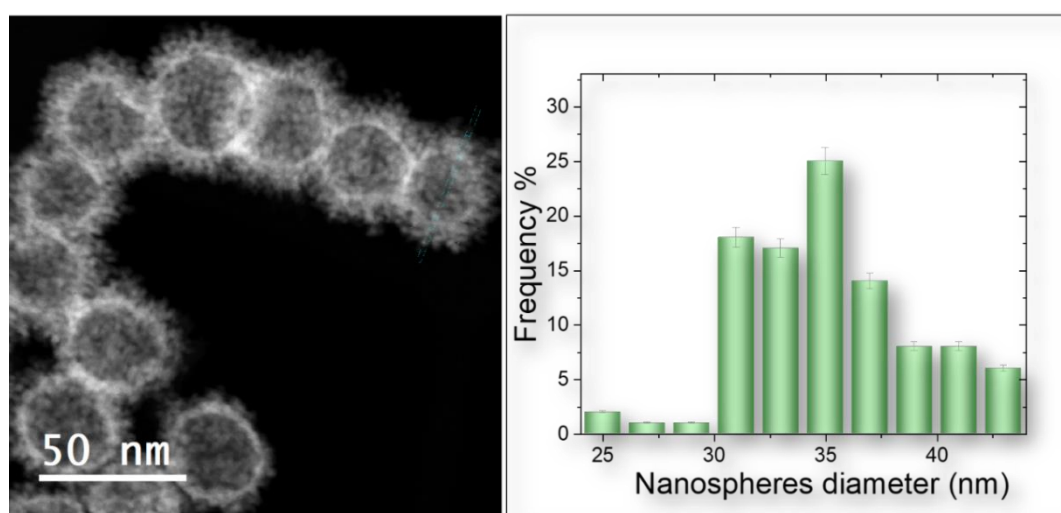


Figure 3.20: Diameter distribution of the Pt-2 nanospheres accompanied by a corresponding STEM-HAADF image showing a chain of nanospheres.

Morphologically, the synthesized particles exhibit nanospheres with a discontinuous shell. These nanospheres have an average diameter of $34 \text{ nm} \pm 4 \text{ nm}$. The nanospheres diameter distribution is presented in Figure 3.20.

A high-resolution STEM-HAADF image of a single nanosphere is presented in Figure 3.21(a). The NPs forming the shell are clearly observed with clear boundaries as marked by the yellow lines of Figure 3.21(a).

The concentric shell thickness is presented in a high-resolution STEM-HAADF image in Figure 3.21(b) with the corresponding FFT pattern consistent with a disordered FCC PtCo crystalline structure. The presence of gaps (indicated by red arrows) within it suggests the presence of nanochannels or pores. The shell presents an average thickness of $5 \text{ nm} \pm 2 \text{ nm}$. Within this shell, the NPs have an average diameter of $2 \text{ nm} \pm 1 \text{ nm}$. The shell thickness distribution along with NPs diameter distribution are respectively presented in Figures 3.21(c) and 3.21(d).

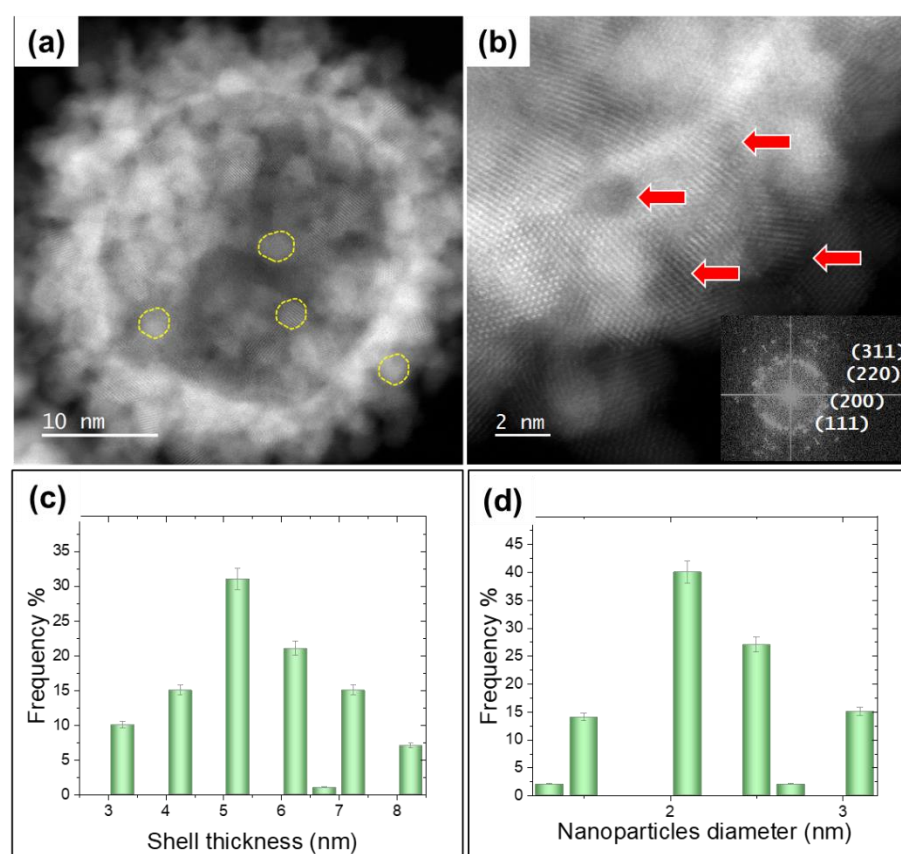


Figure 3.21: High-resolution STEM-HAADF micrograph of (a) individual Pt-2 nanosphere and of (b) nanosphere shell showing the gaps within it (red arrows) with the FFT pattern as an inset. Histograms showing the Pt-2 (c) shell thickness distribution and (d) nanoparticles diameter distribution.

In the following section, results of EDS and SAED analysis of the Pt-2 are briefly presented.

2.3. Chemical composition and crystalline structure by STEM-EDS and SAED

In terms of chemical composition, EDS spectra are acquired over several regions of the sample. The EDS spectrum, presented in Figure 3.22(a) reveals signals of Co K α and Pt M α , indicating the presence of both elements in all particles. It also presents a signal of C from the TEM membrane, Cu signal from the TEM grid and O signal from the sample expose to air prior analysis and probably to the partial oxidation of Co in the sample. No signals of impurities as the ones generated during the Pt-1 analysis which is attributed to the cleaner synthesis process. Similar to the case of Pt-1 particles, statistics are conducted in an attempt to quantify the Co in these particles. An average of 7 ± 3 at. % of Co is determined. The Co at. % distribution per nanospheres is presented in Figure 3.22(b) marking the presence of Co in all analyzed particles.

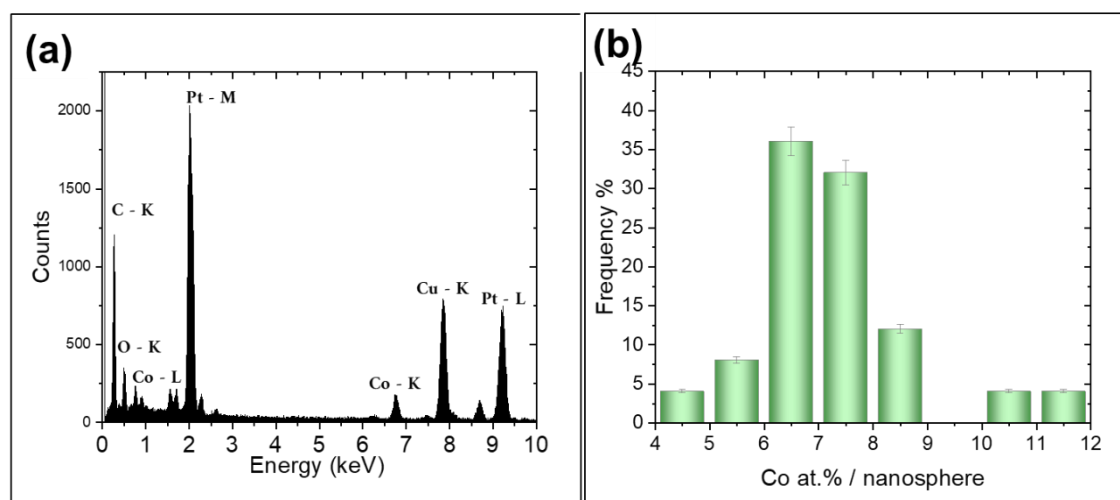


Figure 3.22: (a) EDS spectrum showing the chemical composition of the Pt-2 particles, (b) Co at.% content distribution in Pt-2 nanospheres.

The Co K α line and Pt M α line are used for the construction of Co and Pt maps, along with their superposition displayed in Figure 3.23(a).

Both Pt and Co present high intensities in the shell region of analyzed for all particles and relatively low intensities in their central regions. When overlaying both elements maps, Pt seems to dominate of the outer edge of the shell. EDS profiles linked to the intensities of both Pt and Co along the diameter of a single nanospheres are also examined (Figure 3.23(b)). The

results from these profiles show a shell formed by both Pt and Co and a high Pt intensity at its periphery, while there is no detectable Co signal in this region. This profile also indicates Co-rich and Pt-rich regions randomly distributed across the sample.

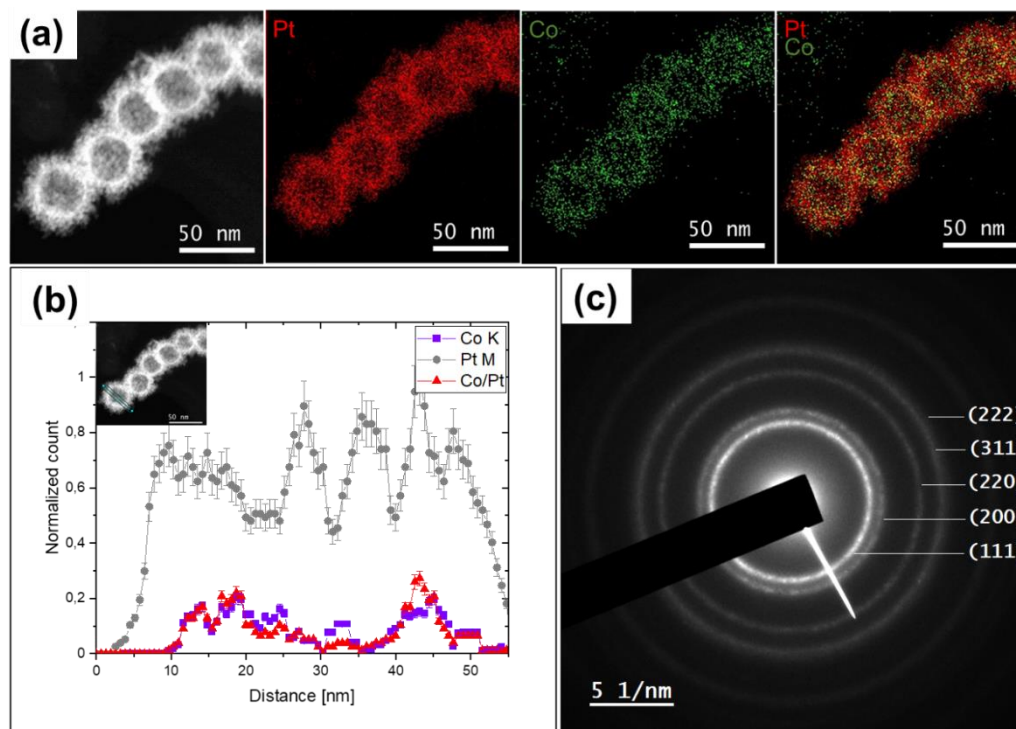


Figure 3.23: (a) EDS elemental maps of a chain of Pt-2 HNS showing the spatial distribution of both Pt and Co along with their superposition, (b) a representative EDS line profiles across a single nanosphere showing a Pt-rich shell, (c) DP of the Pt-2 HNS indexed with lattice planes of the FCC PtCo phase.

The crystalline structure of the Pt-2 particles is identified using SAED. The diffraction pattern (DP) displayed the five concentric rings corresponding to the (111), (200), (220), (311) and (222) crystallographic planes of the disordered FCC phase of PtCo alloy (Figure 3.23(c)). These results are consistent with the XRD analysis of the Pt-2 particles.

In the following section, the porosity within the Pt-2 nanospheres are examined. This electron tomography-based study also aims to ascertain whether any modifications in this aspect have occurred in comparison to the first batch. As previously observed, there are noticeable gaps and channels in the 2D micrographs. This analysis enables us to assess both the accessibility and frequency of these channels within the nanospheres.

2.4. 3D morphology analysis by Electron Tomography

Following the same adapted pathway for the Pt-1 particles, we aim to conduct the same 3D analysis for the second batch of Pt-2 particles.

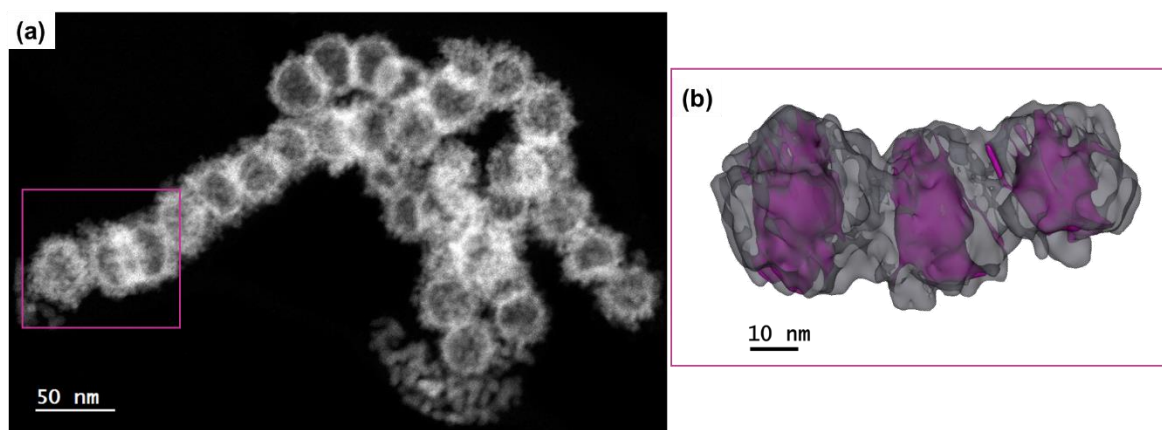


Figure 3.24: (a) STEM-HAADF image of an assembly of the Pt-2 nanospheres (b) 3D model of three Pt-2 nanospheres selected from the nanospheres assembly

Figure 3.24(a) shows the 2D STEM-HAADF projection of the selected nanospheres region for the 3D analysis along with resulting 3D model of three Pt-2 HNS from the nanospheres assembly (Figure 3.24(b)). The electron tomography methodology used here is similar to the one utilized in the 3D analysis of the Pt-1 HNS.

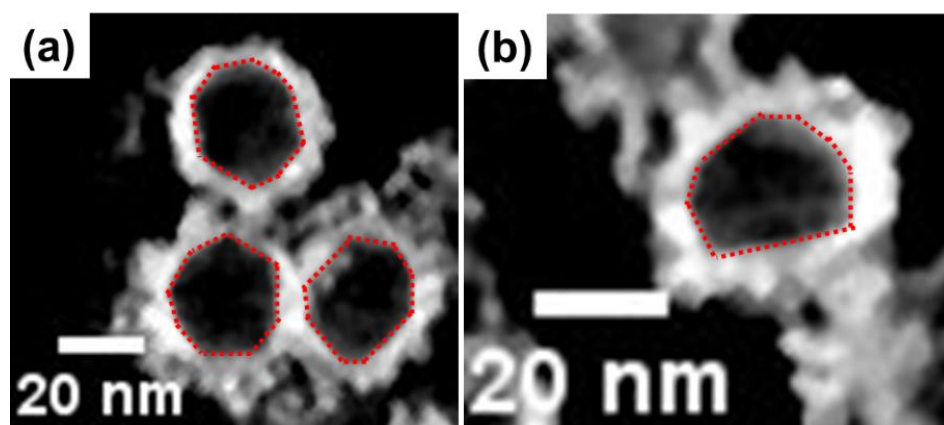


Figure 3.25: (a)(b) (xy)slices through the reconstructed volume of HNS showing the faceted internal shell surface (red lines).

Slices in the (xy) direction withdrawn from the resulted reconstructed volume show the nanospheres with a central void, which confirms the presence of a hollow microstructure

(Figure 3.25). The inner shell appears highly faceted (red lines in Figures 3.25(a) and 3.25(b)), with over than 8 facets observed originating from the Co NPs templates as previously explained. The size distribution information obtained from cross-sectional sections through the volume of the sample aligns consistently with the findings from STEM-HAADF images, indicating an average diameter of 32 ± 2 nm. NPs forming the shell exhibited an average diameter approximately 2 ± 1 nm, as expected.

Slices along different directions of the reconstructed volume of the Pt-2 HNS are presented in Figure 3.26. Due to limitations in the specimen holder's maximum angular rotation, tomographic tilt series have a missing data wedge that corresponds to the unobserved angles[195]. This results artifacts such as elongation and blurring affection the quality of the reconstructed volume. These artifacts are mildly observed in the volume reconstruction of this set of HNS. However, all the required information is clearly seen in the resulting volume. The nanospheres in this batch consistently exhibit unobstructed channels that extend towards the inner void of the nanospheres (indicated by red arrows in Figure 3.26).

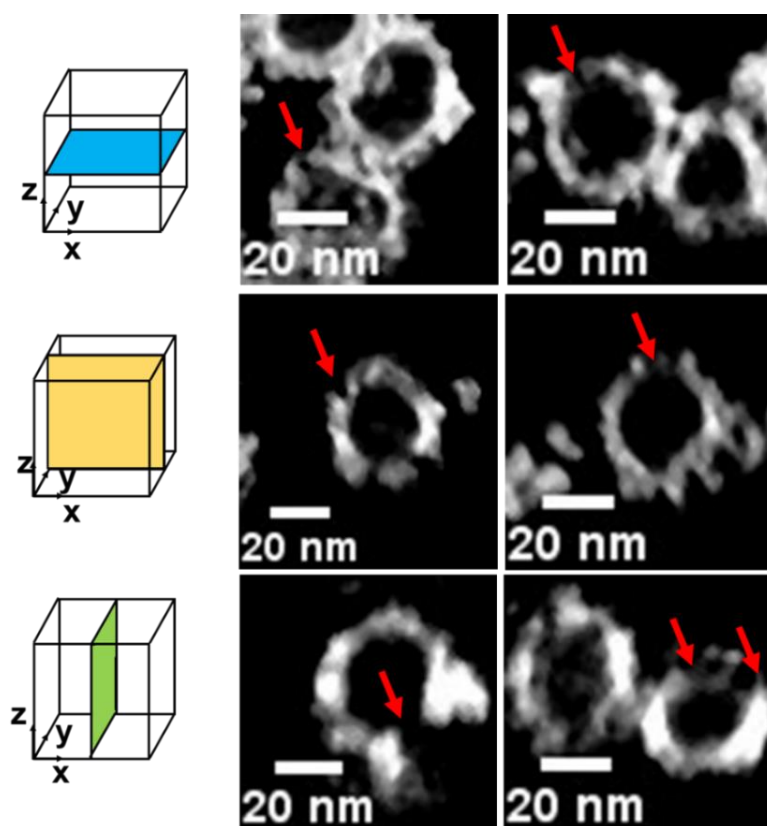


Figure 3.26: (xy), (xz) and (yz) slices through the reconstructed volume of the Pt-2 HNS featuring the large open channels leading to the inner void (indicated by red arrows).

These radial channels, as displayed by sections extracted from the reconstructed volume, are relatively large, surpassing even the thickness of the shell.

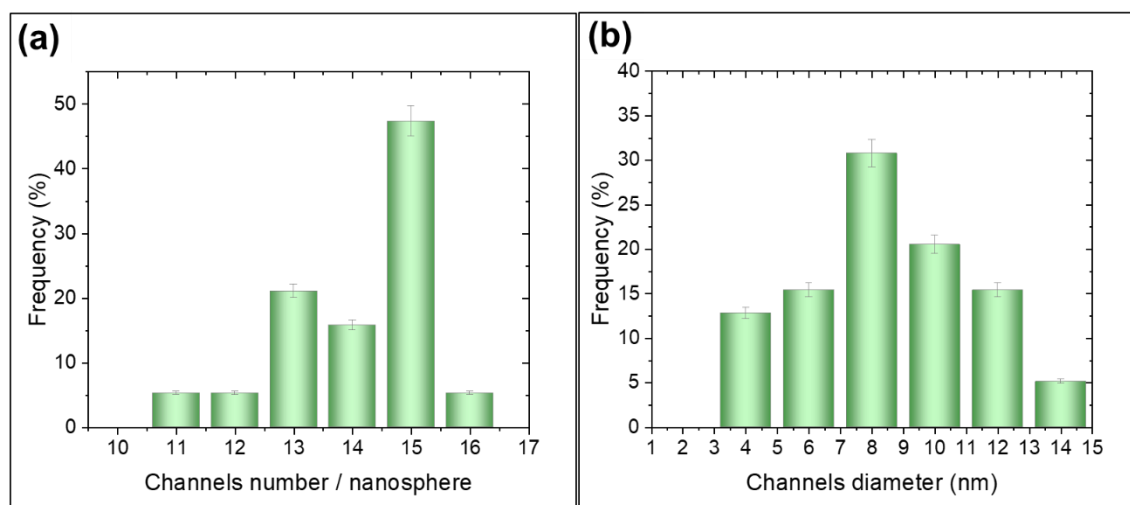


Figure 3.27: Histograms showing the (a) channels number per nanospheres present in the shell and (b) the channels diameter distribution in the Pt-2 HNS and (c)

A statistical examination of the channels number determined a number of 14 channels per nanosphere (Figure 3.27(a)). An average diameter of 8 ± 2 nm for the channels (Figure 3.27(b)), compared to the shell thickness of 6 ± 1 nm is statistically determined. Consequently, the HNS from this batch present a configuration where the inner shell remains nearly always accessible through these sizable channels, facilitating the entry of reaction gases in an effective manner.

3. Discussions

Pt-1 and Pt-2 HNS share similarities and differences in their characteristics at various levels.

Morphology: The Pt-1 set of HNS possess two distinct types of shells, whereas such differentiation is absent in the Pt-2 HNS. It is important to mention that among the various nanospheres morphologies in the first set, those exhibiting a thinner smooth shell are more attractive for catalytic applications due to the greater atomic relaxation on rough surfaces than on their smooth counterparts [196]–[199]. The formation of a smooth-surface structure is likely attributed to the gradual and slow introduction of the Co NPs during the galvanic replacement synthesis. This controlled delivery facilitates the progressive reduction and deposition of Pt ions onto the Co templates at low stoichiometric ratios. [199]

Similar to the Pt-1 HNS, the Pt-2 HNS reveal facets on their inner shell surfaces. Effective adsorption, the first and crucial step in heterogeneous catalysis, is strongly influenced by the exposed atomic arrangement on the catalyst surface. The atomic arrangement and coordination of surface atoms vary among different crystal facets, resulting in different adsorption energies and states for reactant molecules on these various facets. These variations in adsorption states significantly impact the following catalytic steps. A faceted metal catalyst has more atoms located at edges and corners, where atomic density and coordination are much lower, profoundly enhancing surface adsorption.[200]

Hollow structure: The majority of particles in both cases exhibited a hollow microstructure characterized by shells composed of interconnected NPs with similar shell thickness and NPs average diameter. Both particles exhibited channels within their shells and contained a residual presence of Co. The Co content in the Pt-2 nanospheres is approximately half that of the Pt-1 particles (7 vs. 13 at. %). The presence of Co contaminations in both sets does not necessarily have a negative impact on their catalytic activity. Krajczewski et al [201] have investigated the influence of these contaminations on the catalytic activity of the Pt nanostructures. Pt hollow nanospheres are used as catalysts for the reduction of 4-nitrophenol by sodium borohydride in aqueous environments as a model reaction. These investigations confirmed that the enhanced catalytic activity of hollow Pt nanoparticles in this chemical reaction is not solely attributed to their increased surface area. Instead, it is also linked to the geometric and electronic modifications of the catalyst surface due to its contamination with Co (sacrificial template used during the synthesis).

Dimensions: The average nanospheres diameter is twice as the one of the Pt-1 particles (16 vs. 34 nm). The increase of the nanospheres diameter in the second set is probably due to the sintering of Co NPs prior and during the slow addition of the Pt salt solution. The increase in diameter alone evidently leads to a decrease of the active surface area but to a better thermal stability of the nanospheres for high temperature catalytic reactions.

HNS arrangement: The arrangement of particles varies between the two sets. Pt-2 HNS present a chain-like configuration, diverging from the nanosphere agglomerations seen in the first synthesis. The variation in particle arrangement between the two sets of particles originates directly from the synthesis process. More specifically due to modifications in the addition of Co precursors to the Pt salt during the second synthesis. Introducing Pt to the Co NPs led to the formation of the chain-like structures. This outcome may be attributed to the consistent presence

of a high concentration of Co NPs under the experimental conditions, promoting their agglomeration into chains and clusters. As Pt replaces Co, it prints the configuration of the agglomerated or chained Co NPs. In contrast, the first experiment involved the addition of Co to Pt, resulting a lower concentration of Co particles, which are relatively more isolated. In this scenario, Pt replaced Co in a manner that resulted in more discrete HNS.

Channels within the shell: Regarding the channels within the particle shells, the Pt-2 HNS presented a significantly higher number of channels, nearly three times higher than the one in Pt-1 particles (14 vs 4 channels/nanosphere). Furthermore, the average diameter of these channels is considerably larger in the Pt-2 sample compared to the average channel diameter observed in the Pt-1 sample, which is nearly four times smaller (8 vs 2 nm). The higher number of large channels is attributed to the slow and controlled addition of Pt salt to the Co NPs during the second synthesis, enabling the Pt to effectively reduce the Co into solution. Table 3.1 outlines the distinctions observed between the two sets of HNS.

HNS characteristics	Pt-1	Pt-2
HNS arrangement	Agglomerations	Chains
Nanospheres diameter [nm]	16± 4	34± 4
NPs diameter [nm]	3± 1	2± 1
Shell thickness [nm]	4± 1	5± 2
Co content [at. %]	13± 5	7± 3
Channels number/nanosphere	5± 2	14± 2
Channels mean diameter [nm]	3± 2	8± 2

Table 3.1: Summary of the characteristics of both Pt-1 and Pt-2 HNS from the TEM-based measurements

Our research findings align with the work of Lian et al. [92] and Zhou et al. [99], [98]. Lian's study presented similar nanospheres from a morphological point of view but with a larger average diameter (24 nm ± 2 nm) and thinner shell (2 nm), although they didn't provide details on chemical composition or Co quantification. Zhou et al. also synthesized Pt-based HNS arranged in chains, but with larger diameters (200 nm) for a first batch and varying Co content (20%) in the second one. However, they did not deeply investigate the shell porosity or channel characteristics, not the nanospheres chemical composition.

The Pt-2 HNS susceptible to exhibit enhanced active surface area and therefore increased catalytic activity. The unique chain-like arrangement observed in Pt-2 particles, in contrast to agglomerations in the first synthesis, introduces a novel structural element that could enhance catalytic pathways and higher thermal stability. The higher nanospheres diameter of Pt-2 HNS also suggests a higher thermal stability. The larger diameter of Pt-2 HNS nanospheres also implies an increased level of thermal stability due to its lower surface-to-volume ratio resulting a more stable structure. While the lower average diameter of Pt-1 might initially indicate a greater active surface area, this assumption becomes considerably debatable in light of the Pt-2 larger channel diameter and the improved accessibility of the inner shell to gases.

4. Conclusions

All the presented features of HNS makes them promising candidates for catalytic applications. Several studies have reported superior catalytic activity of the hollow metal nanostructures compared to their solid counterparts. Their higher activity is linked to the increased specific surface area with both inner and outer surfaces accessible to reactants. [202]

The inner void of the HNS can only be accessed by reactants through diffusion across the outer shell. The porosity and thickness of the shielding shell are one of the most important factors enhancing the rate of a chemical reaction. The high channels mean number for a nanosphere and their average diameter are crucial parameters in determining their efficiency in a specific catalytic reaction. Their role is supposedly crucial in terms of facilitating the diffusion process of reagents molecules toward and away from the inner surface. [203] Just as with porosity, the thickness of the HNS can also affect the time it takes for reactants to diffuse toward the active sites [204].

Within the inner void itself of hollow materials, a free volume is enclosed by a concave interface, introducing spatial constraints for gases or liquids filling the cavity. It is well-documented that confinement at the nanoscale alters the thermodynamic properties of matter compared to an unconfined state, and these effects can extend to reaction kinetics if a chemical reaction takes place.[202] Studies have proved that the high active surface area of the hollow metal nanostructure cannot explain the extent of catalytic improvement observed. Researchers have therefore proposed void-confinement catalytic effect, where the accumulation of reactant molecules within the inner cavity increases the probability of efficient catalytic events on the inner shell of hollow metallic nanostructures. [202], [205]–[208]

In the next Chapter 4, real-time analyses of the morphological evolution and thermal responses of both sets of Pt-based HNS are conducted by in-situ and operando environmental TEM. A study of their thermal stability profiles under different environments is presented and compared. Pt-based nanocatalysts have proven to be efficient in several chemical reactions, hydrogenation reactions included, as discussed in Chapter 1. The thermal stability of both Pt-based HNS is assessed under CO₂ hydrogenation reaction conditions, chosen as a model hydrogenation reaction.

CHAPTER IV: Exploring Pt-Based Catalyst Behavior with In-Situ and Operando TEM Under Different Environments

1.	Morphological evolution of the Pt-based hollow nanospheres during thermal annealing under vacuum	104
1.1.	Morphological evolution of the Pt-1 system under vacuum.....	105
1.1.1.	In situ TEM/STEM using the furnace-type heating holder	105
1.1.2.	In situ STEM using the MEMS-type holder.....	109
1.2.	Comparison of the thermal stability of the Pt-1 and Pt-2 systems	115
2.	Morphological evolution of the Pt-based hollow nanospheres under hydrogen atmosphere	122
2.1.	Thermal stability of Pt-1 hollow nanospheres	122
2.1.1.	Spatial distribution of Pt and Co post H ₂ assisted experiment in Pt-1 system	125
2.2.	Comparing the behavior of the Pt-1 and Pt-2 system under hydrogen atmosphere	126
2.2.1.	Thermal stability of Pt-2 hollow nanosphere.....	126
2.2.2.	Spatial distribution of Pt and Co post H ₂ assisted experiment in Pt-2 system	129
3.	Investigation of the Pt-based HNS behavior upon CO ₂ hydrogenation reaction.....	132
3.1.	Morphological evolution of Pt-based hollow nanospheres during thermal annealing	132
3.1.1.	Thermal stability of Pt-1 system.....	132
3.1.2.	Thermal stability of Pt-2 system.....	135
3.2.	Identification of CO ₂ hydrogenation pathway over the Pt-based hollow nanospheres	137
3.2.1.	Blank experiment to test the RGA data reliability.....	137
3.2.2.	Identification of the reaction products and onset temperature over the Pt-1 ..	138
3.2.3.	Identification of the reaction products and onset temperature over Pt-2.....	143
3.3.	Study of the thermal stability of Pt-based catalysts during isothermal CO ₂ hydrogenation reaction at 180°C	144
3.3.1.	Pt-1 hollow nanospheres.....	144
3.3.2.	Pt-2 hollow nanospheres.....	146
4.	Conclusions.....	148

1. Morphological evolution of the Pt-based hollow nanospheres during thermal annealing under vacuum

Temperature is a pivotal factor in chemical reactions influencing the performance of a catalyst. Therefore, following the thermal evolution of catalysts has been one of the most important topics of catalysis research. During thermal annealing, nanomaterials always undergo several structural transformations that can lead to their deactivation. Sintering is one of the most important processes, in which the nanoparticles coalesce to create larger and more robust structures, altering their physicochemical characteristics [209]. This originates from the tendency of these metal nanoparticles to minimize their surface energy since larger particles have lower curvature compared to their smaller counterparts (Gibbs-Thomson effect) [210], [211]. The sintering of nanomaterials leads to decrease in active surface sites, causing the inefficient exploitation of the valuable noble metal and a decrease in its catalytic performance during high-temperature catalytic reactions. More details about the sintering mechanisms are provided in Chapter I.

In order to enhance the development of synthesis techniques for achieving more enduring nanocatalysts, it is important to gain a comprehensive understanding of the mechanisms and factors influencing the sintering procedure. This study also enables the identification of optimal operating conditions and the development of catalysts that remain active and efficient over extended timeframes. In heterogeneous catalysis, metallic nanomaterials are typically stabilized with an appropriate support. During this work, the Pt-based HNS are examined on Carbon or SiN_x supports from the TEM grid or the environmental cell in the absence of a conventional material supporting material in order to assess their behavior independently before introducing the influence of a support. The inclusion of a support has a significant influence on the sintering behavior. When metal NPs are placed on a support, their surface energy is reduced, thereby mitigating NP aggregation and prolonging the operational lifespan of the catalyst. The support also enhances the dispersion of metal NPs and augments catalytic activity by facilitating an efficient synergistic and electronic interaction between the metal NPs and the support material [212]. Nevertheless, this aspect remains a subject for future research efforts.

In this section, a thermal treatment under the TEM vacuum is applied to each of the Pt-based set of HNS. Studying the morphological evolution of the catalysts as a function of temperature alone under the TEM vacuum conditions is expected to offer insights into the dynamic behavior

of the catalyst materials. By focusing solely on the influence of temperature, the thermal effect on catalyst microstructures is isolated. It allows for a deeper understanding of how temperature-driven changes impact the sintering process of the synthesized catalysts. This study also sheds the light on the evolution of the hollow microstructure morphology affecting this material active surface area. The high vacuum environment of the TEM column ensures that the catalyst's evolution is observed without interference from external factors.

1.1. Morphological evolution of the Pt-1 system under vacuum

1.1.1. In situ TEM/STEM using the furnace-type heating holder

For this investigation, the furnace-type heating holder from Gatan (see section 5.1 in Chapter II for details) is used for the study of the morphological changes in the Pt-1 HNS as a function of temperature alone. An in-situ characterization of the sample is conducted at six different temperatures as shown in Figure 4.1.

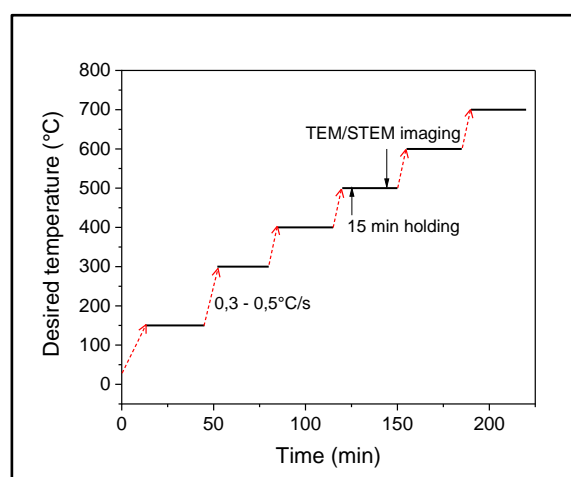


Figure 4.1: Temperature-time profile of the in-situ heating experiment of Pt-1 HNS under the TEM vacuum using the furnace-type holder heating holder.

Throughout this analysis, images of multiple regions of the Pt-1 HNS are captured. Representative images of one of these sections are displayed in Figure 4.2. The TEM mode is preliminary used in this case to perform in-situ SAED analysis of the sample, enabling the simultaneous investigation of its crystalline structure evolution.

Following the in-situ TEM analysis, three main morphological modifications upon thermal treatment are observed. First, a temperature of 300°C induces the growth of the NPs composing the Pt-1 HNS shell (indicated by red lines in Figure 4.2(b)).

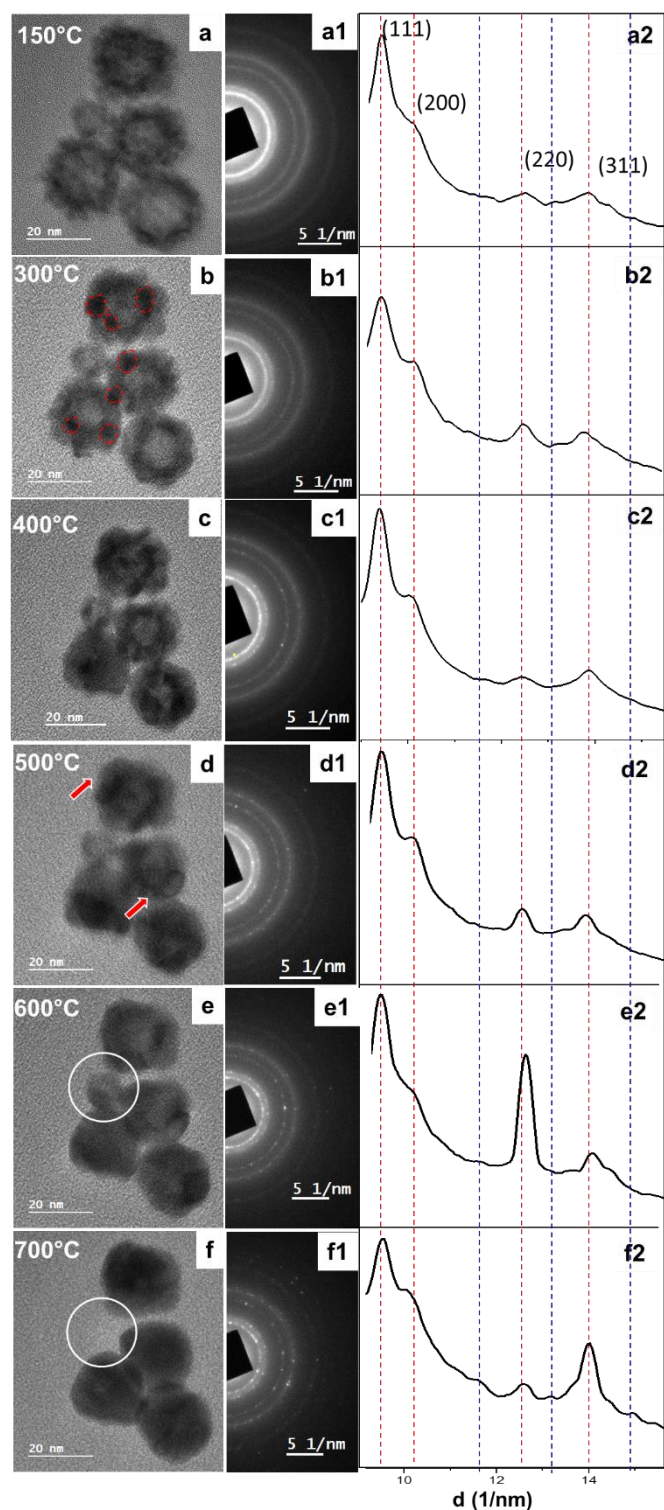


Figure 4.2: (a-f) TEM micrographs showing the morphological evolution of Pt-1 HNS during temperature ramping from 150 to 700 °C, (a1-f-1) corresponding selected area diffraction patterns (a2-f2) Normalized radial electron profiles corresponding to the DPs. The grown NPs forming the shell are indicated by red lines, the formed continuous shell is indicated by the red arrows and the disappearance of a nanosphere beyond 600°C indicated by the white circle.

Secondly, advancing to approximately 500°C, the disconnected shell transforms into a continuous one before attaining this temperature (indicated by red arrows in Figure 4.2(d)). Finally, beyond 500°C and going up to 700°C, the central void degrades, leading to the collapse of the HNS. Beyond 600°C, we observe the disappearance of small-diameter nanospheres (indicated by a white circle in Figures 4.2(e) and 4.2(f)) and the growth of their adjacent ones.

Structural changes in Pt-1 HNS are monitored using in-situ SAED (Figures 4.2 (a1-f1)). From each SAED pattern, a normalized radial diffraction profile is extracted (Figures 4.2 (a2-f2)). At 150°C, the DP of Pt-1 HNS (Figure 4.2 (a1)) displays four concentric rings. The corresponding radial profile (Figure 4.2 (a2)) exhibits characteristic peaks attributed to the (111), (200), (220), and (311) lattice planes of the PtCo disordered FCC phase. The presence of a ring-like diffraction pattern at 150°C indicates the existence of the Pt-based NPs containing multiple crystalline domains. With increasing temperature, the continuous diffraction ring becomes less distinct, and bright spots emerge (Figure 4.2 (f1)). This phenomenon is a consequence of NP crystal growth induced by the elevated temperature. No discernible shifts are observed in the initially identified electron profile peaks as the temperature increases, signifying the absence of any crystal phase modification for the PtCo FCC structure. However, at 700°C, new spots (indicated by the blue lines in Figure 4.2(f2)) emerges and are probably attributed to the partial oxidation of Co segregates at high temperatures to Co₃O₄ [213].

For a better contrast and better visualization of the HNS morphological evolution, the STEM-HAADF mode is used (Figure 4.3). As observed to the STEM micrographs, the image contrast is better at higher temperatures (>300°C) and blurry at 26°C. This is due the presence of surface contaminations (Electron Beam Induced Carbon Contaminations) on the HNS. At the lower temperature 26°C, these contaminants influence the sample-electron beam interactions, thereby affecting the image quality. Higher temperatures promote the desorption of these contaminants leading to the restoration of image quality [214].

The initial state image of Pt-1 HNS (Figure 4.3(a)) exhibits an assembly of HNS including the two categories of HNS (characterized either by a *continuous* or a *discontinuous shell*, see Chapter III for details). Upon heating to 200°C (Figure 4.3(b)), no significant changes in the morphological characteristics of both types of HNS are observed. At 300°C, there is a growth of NPs forming the shell (indicated by red lines in Figure 4.3(c)) for the HNS with a *discontinuous shell*. Additionally, other NPs disappear (indicated by white circles in Figures 4.3(b) and 4.3(c)). No noticeable modifications are seen in the *continuous shell* nanospheres.

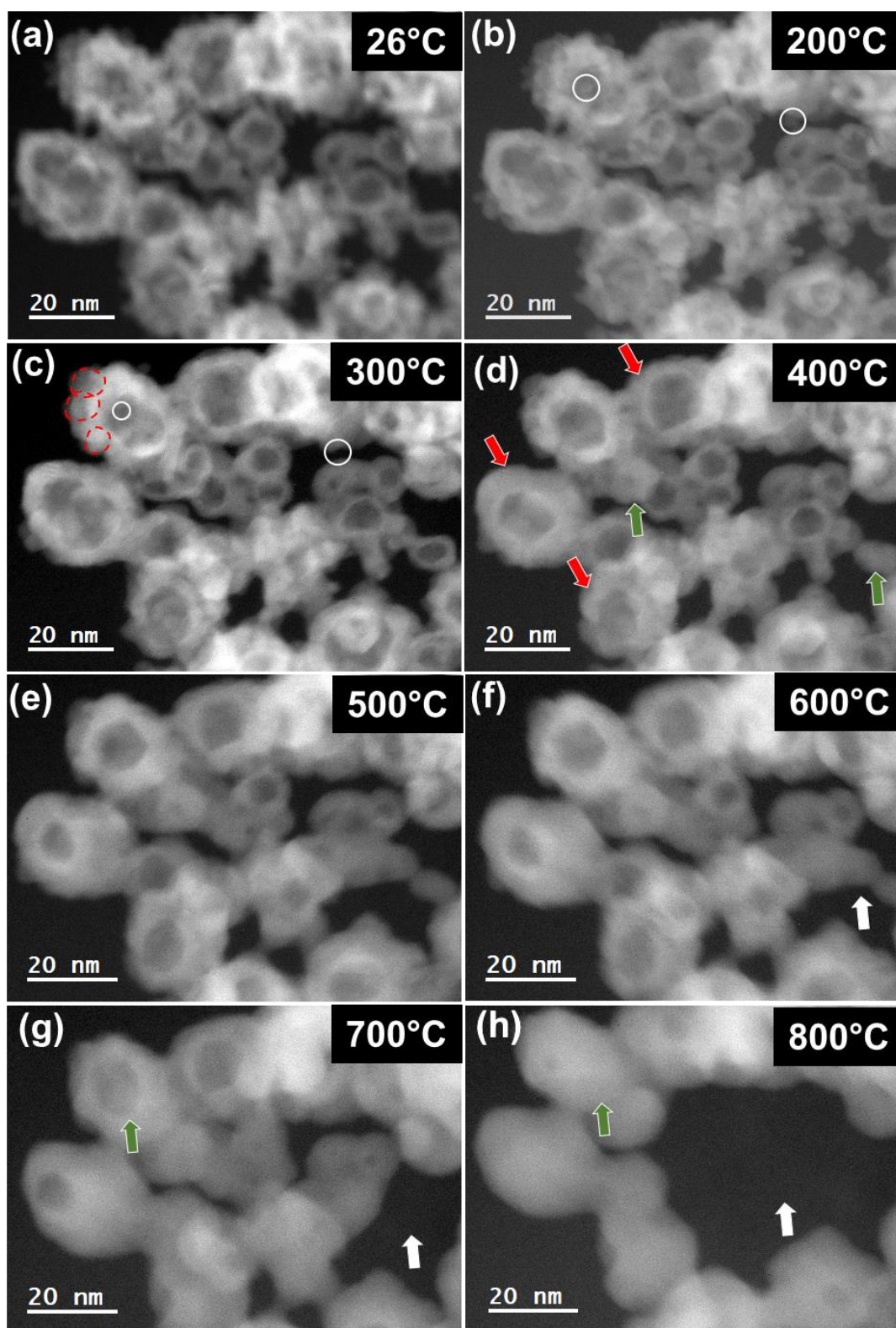


Figure 4.3: (a-h) STEM-HAADF micrographs showing the morphological evolution of Pt-1 HNS at different temperatures from 26°C to 800 °C. The grown NPs forming the shell are indicated by the red lines, the formed continuous shell is indicated by the red arrows, the disappeared NPs forming the shell are indicated by the white circles and the collapse of HNS is indicated by green arrows.

Going up to 400°C, *the nanospheres with a discontinuous shell* transform into a continuous shell configuration (indicated by red arrows in Figure 4.3(d)). Simultaneously, the central void of the *smooth shell nanospheres* is deteriorated (indicated by green arrows in Figure 4.3(d)). At 500°C, the majority of the latter collapse, and simultaneously, the central void diameter of the other nanospheres category starts decreasing, as depicted in Figure 4.3(e). Figures 4.3(f) and 4.3(g) reveal the migration and coalescence phenomena of the collapsed *nanospheres with a smooth shell* with their neighboring nanospheres, indicated by white arrows.

The total collapse of the hollow structure of the system took place at 800°C (Figure 4.3(h)). This critical temperature is higher than the collapse temperature determined through the previously made TEM observations. This discrepancy in temperature that induces the collapse of the Pt-1 HNS raises questions about the uniformity of temperature throughout the sample. Achieving a uniform temperature distribution across the entire sample is crucial for accurate and representative observations. The most important drawback of the furnace-type heating holder is the presence of variations in temperature across the sample specially since the displayed temperature is the one measured at the edge of the grid rather than its center. With this heating technology, the temperatures triggering each morphological modification cannot be accurately identified. The sample drift and lack of an accurate and controlled heating rate are additional challenges encountered using this thermal treatment.

A different in-situ object holder (Protochips®) is used for an accurate heating rate, temperature homogeneity across the sample due to the heating membrane technique and a stationary stable sample during imaging. All of this is achieved by the MEMS technology (see Chapter II for details). The MEMS-type holder is used for conducting principally in-situ gas experiments. Using the same system for the vacuum environment experiments aims to eliminate any potential influence of the supporting membrane (SiN_x for the MEMS-type holder and the Carbon film for the furnace-type holder) on the catalyst system behavior. It facilitates a direct comparison of Pt-based HNS behavior under the different environments with the same experiment conditions.

1.1.2. In situ STEM using the MEMS-type holder

In order to achieve the TEM vacuum inside the E-cell, the membrane of its small chip is completely destroyed. The thermal treatment involves a precise heating rate of 0.4°C/s with a

step of 20-50°C which is used in all experiments later. Smaller temperature increments are selected to refine the temperature range of NPs coalescence and the hollow structure collapse.

This choice helps also to explain the mechanisms governing the sintering of NPs as well as nanospheres collapsing. The temperature-time profile (Figure 4.4(a)) illustrates the exact temperature ramp throughout the in-situ heating experiment. Using the MEMS heating device, the sample drift is considerably reduced, allowing the fast acquisition of images during approximately 3 minutes for each chosen temperature. Series of STEM-HAADF images on the thermal treatment of Pt-1 HNS acquired at each temperature increment are presented in Figures 4.4(b) to 4.4(e).

At 120°C (Figure 4.4(b)), the particle's initial state is observed. This temperature is selected to facilitate the removal of surface contaminants while preserving the HNS morphology. Within this region, both categories of Pt-1 HNS are observed and both of their morphological evolution is monitored. Under a particular orientation, the 2D projection STEM-HAADF image reveals channels leading to the inner void of the hollow nanospheres, indicated by yellow arrows in Figure 4.4(b). The temperature at which these channels will maintain their integrity is identified.

Up to a temperature of 280°C, no modifications in the morphology of the nanospheres are observed, as illustrated in Figures 4.4(c)-4.4(i). The initiation of NPs growth is observed starting with 280°C (red lines in Figure 4.4(j)). The distributions of NPs at temperatures of 280°C and 300°C are depicted in **Figure 4.5**. The average size of the NPs grows from 2 nm to 4.5 nm and reached 6 nm, at 300°C. By heating up to 320°C, the transformation to a continuous shell, from a discontinuous one, becomes clear (indicated by red arrows in Figure 4.4(l)). Simultaneously, the collapse of the hollow structure within both Pt-1 categories initiates (indicated by green arrows in Figure 4.4(l)).

Even after the NPs' enlargement, the central void remains accessible, with the channel leading to it remaining unobstructed (indicated by yellow arrows in Figure 4.4(m)). Finally, the complete collapse of the hollow system structure is observed at 500°C (Figure 4.4(p)). The small-diameter nanospheres migration and coalescence with neighboring larger nanospheres is observed beyond 550°C (indicated by white arrows in Figures 4.4(q) and 4.4(r)).

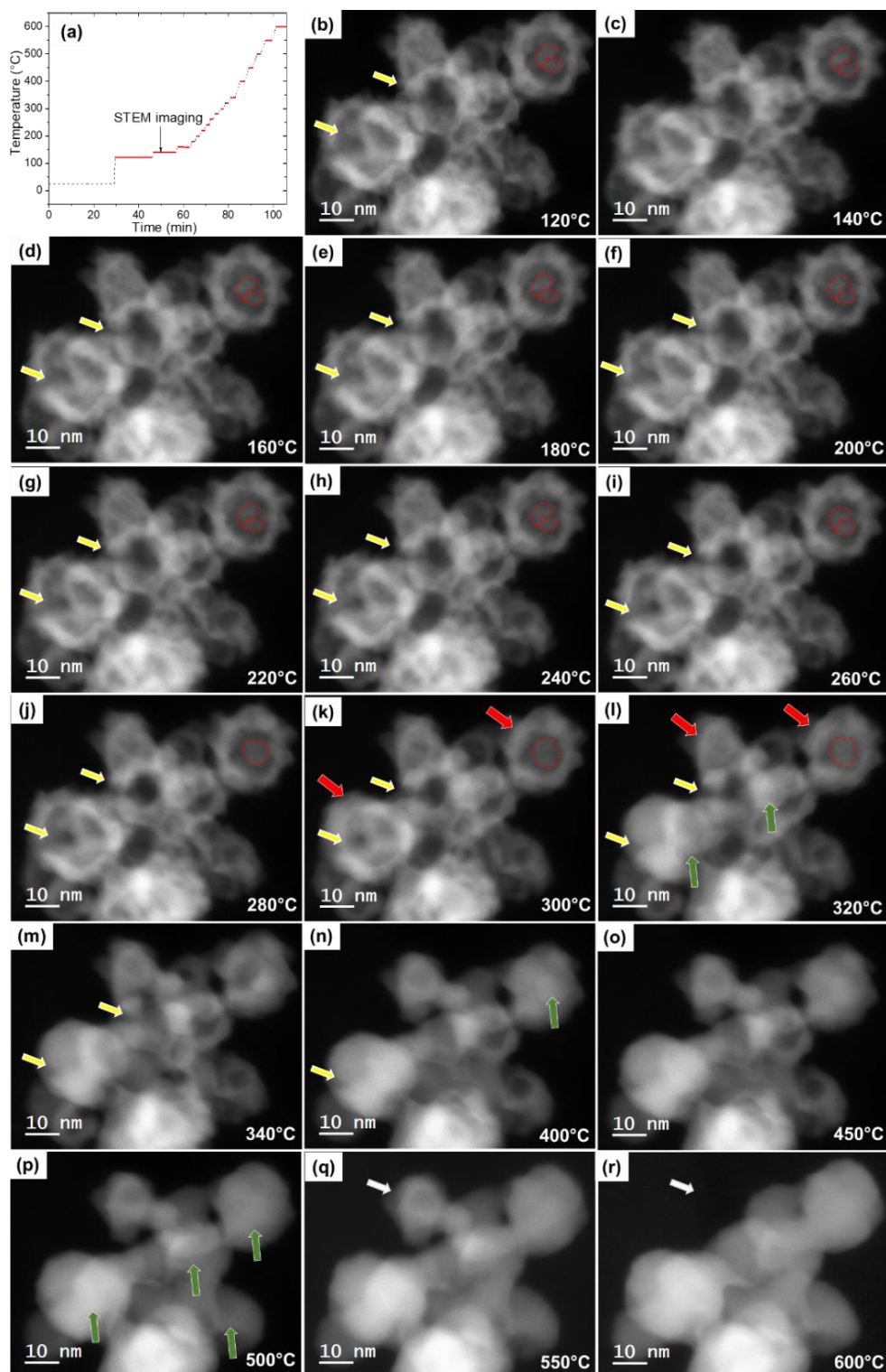


Figure 4.4: (a) Temperature-time profile of the in-situ heating experiment of Pt-1 HNS under the microscope vacuum using MEMS-type holder. (b-r) STEM-HAADF micrographs showing the morphological evolution of Pt-1 HNS during temperature ramping from 120°C to 600 °C. The grown NPs forming the shell are indicated by the red line, the channel leading to the HNS inner void are indicated by the yellow arrows, the continuous shell formed is indicated by the red arrows, the collapse of HNS is indicated by the green arrows and the nanospheres migration is indicated by the white arrows.

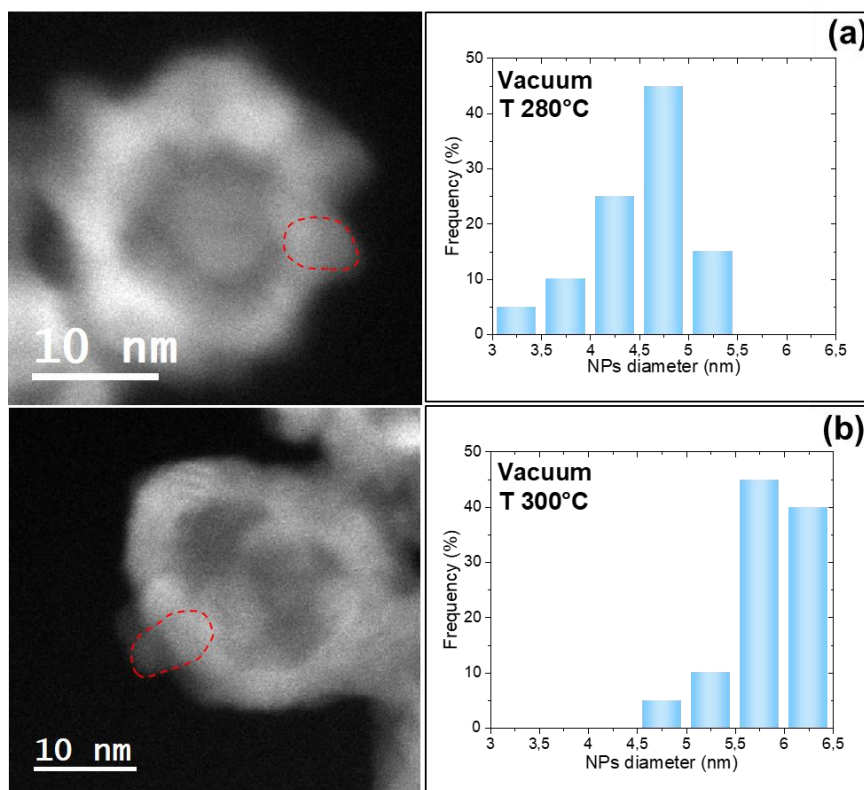


Figure 4.5: Histograms showing the NPs distribution of the Pt-1 HNS at (a) 280°C and (b) 300°C during their thermal annealing under the TEM vacuum. The grown NPs are indicated by the red lines.

– **Discussion: the impact of temperature alone on the behavior of Pt-1 HNS**

The thermal annealing of Pt-1 HNS under vacuum unveils two primary phenomena: the sintering of NPs composing the HNS shell and the structural transformation of the hollow microstructural configuration into solid nanoparticles.

To ascertain that the observed phenomena are not influenced by artifacts of the electron beam, the monitored regions during all experiments have been compared to other regions that are not exposed to electron beam previously. The HNS from both regions exhibit similar behaviors which indicates that the electron beam has no notable influence of the phenomena observed in this study.

Before delving into the mechanisms of the phenomena involved, it is noticed that the temperature triggering the growth of the NPs and the collapse of the hollow nanospheres are different in the thermal annealing experiments under vacuum using the two types of heating holders. When using the MEMS-type holder, these events happen at lower temperatures (280°C for growth and 500°C for collapse) compared to the furnace-type holder (300°C for growth and

800°C for collapse). These observations suggest that the temperature indicated by the furnace-type holder is higher than the actual temperature of the sample. It serves as an additional confirmation of the non-uniformity of temperature in the furnace-type holder as explained in the previous sections.

Going back to the sintering process and explained in details in Chapter I, NPs sintering can be attributed to two distinct mechanisms: the Ostwald ripening (OR) characterized by the migration of atomic species between stationary nanoparticles (Figure 4.6a), and the particle migration and coalescence (PMC) involving the migration and fusion of entire nanoparticles (Figure 4.6b).

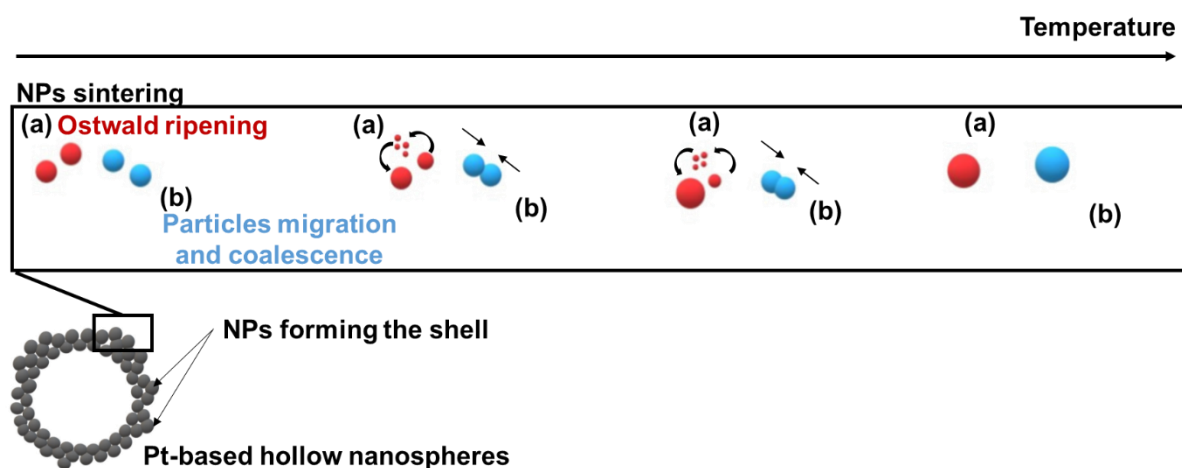


Figure 4.6: Schematic representation of the sintering mechanisms of NPs forming the HNS shell: (a) Ostwald ripening and (b) particle migration and coalescence.

Various methods have been employed to elucidate the mechanisms behind catalyst sintering. One of these approaches involves analyzing the observed particle size distributions (PSD) in the sintered catalysts. Granqvist and Buhrman [215] proposed that the process of PMC results in a log-normal size distribution with a prolonged tail towards larger particle sizes. Conversely, according to the so-called LSW model from Lifshitz and Slyozov [216] and Wagner [217], OR yields a distribution with a tail towards smaller particles and a cut-off in the size distribution, typically occurring at a particle diameter approximately 1.3-1.5 times the mean diameter [218]. Many published PSDs obtained from heterogeneous catalysts can be effectively modeled by a log-normal distribution. Also, it has been demonstrated that the shape of the particle size distributions is influenced by both the coarsening mechanism and the morphology of the

nanoparticles [219]. Therefore, the ability to conclusively determine the underlying mechanisms using this approach is debatable [220].

The in-situ TEM approach employed in this study enabled the determination of the sintering mechanisms of the Pt-based HNS by probing the dynamics of the NPs. Based on the STEM-HAADF micrographs captured with a gradual increase in temperature, no visible particle movement is evident at the level of the NPs composing the shell. On the one hand, an enlargement of specific interconnected nanoparticles due to their coalescence with neighboring NPs is observed. On the other hand, a disappearance of certain NPs without any observable mobility is identified. This observation implies that the latter sintering process is primarily driven by the OR mechanism.

Another phenomenon occurring is the collapse of the HNS. The crystal slip represents the initial stage in the process leading to structural collapse of the HNS. This phenomenon necessitates the presence of atoms having a strong kinetic energy to overcome the slip potential barrier, a threshold energy level essential for the transition of the crystalline system from one configuration to another along a specific crystal plane. [221] Numerous factors can influence the collapse process, including crystal vibrations, thermodynamic fluctuations, and kinetic motion. In this study, the thermal effect is the main factor inducing this collapse.

The restructuring kinetics presents a strong dependence on the diameter of the central void of the Pt-1 HNS. HNS with smaller central voids undergo collapse at lower temperatures in comparison to those with larger voids, as seen in Figure 4.4(1). This observation implies that the structural reconfiguration in HNS is primarily thermodynamically favored (reduction of total surface energy). However, this restructuring is constrained kinetically by the vacancies within the central void, which is inseparably tied to the size of the inner void [222]. A similar investigation was carried out on Pt-Ni hollow nanoparticles under various atmospheres, including vacuum. Accordingly, the collapse temperature turned out to be influenced by the inner void size of the hollow nanoparticles. [222]

Jiang et al. [221] examined the thermal stability of gold HNS with an FCC structure through molecular dynamics (MD) simulations and proposed three potential classifications for their configuration: “stable” if the initial configuration maintains its original shape without collapsing, “half-stable” if there is a partial collapse, yet the central cavity is partially maintained and “unstable” if the HNS undergoes a complete collapse, transforming into a solid

NP. Figure 4.7 provides a cross-sectional representation of the initial and final states of three distinct configurations. In line with the same model, another investigation is carried out to examine the thermal stability of Pt HNS and assess how the temperature ramp impacts their structural changes [223].

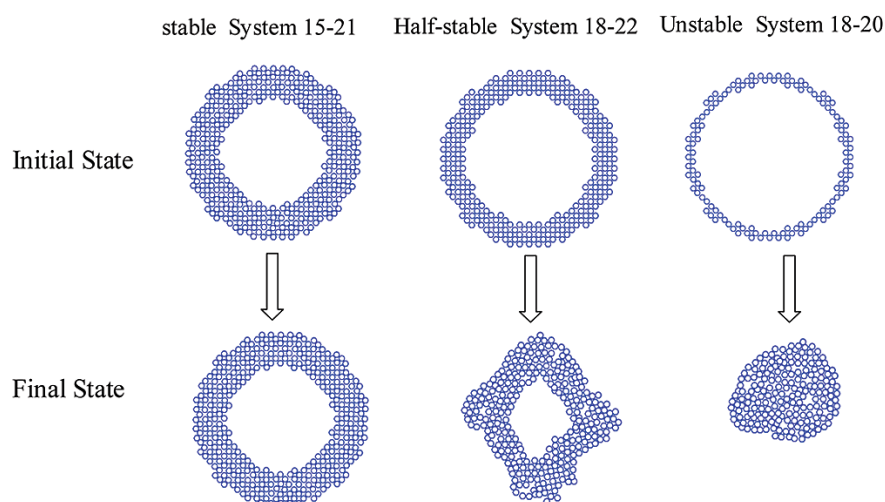


Figure 4.7: Cross-sectional representations showing the initial and final states of the stable model 15-21, unstable model 18-20, and half-stable model 18-22 of HNS.[221]

In our study and during the thermal annealing of the Pt-1 set under TEM vacuum, the HNS can only be classified as ‘unstable’ in their initial state, as the temperature increase leads to their complete isotropic collapse at 500°C and the hollow structure completely disappears. In the stable model, which is not observed here, there is no structural change when compared to the original configuration. In contrast, the half-stable model, while still retaining its hollow structure, experiences a significant reduction in its outer diameter. The final shapes exhibit irregular forms, even though the cross-sectional view may appear somewhat cubic, indicating that the collapse is not isotropic (Figure 4.7). These final configurations represent the global energy minimum achieved through heating. A similar thermal treatment process is applied to the second set of Pt-based hollow nanospheres: Pt-2 HNS. The objective of this study is to examine and compare the behavior of the Pt-2 HNS set with that of the first set when subjected to identical vacuum thermal treatment conditions.

1.2. Comparison of the thermal stability of the Pt-1 and Pt-2 systems

Using the MEMS-type holder with the STEM-HAADF imaging mode, in-situ heating experiment over Pt-2 HNS under the TEM vacuum is conducted under the very same

conditions. This experiment involves a controlled heating rate of $0.4^{\circ}\text{C}/\text{s}$, with temperature steps of 20 and 50°C . STEM-HAADF micrographs (Figure 4.8) showing the evolution of the Pt-2 HNS during thermal annealing are acquired at each temperature step. This approach is used for all experiments described in the subsequent sections.

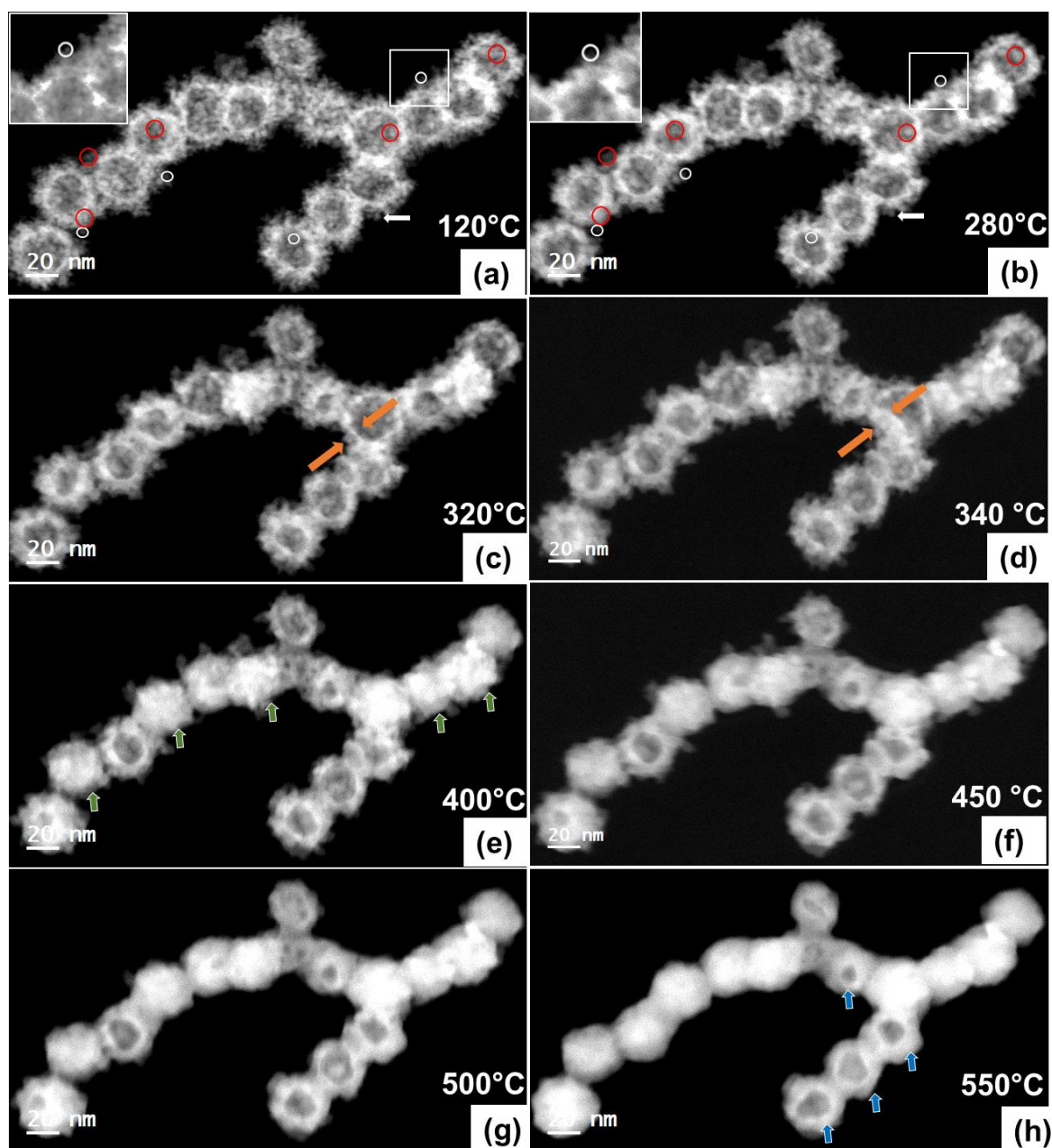


Figure 4.8: (a-h) Selected STEM-HAADF micrographs showing the morphological evolution of Pt-2 HNS during temperature ramping from 120°C to 550°C . The grown NPs forming the shell are indicated by the red circles, the shrunken NPs are indicated by the white circles with a zoomed area as an inset, the mobile NPs are indicated by white arrows, the shell evolution is indicated by the orange arrows, the total collapse of HNS is indicated by the green arrows and the partial anisotropic collapse of HNS is indicated by the blue arrows.

Following the same procedure adapted in thermal treatment of Pt-1 material, the initial state of the HNS is acquired at 120°C where a representative image of a chain of Pt-2 HNS is shown. The NPs from the shell are clearly visible and distinguishable, as compared to the first batch of HNS. Similar to the behavior observed in Pt-1 HNS under the same conditions, Pt-2 HNS exhibit a stable morphology without significant alterations up to a temperature of 280°C. At this critical temperature point, notable changes occur, including the growth of certain NPs forming the shell (indicated by red circles in Figure 4.8(a) and 4.8(b)) and the disappearance of others (indicated by white circles in Figure 4.8(a) and 4.8(b)). An average NPs diameter of approximately 4.3 nm is measured at 280°C and of 5.7 nm at 300°C (NPs size distributions at 280°C and 300°C are depicted in **Figure 4.9**). The mobility of NPs at the shell's periphery has been confirmed by tracking the NPs marked with white arrows in Figure 4.8(a) and 4.8(b).

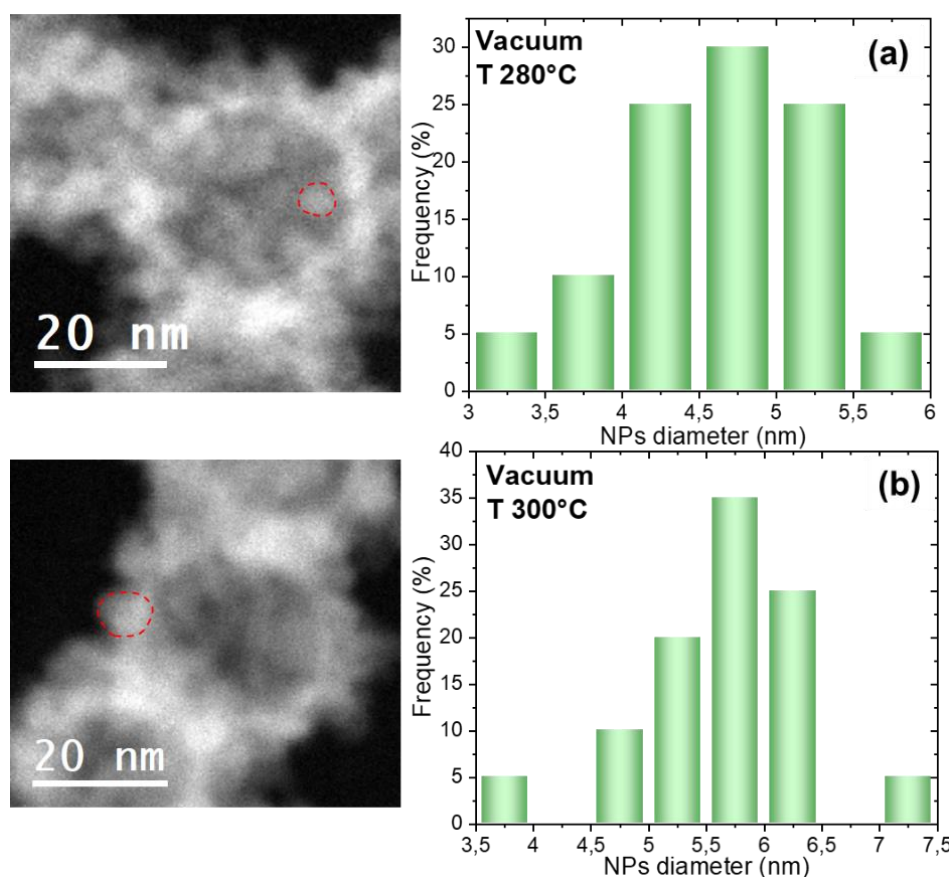


Figure 4.9: Histograms showing the NPs distribution of the Pt-2 HNS at (a) 280°C and (b) 300°C during their thermal annealing under the TEM vacuum.

Upon reaching 320°C, the shell of Pt-2 HNS maintains its discontinuous structure (Figure 4.8(c)), even with the growth of NPs within. The shell at this stage consists of larger NPs distributed randomly yet interconnected. The central void diameter of the HNS gradually

decreases versus an increase in the shell thickness indicated by the orange arrows in Figures 4.8 (c) and 4.8(d). As the temperature increases to 400°C, the hollow microstructure of Pt-2 HNS starts its collapse (indicted by green arrows in Figure 4.8(e)) while retaining a rough surface up to 450°C (Figure 4.8(f)). At 500°C, the surface becomes smoother (Figure 4.8(g)) and finally, the majority of the HNS totally collapse at 550°C (Figure 4.8(h)). Beyond this temperature, about 25% of the HNS of nanospheres preserve their hollow structure indicated by blue arrows in Figure 4.8(h).

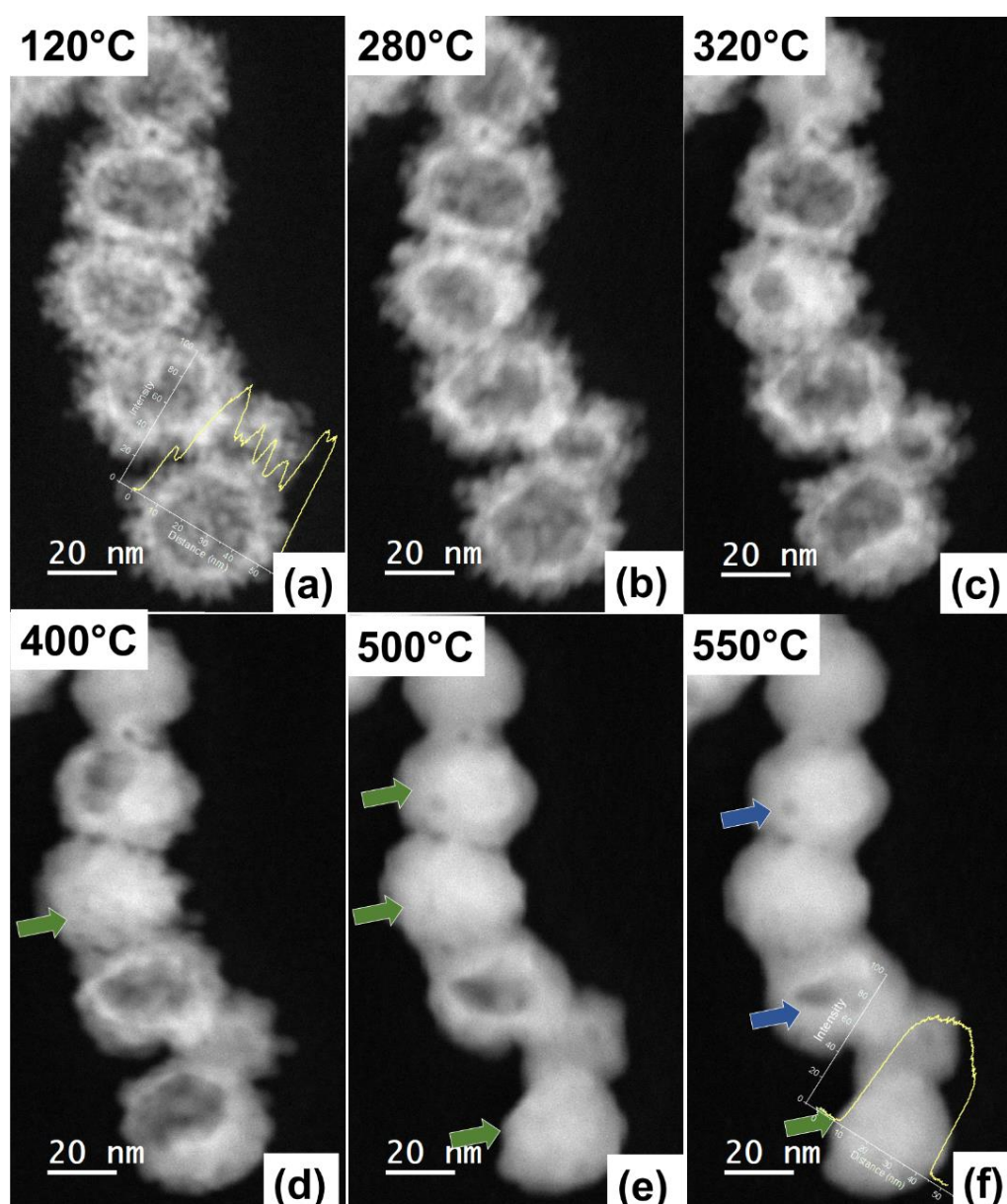


Figure 4.10: (a-f) Selected STEM-HAADF micrographs showing the morphological evolution of Pt-2 HNS during temperature ramping from 120°C to 550 °C. The total collapse of hollow nanospheres is indicated by the green arrows and their partial collapse by the blue arrows.

In order to ensure the uniform coverage of the behavior of the HNS, multiple regions are monitored. Figure 4.10 illustrates the behavior in a different region, which confirms the previously described patterns at 280°C, 320°C, 400°C, 500°C, and 550°C.

The collapse of the HNS (indicated by green arrows) dismisses the theory of the formation of a plate-like structure post collapse. By comparing the intensity profile of the hollow nanosphere in its initial state (Figure 4.10 (a)) and after its collapse (Figure 4.10 (f)), it becomes evident that a smaller solid nanospheres are obtained following the anisotropic collapse of the HNS inner void.

For further confirmation, the volume conservation of this hollow nanosphere undergoing collapse is validated by quantifying its initial and final volume as calculated from the 2D projections. The channels from the nanosphere shell are not considered for the volume calculation. The use of the fundamental formula for a hollow nanosphere volume ($V = \frac{4}{3}\pi(R_{outer}^3 - R_{inner}^3)$, where R_{outer} and R_{inner} are the outer and inner nanospheres radii, respectively) allows to calculate an initial volume of about $6100\pi (\pm 700\pi) \text{ nm}^3$ and a final volume of approximately $4500\pi (\pm 900\pi) \text{ nm}^3$.

The reduction in volume is likely due to measurement errors and the oversight of internal channels within the initial shell configuration, which, if considered, reduces the initial volume of the nanosphere.

– Discussion: differences in Pt-1 and Pt-2 responses to vacuum thermal treatment

Based on our in-situ STEM observations for the Pt-2 HNS set, NPs exhibiting mobility before undergoing coalescence and growth are observed. It is also common to observe immobile NPs with a simultaneous growth in size along with disappearance of others. This suggests that, excluding the diffusion of NPs toward their neighboring connected NPs, the sintering of NPs is probably governed by both OR and PMC mechanisms.

Given the complexity of the 3D HNS and since the OR process occurs rapidly, it is difficult to precisely monitor the shrinkage of such nanoscaled NPs. Hence, our best estimation is that these NPs have dissolved due to atomic migration, as no observable shifts in their positions occurred at the same temperature, unlike what is observed for similar NPs. This conclusion can be supported by previous studies that reported the occurrence of both Ostwald ripening and particle

migration/coalescence in Pt NPs supported on amorphous carbon under vacuum conditions [224].

Due to the comparable size of NPs in both sets of Pt-based HNS, it is reasonable to expect that they undergo sintering through the same mechanisms in a similar temperature range. The observation of the PMC process in some regions can be attributed to the larger number of NPs forming the shell and their more obvious distribution on the peripheric regions of the HNS. This is what makes them more visible when compared to the Pt-1 HNS.

The Pt-2 set presented two type of HNS. The ‘unstable’ and ‘half-stable’ HNS. The first category of HNS are the ones that transform directly to solid NPs in an isotropic manner (indicated by the green arrows in Figures 4.8 and 4.10). The second category are the ones that underwent a gradual degradation of their inner void diameter in an anisotropic way and maintained their cavity at 550°C (blue arrows in Figures 4.8 and 4.10). Jiang et al [221] have showed that in the case of half-stable HNS, the collapse initiates from the (111) crystal surface and subsequently extends gradually to other regions of the sphere.

The collapse phenomenon relies on both the slip barrier and the kinetic energy of the atoms. It occurs when the kinetic energy is sufficiently strong to overcome the slip barrier. Conversely, the collapse is stopped if the kinetic energy fails to surmount the elevated barrier.

In MD studies conducted by Jiang et al [221] and Reyes et al[223], the thermal stability of each type of HNS is studied using the thermal stability diagram. Each HNS is identified, with values for both shell thickness and outer diameter. Additionally, an aspect ratio (denoted as "p"), defined as the ratio of the outer radius (R) to the shell thickness (d), is determined for each HNS. With a constant aspect ratio, an increase in the shell thickness leads to a gradual increase in the HNS thermal stability, aligning with intuitive expectations that thicker shells contribute to greater system stability. When the slipping direction is perpendicular to the inner void surface, the slip potential barrier, as per the potential superposition theory, exhibits a nearly proportional relationship with the atomic layers. However, when slippage tends to occur along a slope, the presence of more atomic layers can hinder this process, resulting in anisotropic collapse. Consequently, an increase in wall thickness augments the slip potential barrier, impeding the collapse process and therefore enhancing the overall stability of the system. In this case, it is primarily because the wall thickness increased progressively as the collapse

progresses (decrease of the outer radius) which attributes a higher thermal stability for the half-stable HNS compared to the unstable ones.

The Pt-2 HNS exhibited a similar sintering behavior of NPs when compared to Pt-1 HNS. This similarity relies first on the sintering mechanism, which is governed by OR, occurring within the same temperature range for both sets. In addition, we are dealing with comparable morphologies of the shell and similar size of NPs composing it.

Several differences are however observed. A notable difference is the value of the temperature at which the formation of the continuous shell occurs. Pt-1 HNS exhibited this process at 320°C, whereas Pt-2 HNS showed it at 400°C. This divergence can be attributed to the higher number of NPs involved in forming the shell of Pt-2 HNS and the presence of a bigger number of larger-diameter channels within it. These factors trigger a higher temperature for shell diffusion. Another contrast is observed in the temperature at which collapse occurred. Pt-1 HNS exhibited collapse at 500°C, whereas Pt-2 HNS experienced it at 550°C. This difference can be attributed to the larger outer diameter of Pt-2 HNS. The Pt-2 HNS possess a better thermal stability than the Pt-1 HNS thanks to its ability to retain a relatively active surface area by preserving its hollow microstructure at high temperatures.

In the next section, a thermal treatment of both sets of Pt-based HNS is conducted in a hydrogen (H₂) atmosphere. Pt nanoparticles play a crucial role in catalyzing hydrogenation and oxidation reactions [26], [225]. In numerous applications, a preliminary step involves reducing Pt in a hydrogen environment to activate it as a catalyst through surface oxide reduction. The catalyst's structure is influenced by the reduction temperature, which, in turn, affects its catalytic properties.

A systematic temperature ramp is conducted and the catalysts' morphological response to different levels of heat under a H₂ atmosphere is monitored. This experiment will provide insights into this Pt-based catalysts performance in hydrogenation reactions and other major applications for Pt-based nanocatalysts involving a H₂ atmosphere such as Proton-exchange membrane fuel cells (PEMFC) [226]. These findings can make important contribution for the optimization of the catalysts' properties to efficiently drive any of these reactions.

2. Morphological evolution of the Pt-based hollow nanospheres under hydrogen atmosphere

This experiment aims to provide insights into the reactivity of Pt-based catalysts in the presence of H_2 gas. The microstructural changes of both sets of HNS is assessed, and a comparison of their behavior under these conditions is established.

2.1. Thermal stability of Pt-1 hollow nanospheres

Figure 4.11 shows the STEM-HAADF images acquired at each step of the temperature ramping.

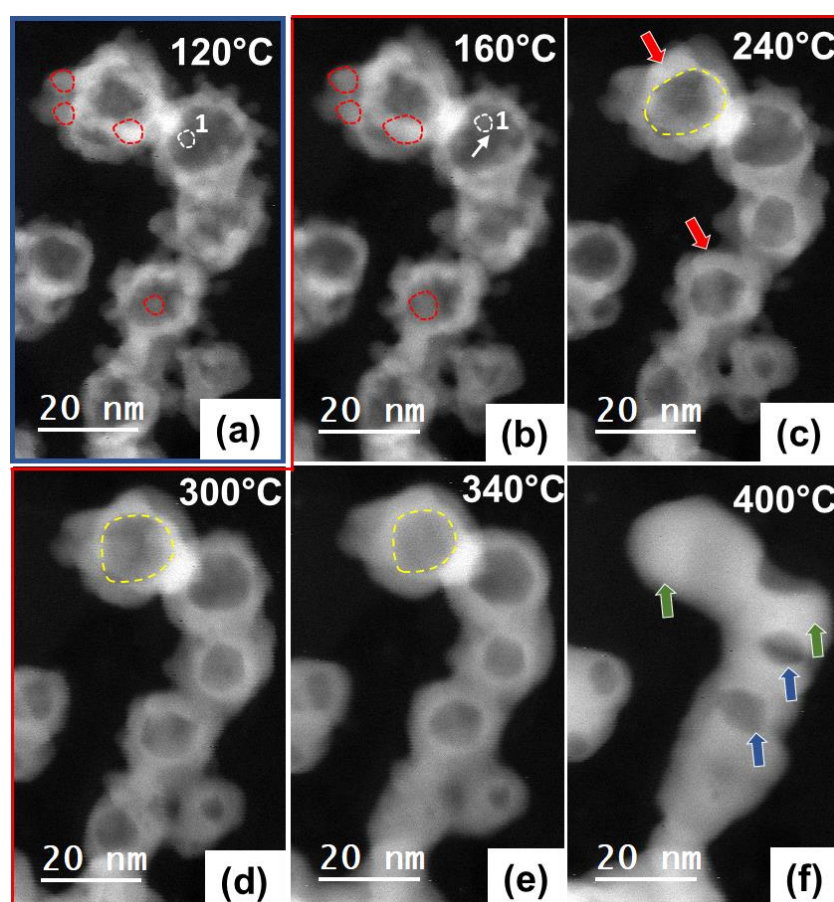


Figure 4.11: STEM-HAADF micrographs showing the morphological evolution of Pt-1 HNS during temperature ramping from 120°C to 400°C under a flow of H_2 gas. The grown NPs forming the shell are indicated by the red circles, the mobile NPs are indicated by white arrows, the continuous shell is indicated by the red arrows, the central void diameter evolution is indicated by the yellow lines, the isotropic collapse of HNS is indicated by the green arrows and the anisotropic collapse of HNS is indicated by blue arrows.

Starting with 160°C, the growth of NPs is observed, as indicated by the red circles in Figures 4.11(a) and 4.11(b). A statistical analysis determined an average NPs diameter of 4.4 nm and 5 nm at 160°C and 180°C, respectively (NPs size distribution illustrated in **Figure 4.12**). The NPs mobility is detected, as evidenced by the observation of particle 1 in Figures 4.11(a) and 4.11(b). At 240°C, there is a notable transformation of the HNS, as a continuous shell is formed instead of the previous discontinuous structure (red arrows in Figure 4.11(c)).

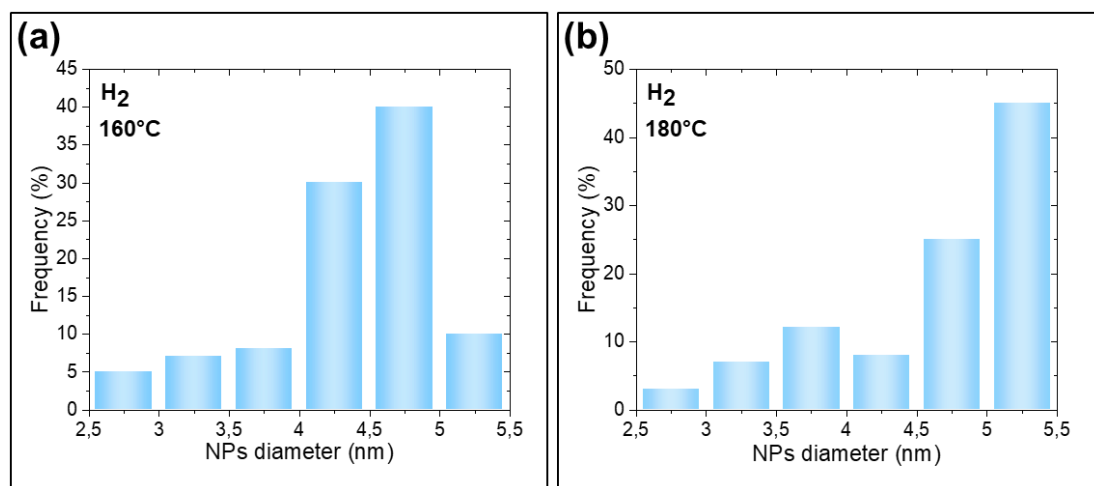


Figure 4.12: Histograms showing the NPs distribution of the Pt-1 HNS at (a) 160°C and (b) 180°C during their thermal annealing under H₂ atmosphere.

Starting at a 300°C, a gradual decrease in the size of the central void inside the HNS is observed (as depicted in Figures 4.11(c)-4.11(e)), with the diameter reducing from 15 nm to approximately 8 nm by the time it reaches 340°C. When the temperature reached 400°C, 80% of the HNS completely collapsed (as shown by the green arrows in Figure 4.11(f)), while the remaining structures retained their inner cavities following an anisotropic collapse, as indicated by the green arrows in Figure 4.11(f).

The behavior of an individual hollow nanosphere is tracked (Figure 4.13). This HNS showed a comparable pattern in the behavior of NPs, which is also observed in four other areas. The coalescence of adjacent connected NPs is marked by red lines. Additionally, a progressive decreasing of the central void diameter, initiated at 300°C as denoted by yellow lines. The complete collapse of the hollow structure occurred at 400°C.

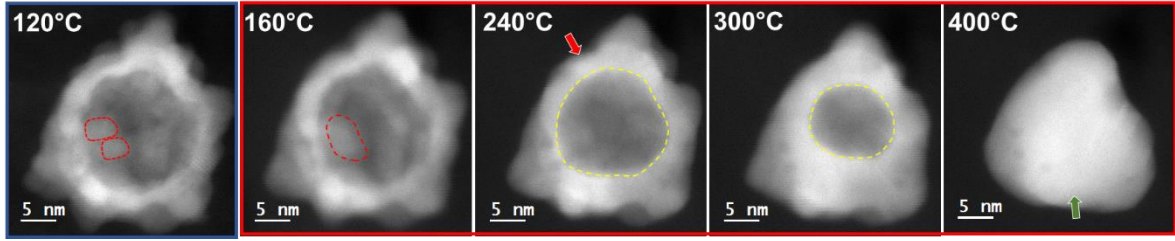


Figure 4.13: STEM-HAADF micrographs showing the morphological evolution of a single Pt-1 HNS during temperature ramping from 120°C to 400°C under a flow of H₂ gas. The grown NPs forming the shell are indicated by the red lines, the continuous shell is indicated by the red arrows, the central void diameter decreasing is indicated by the yellow lines and the collapse of hollow nanospheres is indicated by the green arrow.

These findings are a confirmation of the similar behavior exhibited by individual HNS and their agglomerated counterparts, particularly with respect to the continuous shell formation and the eventual collapse of their hollow structures.

– **Discussion: the impact of H₂ gas on Pt-1 HNS behavior upon thermal treatment**

These results demonstrate that the sintering process of Pt-based NPs is predominantly governed by the PMC mechanism when they are exposed to a H₂ environment. The OR mechanism does not appear to exert any significant influence in this setting. The direct comparison of NPs behavior during thermal treatment under vacuum and H₂ atmosphere supports these conclusions. The latter comparison reveals a lower temperature triggering the sintering of NPs under H₂ (160°C) than it is under vacuum (280°C) which is explained also by the H₂ influence on the surface atomic mobility of the NPs and self-diffusion. These observations also contrast with the sintering behavior of supported Pt NPs in an oxidizing environment, where OR exclusively dominates [227], [228].

Assuming the study of spherical non-wetting NPs migration, the particle diffusivity (D_p) is expressed as a function of the surface diffusion coefficient (D_s), the atom diameter (a) and the particle radius (R) [229].

$$D_p = 0.3D_s\left(\frac{a}{R}\right)^4 \quad [\text{Eq. 4.1}]$$

Using Eq. 4.1 and assuming isothermal conditions, the average migration X_p for the randomly distributed nanoparticles is expressed by the following equation:

$$X_p = \sqrt{4D_p t} = \frac{\sqrt{1.2D_s a^4 t}}{R^2} \quad [\text{Eq. 4.2}]$$

In the presence of H₂, there is an enhancement of the Pt atom surface self-diffusion [230]. This suggests that the presence of H₂ has promoted the particle migration by the increase in the value of D_s in Eq 4.2.

Dubau et al [222] have studied the impact of gaseous atmosphere on the restructuring kinetics in 15 nm Pt-Ni HNS. In this study, the collapse of the HNS occurs within a temperature range of 600°C to 700°C during thermal annealing under vacuum. In the presence of hydrogen or oxygen, Pt-Ni atoms rearrangement begins at 210°C and is completed with a temperature range of 280°C to 350°C. This phenomenon is attributed to the reduction in surface energy due to chemisorption and the enhanced mobility of Pt atoms in the presence of hydrogen or oxygen coverage.

As observed on Pt single atoms and clusters, the mobility of Pt surface atoms presents significantly increased rates in a hydrogen-rich environment [222]. Therefore, the presence of this gas during thermal annealing contributes to the enhancement of atomic kinetic energy enough for it to overcome the slip barrier. This phenomenon leads to the structural collapse of the Pt-1 HNS at lower temperature (400°C) than its collapse under vacuum (500°C). ‘Unstable’ HNS undergo a total isotropic collapse and ‘half-stable’ exhibit an anisotropic partial collapse.

In order to investigate the spatial distribution of both Pt and Co intensities within an individual hollow nanosphere in response to a H₂ atmosphere, an EDS analysis is conducted.

2.1.1. Spatial distribution of Pt and Co post H₂ assisted experiment in Pt-1 system

In Figure 4.14, the EDS profile across a single hollow nanosphere is presented. This experiment is conducted at 300°C before the HNS collapse. Individual spectra are collected as a line scan is performed across the outer diameter of the nanosphere, as shown in the inset of Figure 4.14.

The interfaces are indicated colored squares in the inset image of the nanosphere. The EDS profile reveals that Pt-rich regions are located at the HNS surface in the presence of H₂. Such, the Pt tends to migrate towards the inner and outer surface. These findings indicate that, when exposed to a reducing H₂ atmosphere, Pt segregates to the surface. Alayoglu et al. [231] have conducted a study involving TEM and X-ray photoelectron spectroscopy (XPS) analysis of PtCo bimetallic NPs under a H₂ atmosphere. In this reducing environment, a similar behavior is observed, with Pt atoms being segregated on the surface of the NPs. A similar trend is identified in the investigation of Pt-Ni HNS when exposed to a H₂ atmosphere during thermal

annealing, with a slight segregation of Pt atoms observed on both the surface and sublayers [222]. All of these studies are consistent our investigation.

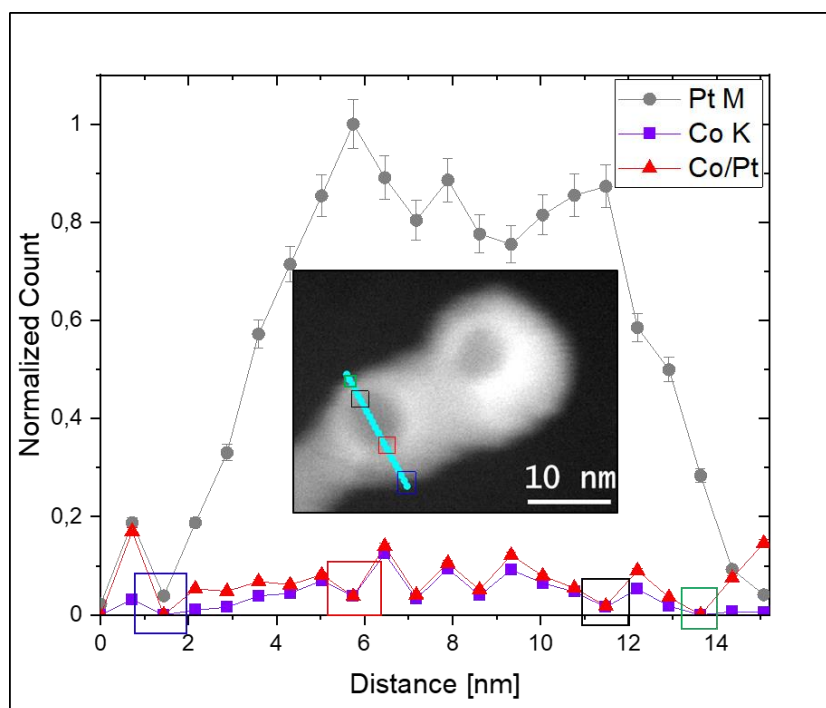


Figure 4.14: A representative EDS line profile showing the intensities of both Pt and Co across a solitary nanosphere. The red, black and blue squares correspond to Pt-rich regions in the nanosphere image as inset.

Previous research have also demonstrated that subjecting the Pt-Co system to H_2 or similar non-oxidative environments at elevated temperatures can facilitate the homogenization of Co and Pt, resulting in the creation of an intermetallic alloy solution [232]–[234]. When exposed to H_2 , the chemically reactive Co oxide is reduced and integrated into a mixed phase of both Pt and Co. In this case, the temperature at $300^\circ C$ is probably not high enough for Co oxides to be fully reduced and distributed homogeneously across the sample which is already mentioned in the literature [191].

2.2. Comparing the Pt-1 and Pt-2 system behavior under H_2 atmosphere

2.2.1. Thermal stability of Pt-2 hollow nanospheres

The behavior of Pt-2 HNS in a H_2 -rich environment is investigated using an experimental protocol identical to that applied for Pt-1 HNS. Representative STEM-HAADF images of the morphological evolution of Pt-2 HNS are presented in Figure 4.15.

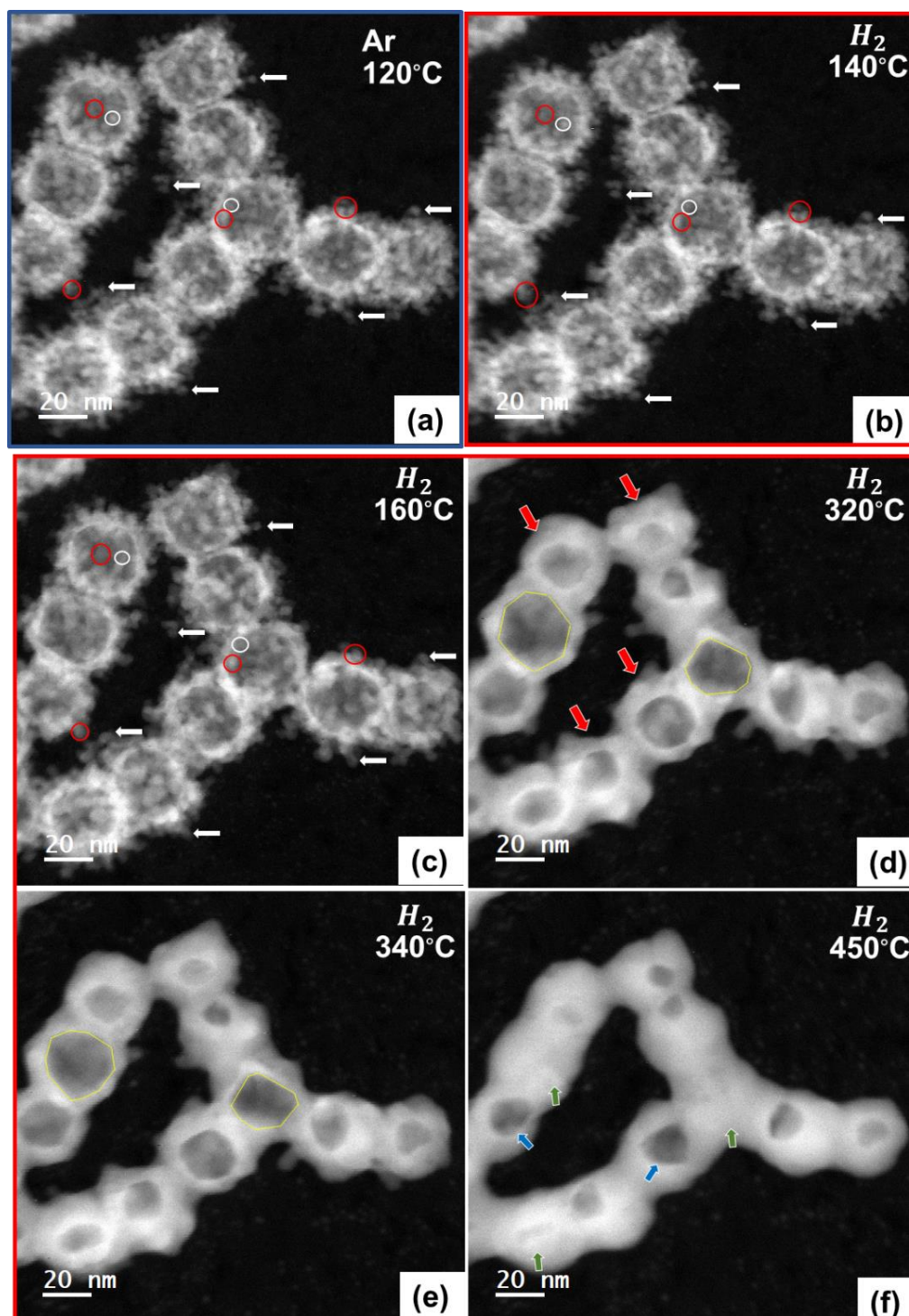


Figure 4.15: (a-f) Selected STEM-HAADF micrographs showing the morphological evolution of Pt-2 HNS during temperature ramping from 120°C to 450 °C under a flow of H₂ gas. The grown NPs forming the shell are indicated by the red circles, the disappeared NPs are indicated by the white circles, the mobile NPs are indicated by white arrows, the continuous shell is indicated by the red arrows, the inner shell facets are indicated by the yellow lines and the total and partial collapse of hollow nanospheres are indicated by the green and blue arrows, respectively.

A mobility of NPs is observed starting 160°C (as indicated by white arrows in Figure 4.15(a)-4.15(c)) preceding their growth. An infrequent reduction in size or disappearance of NPs have been observed, while adjacent others have grown (as indicated by white and red circles in Figures 4.15(a)-4.15(c), respectively). The average NPs diameter have growth from an average of 2 nm at 120°C to an average of 4.8 nm at 160°C reaching a diameter of 5.7 nm at 180°C (NPs size distribution in **Figure 4.16**). At 320°C, a transition to a continuous shell structure, marked by red arrows in Figure 4.15(d) is observed. Between 320°C and 340°C, facets became evident within the inner nanospheres surfaces nanospheres (indicated by yellow lines in Figures 4.15(d) and 4.15(e)). In this temperature range, the inner void diameter of the hollow nanospheres started to decrease while the shell thickness increased. At 450°C, about a half of the HNS totally collapsed while others maintained their inner cavity (indicated by green and blue arrows in Figure 4.15(f), respectively).

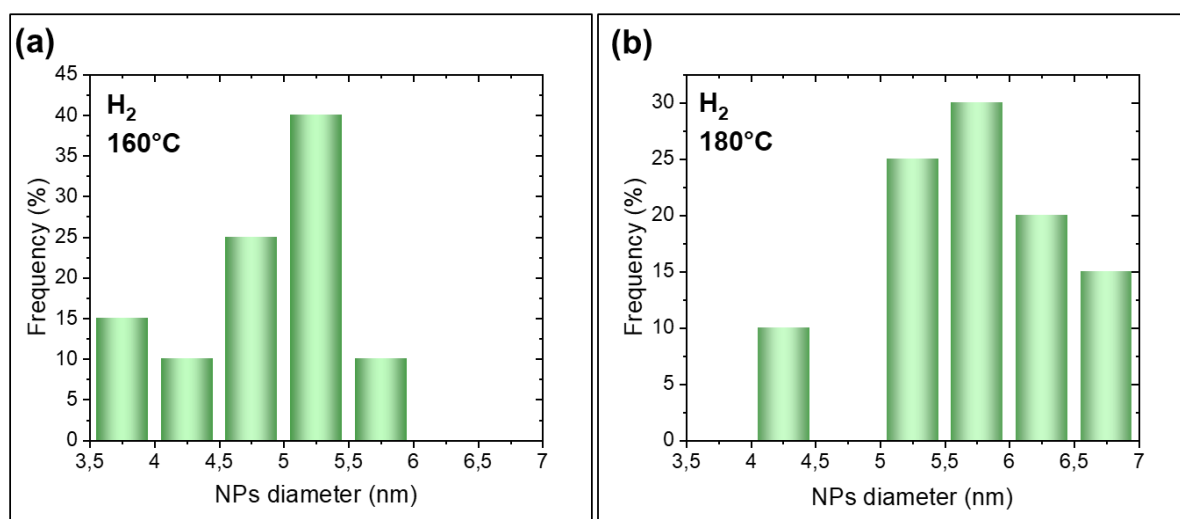


Figure 4.16: Histograms showing the NPs distribution of the Pt-2 HNS at (a) 160°C and (b) 180°C during their thermal annealing under H₂ atmosphere.

– **Discussion: differences in Pt-1 and Pt-2 responses to thermal treatment under H₂**

The observations made in this experiment suggest that the NPs sintering is strongly governed by the PMC mechanism. However, the OR process observed at early stages of heating cannot be ignored. Two temperature ranges can be identified. The first one is between 140°C and 160°C in which the OR mechanism governed the sintering of the NPs. The other one is for temperatures above 160°C where the sintering of NPs occurred following the PMC mechanism. This result is logical and consistent with the behavior of the NPs in the case of the Pt-1 HNS where a H₂ rich environment has favored the particles migration starting from 160°C. The

distribution of NPs across the Pt-1 shell prevented the clear observation of the NPs shrinkage implying the OR occurrence.

For the Pt-2 HNS, the NPs sintering process started at 160°C which is a lower temperature than the one that triggered the sintering of the NPs in vacuum (280°C). There are two types of HNS: unstable and partially stable nanospheres as deduced in section 1.1.2 in Chapter IV. The collapse of the unstable HNS occurred at lower temperature (450°C) than the one in thermal heating under the vacuum (550°C). This is due to the presence of H₂ gas that has enhanced the atomic mobility within the Pt-2 HNS, as also observed in Pt-1 HNS.

Compared to the Pt-1 behavior under the same conditions, the difference observed are similar to the vacuum case regarding the higher temperatures for the continuous shell formation and hollow microstructure collapse.

2.2.2. Spatial distribution of Pt and Co post H₂ assisted experiment in Pt-2 system

EDS analysis is conducted to determine the relative distribution of Pt and Co under the hydrogen atmosphere. The EDS elemental mapping is employed to investigate the spatial distribution of constituent elements within the Pt-2 HNS within one of its non-collapsed regions at 300°C. The Co K α line and Pt M α line are used for the construction of the EDS maps, along with the superposition of Pt and Co displayed in Figure 4.17(a).

When examining the EDS profile lines (Figure 4.17(b)) drawn across an individual HNS, a noticeable abundance of Pt is observed in the peripheral areas of the shell characterized by a Co/Pt ratio that is lower, while the ratio across the other regions of the hollow nanospheres is non-uniform. These findings imply the presence of a Pt-rich shell periphery, while in the remain of the HNS, Pt and Co are randomly distributed. So far, these observations are similar to those in the initial state of the Pt-2 HNS.

The EDS profile indicates the existence of two Pt-enriched regions on both inner and outer shell surface in a more obvious way that it is before the H₂ exposure. Co displays a more uniform distribution throughout the HNS. This observation confirms the hypothesis of Pt segregation at this surface, consistent with the findings observed in Pt-1 under an H₂ atmosphere and in accordance with prior literature on this subject.

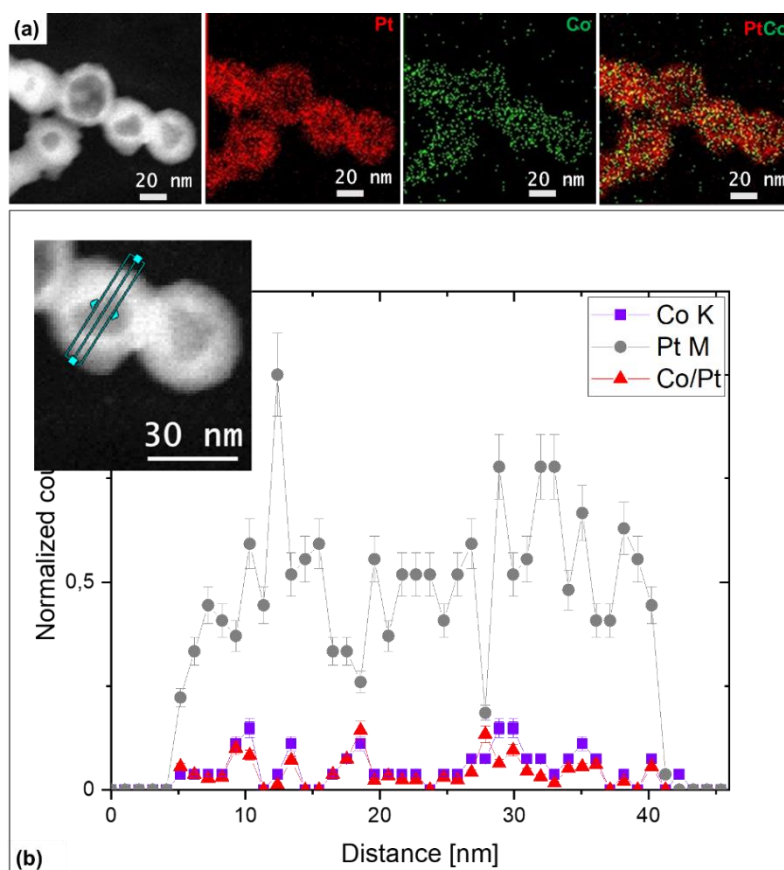


Figure 4.17: (a) EDS elemental maps of an assembly of a non-collapsed Pt-2 HNS under H₂ atmosphere showing the spatial distribution of both Pt and Co with their superposition. (b)(c) EDS line profiles associated to the Pt and Co intensities across single nanospheres.

Another EDS elemental mapping scan is conducted over a fully collapsed region of the Pt-2 system at 600°C. This scan served the dual purpose of assessing the spatial distribution of the constituent elements within the HNS and investigating the presence and distribution of carbon, oxygen, and the elements composition the E-cell membranes. Such analysis also validates the accuracy of the signals obtained through EDS. The Co K α line, Pt M α line, C K α and O K α are used for the construction of the EDS maps, along with the superposition of Pt and Co displayed in Figure 4.18. Pt and Co exhibit a uniform distribution across the entirety of the collapsed HNS assembly. Carbon is distributed across the membranes but more obviously over the collapsed Pt-2 HNS. This observation implies that there is electron beam inducing carbon contaminations on the sample. Oxygen is observed to be distributed within the particles and membrane in a uniform manner. The O signal is generated by two distinct sources: slightly from the presence of oxygen in the Pt-based HNS sample (in Cobalt oxide), and more significantly, from the windows of the E-cell, as the SiN_x windows inherently contain SiO₂ traces as stipulated by the previous studies [191].

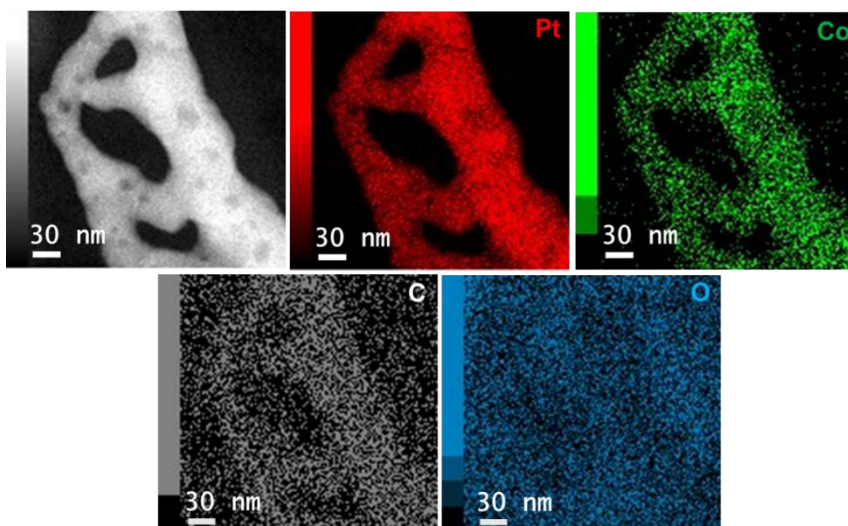


Figure 4.18: EDS elemental maps of an assembly of a collapsed Pt-2 HNS under H_2 atmosphere showing the spatial distribution of both Pt and Co with their superposition, of C, O, Si and N.

The homogeneity of Pt and Co distribution is further corroborated by an EDS profile associated with the Co and Pt signals presented in Figure 4.19. It demonstrates a constant Co/Pt ratio throughout the sample thermally heated under H_2 flow, affirming the homogeneous distribution of these two elements. The temperature of 600°C is high enough to fully reduce Co oxides which led to their redistribution due to hydrogen-induced diffusion processes [191].

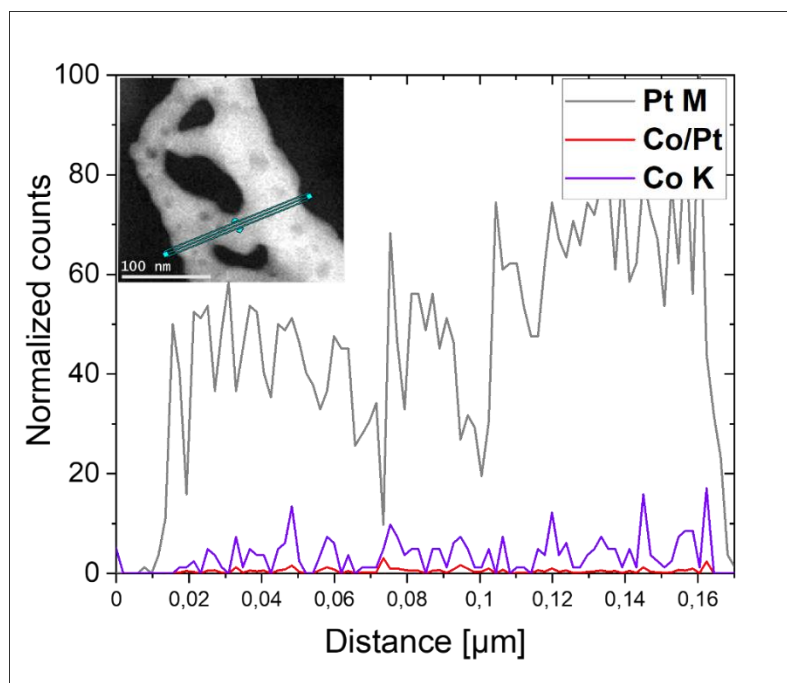


Figure 4.19: EDS line profiles across different collapsed regions showing a constant Co/Pt ratio across the sample.

In the next section, both sets of Pt-based HNS is investigated under the CO₂ hydrogenation reaction conditions of gas composition and pressure. Pt-based catalysts are not the most attractive for this application. However, prior research have demonstrated the selectivity of Pt-based systems towards formic acid and methanol when combined with appropriate support materials [58]–[65]. Therefore, this reaction serves as a model hydrogenation reaction chosen for catalyst analysis.

3. Investigation of the Pt-based HNS behavior upon CO₂ hydrogenation reaction

The analysis in this section will involve examining the microstructural changes occurring in both sets of Pt-based HNS during a thermal treatment process under the CO₂ hydrogenation reaction conditions. A similar methodology to the one previously employed in vacuum and hydrogen atmospheres is adapted. Simultaneously, using the RGA, an examination of the products generated during the CO₂ hydrogenation reaction is conducted to ascertain the specific reaction pathway taken under these conditions.

3.1. Morphological evolution of Pt-based hollow nanospheres during thermal annealing

3.1.1. Thermal stability of Pt-1 system

The objective of this study is to investigate the behavior of Pt-1 HNS during the CO₂ hydrogenation reaction. To do so, the initial state of the HNS is examined while they are exposed to Ar atmosphere at 120°C, consistent with the procedures employed in previous experiments. A gas mixture of CO₂ and H₂ is then dynamically flown inside the E-cell with a pressure of 1 bar and H₂/CO₂ ratio of 4 and a flow rate of 0.05 cm³/min. Following this, a controlled thermal treatment starting 120°C until 450°C is conducted, involving temperature increments of 20-50°C steps, in order to monitor the sintering process of this system under these specific reaction conditions. Similar to H₂ and vacuum experiments, STEM-HAADF images are acquired at each temperature to facilitate the observation and analysis of the morphological changes occurring in the Pt-1 HNS.

In Figure 4.20, only STEM-HAADF images depicting the morphological changes of Pt-1 HNS over time as a function of temperature are presented. Figure 4.20(a) illustrates the initial state of the two distinct HNS categories: one characterized by a rough and discontinuous shell, and

the other with a continuous shell as previously defined in chapter III. Figures 4.20(b) and 4.20(c) provide visual evidence of particle mobility before coalescence, indicated by white arrows. These images reveal the apparent shrinking of nanoparticles (denoted by white circles in Figures 4.20(a)-4.20(c)) and the growth of others, indicated by red circles starting 180°C. The transformation of the first category of HNS from a discontinuous to a continuous shell is observed to start at 260°C, as marked by red arrows in Figure 4.20(d). At this temperature, the facets of the inner shell become distinctly visible as indicated by yellow lines. At 300°C, the nanospheres characterized by small diameters and smooth shells collapsed. Finally, the hollow microstructure of the HNS is deteriorated at 450°C alongside with the coalescence of the collapsed small diameter nanospheres.

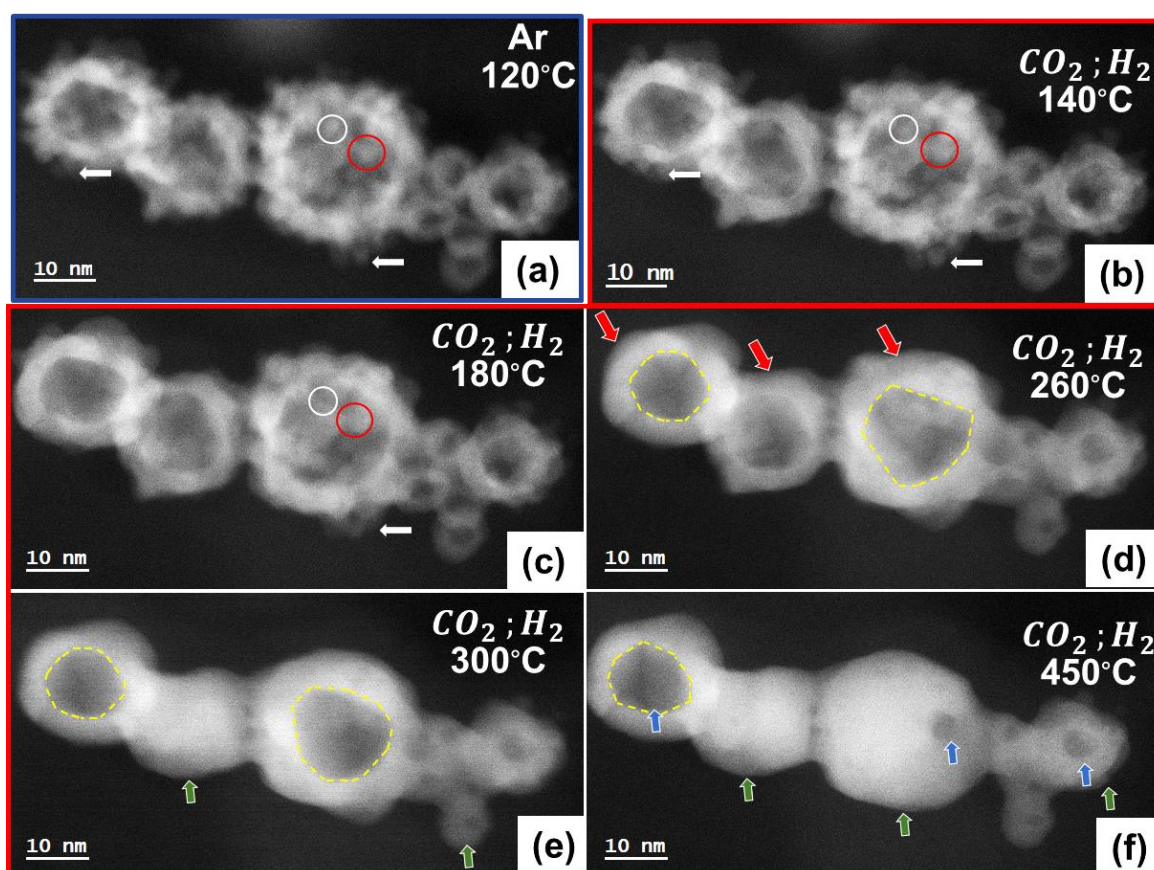


Figure 4.20: STEM-HAADF micrographs showing the morphological evolution of Pt-1 HNS during temperature ramping from 120°C to 450 °C under a flow of (CO₂:H₂) gas mixture. The grown NPs forming the shell are indicated by the red circles, the disappeared NPs are indicated by the white circles, the continuous shell is indicated by the red arrows, the inner shell facets are indicated by the yellow lines, the mobile NPs are indicated by the white arrows and the total and partial collapse of HNS indicated by the green and blue arrows, respectively.

By monitoring another region, we can confirm the homogeneity of the HNS behavior across the sample. Figure 4.21 shows the selected STEM-HAADF images. It presents the morphological changes in another region, which are monitored to validate the uniformity of NPs behavior across the sample. The reduction in size of particle 1 and 2 and their disappearance are clearly observed in Figure 4.21 (indicated by white circles). Simultaneously, evidence of NPs mobility followed by their coalescence is observed, as denoted by white arrows. Ultimately, the structural collapse of certain HNS occurs at 450°C, confirming the observations from the first Pt-1 HNS region. These findings suggest that the presence of 20% CO₂ has moderately favored the OR process while hindering the PMC process for isolated particles. Nonetheless, the coalescence of interconnected NPs remains a consistent phenomenon. Finally, the partial anisotropic collapse of a majority of the Pt-1 HNS allows for their categorization as 'half-stable.'

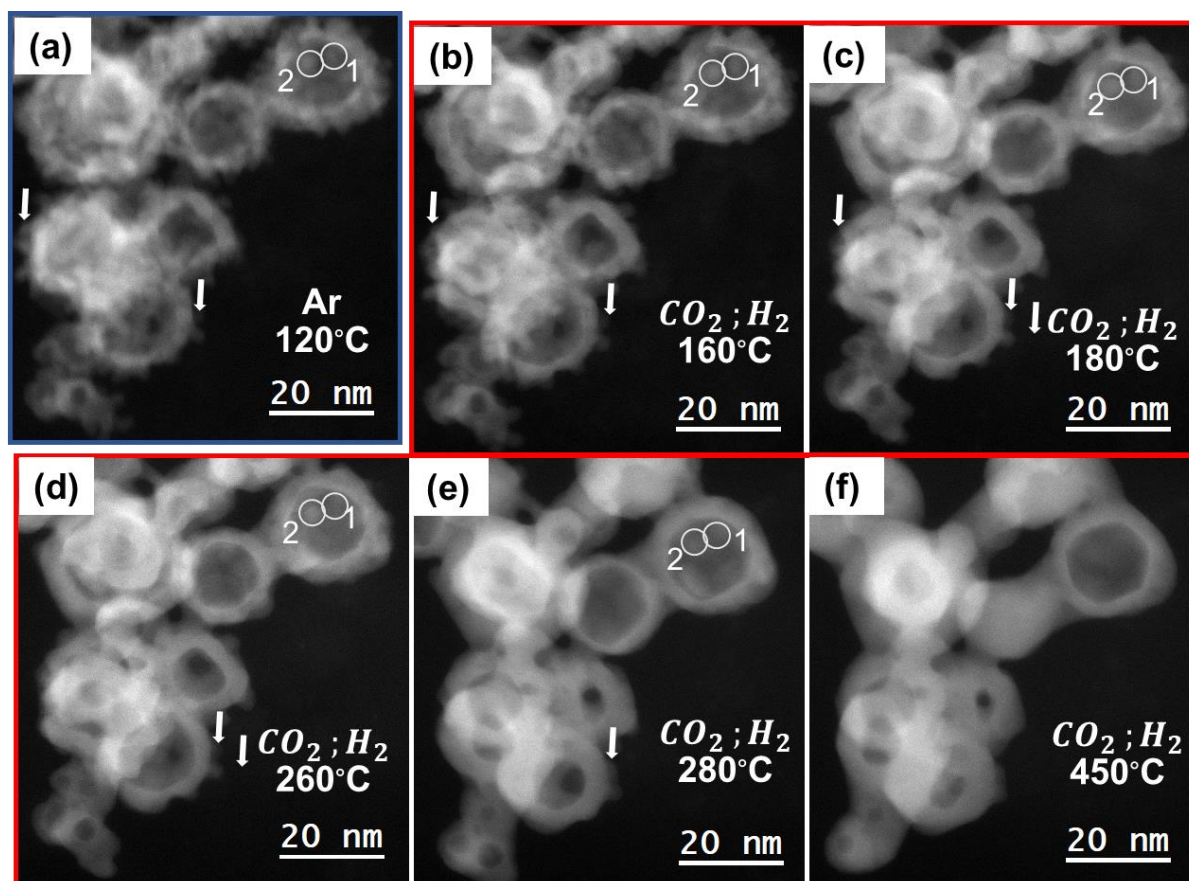


Figure 4.21: STEM-HAADF micrographs showing the morphological evolution of Pt-1 HNS at different temperatures from 120°C to 450 °C under a flow of (CO₂ - H₂) gas mixture. The sintering of NP 1 and 2 following the OR mechanism are indicated by the white circles and the mobility of peripheric NPs are indicated by the white arrows.

3.1.2. Thermal stability of Pt-2 system

Figure 4.22 illustrates the morphological evolution of Pt-2 HNS under the same conditions of CO_2 hydrogenation reaction as applied to the Pt-1 HNS batch. Initially, in Figure 4.22(a), the initial state of a chain of nanospheres under Ar at 120°C is presented.

As the temperature is raised, starting at 180°C , a prominent mobility of NPs is observed as indicated by the white arrows in Figure 4.22(a)-4.22(c). There is no proof of NPs shrinking or dissolution. In line with all our past observations for agglomerated NPs forming the shell, a fusion of these NPs with their adjacent neighboring NPs is observed. This phenomenon is noticeable at 180°C .

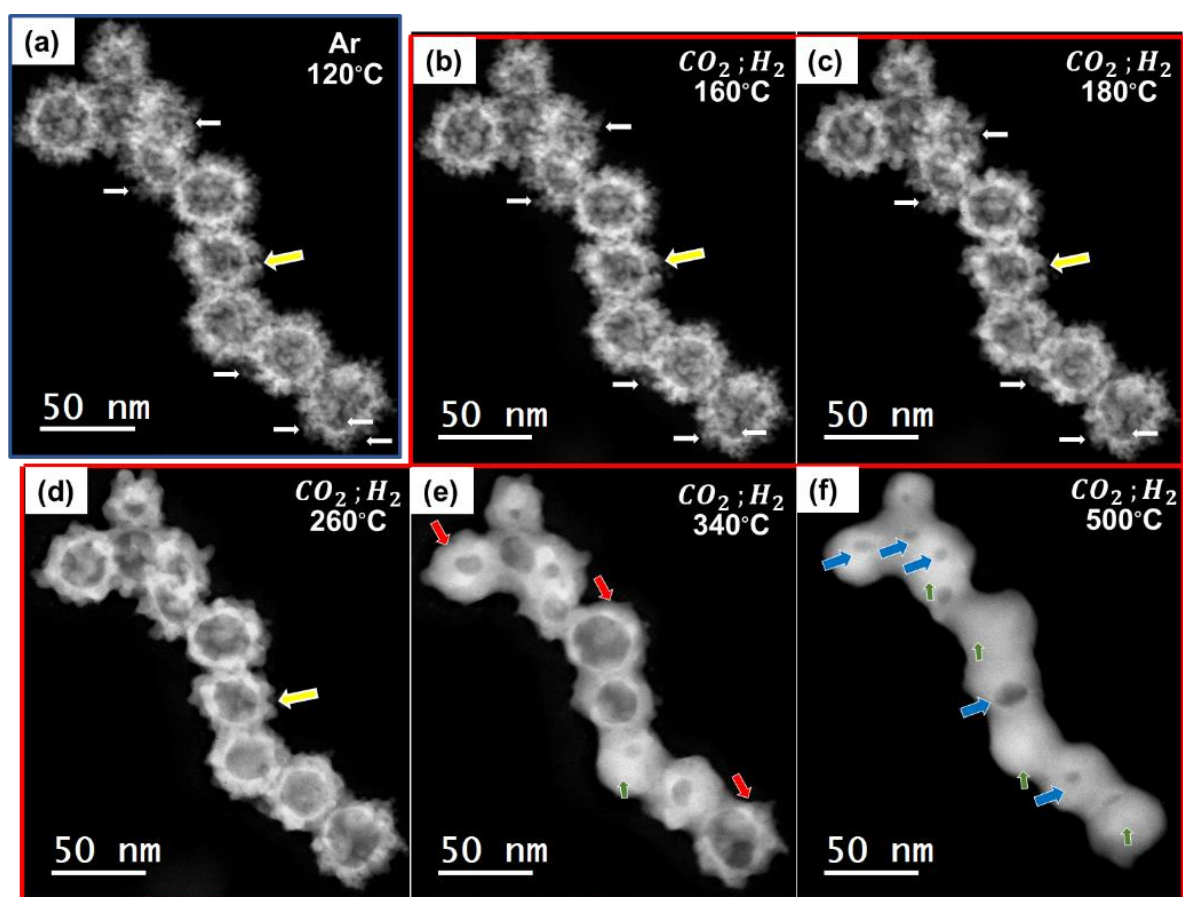


Figure 4.22: Selected STEM-HAADF micrographs showing the morphological evolution of Pt-2 HNS during temperature ramping from 120°C to 500°C under $(\text{CO}_2 - \text{H}_2)$ gas mixture. The continuous shell is indicated by the red arrows, the mobile NPs are indicated by the white arrows, the open channels are indicated by the yellow arrows, the total and partial collapse of HNS are indicated by the blue and green arrows, respectively.

The 2D projections of this assembly of nanospheres reveal the presence of open channels, as indicated by the yellow arrows in Figures 4.22(a) to 4.22 (d). These channels remain most probably accessible even at higher temperatures, up to 260°C. A continuous shell formation becomes prominent at 340°C, and eventually, at 500°C, we observe the complete and partial collapse of the hollow nanosphere structure.

Multiple regions are simultaneously examined to confirm the uniform behavior of the NPs. In Figure 4.23, the morphological changes of one nanosphere are presented as a function of temperature. Two separate NPs are identified in their initial state in Figure 4.23 (a). These NPs underwent a reduction in size as the temperature increased, starting at 180°C, as observed in Figures 4.23(b) and 4.23(c). Similar to features from the first region under investigation, a continuous shell formation occurred at 340°C (Figure 4.23(d)). A partial collapse of the hollow nanosphere configuration is observed at 500°C (indicated by blue arrows in Figure 4.23(e) and 4.23(f)).

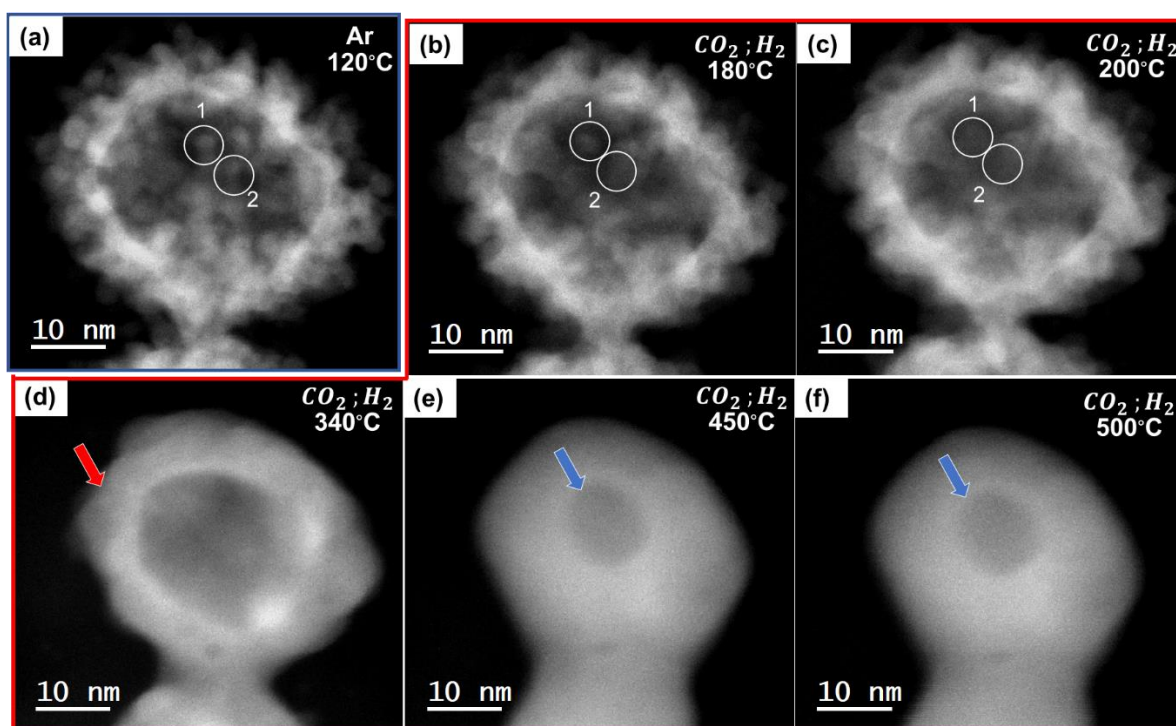


Figure 4.23: STEM-HAADF micrographs showing the morphological evolution of Pt-2 HNS during temperature ramping from 120°C to 500 °C under a flow of (CO₂; H₂) gas mixture. The NPs 1 and 2 shrinkage and disappearance are indicated by the white circles, the continuous shell is indicated by the red arrows and the partial anisotropic collapse of HNS is indicated by the blue arrows.

– **Discussion: the impact of H₂-CO₂ gas mixture on the Pt-based HNS behavior**

Similar to the Pt-1 HNS sets of samples, in the case of Pt-2 HNS, the presence of 20% CO₂ has slightly promoted the OR phenomenon. This can be explained by the fact that H₂ gas is highly reactive, and when it is diluted with 20% CO₂, its reactivity is reduced. As a result, its influence on the atoms mobility on the surface i.e. surface diffusion is also reduced.

The triggering temperature for NPs sintering for both sets of Pt-based HNS exposed to a CO₂ and H₂ gas mixture is found to be similar. Consistent with the observed trend under vacuum and H₂ atmospheres, continuous shell formation occurred at lower temperature (260°C) for the Pt-1 system than it is for the Pt-2 (340°C). This difference is attributed to the larger number and bigger diameter of channels in Pt-2. The collapse temperature for Pt-2, standing at 500°C under CO₂ and H₂ conditions, surpassed the 450°C collapse temperature of Pt-1 under the same circumstances. This discrepancy is attributed to the larger outer diameter of the Pt-2 set, as previously elucidated the previous studied atmospheres.

If the same reasoning is applied for both sets of Pt-based HNS, one may conclude that they exhibit a structural collapse that necessitates a higher energy level. More specific, a higher temperature is needed, in the presence of the CO₂ and H₂ gas mixture compared to pure H₂ environments. This explains the higher temperatures required for the hollow configuration collapse in Pt-1 (450°C in CO₂-H₂ vs. 400°C in H₂) and Pt-2 (500°C in CO₂-H₂ vs. 450°C in H₂).

Both sets of Pt-based HNS presented nanospheres categorized as 'half stable,' in accordance with the classification proposed by Jiang et al [221]. This classification is due to the anisotropic nature of the HNS collapse, while other 'unstable' HNS structures underwent a more rapid isotropic collapse, resulting in the formation of solid nanoparticles at the same temperature.

3.2. Identification of CO₂ hydrogenation pathway over the Pt-based hollow nanospheres

3.2.1. Blank experiment to test the RGA data reliability

Conducting a blank reaction with the RGA before probing catalytic reaction products is a practice to ensure the accuracy and reliability of data. By running the reactor under identical conditions of pressure and temperature but without reactants, a baseline measurement is

established, aiding in distinguishing genuine signal changes from background noise or system artifacts.

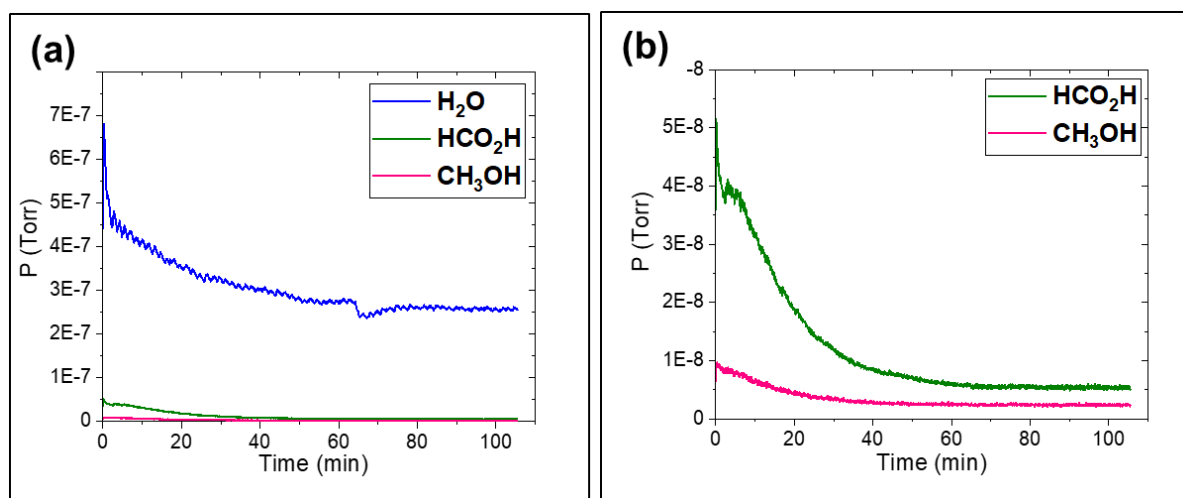


Figure 4.24: RGA spectra: Time-dependent monitoring of the partial pressure (PP) for products of the CO₂ hydrogenation reaction, including (a) water (H₂O), (b) formic acid (HCO₂H), and methanol (CH₃OH).

Figure 4.24 displays spectra from the RGA in its “pressure vs time” scan showing the partial pressure (PP) of the expected CO₂ hydrogenation reaction products as a function of time: water (H₂O), formic acid (HCO₂H) and methanol (CH₃OH). These spectra do not present any increase in the products for about 2 hours. In contrast, running the system with a flow of inert gas (Ar) for this time have caused the evacuation of the residual gases present in it (specially water) and therefore cleaning it. A decrease of the water PP is observed because, when the system is operated with a flow of inert gas (argon, Ar) during this period, it effectively removes any remaining gases, particularly water, thereby cleaning the system. This experiment indicates that any increase in one of these signals in the following experiments is a confirmation of the CO₂ hydrogenation occurrence in the presence of the Pt-based catalysts.

3.2.2. Identification of the reaction products and onset temperature over the Pt-1

In Chapter I (section 3.2), we highlighted the two main routes for the CO₂ hydrogenation process. The first pathway involves the production of a CO intermediate through the reverse-water-gas-shift (RWGS) reaction ($\text{CO}_2 + \text{H}_2 \rightarrow \text{CO} + \text{H}_2\text{O}$). This intermediate is then hydrogenated to produce CH₃OH, and we refer to this as the *CO-Hydro pathway*.

The second pathway centers around the formation of a formate (*HCOO) intermediate during CO_2 hydrogenation. This formate intermediate eventually leads to the production of CH_3OH through the breaking of the C-O bond, with involvement of $\text{*H}_2\text{CO}$ or $\text{*HCO}_2\text{H}$ intermediates. This pathway is termed the *Formate pathway*.

The RGA is a valuable tool for assessing relative changes in gas signals during experiments, but it is not suitable for precisely quantifying the absolute concentration of a particular gas species. Like other mass spectrometers, the RGA exhibits variations in ionization efficiency as gases enter its ionizer, often resulting in incomplete ionization. Given these inherent fluctuations in ionization, it's important to recognize that the RGA should not be employed as a quantitative measurement device, specially to determine the yield of the reaction.

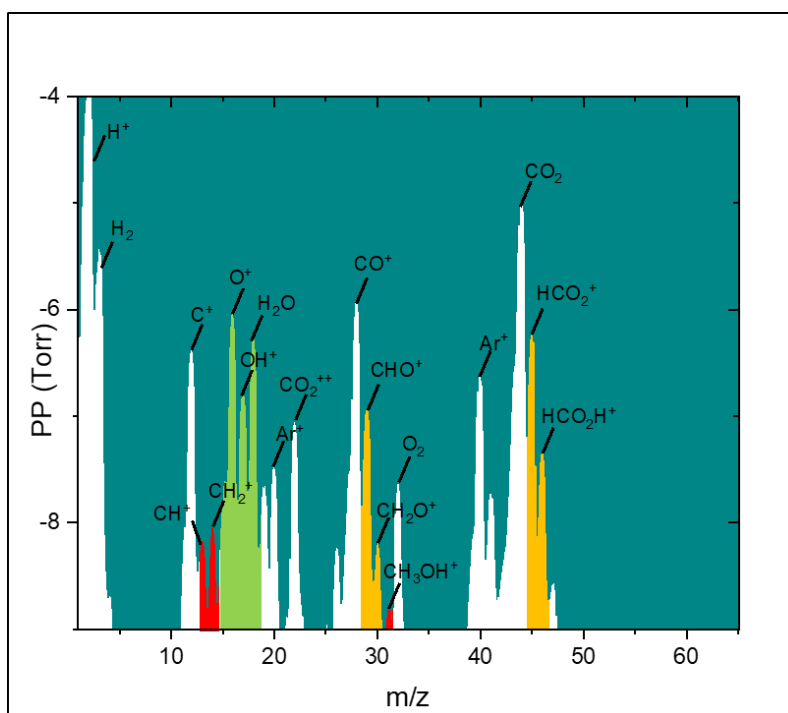


Figure 4.25: Analog spectrum of the gas at the cell's outlet, indicating peaks that correspond to the reaction products and their fragmentations (yellow for HCO_2H , green for H_2O and red for CH_3OH).

To investigate the CO_2 hydrogenation pathway in this research, an analytical scan is conducted to identify the reaction products, as shown in Figure 4.25. The resulting spectrum reveals discernible peaks corresponding to the reactants used CO_2 and H_2 along with their primary and secondary fragmentations. Additionally, it shows peaks corresponding to HCO_2H (highlighted in yellow), H_2O (highlighted in green), and CH_3OH (highlighted in red). These observations

eliminate the possibility of the RWGS reaction pathway and certify the occurrence of the CO₂ hydrogenation reaction through the formate pathway.

The reaction products analyses are conducted simultaneously while monitoring the morphological evolution of the Pt-based HNS.

In order to identify the reaction onset temperature for each product and try to correlate the morphological evolution of the catalysts to the reaction response, the RGA is operated in "Pressure vs time" mode. This method allows to track the increase of several key compounds partial pressure (PP), including carbon monoxide (CO), water (H₂O), formic acid (HCO₂H), and methanol (CH₃OH). Additionally, the potential formation of methane (CH₄) resulting from the CO₂ hydrogenation using an H₂/CO₂ ratio of 4 is explored. In this mode, specific mass-to-charge ratios (m/z) corresponding to the primary fragmentation peak of the chosen products are selectively monitored. Specifically, we focus on m/z 28 for CO, m/z 18 for H₂O, m/z 29 for HCO₂H, m/z 31 for CH₃OH, and m/z 16 for CH₄. In our monitoring efforts, we also track the reactants CO₂ and H₂. One notable observation in our experiments is that the partial pressure of H₂ increases significantly, by a factor of 100, while the PP of other gases experiences only slightly increases. This disparity arises due to the limited compression ratio of turbo pumps for lightweight gases.

Heavier gases tend to accumulate in the dead volume between the turbo pump exit and the isolation valve, benefiting from sufficient compression. However, the turbo pump lacks the necessary compression ratio to retain H₂ in this manner, leading to an increase in the partial pressure of H₂. To establish a reference point, the PP of CO₂ gas is used, and the PP of the reaction products are divided by the PP of CO₂ to assess their evolution over time.

Figure 4.26 displays the resulting RGA spectrum during the heating treatment of the Pt-1 HNS under atmospheric pressure and under the CO₂ and H₂ gas mixture. The corresponding morphological evolution of the Pt- HNS is presented in section 3.1.1 of Chapter IV. Figure 4.26(a) illustrates the variation in product PP for the anticipated CO₂ hydrogenation reaction products over time and across different temperatures, with data normalized to the CO₂ signal. Accordingly, one could expect an event at 180°C, the formation of the continuous shell and at 450°C which correspond to the HNs collapse.

Figure 4.26(b) displays the signals for CO and CH₄, both of which exhibited no noticeable increase in PP. In Figure 4.26(c), the signals corresponding to H₂O and HCO₂H are depicted, revealing a PP rise initiating at approximately 180°C ± 10°C (highlighted in red), signifying the onset temperature for this product's reaction.

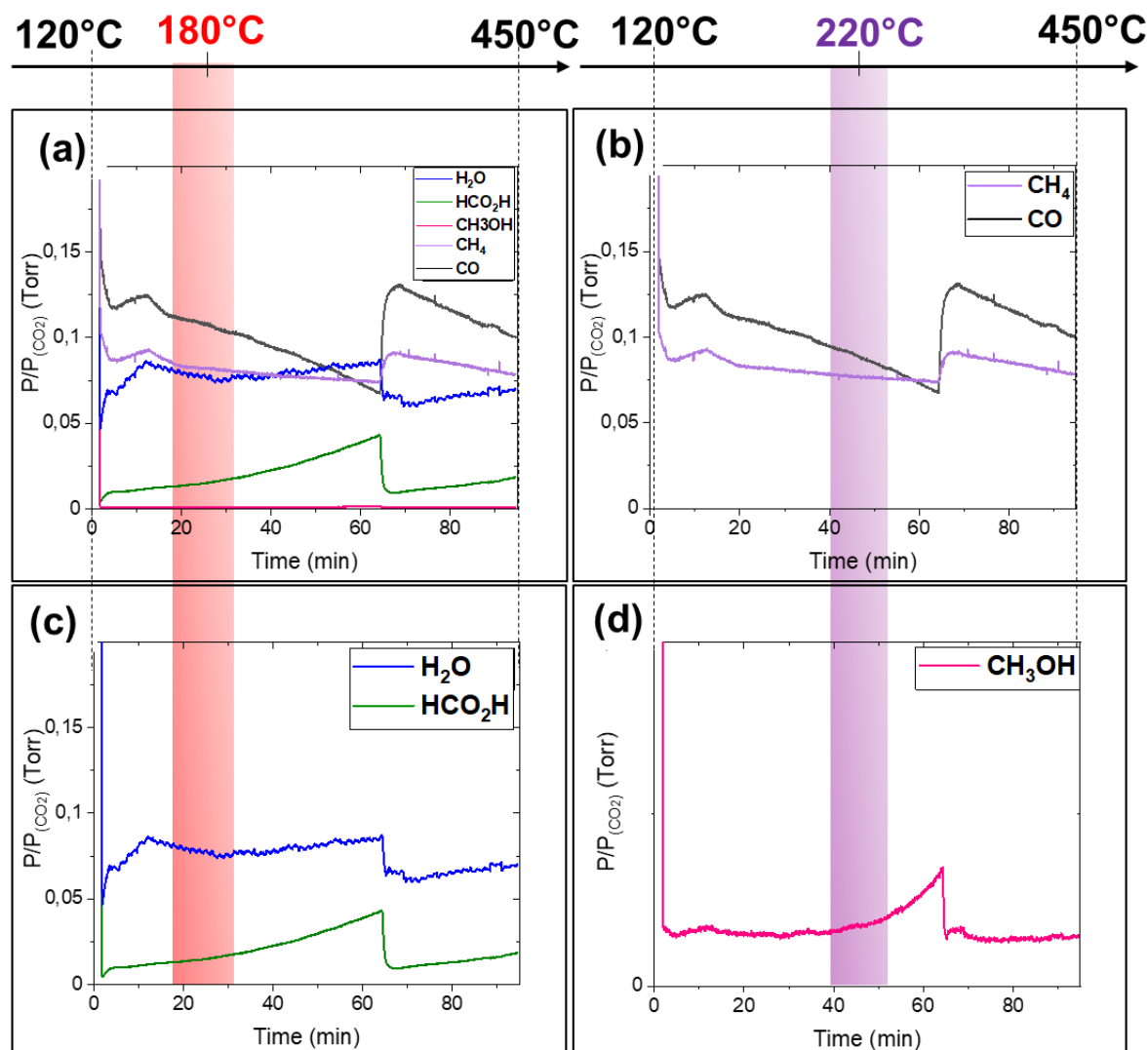


Figure 4.26: RGA Spectra illustrating the evolution of PP for (a) CO₂ hydrogenation reaction products over Pt-1 HNS as a function over time and temperature; (b) CO and CH₄; (c) HCO₂H and H₂O; and (d) CH₃OH. The initial rise of PP of both formic acid and methanol are highlighted by the red and purple columns, respectively indicating the onset reaction temperature for each product. The temperatures shown on the upper part are shared across the spectra presented below.

The water signal, a by-product of the CO₂ hydrogenation reaction, displayed a modest increase during the reaction. Lastly, Figure 4.26(d) exhibits the PP of methanol, showing an increase (parked by a purple arrow) starting at around 220°C ± 10°C (highlighted in purple), which serves as the reaction onset temperature for this particular product. The continuous increase in

reaction products dismisses the possibility of catalyst deactivation by CO surface poisoning (carbon monoxide CO poisoning is one the most common surface poisons for Pt catalysts [235], [236]).

When considering both the reaction rate and the fact that CO₂ is chemically inert, past research have proved that raising the reaction temperature above 200°C actually accelerates CO₂ activation and, consequently, the formation of methanol. [237] This validates the reaction onset temperature identified during this work.

In this case, the formation of *HCOO from *CO₂ and *H involves a series of steps that include both bonds breaking (specifically, C-Pt and H-Pt bonds) and bond formation (specifically, O-Pt and C-H bonds). Starting from the initial state of CO₂* and H* co-adsorption, an interaction occurs where H* is drawn towards the carbon atom of CO₂*, forming an *HCOO adduct. The co-adsorption energy (E_{ads}) for the combination of CO₂* and H* is -0.60 eV, which is lower than the adsorption energy of pure CO₂* (-0.52 eV). This suggests that the presence of the H* adatom stabilizes the adsorption of CO₂*, potentially enhancing its reactivity by spreading electrons around the adsorbed CO₂*. [238]

Subsequently, *HCOO undergoes hydrogenation, forming either *HCO₂H or *H₂COO. It is noteworthy that the reaction *HCOO + *H → *HCOOH + * is more favorable with a lower energy change (ΔE = 0.07 eV) and a lower activation energy (E_a = 0.95 eV) than the alternative reaction *HCOO + *H → *H₂COO + * (ΔE = 1.75 eV; E_a = 2.61 eV) [238].

Consequently, HCOOH* is generated when H* approaches the oxygen atom of HCOO*. Subsequently, the bond between carbon and oxygen in HCOOH* can be broken to produce HCO* and OH*, this dissociation step faces a high energy barrier. It's worth noting that the barrier for HCOOH* dissociation is higher than its desorption. This indicates that HCOOH* is released into the gas phase before undergoing dissociation.

Further hydrogenation of HCOOH* leads to the formation of *H₂COOH intermediates, which dissociate into *H₂CO and *OH. When *H₂CO is generated, it serves as a precursor for the production of *CH₃OH through continued hydrogenation. In qualitative terms, the conversion of CO₂ to CH₃OH through the formate pathway is limited by the hydrogenation of *HCOOH to *H₂COOH, as these processes are associated with high activation energies.

This clarifies the reason behind the significant increase in HCOOH PP signal when compared to the considerably modest signal of CH₃OH.

3.2.3. Identification of the reaction products and onset temperature over Pt-2

In order to determine the course of the CO₂ hydrogenation reaction, an RGA scan is conducted to track the PP pressure evolution of the main expected reaction products.

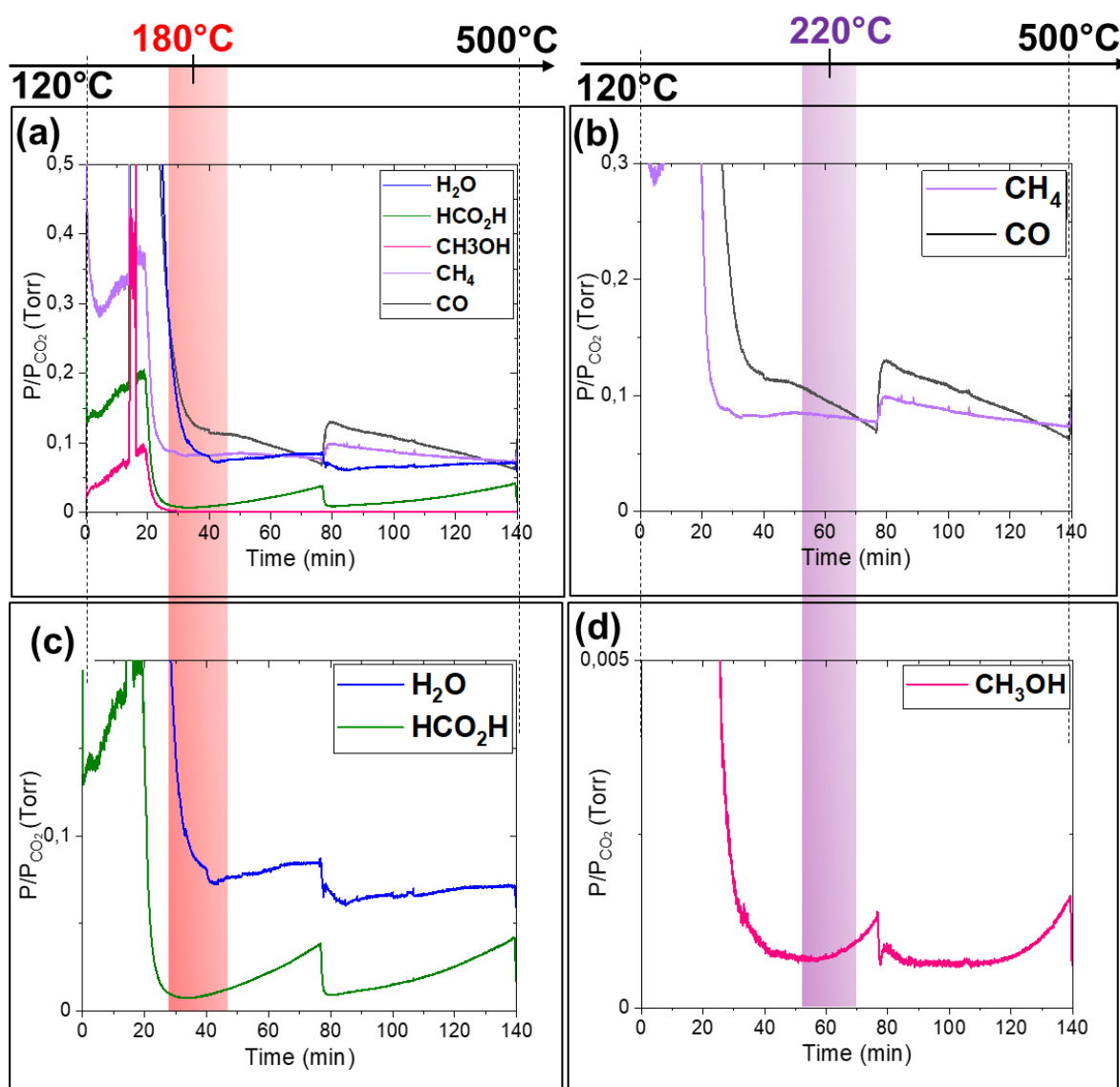


Figure 4.27: RGA Spectra illustrating the evolution of PP for (a) CO₂ hydrogenation reaction products over Pt-2 HNS as a function over time and temperature; (b) CO and CH₄; (c) HCO₂H and H₂O; and (d) CH₃OH. The initial rise of PP of both formic acid and methanol are highlighted by the red and purple columns, respectively indicating the onset reaction temperature for each product.

Figure 4.27(a) illustrates the PP of CO, CH₄, CH₃OH, HCO₂H and H₂O as functions of time and temperature. Similar to the procedure advanced for the Pt-1 HNS case, the temperature ramp has been manually added from the “Clarity” software (Protochips) recorded data. The resulting spectrum exhibits significant pressure fluctuations after 15-min period. These fluctuations are attributed to the evacuation of the initially inserted Ar gas from the experimental tank and the introduction of the reaction gas mixture CO₂ and H₂.

For a clear view of each product signal, Figure 4.27(b) focuses on the CO and CH₄ signals, both of which show no observable increases. In Figure 4.27(c), the signals for HCO₂H and water are displayed, demonstrating an increase in the HCO₂H signal at 180°C, similar to the water signal. Lastly, methanol PP exhibits an increase at 220°C (Figure 4.27(d)). These findings prove that the CO₂ hydrogenation over Pt-2 HNS catalysts followed the same pathway as observed with Pt-1 HNS, which is the formate pathway.

They also prove a similar reaction onset at 180°C for the formic acid (HCO₂H) and 220°C for methanol (CH₃OH). It's worth noting that the elevated CO signal can be attributed to the ionization of CO₂ into several fragmentations, with CO⁺ being a predominant fragment. The continuous rise in the reaction products PP throughout this process, including after the HNS particles collapse at elevated temperatures, eliminates the possibility of catalyst deactivation due to surface poisoning.

3.3. Study of the thermal stability of Pt-based catalysts during isothermal CO₂ hydrogenation reaction at 180°C

Isothermal reactions are conducted at the CO₂ hydrogenation reaction onset temperature (180°C) for each set of Pt-based HNS. The main goal of these experiments is to examine the system's thermal stability over an extended duration while isolating time as the variable of interest. The probability of surface poisoning deactivating the catalyst is also assessed.

3.3.1. Pt-1 hollow nanospheres

Following the same methodology as before, the Pt-1 HNS initial state is observed at 120°C under Ar. A flow of the CO₂ and H₂ gas mixture (H₂/CO₂ ratio of 4) is introduced into the E-cell with a flow rate of 0.05 cm³/min.

The system is then heated to 180°C with a relatively fast rate of 1°C/s and subjected to a 5-hour thermal treatment. STEM-HAADF images are collected at intervals of 10 to 20 minutes. Representative images illustrating the evolution of a single HNS over the course of 5 hours are presented in Figure 4.28(a).

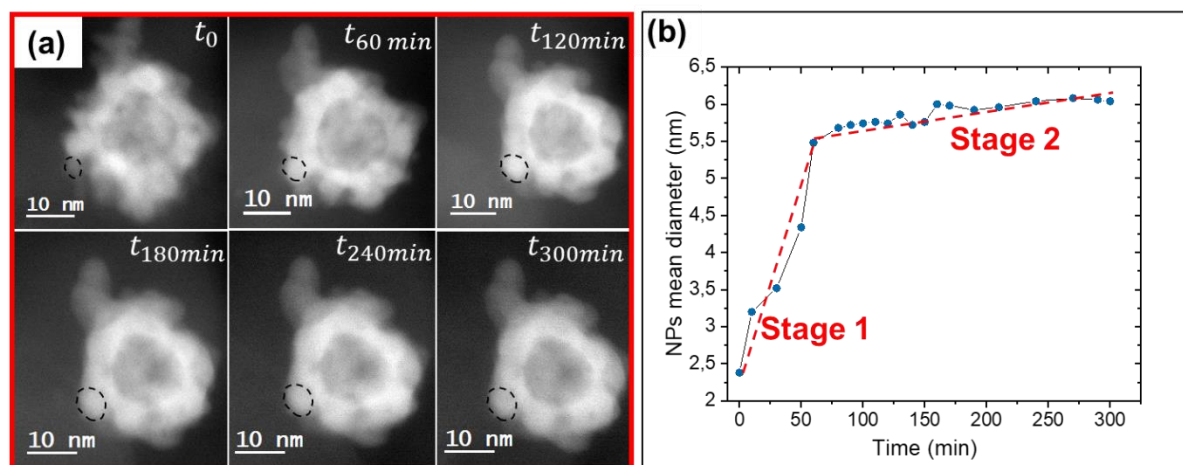


Figure 4.28: (a) STEM-HAADF images showing the morphological evolution of an individual Pt-1 HNS as a function of time at 60-minute intervals. The NPs grown are indicated by black lines. (b) Time-dependent plot of the average NP diameter comprising the Pt-1 HNS shell. The two growth stages are indicated by the red lines.

Using the total STEM-HAADF micrographs, the average diameter of the NPs is determined at each time interval. The NPs' diameters (as indicated by the black lines in figure 4.28(a)) are continuously monitored throughout this 5-hour duration and plotted as a function of time in Figure 4.28(b).

The NPs diameter exhibits a two-stages growth (indicated by red lines in Figure 4.28 (b)), starting from an average size of 2.5 nm and eventually reaching 6 nm. The first stage presents a rapid growth that is primarily attributed to the coalescence of neighboring NPs. It arises from the NPs coalescence, characterized by the addition of numerous atoms to the particles in a single step. This is in contrast to an Ostwald ripening mechanism, where the growth or shrinkage of individual particles is characterized by a more gradual and continuous net addition or loss of atoms, resulting in a smoother growth curve [227], [228], [239]. Following the rapid size increase, mild fluctuations in size are observed before a more stable and sustained particle morphology is formed and maintained throughout the remaining 5-hour thermal treatment period. Simultaneously, within this process, an examination of the products resulting from the CO₂ hydrogenation reaction is conducted using the RGA.

In Figure 4.29, the evolution of all three products (HCO_2H , CH_3OH , and H_2O) over the course of 5 hours is presented.

The observed fluctuations are previously explained in chapter II and are due to a safety measurement for the RGA: once a pressure threshold is attained, the system pumps down to protect the RGA filament. Knowing the origin of these fluctuations, the response of the reaction to the morphological changes in the catalyst is uniform in terms of the continuous increase in products PP. This response only suggests the absence of surface poisoning completely deactivating the catalyst.

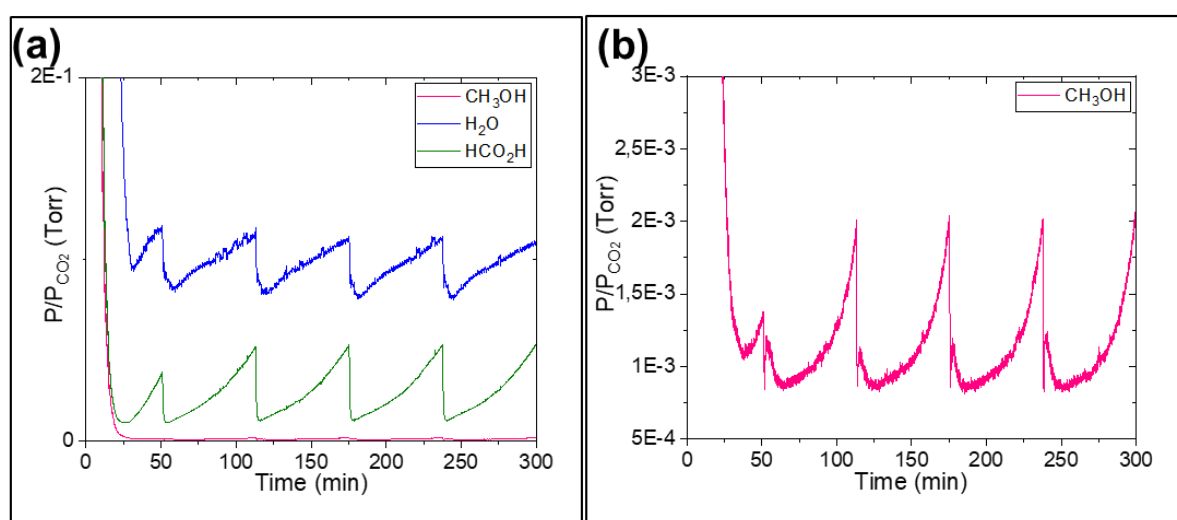


Figure 4.29: (a)(b) RGA Spectra illustrating the evolution of PP for CO_2 hydrogenation reaction products during 5 hours isothermal reaction at 180°C over Pt-1 HNS.

It is worth noting that the growth of particles influences the active surface area, which typically impacts the catalyst activity. However, given that the RGA is primarily utilized for qualitative analysis of the products, any smooth changes in reaction yield cannot be detected.

3.3.2. Pt-2 hollow nanospheres

Identical experimental conditions are employed for the isothermal CO_2 hydrogenation reaction at 180°C involving the Pt-2 HNS. The thermal annealing process in this context is conducted over a duration of 3 hours, during which micrographs and STEM-HAADF images are acquired at 20-minute intervals.

Figure 4.30(a) displays representative STEM images illustrating the morphological evolution observed in the Pt-2 HNS during this reaction. The measured NPs (indicated by black lines) mean diameter as a function of time is presented in Figure 4.30(b).

The Pt-2 HNS exhibit a comparable pattern in the evolution of their shell NPs size over time: a two-stages growth same as the Pt-1 NPs present. However, the NPs have exhibited an increase in diameter, growing from an initial average of 3.5 nm to approximately 5 nm. This diameter remains smaller than that of Pt-1 NPs, which are 6 nm in size. This variation in size can be attributed to the higher Co content within the Pt-1 NPs (with higher reactivity), which has acted as a growth-promoting factor. This Co content is approximately half of that found in the Pt-2 NPs, as detailed in Chapter III.

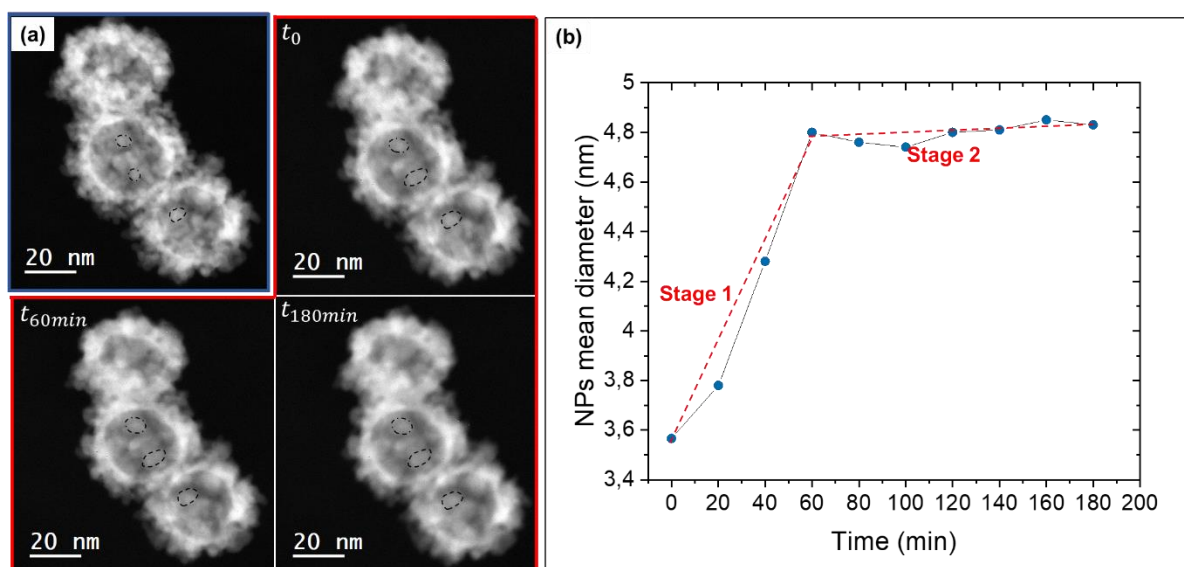


Figure 4.30: (a) STEM-HAADF images showing the morphological evolution of an individual Pt-2 HNS as a function of time at 60-minute intervals. The NPs shown are indicated by black lines. (b) Time-dependent plot of the average NP diameter comprising the Pt-2 HNS shell. The two growth stages are indicated by the red lines.

The simultaneous monitoring of the CO₂ hydrogenation reaction products (Figure 4.31) indicates a continuous increase of the reaction products PP, as it is in the case of the Pt-1 HNS. This dismisses any probability of catalyst deactivation by surface poisoning during the course of this reaction.

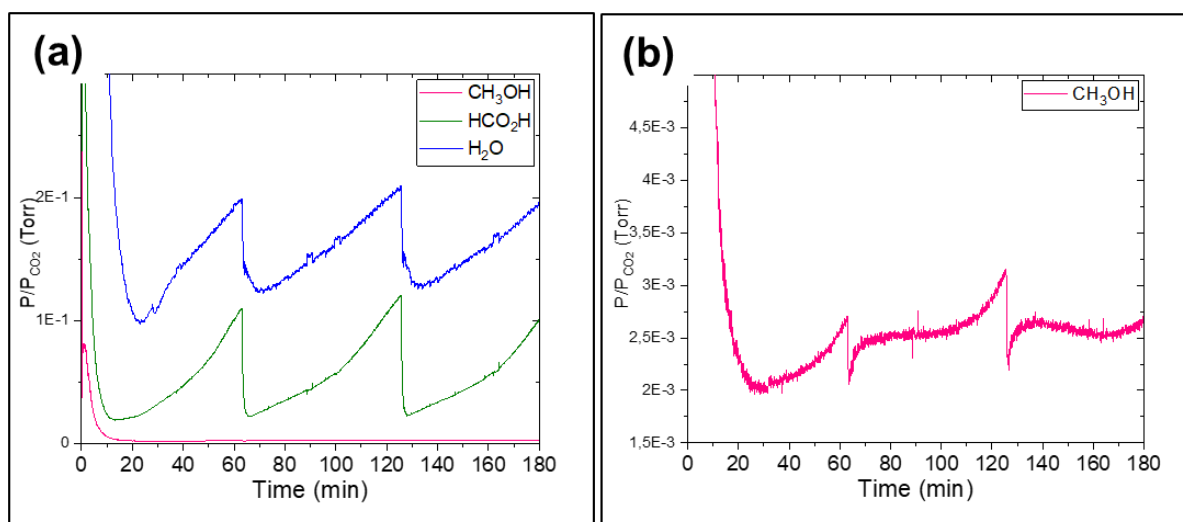


Figure 4.31: (a)(b) RGA Spectra illustrating the evolution of PP for CO₂ hydrogenation reaction products during 3 hours isothermal reaction at 180°C over Pt-2 HNS.

4. Conclusions

In conclusion, this chapter delved into the thermal stability of two sets of Pt-based HNS under varying atmospheric conditions, including TEM vacuum, hydrogen and the gas mixture of CO₂ and H₂. Through our investigations, we are able to determine the NPs sintering mechanisms operating in each environment, and it is found that these mechanisms are consistent for both Pt-1 and Pt-2 HNS. Under the TEM vacuum, the sintering process is primarily driven by the OR mechanism, with sintering triggered by a temperature of 280°C for both Pt-1 and Pt-2 HNS. In contrast, the particle migration and coalescence (PMC) mechanism governed the sintering process of NPs for both sets of Pt-based HNS during a flow of hydrogen gas atmosphere at 1 bar, with a similar sintering onset temperature of 160°C. Furthermore, both mechanisms are involved in the sintering process during CO₂ hydrogenation reaction conditions with a domination of the PMC. The differences between the two sets are observed in the collapse of their hollow structures. Pt-2 HNS, with its larger outer diameter and a greater number of larger-diameter channels within the shell, exhibited a higher temperature of collapse in all three atmospheres.

By isolating the behavior of each set, we observed that the temperature of collapse is highest under vacuum, lowest under the highly reactive hydrogen atmosphere, and slightly elevated under the 20% CO₂ gas atmosphere compared to hydrogen. Finally, the CO₂ hydrogenation reaction over both sets of catalysts followed the formate pathway, resulting primarily in the

formation of formic acid (HCO_2H) and methanol (CH_3OH). A common onset temperature of 180°C for HCO_2H and 220°C for CH_3OH . When subjected to an isothermal reaction at 180°C , both sets of Pt-based HNS displayed a noticeable increase in nanoparticle (NPs) size until reaching a thermally stable state. For the Pt-1 system, this stable state persisted for a minimum of 5 hours, while for the Pt-2 system, it remained stable for at least 3 hours. Finally, there are no indications of surface poisoning even after extended periods and at elevated temperatures in any of the conducted experiments in this work.

CONCLUSIONS AND PERSPECTIVES

The research carried out in this thesis have offered a thorough investigation of two sets Pt-based hollow nanospheres, Pt-1 and Pt-2 HNS, providing a wide-range view into their synthesis, characteristics and behavior under varying conditions.

Chapter III sets the stage by exploring the morphological and structural aspects of each set of nanospheres. The study reveals crucial distinctions and commonalities in the characteristics of Pt-1 and Pt-2 HNS. Morphologically, Pt-1 HNS exhibit two different shell types: a continuous and discontinuous shells. Although both inner Pt-1 and Pt-2 HNS display inner shell surface facets, Pt-2 HNS present only a discontinuous shell type. Both HNS sets exhibit a hollow microstructure with similarly thick shells composed of interconnected NPs, but they vary in Co content and particle arrangement. Pt-2 HNS have notably lower Co content and present a chain-like arrangement due to the experimental synthesis conditions, which differentiate from the agglomerated structures in Pt-1 HNS. Dimensionally, Pt-2 particles are larger and they feature a higher number and larger diameter of channels within their shells, attributed to the methodology employed during the second synthesis. Thus, the disparities and resemblances across both HNS sets emerge significantly from the differing synthetic processes and conditions, influencing their morphological and structural traits. The Pt-2 HNS display a possibility for increased active surface area and thereby, a boost in catalytic activity. This is due to their unique chain-like shape and better thermal stability from a larger diameter compared to Pt-1 HNS. Although having a larger mean diameter, Pt-2 HNS offset the apparent enhanced active surface area of Pt-1 through its considerable channel diameter and improved access to the inner shell. The hollow configuration of these nanospheres offers advantageous catalytic attributes, such as reactant accessibility to both inner and outer surfaces owing to their specific surface area.

Bridging to Chapter IV, an investigation into the thermal stability of both sets of Pt-based HNS is conducted, with emphasis on these material's behavior during thermal annealing under varying atmospheric conditions, such as TEM vacuum, H₂ and CO₂/H₂ gas mixture. These investigations reveal the NPs forming the shell sintering mechanisms such as Ostwald ripening and particle migration and coalescence. These mechanisms, influenced by the temperature and gas nature, are identified as pivotal in influencing the Pt-based HNS morphological evolution. The crystal slip, also affected by the temperature and the gas nature, is recognized as the mechanism governing their collapse. Both catalysts presented the highest thermal stability

under vacuum with the highest temperature triggering both NPs sintering and hollow nanospheres collapse. H₂ atmosphere have promoted the NPs sintering following the particles migration and coalescence at lowest temperature of the three studied environments, same as for the nanospheres collapse. EDS analyses reveal Pt segregation under this atmosphere at 300°C and shows a homogeneous distribution of Pt and Co across the sample after their hollow nanospheres collapse. Under the CO₂/H₂ gas mixture, A higher temperature of sintering and collapse is identified. Using the RGA, formic acid and methanol are identified as CO₂ hydrogenation reaction products confirming the formate reaction pathway of the reaction. The continuous rise in reaction products throughout the experiments, even following the collapse of the hollow nanospheres at elevated temperatures, confirms that the particles did not experience surface poisoning. Isothermal CO₂ hydrogenation reactions prove the same result at extended period. A growth of NPs to a bigger diameter in the Pt-1 HNS than it is in the Pt-2 is promoted by the higher Co content in the first set of HNS. The superior thermal stability of Pt-2 HNS, in particular, emerge as a noteworthy observation in all experiments. This makes its properties more suitable for applications that demand high thermal resilience and stability.

The investigations conducted during this thesis has opened up a wide range of opportunities and provide a solid base for more research. The upcoming possibilities outline a path that future research could take.

The use of X-ray Photoelectron Spectroscopy (XPS) is important for the study of the surface oxidation nuances, particularly focusing on the oxidation of Cobalt content within the Pt-based catalysts. Investigating how the oxidation state evolves, interacts, and possibly influences the thermal stability of Pt-based HNS could be crucial. Not only will this delve into the impacts of Cobalt oxidation on catalytic activities.

By taking a step further into the investigation of the interactions between Pt-based HNS and their supports, integrating inert supports like graphene can unravel a new chapter. Studying how the interactions between Pt-based HNS and graphene influence the catalyst's behavior and stability would be instrumental. Understanding how such inert supports impact the catalysts, not only in the preservation of their structural integrity but also in their catalytic performance, might enhance their applicability and efficiency across diverse chemical processes and reactions.

Zeolites, with their intriguing characteristics of acting as both catalysts and supports, present an interesting trajectory for research. Using zeolites as supports for Pt-based HNS might bring about a paradigm shift, offering a dual-functional platform that might influence the catalyst's functionality, stability, and potential application in novel ways. Comparing and contrasting the impacts of zeolite supports with previously utilized graphene could offer rich insights into how different supports modulate the behavior, stability, and catalytic capacity of Pt-based HNS. Such a comparative study can contribute to development of strategies of Pt-based catalysts, enhancing their performance in the several catalytic applications.

Conducting a thorough study on the morphological evolution of Pt-based HNS under oxidative environments (such as O₂) and during CO oxidation reactions can reveal the mechanisms governing their behavior and structural evolution. These experiments help to understand how these catalysts morphologically evolve and possibly degrade in oxidative atmospheres, and how this influences their catalytic activities.

Finally, this research on the Pt-based HNS is a contribution to the design and development of new catalytical complex systems. It lays the groundwork for future research that could revolutionize state of art catalytic applications by improving both stability and efficiency of the employed nanocatalysts.

APPENDIX

Appendix 1: The CCD and RioTM camera characteristics

The commercial CCD cameras are appropriate for the TEM because they have fast image access in electronic form, high sensitivity, low noise, and varied coverage from submicrometric to millimetric spatial resolution, as well as good dependability. [110] Gatan, Inc. has designed the US1000XP CCD camera in response to the requirement for a camera with better speed and lower noise for both life science and materials science applications. The CCD camera incorporates Gatan's advanced technology, enabling tunable brightness and thickness. It offers low-noise full frame readout in 0.25 seconds, live preview at 10 MHz, and ultra-low read noise at 1 MHz for low dose applications. Flexible binning allows for various image resolutions, ranging from 2x to 8x, with effective pixel size/resolution combinations. It also allows for extremely low-dose previewing at 512 x 512 resolution and up to 30 frames per second [240].

The CCD camera was afterwards replaced by the RioTM. Gatan's latest CMOS camera. The latter has a wide field of vision, high resolution, speed, and sensitivity. Unlike traditional CCD cameras, Rio maximizes light generation and collection by utilizing improved scintillators and 1:1 fiber optic coupling. The Rio camera features a Gpixel CMOS sensor with ultra-low readout noise and 9 μm pixel size, ideal for 30 to 200 kV operation. It includes drift correction, full-resolution live image display, and automatic compensation for drift during image recording. The Rio camera was meant to be used for conducting in-situ TEM experiments during this thesis. When combined with the In-Situ Explorer module, the Rio camera proves to be highly advantageous, providing the essential temporal and spatial resolution required for monitoring complex high-speed experiments. Moreover, it offers complete in-situ control and efficient data handling capabilities, making it an invaluable tool for conducting such experiments.[241]

Appendix 2: Statistical measurements of the STEM-HAADF micrographs

When examining the nanospheres with a continuous shell, there is no ambiguity in determining the outer diameter and the shell thickness. In fact, the smooth and well-defined outer shell allows for clear identification of its boundaries and therefore of the nanospheres outer diameter. The dimensions of the 2D projection of the nanospheres with a discontinuous shell can be misleading as the visibility of the NPs varies based on the contrast and brightness settings. Particularly, some NPs on the periphery of the shell may not be visible in the presented STEM images which influences the outer diameter and the shell thickness measurements. Therefore,

size measurements were obtained by analyzing intensity profiles across the nanospheres. Detailed explanations of the statistical measurements are supported by Figure A2.

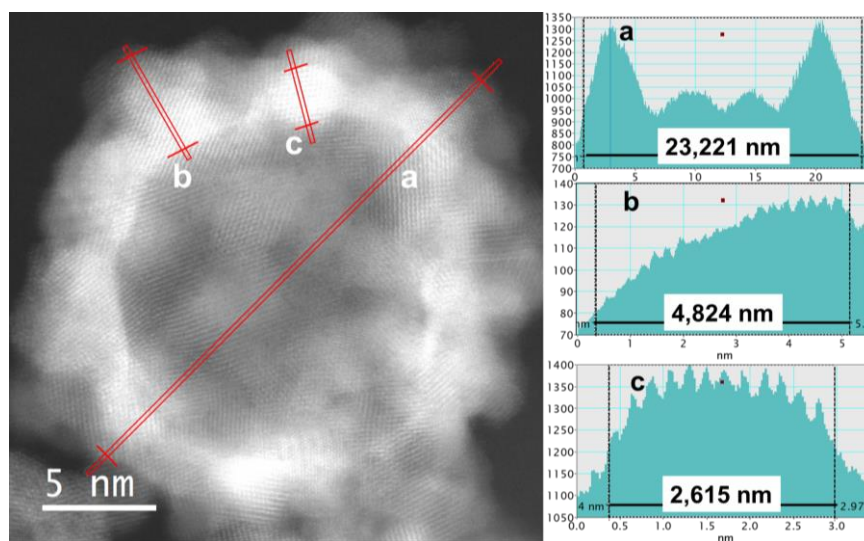


Figure A2: STEM-HAADF images of a single nanosphere with high brightness along with the corresponding intensity profiles taken from the indicated lines showing (a) the diameter of the nanospheres, (b) the thickness of the shell and (c) the diameter of the NP.

Three measurements are conducted: the nanospheres diameter (Figure 1a), the shell thickness (Figure 1b) and the NPs diameter (Figure 1c). After identifying a single nanosphere, a line profile is drawn across it. GMS3 generates an electron intensity profile plot along the line that represents the variation in electron intensity as a function of position. The measurements are taken at positions corresponding to 20 to 50 % of the intensities of the peaks located at the extremes (Figure 1a). Considering the roughness of the shells, measurements of the outer diameter are conducted in various directions, and subsequently, the mean value of these measurements is calculated. The same measurement approach is applied for the shell thickness (Figure 1b) and NPs diameter (Figure 1c) assessments.

Appendix 3: EDS quantification method

For an accurate identification of peaks in an EDS spectrum, it is essential to begin by identifying the predominant peak corresponding to each element. Additionally, only peaks with a statistically significant presence should be considered for the identification of the characteristic X-rays. [242]

Quantifications were conducted using the Analysis Station Software from JEOL ®. For quantitative analysis using EDS, an initial concentration value is estimated through an intensity ratio of characteristic X-rays emitted by the unknown specimen to those of a standard specimen (mass concentrations of the constituting elements are known). This ratio is expressed as the K ratio (K ratio = C^U/C^{Std}). Since the unknown specimen has different elements with different proportions compared to the standard specimen, the measured K ratio doesn't directly represent the concentration ratio between the two. Consequently, corrections to determine the accurate concentrations of the unknown specimen are applied. These corrections make up the correction factor and consist of three parts: atomic number correction (G^Z) (for differences in how efficiently characteristic X-rays are produced due to variations in element atomic numbers), **absorption Correction (G^A)** (for differences in X-ray absorption as they travel through the specimen) and **fluorescence Correction (G^F)** (for differences in the efficiency of generating fluorescence X-rays).

Multiple techniques are available for calculating these correction factors, including the ZAF correction method and the Phi-Rho-Z method ($\phi(\rho z)$ method). In the $\phi(\rho z)$ method, both the atomic number (Z) effect and the absorption (A) effect are addressed simultaneously. In contrast, the ZAF correction method treats these effects separately. The $\phi(\rho z)$ method tends to provide more accurate results when accurate absorption corrections are necessary. This is particularly beneficial for specimens containing both light and heavy elements. There are no light elements in the studied samples during this work, therefore the conventional ZAF method is enough for the quantification. Additionally, a standard-less quantification approach was adapted for determining the initial K ratio, in which theoretical calculations or reference data provided by the EDS manufacturer (JEOL ®) was used. [243]

REFERENCES

- [1] J. Wisniak, “The History of Catalysis. From the Beginning to Nobel Prizes,” *Educación Química*, vol. 21, no. 1, pp. 60–69, Jan. 2010, doi: 10.1016/S0187-893X(18)30074-0.
- [2] “The Nobel Prize in Chemistry 1909,” NobelPrize.org. Accessed: Oct. 24, 2023. [Online]. Available: <https://www.nobelprize.org/prizes/chemistry/1909/summary/>
- [3] “The Nobel Prize in Chemistry 1912,” NobelPrize.org. Accessed: Oct. 24, 2023. [Online]. Available: <https://www.nobelprize.org/prizes/chemistry/1912/grignard/facts/>
- [4] R. Schlögl, “Heterogeneous Catalysis,” *Angew. Chem. Int. Ed.*, vol. 54, no. 11, pp. 3465–3520, Mar. 2015, doi: 10.1002/anie.201410738.
- [5] P. W. N. M. van Leeuwen, “Homogeneous Metal Catalysis,” in *Reference Module in Chemistry, Molecular Sciences and Chemical Engineering*, Elsevier, 2016, p. B9780124095472112000. doi: 10.1016/B978-0-12-409547-2.11101-1.
- [6] R. Karan, R. Bhatia, and R. K. Rawal, “Applications of homogeneous catalysis in organic synthesis,” in *Green Sustainable Process for Chemical and Environmental Engineering and Science*, Elsevier, 2021, pp. 159–188. doi: 10.1016/B978-0-12-819720-2.00010-2.
- [7] Ostwald, W., “Definition der Katalyse,” *Z. Phys. Chem*, pp. 705–706, 1894.
- [8] C. Becker, “From Langmuir to Ertl: The ‘Nobel’ History of the Surface Science Approach to Heterogeneous Catalysis,” in *Encyclopedia of Interfacial Chemistry*, Elsevier, 2018, pp. 99–106. doi: 10.1016/B978-0-12-409547-2.13527-9.
- [9] I. Langmuir, “The Evaporation, Condensation and Reflection of Molecules and the Mechanism of Adsorption,” *Phys. Rev.*, vol. 8, no. 2, pp. 149–176, Aug. 1916, doi: 10.1103/PhysRev.8.149.
- [10] T. Mikołajczyk, “The impact of pollutants on catalyst performance during hydrogen evolution reaction: A brief review,” *Synthetic Metals*, vol. 296, p. 117379, Jul. 2023, doi: 10.1016/j.synthmet.2023.117379.
- [11] D. Y. Chung *et al.*, “Inhibition of CO poisoning on Pt catalyst coupled with the reduction of toxic hexavalent chromium in a dual-functional fuel cell,” *Sci Rep*, vol. 4, no. 1, p. 7450, Dec. 2014, doi: 10.1038/srep07450.
- [12] M. Králik, “Adsorption, chemisorption, and catalysis,” *Chemical Papers*, vol. 68, no. 12, Jan. 2014, doi: 10.2478/s11696-014-0624-9.
- [13] Langmuir, I., “Chemical Reactions on Surfaces,” *Trans. Faraday Soc.*, pp. 607–620, 1922.
- [14] Hinshelwood, C. N., “On the Theory of Unimolecular Reactions,” *Proc. R. Soc. Lond. A Math. Phys. Sci.*, pp. 230–233, 1926.
- [15] Y. Zhou, Z. Wang, and C. Liu, “Perspective on CO oxidation over Pd-based catalysts,” *Catal. Sci. Technol.*, vol. 5, no. 1, pp. 69–81, 2015, doi: 10.1039/C4CY00983E.
- [16] Rideal, E. K., “A Note on a Simple Molecular Mechanism for Heterogeneous Catalytic Reactions,” *Proc. Camb. Philos. Soc.*, pp. 130–132, 1939.
- [17] S. Xu *et al.*, “CO Poisoning of Ru Catalysts in CO₂ Hydrogenation under Thermal and Plasma Conditions: A Combined Kinetic and Diffuse Reflectance Infrared Fourier Transform Spectroscopy–Mass Spectrometry Study,” *ACS Catal.*, vol. 10, no. 21, pp. 12828–12840, Nov. 2020, doi: 10.1021/acscatal.0c03620.
- [18] O. Deutschmann, H. Knözinger, K. Kochloefl, and T. Turek, “Heterogeneous Catalysis and Solid Catalysts, 2. Development and Types of Solid Catalysts,” in *Ullmann’s Encyclopedia of Industrial Chemistry*, Wiley-VCH Verlag GmbH & Co. KGaA, Ed., Weinheim, Germany: Wiley-VCH Verlag GmbH & Co. KGaA, 2011, p. o05_o02. doi: 10.1002/14356007.o05_o02.

- [19] R. Bai, Y. Song, Y. Li, and J. Yu, "Creating Hierarchical Pores in Zeolite Catalysts," *Trends in Chemistry*, vol. 1, no. 6, pp. 601–611, Sep. 2019, doi: 10.1016/j.trechm.2019.05.010.
- [20] C. Martínez and A. Corma, "Inorganic molecular sieves: Preparation, modification and industrial application in catalytic processes," *Coordination Chemistry Reviews*, vol. 255, no. 13–14, pp. 1558–1580, Jul. 2011, doi: 10.1016/j.ccr.2011.03.014.
- [21] Y. Li and J. Yu, "New Stories of Zeolite Structures: Their Descriptions, Determinations, Predictions, and Evaluations," *Chem. Rev.*, vol. 114, no. 14, pp. 7268–7316, Jul. 2014, doi: 10.1021/cr500010r.
- [22] J. Weitkamp, "Zeolites and catalysis," *Solid State Ionics*, vol. 131, no. 1–2, pp. 175–188, Jun. 2000, doi: 10.1016/S0167-2738(00)00632-9.
- [23] E. Wagner, T. Fetzter in G. Ertl, H. Knozinger, J. and Weitkamp (eds.), *Handbook of Heterogeneous Catalysis*, Wiley-VCH., vol. 4. Weinheim, 1997.
- [24] H. Jüntgen, H. Köhl, "Carbon," *Chem. Phys.*, p. 145, 1990.
- [25] L. R. Radovic, F. Rodriguez-Reinoso, "Carbon," *Chem. Phys.*, p. 243, 1997.
- [26] L. Liu and A. Corma, "Metal Catalysts for Heterogeneous Catalysis: From Single Atoms to Nanoclusters and Nanoparticles," *Chem. Rev.*, vol. 118, no. 10, pp. 4981–5079, May 2018, doi: 10.1021/acs.chemrev.7b00776.
- [27] M. Boudart, "Catalysis by Supported Metals," in *Advances in Catalysis*, vol. 20, Elsevier, 1969, pp. 153–166. doi: 10.1016/S0360-0564(08)60271-0.
- [28] R. Narayanan and M. A. El-Sayed, "Catalysis with Transition Metal Nanoparticles in Colloidal Solution: Nanoparticle Shape Dependence and Stability," *J. Phys. Chem. B*, vol. 109, no. 26, pp. 12663–12676, Jul. 2005, doi: 10.1021/jp051066p.
- [29] C. Gao, F. Lyu, and Y. Yin, "Encapsulated Metal Nanoparticles for Catalysis," *Chem. Rev.*, vol. 121, no. 2, pp. 834–881, Jan. 2021, doi: 10.1021/acs.chemrev.0c00237.
- [30] H. Wang and J. Lu, "A Review on Particle Size Effect in METAL-CATALYZED Heterogeneous Reactions," *Chin. J. Chem.*, vol. 38, no. 11, pp. 1422–1444, Nov. 2020, doi: 10.1002/cjoc.202000205.
- [31] G. C. Bond, "The origins of particle size effects in heterogeneous catalysis," *Surface Science*, vol. 156, pp. 966–981, Jun. 1985, doi: 10.1016/0039-6028(85)90273-0.
- [32] M. Che and C. O. Bennett, "The Influence of Particle Size on the Catalytic Properties of Supported Metals," in *Advances in Catalysis*, vol. 36, Elsevier, 1989, pp. 55–172. doi: 10.1016/S0360-0564(08)60017-6.
- [33] W. P. Halperin, "Quantum size effects in metal particles," *Rev. Mod. Phys.*, vol. 58, no. 3, pp. 533–606, Jul. 1986, doi: 10.1103/RevModPhys.58.533.
- [34] A. Taketoshi and M. Haruta, "Size- and Structure-specificity in Catalysis by Gold Clusters," *Chem. Lett.*, vol. 43, no. 4, pp. 380–387, Apr. 2014, doi: 10.1246/cl.131232.
- [35] B. Qiao, J.-X. Liang, A. Wang, J. Liu, and T. Zhang, "Single atom gold catalysts for low-temperature CO oxidation," *Chinese Journal of Catalysis*, vol. 37, no. 10, pp. 1580–1586, Oct. 2016, doi: 10.1016/S1872-2067(16)62529-9.
- [36] L. Zhang, Y. Ren, W. Liu, A. Wang, and T. Zhang, "Single-atom catalyst: a rising star for green synthesis of fine chemicals," *National Science Review*, vol. 5, no. 5, pp. 653–672, Sep. 2018, doi: 10.1093/nsr/nwy077.
- [37] B. Qiao *et al.*, "Single-atom catalysis of CO oxidation using Pt1/FeOx," *Nature Chem.*, vol. 3, no. 8, pp. 634–641, Aug. 2011, doi: 10.1038/nchem.1095.
- [38] Z. Zhang, Z. Jiang, and W. Shangguan, "Low-temperature catalysis for VOCs removal in technology and application: A state-of-the-art review," *Catalysis Today*, vol. 264, pp. 270–278, Apr. 2016, doi: 10.1016/j.cattod.2015.10.040.

- [39] B. Qiao *et al.*, “Ultrastable single-atom gold catalysts with strong covalent metal-support interaction (CMSI),” *Nano Res.*, vol. 8, no. 9, pp. 2913–2924, Sep. 2015, doi: 10.1007/s12274-015-0796-9.
- [40] A. Abad, P. Concepción, A. Corma, and H. García, “A Collaborative Effect between Gold and a Support Induces the Selective Oxidation of Alcohols,” *Angew. Chem. Int. Ed.*, vol. 44, no. 26, pp. 4066–4069, Jun. 2005, doi: 10.1002/anie.200500382.
- [41] S. E. Davis, M. S. Ide, and R. J. Davis, “Selective oxidation of alcohols and aldehydes over supported metal nanoparticles,” *Green Chem.*, vol. 15, no. 1, pp. 17–45, 2013, doi: 10.1039/C2GC36441G.
- [42] W. Zang, G. Li, L. Wang, and X. Zhang, “Catalytic hydrogenation by noble-metal nanocrystals with well-defined facets: a review,” *Catal. Sci. Technol.*, vol. 5, no. 5, pp. 2532–2553, 2015, doi: 10.1039/C4CY01619J.
- [43] G. C. Bond, P. A. Sermon, G. Webb, D. A. Buchanan, and P. B. Wells, “Hydrogenation over supported gold catalysts,” *J. Chem. Soc., Chem. Commun.*, no. 13, p. 444b, 1973, doi: 10.1039/c3973000444b.
- [44] C. Mohr, H. Hofmeister, J. Radnik, and P. Claus, “Identification of Active Sites in Gold-Catalyzed Hydrogenation of Acrolein,” *J. Am. Chem. Soc.*, vol. 125, no. 7, pp. 1905–1911, Feb. 2003, doi: 10.1021/ja027321q.
- [45] G. J. Leong *et al.*, “Shape-directed platinum nanoparticle synthesis: nanoscale design of novel catalysts: A review of shape-directed platinum nanoparticle synthesis,” *Appl. Organometal. Chem.*, vol. 28, no. 1, pp. 1–17, Jan. 2014, doi: 10.1002/aoc.3048.
- [46] Md. A. R. Khan, M. S. A. Mamun, and M. H. Ara, “Review on platinum nanoparticles: Synthesis, characterization, and applications,” *Microchemical Journal*, vol. 171, p. 106840, Dec. 2021, doi: 10.1016/j.microc.2021.106840.
- [47] D. McDonald, L. B. Hunt, *A History of Platinum and its Allied Metals*, Johnson Matthey. London, 1982.
- [48] N. V. Long, Y. Yang, C. Minh Thi, N. V. Minh, Y. Cao, and M. Nogami, “The development of mixture, alloy, and core-shell nanocatalysts with nanomaterial supports for energy conversion in low-temperature fuel cells,” *Nano Energy*, vol. 2, no. 5, pp. 636–676, Sep. 2013, doi: 10.1016/j.nanoen.2013.06.001.
- [49] S. E. Voltz, C. R. Morgan, D. Liederman, and S. M. Jacob, “Kinetic Study of Carbon Monoxide and Propylene Oxidation on Platinum Catalysts,” *Product R&D*, vol. 12, no. 4, pp. 294–301, Dec. 1973, doi: 10.1021/i360048a006.
- [50] H. A. Gasteiger, S. S. Kocha, B. Sompalli, and F. T. Wagner, “Activity benchmarks and requirements for Pt, Pt-alloy, and non-Pt oxygen reduction catalysts for PEMFCs,” *Applied Catalysis B: Environmental*, vol. 56, no. 1–2, pp. 9–35, Mar. 2005, doi: 10.1016/j.apcatb.2004.06.021.
- [51] R. Burch, J. P. Breen, and F. C. Meunier, “A review of the selective reduction of NO_x with hydrocarbons under lean-burn conditions with non-zeolitic oxide and platinum group metal catalysts,” *Applied Catalysis B: Environmental*, vol. 39, no. 4, pp. 283–303, Dec. 2002, doi: 10.1016/S0926-3373(02)00118-2.
- [52] X. Lin, M. Wu, D. Wu, S. Kuga, T. Endo, and Y. Huang, “Platinum nanoparticles using wood nanomaterials: eco-friendly synthesis, shape control and catalytic activity for p-nitrophenol reduction,” *Green Chem.*, vol. 13, no. 2, pp. 283–287, 2011, doi: 10.1039/C0GC00513D.
- [53] D. Ren *et al.*, “An Unusual Chemoselective Hydrogenation of Quinoline Compounds Using Supported Gold Catalysts,” *J. Am. Chem. Soc.*, vol. 134, no. 42, pp. 17592–17598, Oct. 2012, doi: 10.1021/ja3066978.
- [54] H. Cheng, C. Xi, X. Meng, Y. Hao, Y. Yu, and F. Zhao, “Polyethylene glycol-stabilized platinum nanoparticles: The efficient and recyclable catalysts for selective hydrogenation

- of o-chloronitrobenzene to o-chloroaniline,” *Journal of Colloid and Interface Science*, vol. 336, no. 2, pp. 675–678, Aug. 2009, doi: 10.1016/j.jcis.2009.04.076.
- [55] P. Lara and K. Philippot, “The hydrogenation of nitroarenes mediated by platinum nanoparticles: an overview,” *Catal. Sci. Technol.*, vol. 4, no. 8, pp. 2445–2465, 2014, doi: 10.1039/C4CY00111G.
- [56] A. Roucoux, J. Schulz, and H. Patin, “Reduced Transition Metal Colloids: A Novel Family of Reusable Catalysts?,” *Chem. Rev.*, vol. 102, no. 10, pp. 3757–3778, Oct. 2002, doi: 10.1021/cr010350j.
- [57] S. A. Gama-Lara, Raúl. A. Morales-Luckie, L. Argueta-Figueroa, J. P. Hinestroza, I. García-Orozco, and R. Natividad, “Synthesis, Characterization, and Catalytic Activity of Platinum Nanoparticles on Bovine-Bone Powder: A Novel Support,” *Journal of Nanomaterials*, vol. 2018, pp. 1–8, 2018, doi: 10.1155/2018/6482186.
- [58] K. Sun, N. Rui, C. Shen, and C. Liu, “Theoretical Study of Selective Hydrogenation of CO₂ to Methanol over Pt₄/In₂O₃ Model Catalyst,” *J. Phys. Chem. C*, vol. 125, no. 20, pp. 10926–10936, May 2021, doi: 10.1021/acs.jpcc.1c00638.
- [59] W. Wang, S. Wang, X. Ma, and J. Gong, “Recent advances in catalytic hydrogenation of carbon dioxide,” *Chem. Soc. Rev.*, vol. 40, no. 7, p. 3703, 2011, doi: 10.1039/c1cs15008a.
- [60] E. S. Gutterød *et al.*, “Influence of Defects and H₂O on the Hydrogenation of CO₂ to Methanol over Pt Nanoparticles in UiO-67 Metal–Organic Framework,” *J. Am. Chem. Soc.*, vol. 142, no. 40, pp. 17105–17118, Oct. 2020, doi: 10.1021/jacs.0c07153.
- [61] E. S. Gutterød *et al.*, “Hydrogenation of CO₂ to Methanol by Pt Nanoparticles Encapsulated in UiO-67: Deciphering the Role of the Metal–Organic Framework,” *J. Am. Chem. Soc.*, vol. 142, no. 2, pp. 999–1009, Jan. 2020, doi: 10.1021/jacs.9b10873.
- [62] Y.-L. Men *et al.*, “Highly dispersed Pt-based catalysts for selective CO₂ hydrogenation to methanol at atmospheric pressure,” *Chemical Engineering Science*, vol. 200, pp. 167–175, Jun. 2019, doi: 10.1016/j.ces.2019.02.004.
- [63] T. Toyao, S. Kayamori, Z. Maeno, S. M. A. H. Siddiki, and K. Shimizu, “Heterogeneous Pt and MoO_x Co-Loaded TiO₂ Catalysts for Low-Temperature CO₂ Hydrogenation To Form CH₃OH,” *ACS Catal.*, vol. 9, no. 9, pp. 8187–8196, Sep. 2019, doi: 10.1021/acscatal.9b01225.
- [64] Z. Han, C. Tang, J. Wang, L. Li, and C. Li, “Atomically dispersed Ptn+ species as highly active sites in Pt/In₂O₃ catalysts for methanol synthesis from CO₂ hydrogenation,” *Journal of Catalysis*, vol. 394, pp. 236–244, Feb. 2021, doi: 10.1016/j.jcat.2020.06.018.
- [65] K. Sun, N. Rui, Z. Zhang, Z. Sun, Q. Ge, and C.-J. Liu, “A highly active Pt/In₂O₃ catalyst for CO₂ hydrogenation to methanol with enhanced stability,” *Green Chem.*, vol. 22, no. 15, pp. 5059–5066, 2020, doi: 10.1039/D0GC01597K.
- [66] P. Frontera, A. Macario, M. Ferraro, and P. Antonucci, “Supported Catalysts for CO₂ Methanation: A Review,” *Catalysts*, vol. 7, no. 12, p. 59, Feb. 2017, doi: 10.3390/catal7020059.
- [67] M. González-Castaño, B. Dorneanu, and H. Arellano-García, “The reverse water gas shift reaction: a process system engineering perspective,” *React. Chem. Eng.*, vol. 6, no. 6, pp. 954–976, 2021, doi: 10.1039/D0RE00478B.
- [68] M. Bowker, “Methanol Synthesis from CO₂ Hydrogenation,” *ChemCatChem*, vol. 11, no. 17, pp. 4238–4246, Sep. 2019, doi: 10.1002/cctc.201900401.
- [69] D. Xu, Y. Wang, M. Ding, X. Hong, G. Liu, and S. C. E. Tsang, “Advances in higher alcohol synthesis from CO₂ hydrogenation,” *Chem*, vol. 7, no. 4, pp. 849–881, Apr. 2021, doi: 10.1016/j.chempr.2020.10.019.

- [70] R. Sun *et al.*, “Heterogeneous catalysts for CO₂ hydrogenation to formic acid/formate: from nanoscale to single atom,” *Energy Environ. Sci.*, vol. 14, no. 3, pp. 1247–1285, 2021, doi: 10.1039/D0EE03575K.
- [71] H. Yang *et al.*, “A review of the catalytic hydrogenation of carbon dioxide into value-added hydrocarbons,” *Catal. Sci. Technol.*, vol. 7, no. 20, pp. 4580–4598, 2017, doi: 10.1039/C7CY01403A.
- [72] L. H. Vieira *et al.*, “Noble Metals in Recent Developments of Heterogeneous Catalysts for CO₂ Conversion Processes,” *ChemCatChem*, p. e202300493, Jul. 2023, doi: 10.1002/cctc.202300493.
- [73] S. Zhang *et al.*, “A Short Review of Recent Advances in Direct CO₂ Hydrogenation to Alcohols,” *Top Catal.*, vol. 64, no. 5–6, pp. 371–394, May 2021, doi: 10.1007/s11244-020-01405-w.
- [74] P. Schwiderowski, H. Ruland, and M. Muhler, “Current developments in CO₂ hydrogenation towards methanol: A review related to industrial application,” *Current Opinion in Green and Sustainable Chemistry*, vol. 38, p. 100688, Dec. 2022, doi: 10.1016/j.cogsc.2022.100688.
- [75] F. Sha, Z. Han, S. Tang, J. Wang, and C. Li, “Hydrogenation of Carbon Dioxide to Methanol over Non-Cu-based Heterogeneous Catalysts,” *ChemSusChem*, p. cssc.202002054, Nov. 2020, doi: 10.1002/cssc.202002054.
- [76] S. Kattel, B. Yan, Y. Yang, J. G. Chen, and P. Liu, “Optimizing Binding Energies of Key Intermediates for CO₂ Hydrogenation to Methanol over Oxide-Supported Copper,” *J. Am. Chem. Soc.*, vol. 138, no. 38, pp. 12440–12450, Sep. 2016, doi: 10.1021/jacs.6b05791.
- [77] L. F. Rasteiro, M. A. L. S. Rossi, J. M. Assaf, and E. M. Assaf, “Low-pressure hydrogenation of CO₂ to methanol over Ni-Ga alloys synthesized by a surfactant-assisted co-precipitation method and a proposed mechanism by DRIFTS analysis,” *Catalysis Today*, vol. 381, pp. 261–271, Dec. 2021, doi: 10.1016/j.cattod.2020.05.067.
- [78] A. Álvarez *et al.*, “Challenges in the Greener Production of Formates/Formic Acid, Methanol, and DME by Heterogeneously Catalyzed CO₂ Hydrogenation Processes,” *Chem. Rev.*, vol. 117, no. 14, pp. 9804–9838, Jul. 2017, doi: 10.1021/acs.chemrev.6b00816.
- [79] J. R. Crockett, M. Wang, J. E. Doebler, T. Pawale, X. Li, and Y. Bao, “Impact on the Formation and Catalytic Property of Pt-Based Nanocatalysts by Galvanic Reaction with Co-Reduction Agents,” *Chem. Mater.*, vol. 34, no. 20, pp. 9282–9293, Oct. 2022, doi: 10.1021/acs.chemmater.2c02659.
- [80] M. Xiao *et al.*, “Hollow Nanostructures for Photocatalysis: Advantages and Challenges,” *Adv. Mater.*, vol. 31, no. 38, p. 1801369, Sep. 2019, doi: 10.1002/adma.201801369.
- [81] S. Cohen-Pope, J. R. Crockett, M. Wang, K. Flynn, A. Hoff, and Y. Bao, “Morphology control of SERS-active 2D gold nanosnowflakes,” *J. Mater. Chem. C*, vol. 8, no. 36, pp. 12427–12436, 2020, doi: 10.1039/D0TC02183K.
- [82] S. Tominaka, Y. Nakamura, and T. Osaka, “Nanostructured catalyst with hierarchical porosity and large surface area for on-chip fuel cells,” *Journal of Power Sources*, vol. 195, no. 4, pp. 1054–1058, Feb. 2010, doi: 10.1016/j.jpowsour.2009.08.082.
- [83] A. G. M. da Silva, T. S. Rodrigues, S. J. Haigh, and P. H. C. Camargo, “Galvanic replacement reaction: recent developments for engineering metal nanostructures towards catalytic applications,” *Chem. Commun.*, vol. 53, no. 53, pp. 7135–7148, 2017, doi: 10.1039/C7CC02352A.
- [84] J. Park *et al.*, “Hollow nanoparticles as emerging electrocatalysts for renewable energy conversion reactions,” *Chem. Soc. Rev.*, vol. 47, no. 22, pp. 8173–8202, 2018, doi: 10.1039/C8CS00336J.

- [85] H. Li and S. Yu, "Recent Advances on Controlled Synthesis and Engineering of Hollow Alloyed Nanotubes for Electrocatalysis," *Adv. Mater.*, vol. 31, no. 38, p. 1803503, Sep. 2019, doi: 10.1002/adma.201803503.
- [86] H. Zhang *et al.*, "Synthesis of Pd–Pt Bimetallic Nanocrystals with a Concave Structure through a Bromide-Induced Galvanic Replacement Reaction," *J. Am. Chem. Soc.*, vol. 133, no. 15, pp. 6078–6089, Apr. 2011, doi: 10.1021/ja201156s.
- [87] Y. Sun, B. Mayers, and Y. Xia, "Metal Nanostructures with Hollow Interiors," *Adv. Mater.*, vol. 15, no. 78, pp. 641–646, Apr. 2003, doi: 10.1002/adma.200301639.
- [88] X. Xia, Y. Wang, A. Ruditskiy, and Y. Xia, "25th Anniversary Article: Galvanic Replacement: A Simple and Versatile Route to Hollow Nanostructures with Tunable and Well-Controlled Properties," *Adv. Mater.*, vol. 25, no. 44, pp. 6313–6333, Nov. 2013, doi: 10.1002/adma.201302820.
- [89] K. An and T. Hyeon, "Synthesis and biomedical applications of hollow nanostructures," *Nano Today*, vol. 4, no. 4, pp. 359–373, Aug. 2009, doi: 10.1016/j.nantod.2009.06.013.
- [90] T. S. Rodrigues, A. G. M. da Silva, and P. H. C. Camargo, "Nanocatalysis by noble metal nanoparticles: controlled synthesis for the optimization and understanding of activities," *J. Mater. Chem. A*, vol. 7, no. 11, pp. 5857–5874, 2019, doi: 10.1039/C9TA00074G.
- [91] J. Zeng, Q. Zhang, J. Chen, and Y. Xia, "A Comparison Study of the Catalytic Properties of Au-Based Nanocages, Nanoboxes, and Nanoparticles," *Nano Lett.*, vol. 10, no. 1, pp. 30–35, Jan. 2010, doi: 10.1021/nl903062e.
- [92] H.-P. Liang, H.-M. Zhang, J.-S. Hu, Y.-G. Guo, L.-J. Wan, and C.-L. Bai, "Pt Hollow Nanospheres: Facile Synthesis and Enhanced Electrocatalysts," *Angew. Chem. Int. Ed.*, vol. 43, no. 12, pp. 1540–1543, Mar. 2004, doi: 10.1002/anie.200352956.
- [93] Y.-P. Xiao, S. Wan, X. Zhang, J.-S. Hu, Z.-D. Wei, and L.-J. Wan, "Hanging Pt hollow nanocrystal assemblies on graphene resulting in an enhanced electrocatalyst," *Chem. Commun.*, vol. 48, no. 83, p. 10331, 2012, doi: 10.1039/c2cc35562k.
- [94] J. Zhao, W. Chen, Y. Zheng, and X. Li, "Novel carbon supported hollow Pt nanospheres for methanol electrooxidation," *Journal of Power Sources*, vol. 162, no. 1, pp. 168–172, Nov. 2006, doi: 10.1016/j.jpowsour.2006.06.090.
- [95] J. X. Wang *et al.*, "Kirkendall Effect and Lattice Contraction in Nanocatalysts: A New Strategy to Enhance Sustainable Activity," *J. Am. Chem. Soc.*, vol. 133, no. 34, pp. 13551–13557, Aug. 2011, doi: 10.1021/ja204518x.
- [96] Y. Vasquez, A. K. Sra, and R. E. Schaak, "One-Pot Synthesis of Hollow Superparamagnetic CoPt Nanospheres," *J. Am. Chem. Soc.*, vol. 127, no. 36, pp. 12504–12505, Sep. 2005, doi: 10.1021/ja054442s.
- [97] X. Zhou *et al.*, "A review of hollow Pt-based nanocatalysts applied in proton exchange membrane fuel cells," *Journal of Power Sources*, vol. 232, pp. 310–322, Jun. 2013, doi: 10.1016/j.jpowsour.2013.01.062.
- [98] X.-W. Zhou, Q.-S. Chen, Z.-Y. Zhou, and S.-G. Sun, "Synthesis, Electrocatalytic and Anomalous IR Properties of Hollow CoPt Chainlike Nanomaterials," *J. Nanosci. Nanotech.*, vol. 9, no. 4, pp. 2392–2397, Apr. 2009, doi: 10.1166/jnn.2009.SE34.
- [99] X. W. Zhou, R. H. Zhang, D. M. Zeng, and S. G. Sun, "One-dimensional CoPt nanorods and their anomalous IR optical properties," *Journal of Solid-State Chemistry*, vol. 183, no. 6, pp. 1340–1346, Jun. 2010, doi: 10.1016/j.jssc.2010.04.003.
- [100] Q. Sun, S. Wang, and R. Wang, "Well-Aligned CoPt Hollow Nanochains Synthesized in Water at Room Temperature," *J. Phys. Chem. C*, vol. 116, no. 9, pp. 5352–5357, Mar. 2012, doi: 10.1021/jp210144p.
- [101] M. Argyle and C. Bartholomew, "Heterogeneous Catalyst Deactivation and Regeneration: A Review," *Catalysts*, vol. 5, no. 1, pp. 145–269, Feb. 2015, doi: 10.3390/catal5010145.

- [102] P. G. Menon, "Coke on catalysts-harmful, harmless, invisible and beneficial types," *Journal of Molecular Catalysis*, vol. 59, no. 2, pp. 207–220, Apr. 1990, doi: 10.1016/0304-5102(90)85053-K.
- [103] E. B. Maxted, "The Poisoning of Metallic Catalysts," in *Advances in Catalysis*, vol. 3, Elsevier, 1951, pp. 129–178. doi: 10.1016/S0360-0564(08)60106-6.
- [104] C. H. Bartholomew, "Mechanisms of Nickel Catalyst Poisoning," in *Studies in Surface Science and Catalysis*, vol. 34, Elsevier, 1987, pp. 81–104. doi: 10.1016/S0167-2991(09)60352-9.
- [105] L. L. Hegedus and R. W. McCabe, "Catalyst Poisoning," in *Studies in Surface Science and Catalysis*, vol. 6, Elsevier, 1980, pp. 471–505. doi: 10.1016/S0167-2991(08)65254-4.
- [106] Juan Inga, Paul Kennedy, and Stephen Leviness, "FISCHER-TROPSCH PROCESS IN THE PRESENCE OF NITROGEN CONTAMINANTS," WIPO Patent WO 2005/071044, Aug. 04, 2005
- [107] Bartholomew, C.H.; Farrauto, R.J., *Fundamentals of Industrial Catalytic Processes*, 2nd ed.; Wiley-Interscience: Hoboken, NJ, USA, 2006.
- [108] C. H. Bartholomew, "Sintering kinetics of supported metals: new perspectives from a unifying GPLE treatment," *Applied Catalysis A: General*, vol. 107, no. 1, pp. 1–57, Dec. 1993, doi: 10.1016/0926-860X(93)85114-5.
- [109] A. Kabalnov, "Ostwald Ripening and Related Phenomena," *Journal of Dispersion Science and Technology*, vol. 22, no. 1, pp. 1–12, Feb. 2001, doi: 10.1081/DIS-100102675.
- [110] D. B. Williams and C. B. Carter, *Transmission Electron Microscopy*. Boston, MA: Springer US, 2009. doi: 10.1007/978-0-387-76501-3.
- [111] A. Einstein, "Über einen die Erzeugung und Verwandlung des Lichtes betreffenden heuristischen Gesichtspunkt," *Ann. Phys.*, vol. 322, no. 6, pp. 132–148, 1905, doi: 10.1002/andp.19053220607.
- [112] L. De Broglie, "Recherches sur la théorie des Quanta," *Ann. Phys.*, vol. 10, no. 3, pp. 22–128, 1925, doi: 10.1051/anphys/192510030022.
- [113] C. Davisson and L. H. Germer, "Diffraction of Electrons by a Crystal of Nickel," *Phys. Rev.*, vol. 30, no. 6, pp. 705–740, Dec. 1927, doi: 10.1103/PhysRev.30.705.
- [114] M. Knoll and E. Ruska, "Das Elektronenmikroskop," *Z. Physik*, vol. 78, no. 5–6, pp. 318–339, May 1932, doi: 10.1007/BF01342199.
- [115] H.-Y. Chao *et al.*, "In Situ and Emerging Transmission Electron Microscopy for Catalysis Research," *Chem. Rev.*, p. acs.chemrev.2c00880, Jun. 2023, doi: 10.1021/acs.chemrev.2c00880.
- [116] J. Frank, "J. Frank – Electron Tomography – Plenum, New York, 1992, p.399.," *Electron Tomography- Plenum*, New York, p. 399, 1992.
- [117] M. Radermacher, "Three-Dimensional reconstruction of single particles from random and nonrandom tilt series," *Journal of Electron Microscopy Technique*, vol. 9, no. 4, pp. 359–394, 1988, doi: 10.1002/jemt.1060090405.
- [118] Johann Radon, "Über die bestimmung von funktionen durch ihre integralwerte langs gewisser mannigfaltigkeiten," *Journal of Mathematical Physics*, pp. 262–277, 1917.
- [119] M. Radermacher, "Three-dimensional reconstruction from random projections: orientational alignment via Radon transforms," *Ultramicroscopy*, vol. 53, no. 2, pp. 121–136, Feb. 1994, doi: 10.1016/0304-3991(94)90003-5.
- [120] R. G. Hart, "Electron Microscopy of Unstained Biological Material: The Polytropic Montage," *Science*, vol. 159, no. 3822, pp. 1464–1467, Mar. 1968, doi: 10.1126/science.159.3822.1464.

- [121] A. J. Koster, U. Ziese, A. J. Verkleij, A. H. Janssen, and K. P. de Jong, “Three-Dimensional Transmission Electron Microscopy: A Novel Imaging and Characterization Technique with Nanometer Scale Resolution for Materials Science,” *J. Phys. Chem. B*, vol. 104, no. 40, pp. 9368–9370, Oct. 2000, doi: 10.1021/jp0015628.
- [122] A. H. Janssen, C.-M. Yang, Y. Wang, F. Schüth, A. J. Koster, and K. P. de Jong, “Localization of Small Metal (Oxide) Particles in SBA-15 Using Bright-Field Electron Tomography,” *J. Phys. Chem. B*, vol. 107, no. 38, pp. 10552–10556, Sep. 2003, doi: 10.1021/jp034750h.
- [123] C. J. Gommers, K. de Jong, J.-P. Pirard, and S. Blacher, “Assessment of the 3D Localization of Metallic Nanoparticles in Pd/SiO₂ Cogelled Catalysts by Electron Tomography,” *Langmuir*, vol. 21, no. 26, pp. 12378–12385, Dec. 2005, doi: 10.1021/la051682c.
- [124] J. Miao, T. Ohsuna, O. Terasaki, K. O. Hodgson, and M. A. O’Keefe, “Atomic Resolution Three-Dimensional Electron Diffraction Microscopy,” *Phys. Rev. Lett.*, vol. 89, no. 15, p. 155502, Sep. 2002, doi: 10.1103/PhysRevLett.89.155502.
- [125] Y. Mao, B. P. Fahimian, S. J. Osher, and J. Miao, “Development and optimization of regularized tomographic reconstruction algorithms utilizing equally-sloped tomography,” *IEEE Trans Image Process*, vol. 19, no. 5, pp. 1259–1268, May 2010, doi: 10.1109/TIP.2009.2039660.
- [126] S. Bals *et al.*, “Quantitative Three-Dimensional Modeling of Zeolite Through Discrete Electron Tomography,” *J. Am. Chem. Soc.*, vol. 131, no. 13, pp. 4769–4773, Apr. 2009, doi: 10.1021/ja8089125.
- [127] P. A. Midgley, M. Weyland, J. M. Thomas, and B. F. G. Johnson, “Z-Contrast tomography: a technique in three-dimensional nanostructural analysis based on Rutherford scattering,” *Chem. Commun.*, no. 10, pp. 907–908, Jan. 2001, doi: 10.1039/B101819C.
- [128] I. Arslan, T. J. V. Yates, N. D. Browning, and P. A. Midgley, “Embedded Nanostructures Revealed in Three Dimensions,” *Science*, vol. 309, no. 5744, pp. 2195–2198, Sep. 2005, doi: 10.1126/science.1116745.
- [129] R. Krsmanović, S. Bals, G. Bertoni, and G. Van Tendeloo, “Structural characterization of Er-doped Li₂O–Al₂O₃–SiO₂ glass ceramics,” *Optical Materials*, vol. 30, no. 7, pp. 1183–1188, Mar. 2008, doi: 10.1016/j.optmat.2007.05.045.
- [130] L. C. Gontard, R. e. Dunin-Borkowski, and D. Ozkaya, “Three-dimensional shapes and spatial distributions of Pt and PtCr catalyst nanoparticles on carbon black,” *Journal of Microscopy*, vol. 232, no. 2, pp. 248–259, 2008, doi: 10.1111/j.1365-2818.2008.02096.x.
- [131] P. A. Crozier and T. W. Hansen, “*In situ* and *operando* transmission electron microscopy of catalytic materials,” *MRS Bull.*, vol. 40, no. 1, pp. 38–45, Jan. 2015, doi: 10.1557/mrs.2014.304.
- [132] J. F. Creemer *et al.*, “Atomic-scale electron microscopy at ambient pressure,” *Ultramicroscopy*, vol. 108, no. 9, pp. 993–998, Aug. 2008, doi: 10.1016/j.ultramic.2008.04.014.
- [133] R. T. K. Baker and P. S. Harris, “Controlled atmosphere electron microscopy,” *J. Phys. E: Sci. Instrum.*, vol. 5, no. 8, pp. 793–797, Aug. 1972, doi: 10.1088/0022-3735/5/8/024.
- [134] L. F. Allard, S. H. Overbury, W. C. Bigelow, M. B. Katz, D. P. Nackashi, and J. Damiano, “Novel MEMS-Based Gas-Cell/Heating Specimen Holder Provides Advanced Imaging Capabilities for *In Situ* Reaction Studies,” *Microsc Microanal*, vol. 18, no. 4, pp. 656–666, Aug. 2012, doi: 10.1017/S1431927612001249.
- [135] Y. Jiang, Z. Zhang, W. Yuan, X. Zhang, Y. Wang, and Z. Zhang, “Recent advances in gas-involved *in situ* studies via transmission electron microscopy,” *Nano Res.*, vol. 11, no. 1, pp. 42–67, Jan. 2018, doi: 10.1007/s12274-017-1645-9.

- [136] N. Ortiz Peña *et al.*, “*In situ* liquid transmission electron microscopy reveals self-assembly-driven nucleation in radiolytic synthesis of iron oxide nanoparticles in organic media,” *Nanoscale*, vol. 14, no. 30, pp. 10950–10957, 2022, doi: 10.1039/D2NR01511K.
- [137] N. Ahmad, G. Wang, J. Nelayah, C. Ricolleau, and D. Alloyeau, “Exploring the Formation of Symmetric Gold Nanostars by Liquid-Cell Transmission Electron Microscopy,” *Nano Lett.*, vol. 17, no. 7, pp. 4194–4201, Jul. 2017, doi: 10.1021/acs.nanolett.7b01013.
- [138] N. de Jonge, M. Pfaff, and D. B. Peckys, “Practical Aspects of Transmission Electron Microscopy in Liquid,” in *Advances in Imaging and Electron Physics*, vol. 186, Elsevier, 2014, pp. 1–37. doi: 10.1016/B978-0-12-800264-3.00001-0.
- [139] A. Khelfa, J. Nelayah, G. Wang, C. Ricolleau, and D. Alloyeau, “Studying the Effects of Temperature on the Nucleation and Growth of Nanoparticles by Liquid-Cell Transmission Electron Microscopy,” *JoVE*, no. 168, p. 62225, Feb. 2021, doi: 10.3791/62225.
- [140] D. Alloyeau *et al.*, “Unravelling Kinetic and Thermodynamic Effects on the Growth of Gold Nanoplates by Liquid Transmission Electron Microscopy,” *Nano Lett.*, vol. 15, no. 4, pp. 2574–2581, Apr. 2015, doi: 10.1021/acs.nanolett.5b00140.
- [141] E. Ruska, “Beitrag zur \diamond bermikroskopischen Abbildung bei h \diamond heren Drucken,” *Kolloid-Zeitschrift*, vol. 100, no. 2, pp. 212–219, Aug. 1942, doi: 10.1007/BF01519549.
- [142] J. B. Wagner, F. Cavalca, C. D. Damsgaard, L. D. L. Duchstein, and T. W. Hansen, “Exploring the environmental transmission electron microscope,” *Micron*, vol. 43, no. 11, pp. 1169–1175, Nov. 2012, doi: 10.1016/j.micron.2012.02.008.
- [143] P. L. Gai and K. Kourtakis, “Solid-State Defect Mechanism in Vanadyl Pyrophosphate Catalysts: Implications for Selective Oxidation,” *Science*, vol. 267, no. 5198, pp. 661–663, Feb. 1995, doi: 10.1126/science.267.5198.661.
- [144] J. Y. Huang, S. Chen, Z. F. Ren, G. Chen, and M. S. Dresselhaus, “Real-Time Observation of Tubule Formation from Amorphous Carbon Nanowires under High-Bias Joule Heating,” *Nano Lett.*, vol. 6, no. 8, pp. 1699–1705, Aug. 2006, doi: 10.1021/nl0609910.
- [145] P. A. Crozier, R. Sharma, and A. K. Datye, “Oxidation and Reduction of Small Palladium Particles on Silica,” *Microsc Microanal.*, vol. 4, no. 3, pp. 278–285, Jun. 1998, doi: 10.1017/S143192769898028X.
- [146] S. Helveg and P. L. Hansen, “Atomic-scale studies of metallic nanocluster catalysts by *in situ* high-resolution transmission electron microscopy,” *Catalysis Today*, vol. 111, no. 1–2, pp. 68–73, Jan. 2006, doi: 10.1016/j.cattod.2005.10.019.
- [147] J. R. Jinschek, “Advances in the environmental transmission electron microscope (ETEM) for nanoscale *in situ* studies of gas–solid interactions,” *Chem. Commun.*, vol. 50, no. 21, pp. 2696–2706, 2014, doi: 10.1039/C3CC49092K.
- [148] P. L. Hansen, J. B. Wagner, S. Helveg, J. R. Rostrup-Nielsen, B. S. Clausen, and H. Topsøe, “Atom-Resolved Imaging of Dynamic Shape Changes in Supported Copper Nanocrystals,” *Science*, vol. 295, no. 5562, pp. 2053–2055, Mar. 2002, doi: 10.1126/science.1069325.
- [149] J. F. Creemer, S. Helveg, P. J. Kooyman, A. M. Molenbroek, H. W. Zandbergen, and P. M. Sarro, “A MEMS Reactor for Atomic-Scale Microscopy of Nanomaterials Under Industrially Relevant Conditions,” *J. Microelectromech. Syst.*, vol. 19, no. 2, pp. 254–264, Apr. 2010, doi: 10.1109/JMEMS.2010.2041190.
- [150] S. Dai, S. Zhang, G. W. Graham, and X. Pan, “*In situ* Scanning Transmission Electron Microscopy with Atomic Resolution under Atmospheric Pressure,” *Microsc. Today*, vol. 27, no. 03, pp. 16–21, May 2019, doi: 10.1017/S1551929519000439.

- [151] I. M. Abrams and J. W. McBain, "A Closed Cell for Electron Microscopy," *Science*, vol. 100, no. 2595, pp. 273–274, Sep. 1944, doi: 10.1126/science.100.2595.273.
- [152] H. Hashimoto, T. Naiki, T. Eto, and K. Fujiwara, "High Temperature Gas Reaction Specimen Chamber for an Electron Microscope," *Jpn. J. Appl. Phys.*, vol. 7, no. 8, p. 946, Aug. 1968, doi: 10.1143/JJAP.7.946.
- [153] E. D. Boyes and P. L. Gai, "Environmental high resolution electron microscopy and applications to chemical science," *Ultramicroscopy*, vol. 67, no. 1–4, pp. 219–232, Jun. 1997, doi: 10.1016/S0304-3991(96)00099-X.
- [154] F. Zhang, M. Pen, R. G. Spruit, H. Perez Garza, W. Liu, and D. Zhou, "Data Synchronization in Operando Gas and Heating TEM," Chemistry, preprint, Oct. 2021. doi: 10.26434/chemrxiv-2021-j1t52.
- [155] B. Song *et al.*, "Revealing High-Temperature Reduction Dynamics of High-Entropy Alloy Nanoparticles via *In Situ* Transmission Electron Microscopy," *Nano Lett.*, vol. 21, no. 4, pp. 1742–1748, Feb. 2021, doi: 10.1021/acs.nanolett.0c04572.
- [156] X. Huang *et al.*, "Phase Coexistence and Structural Dynamics of Redox Metal Catalysts Revealed by Operando TEM," *Advanced Materials*, vol. 33, no. 31, p. 2101772, Aug. 2021, doi: 10.1002/adma.202101772.
- [157] T. W. Hansen, A. T. DeLaRiva, S. R. Challa, and A. K. Datye, "Sintering of Catalytic Nanoparticles: Particle Migration or Ostwald Ripening?," *Acc. Chem. Res.*, vol. 46, no. 8, pp. 1720–1730, Aug. 2013, doi: 10.1021/ar3002427.
- [158] M. de Assumpção Pereira-da-Silva and F. A. Ferri, "Scanning Electron Microscopy," in *Nanocharacterization Techniques*, Elsevier, 2017, pp. 1–35. doi: 10.1016/B978-0-323-49778-7.00001-1.
- [159] J. Epp, "X-ray diffraction (XRD) techniques for materials characterization," in *Materials Characterization Using Nondestructive Evaluation (NDE) Methods*, Elsevier, 2016, pp. 81–124. doi: 10.1016/B978-0-08-100040-3.00004-3.
- [160] L. Zhang, W. Shi, and B. Zhang, "A review of electrocatalyst characterization by transmission electron microscopy," *Journal of Energy Chemistry*, vol. 26, no. 6, pp. 1117–1135, Nov. 2017, doi: 10.1016/j.jechem.2017.10.016.
- [161] A. K. Datye and D. J. Smith, "The Study of Heterogeneous Catalysts by High-Resolution Transmission Electron Microscopy," *Catalysis Reviews*, vol. 34, no. 1–2, pp. 129–178, Feb. 1992, doi: 10.1080/01614949208021920.
- [162] C. Y. Tang and Z. Yang, "Transmission Electron Microscopy (TEM)," in *Membrane Characterization*, Elsevier, 2017, pp. 145–159. doi: 10.1016/B978-0-444-63776-5.00008-5.
- [163] S. J. Pennycook and P. D. Nellist, Eds., *Scanning Transmission Electron Microscopy*. New York, NY: Springer New York, 2011. doi: 10.1007/978-1-4419-7200-2.
- [164] S. Uhlemann and M. Haider, "Residual wave aberrations in the first spherical aberration corrected transmission electron microscope," *Ultramicroscopy*, vol. 72, no. 3–4, pp. 109–119, May 1998, doi: 10.1016/S0304-3991(97)00102-2.
- [165] "JEM-ARM 200F Atomic Resolution Analytical Microscope: Instruction Manual. JEOL Ltd." 2014.
- [166] P. E. Champness, *Electron Diffraction in the Transmission Electron Microscope*, 1st ed. Garland Science, 2020. doi: 10.1201/9781003076872.
- [167] D. A. Basha, J. M. Rosalie, H. Somekawa, T. Miyawaki, A. Singh, and K. Tsuchiya, "Microstructure study of a severely plastically deformed Mg-Zn-Y alloy by application of low angle annular dark field diffraction contrast imaging," *Science and Technology of Advanced Materials*, vol. 17, no. 1, pp. 115–127, Jan. 2016, doi: 10.1080/14686996.2016.1140304.

- [168] R. Van Grieken and A. Markowicz, Eds., *Handbook of X-Ray Spectrometry*, 0 ed. CRC Press, 2001. doi: 10.1201/9780203908709.
- [169] “Centurio Large Angle SDD-EDS | JEOL Benelux.” Accessed: Jun. 15, 2023. [Online]. Available: <https://www.jeolbenelux.com/JEOL-BV-News/centurio-large-angle-sdd-eds>
- [170] R. Hovden and D. A. Muller, “Electron tomography for functional nanomaterials,” *MRS Bull.*, vol. 45, no. 4, pp. 298–304, Apr. 2020, doi: 10.1557/mrs.2020.87.
- [171] J. Radon, “Mathematische-Physische,” p. 262, 1917.
- [172] C. Messaoudi, T. Boudier, C. O. S. Sorzano, and S. Marco, “TomoJ: tomography software for three-dimensional reconstruction in transmission electron microscopy,” *BMC Bioinformatics*, vol. 8, no. 1, p. 288, Dec. 2007, doi: 10.1186/1471-2105-8-288.
- [173] Y. Liu, P. A. Penczek, B. F. McEwen, and J. Frank, “A marker-free alignment method for electron tomography,” *Ultramicroscopy*, vol. 58, no. 3–4, pp. 393–402, Jun. 1995, doi: 10.1016/0304-3991(95)00006-m.
- [174] J. R. Kremer, D. N. Mastrorade, and J. R. McIntosh, “Computer visualization of three-dimensional image data using IMOD,” *J Struct Biol*, vol. 116, no. 1, pp. 71–76, 1996, doi: 10.1006/jsbi.1996.0013.
- [175] P. D. C. Kübel, “INT- Research - Microscopy Development - Electron Tomography.” Accessed: Jun. 21, 2023. [Online]. Available: <https://www.int.kit.edu/1731.php>
- [176] M. Radermacher, “Weighted Back-projection Methods,” in *Electron Tomography: Methods for Three-Dimensional Visualization of Structures in the Cell*, J. Frank, Ed., New York, NY: Springer, 2006, pp. 245–273. doi: 10.1007/978-0-387-69008-7_9.
- [177] A. Klug and R. A. Crowther, “Three-dimensional Image Reconstruction from the Viewpoint of information Theory,” *Nature*, vol. 238, no. 5365, Art. no. 5365, Aug. 1972, doi: 10.1038/238435a0.
- [178] H. Friedrich, P. E. de Jongh, A. J. Verkleij, and K. P. de Jong, “Electron Tomography for Heterogeneous Catalysts and Related Nanostructured Materials,” *Chem. Rev.*, vol. 109, no. 5, pp. 1613–1629, May 2009, doi: 10.1021/cr800434t.
- [179] M. Xu and P. Thulasiraman, “Mapping Iterative Medical Imaging Algorithm on Cell Accelerator,” *International Journal of Biomedical Imaging*, vol. 2011, pp. 1–11, 2011, doi: 10.1155/2011/843924.
- [180] Q. Zheng, J. Jiang, X. Li, K. C. Bustillo, and H. Zheng, “In situ TEM observation of calcium silicate hydrate nanostructure at high temperatures,” *Cement and Concrete Research*, vol. 149, p. 106579, Nov. 2021, doi: 10.1016/j.cemconres.2021.106579.
- [181] K. A. Unocic *et al.*, “Performing In Situ Closed-Cell Gas Reactions in the Transmission Electron Microscope,” *JoVE*, no. 173, p. 62174, Jul. 2021, doi: 10.3791/62174.
- [182] “Protochips, Inc., Atmosphere: User manual.” 2020.
- [183] L. Sun, K. W. Noh, J.-G. Wen, and S. J. Dillon, “In Situ Transmission Electron Microscopy Observation of Silver Oxidation in Ionized/Atomic Gas,” *Langmuir*, vol. 27, no. 23, pp. 14201–14206, Dec. 2011, doi: 10.1021/la202949c.
- [184] “Stanford Research Systems (SRS), RGA100, RGA200, and RGA300 Residual Gas Analyzer: Operating manuel and programming reference.” 2009.
- [185] Y. Wang, Q. Liu, Y. Sun, and R. Wang, “Magnetic field modulated SERS enhancement of CoPt hollow nanoparticles with sizes below 10 nm,” *Nanoscale*, vol. 10, no. 26, pp. 12650–12656, Jul. 2018, doi: 10.1039/C8NR03781G.
- [186] R. Devivaraprasad, R. Ramesh, N. Naresh, T. Kar, R. K. Singh, and M. Neergat, “Oxygen Reduction Reaction and Peroxide Generation on Shape-Controlled and Polycrystalline Platinum Nanoparticles in Acidic and Alkaline Electrolytes,” *Langmuir*, vol. 30, no. 29, pp. 8995–9006, Jul. 2014, doi: 10.1021/la501109g.
- [187] D. Alloyeau, C. Langlois, C. Ricolleau, Y. Le Bouar, and A. Loiseau, “A TEM *in situ* experiment as a guideline for the synthesis of as-grown ordered CoPt nanoparticles,”

- Nanotechnology*, vol. 18, no. 37, p. 375301, Sep. 2007, doi: 10.1088/0957-4484/18/37/375301.
- [188] B. Farkaš, C. B. Perry, G. Jones, and N. H. de Leeuw, “Adsorbate-Induced Segregation of Cobalt from PtCo Nanoparticles: Modeling Au Doping and Core AuCo Alloying for the Improvement of Fuel Cell Cathode Catalysts,” *J. Phys. Chem. C*, vol. 124, no. 33, pp. 18321–18334, Aug. 2020, doi: 10.1021/acs.jpcc.0c04460.
- [189] Z. Liu, Y. Lei, and G. Wang, “First-principles computation of surface segregation in L10 CoPt magnetic nanoparticles,” *J. Phys.: Condens. Matter*, vol. 28, no. 26, p. 266002, May 2016, doi: 10.1088/0953-8984/28/26/266002.
- [190] Z. Yu *et al.*, “Comparison between Dealloyed PtCo₃ and PtCu₃ Cathode Catalysts for Proton Exchange Membrane Fuel Cells,” *J. Phys. Chem. C*, vol. 116, no. 37, pp. 19877–19885, Sep. 2012, doi: 10.1021/jp306107t.
- [191] A. C. Foucher *et al.*, “Structural and Valence State Modification of Cobalt in CoPt Nanocatalysts in Redox Conditions,” *ACS Nano*, vol. 15, no. 12, pp. 20619–20632, Dec. 2021, doi: 10.1021/acsnano.1c09450.
- [192] D. Yi *et al.*, “Epsilon Cobalt Nanoparticles as Highly Performant Catalysts in Cinnamaldehyde Selective Hydrogenation,” 2022.
- [193] A. F. Khusnuriyalova, M. Caporali, E. Hey-Hawkins, O. G. Sinyashin, and D. G. Yakhvarov, “Preparation of Cobalt Nanoparticles,” *European Journal of Inorganic Chemistry*, vol. 2021, no. 30, pp. 3023–3047, 2021, doi: 10.1002/ejic.202100367.
- [194] V. F. Puentes, K. M. Krishnan, and A. P. Alivisatos, “Colloidal Nanocrystal Shape and Size Control: The Case of Cobalt,” vol. 291, 2001.
- [195] O. Ersen, “Exploring nanomaterials with 3D electron microscopy,” *Materials Today*, vol. 00, no. 00, 2015.
- [196] L. Zhang *et al.*, “Platinum-based nanocages with subnanometer-thick walls and well-defined, controllable facets,” *Science*, vol. 349, no. 6246, pp. 412–416, Jul. 2015, doi: 10.1126/science.aab0801.
- [197] E. González *et al.*, “Enhanced reactivity of high-index surface platinum hollow nanocrystals,” *J. Mater. Chem. A*, vol. 4, no. 1, pp. 200–208, 2016, doi: 10.1039/C5TA07504A.
- [198] H. Zhang *et al.*, “Facile Synthesis of Pd–Pt Alloy Nanocages and Their Enhanced Performance for Preferential Oxidation of CO in Excess Hydrogen,” *ACS Nano*, vol. 5, no. 10, pp. 8212–8222, Oct. 2011, doi: 10.1021/nn202896q.
- [199] F. Merkoçi *et al.*, “Understanding galvanic replacement reactions: the case of Pt and Ag,” *Materials Today Advances*, vol. 5, p. 100037, Mar. 2020, doi: 10.1016/j.mtadv.2019.100037.
- [200] J. (Jeffery) Pan, “Facets Engineering on Catalysts,” in *Heterogeneous Catalysts*, John Wiley & Sons, Ltd, 2021, pp. 21–37. doi: 10.1002/9783527813599.ch2.
- [201] J. Krajczewski, “Enhanced catalytic activity of solid and hollow platinum-cobalt nanoparticles towards reduction of 4-nitrophenol,” *Applied Surface Science*, 2016.
- [202] G. Prieto, H. Tu, and F. Schu, “Hollow Nano- and Microstructures as Catalysts,” *Chem. Rev.*, 2016.
- [203] X. Liang *et al.*, “Diffusion through the Shells of Yolk–Shell and Core–Shell Nanostructures in the Liquid Phase,” *Angewandte Chemie International Edition*, vol. 51, no. 32, pp. 8034–8036, 2012, doi: 10.1002/anie.201203456.
- [204] X. Fang *et al.*, “Precisely controlled resorcinol–formaldehyde resin coating for fabricating core–shell, hollow, and yolk–shell carbon nanostructures,” *Nanoscale*, vol. 5, no. 15, pp. 6908–6916, Jul. 2013, doi: 10.1039/C3NR01723K.

- [205] M. A. Mahmoud, R. Narayanan, and M. A. El-Sayed, "Enhancing Colloidal Metallic Nanocatalysis: Sharp Edges and Corners for Solid Nanoparticles and Cage Effect for Hollow Ones".
- [206] M. A. Mahmoud, F. Saira, and M. A. El-Sayed, "Experimental Evidence For The Nanocage Effect In Catalysis With Hollow Nanoparticles," *Nano Lett.*, 2010.
- [207] M. A. Mahmoud, B. Snyder, and M. A. El-Sayed, "Polystyrene Microspheres: Inactive Supporting Material for Recycling and Recovering Colloidal Nanocatalysts in Solution," ACS Publications. Accessed: Oct. 06, 2023. [Online]. Available: <https://pubs.acs.org/doi/pdf/10.1021/jz9000449>
- [208] G. Weng, M. A. Mahmoud, and M. A. El-Sayed, "Nanocatalysts Can Change the Number of Electrons Involved in Oxidation–Reduction Reaction with the Nanocages Being the Most Efficient," *J. Phys. Chem. C*, vol. 116, no. 45, pp. 24171–24176, Nov. 2012, doi: 10.1021/jp308869m.
- [209] C. H. Bartholomew, "Sintering and redispersion of supported metals: Perspectives from the literature of the past decade," in *Studies in Surface Science and Catalysis*, vol. 111, Elsevier, 1997, pp. 585–592. doi: 10.1016/S0167-2991(97)80203-0.
- [210] I. K. Ravenhorst *et al.*, "In Situ Local Temperature Mapping in Microscopy Nano-Reactors with Luminescence Thermometry," *ChemCatChem*, vol. 11, no. 22, pp. 5505–5512, Nov. 2019, doi: 10.1002/cctc.201900985.
- [211] S. Pfaff, H. Karlsson, F. A. Nada, E. Lundgren, and J. Zetterberg, "Temperature characterization of an operando flow reactor for heterogeneous catalysis," *J. Phys. D: Appl. Phys.*, vol. 52, no. 32, p. 324003, Aug. 2019, doi: 10.1088/1361-6463/ab236e.
- [212] Q. Chen, Y. Nie, M. Ming, G. Fan, Y. Zhang, and J.-S. Hu, "Sustainable synthesis of supported metal nanocatalysts for electrochemical hydrogen evolution," *Chinese Journal of Catalysis*, vol. 41, no. 12, pp. 1791–1811, Dec. 2020, doi: 10.1016/S1872-2067(20)63652-X.
- [213] S. J. Oh and J.-H. Lee, "Preparation and oxidation behaviour of cobalt-coated copper powder," *Micro & Nano Letters*, vol. 12, no. 10, pp. 717–721, 2017, doi: 10.1049/mnl.2017.0086.
- [214] T. Tokunaga, K. Saito, K. Kuno, K. Higuchi, Y. Yamamoto, and T. Yamamoto, "Removal of carbon contamination in ETEM by introducing Ar during electron beam irradiation," *J Microsc.*, vol. 273, no. 1, pp. 46–52, Jan. 2019, doi: 10.1111/jmi.12759.
- [215] C. G. Granqvist and R. A. Buhrman, "Statistical model for coalescence of islands in discontinuous films," *Applied Physics Letters*, vol. 27, no. 12, pp. 693–694, Dec. 1975, doi: 10.1063/1.88342.
- [216] I. M. Lifshitz and V. V. Slyozov, "The kinetics of precipitation from supersaturated solid solutions," *Journal of Physics and Chemistry of Solids*, vol. 19, no. 1–2, pp. 35–50, Apr. 1961, doi: 10.1016/0022-3697(61)90054-3.
- [217] "C. Wagner, 'Theorie der Alterung von Niederschlagen durch Umlosen (Ostwald-Reifung),' *Z. Elektrochem.*, Vol. 65, No. 7-8, 1961, p. 581-591."
- [218] P. Wynblatt and N. A. Gjostein, "Supported metal crystallites," *Progress in Solid State Chemistry*, vol. 9, pp. 21–58, Jan. 1975, doi: 10.1016/0079-6786(75)90013-8.
- [219] S. B. Simonsen *et al.*, "Effect of Particle Morphology on the Ripening of Supported Pt Nanoparticles," *J. Phys. Chem. C*, vol. 116, no. 9, pp. 5646–5653, Mar. 2012, doi: 10.1021/jp2098262.
- [220] A. K. Datye, Q. Xu, K. C. Kharas, and J. M. McCarty, "Particle size distributions in heterogeneous catalysts: What do they tell us about the sintering mechanism?," *Catalysis Today*, vol. 111, no. 1–2, pp. 59–67, Jan. 2006, doi: 10.1016/j.cattod.2005.10.013.

- [221] L. Jiang *et al.*, “Theoretical Investigation on the Thermal Stability of Hollow Gold Nanoparticles,” *J. Phys. Chem. C*, vol. 113, no. 47, pp. 20193–20197, Nov. 2009, doi: 10.1021/jp905280g.
- [222] L. Dubau *et al.*, “Defects do Catalysis: CO Monolayer Oxidation and Oxygen Reduction Reaction on Hollow PtNi/C Nanoparticles,” *ACS Catal.*, vol. 6, no. 7, pp. 4673–4684, Jul. 2016, doi: 10.1021/acscatal.6b01106.
- [223] P. N. Reyes *et al.*, “The stability of hollow nanoparticles and the simulation temperature ramp,” *Inorg. Chem. Front.*, vol. 5, no. 5, pp. 1139–1144, May 2018, doi: 10.1039/C7QI00822H.
- [224] E. Prestat, R. Popescu, H. Blank, R. Schneider, and D. Gerthsen, “Coarsening of Pt nanoparticles on amorphous carbon film,” *Surface Science*, vol. 609, pp. 195–202, Mar. 2013, doi: 10.1016/j.susc.2012.12.014.
- [225] A. Beck, H. Frey, M. Becker, L. Artiglia, M. G. Willinger, and J. A. van Bokhoven, “Influence of Hydrogen Pressure on the Structure of Platinum–Titania Catalysts,” *J. Phys. Chem. C*, vol. 125, no. 41, pp. 22531–22538, Oct. 2021, doi: 10.1021/acs.jpcc.1c05939.
- [226] P. C. Okonkwo *et al.*, “Platinum degradation mechanisms in proton exchange membrane fuel cell (PEMFC) system: A review,” *International Journal of Hydrogen Energy*, vol. 46, no. 29, pp. 15850–15865, Apr. 2021, doi: 10.1016/j.ijhydene.2021.02.078.
- [227] S. B. Simonsen, I. Chorkendorff, S. Dahl, M. Skoglundh, J. Sehested, and S. Helveg, “Direct Observations of Oxygen-induced Platinum Nanoparticle Ripening Studied by In Situ TEM,” *J. Am. Chem. Soc.*, vol. 132, no. 23, pp. 7968–7975, Jun. 2010, doi: 10.1021/ja910094r.
- [228] S. B. Simonsen, I. Chorkendorff, S. Dahl, M. Skoglundh, J. Sehested, and S. Helveg, “Ostwald ripening in a Pt/SiO₂ model catalyst studied by in situ TEM,” *Journal of Catalysis*, vol. 281, no. 1, pp. 147–155, Jul. 2011, doi: 10.1016/j.jcat.2011.04.011.
- [229] P. Wynblatt and N. A. Gjostein, “Particle growth in model supported metal catalysts—I. Theory,” *Acta Metallurgica*, vol. 24, no. 12, pp. 1165–1174, Dec. 1976, doi: 10.1016/0001-6160(76)90034-1.
- [230] S. Horch *et al.*, “Enhancement of surface self-diffusion of platinum atoms by adsorbed hydrogen,” *Nature*, vol. 398, no. 6723, pp. 134–136, Mar. 1999, doi: 10.1038/18185.
- [231] S. Alayoglu *et al.*, “CO₂ Hydrogenation Studies on Co and CoPt Bimetallic Nanoparticles Under Reaction Conditions Using TEM, XPS and NEXAFS,” *Top Catal.*, vol. 54, no. 13–15, pp. 778–785, Sep. 2011, doi: 10.1007/s11244-011-9695-9.
- [232] P. Karipoth and R. J. Joseyphus, “Evolution of High Coercivity in CoPt Nanoparticles Through Nitrogen Assisted Annealing,” *J Supercond Nov Magn*, vol. 27, no. 9, pp. 2123–2130, Sep. 2014, doi: 10.1007/s10948-014-2564-6.
- [233] X. Sun *et al.*, “Synthesis and magnetic properties of CoPt nanoparticles,” *Journal of Applied Physics*, vol. 95, no. 11, pp. 6747–6749, May 2004, doi: 10.1063/1.1667441.
- [234] J. D. Lee *et al.*, “Tuning the Electrocatalytic Oxygen Reduction Reaction Activity of Pt–Co Nanocrystals by Cobalt Concentration with Atomic-Scale Understanding,” *ACS Appl. Mater. Interfaces*, vol. 11, no. 30, pp. 26789–26797, Jul. 2019, doi: 10.1021/acsami.9b06346.
- [235] S. Xu *et al.*, “CO Poisoning of Ru Catalysts in CO₂ Hydrogenation under Thermal and Plasma Conditions: A Combined Kinetic and Diffuse Reflectance Infrared Fourier Transform Spectroscopy–Mass Spectrometry Study,” *ACS Catal.*, vol. 10, no. 21, pp. 12828–12840, Nov. 2020, doi: 10.1021/acscatal.0c03620.
- [236] S. W. Chee, J. M. Arce-Ramos, W. Li, A. Genest, and U. Mirsaidov, “Structural changes in noble metal nanoparticles during CO oxidation and their impact on catalyst activity,” *Nat Commun*, vol. 11, no. 1, Art. no. 1, May 2020, doi: 10.1038/s41467-020-16027-9.

- [237] J. Ma *et al.*, “A short review of catalysis for CO₂ conversion,” *Catalysis Today*, vol. 148, no. 3–4, pp. 221–231, Nov. 2009, doi: 10.1016/j.cattod.2009.08.015.
- [238] X. Wang, J. Pan, H. Wei, W. Li, J. Zhao, and Z. Hu, “Mechanism of Methanol Synthesis from CO₂ Hydrogenation over Pt₈/In₂O₃ Catalysts: A Combined Study on Density Functional Theory and Microkinetic Modeling,” *J. Phys. Chem. C*, vol. 126, no. 4, pp. 1761–1769, Feb. 2022, doi: 10.1021/acs.jpcc.1c08098.
- [239] S. B. Simonsen, Y. Wang, J. O. Jensen, and W. Zhang, “Coarsening of carbon black supported Pt nanoparticles in hydrogen,” *Nanotechnology*, vol. 28, no. 47, p. 475710, Nov. 2017, doi: 10.1088/1361-6528/aa91a8.
- [240] A. E. Turner, C. W. Johnson, P. Kruit, and B. J. McMorran, “Interaction-Free Measurement with Electrons,” *Phys. Rev. Lett.*, vol. 127, no. 11, p. 110401, Sep. 2021, doi: 10.1103/PhysRevLett.127.110401.
- [241] “Rio Camera | Gatan, Inc.” Accessed: Jun. 12, 2023. [Online]. Available: <https://www.gatan.com/products/tem-imaging-spectroscopy/rio-camera>
- [242] D. E. Newbury, “Mistakes encountered during automatic peak identification of minor and trace constituents in electron-excited energy dispersive X-ray microanalysis: Automatic peak identification,” *Scanning*, vol. 31, no. 3, pp. 91–101, May 2009, doi: 10.1002/sca.20151.
- [243] “quantitative correction | Glossary | JEOL Ltd.,” quantitative correction | Glossary | JEOL Ltd. Accessed: Sep. 25, 2023. [Online]. Available: <https://www.jeol.com/>